Doctoral Dissertation
Doctoral Program in Chemical Engineering (30th Cycle)

Design of Visible Light Driven Bismuth based Catalysts for Degradation of Organic Pollutants

By

Tanveer Ahmed Gadhi

******

Supervisor:
Prof. Alberto Tagliaferro

Doctoral Examination Committee:

Prof. Enzo Laurenti, Referee, Università degli Studi di Torino (Italy)

Prof. Andreas Zeinert, Referee, Université de Picardie Jules Verne (France)

Prof. Antonio Arques Sanz, Universitat Politècnica de València (Spain)

Prof. Maria Cristina Paganini, Università degli Studi di Torino (Italy)

Prof. Monica Ferraris, Politecnico di Torino (Italy)

Prof. Alberto Tagliaferro, Politecnico di Torino (Italy)

Politecnico di Torino
2017

Declaration

I hereby declare that, the contents and organization of this dissertation constitute my own original work and does not compromise in any way the rights of third parties, including those relating to the security of personal data.

Tanveer Ahmed Gadhi

2017

* This dissertation is presented in partial fulfillment of the requirements for **Ph.D. degree** in the Graduate School of Politecnico di Torino (ScuDo).

I would like to dedicate this thesis to my family and well-wishers.

“Ô, Sunlight! The most precious gold to be found on Earth.” by **Roman Payne.**

Acknowledgment

Foremost, I want to share my gratitude to prof. Alberto Tagliaferro for providing me opportunity to pursue Ph.D under his supervision and further his continuous support.

Thanks to Dr. Pravin Jagdale and Dr. Mauro Giorcelli for their assistance in all the research activities. A great thanks to Dr. Simelys Hernández, who helped me in shaping and refining most of my research work.

Many thanks to Dr. Mauro Raimondo, Dr. Micaella Castellino, Dr. Stefano Bianco and Dr. Fabio Deorsola for their technical assistance in characterization.

A sincere gratitude to Prof. Sandra E. Rodil, Prof. Monserrat Bizzaro and Prof. Agileo Hernández from the Universidad Nacional Autónoma de México, for their support, guidance and valuable discussion during research work in Mexico.

Many thanks to Prof. Franco Gaspari and Dr. Simone Quaranta, from the University of Ontario Institute of Technology, for assistance during research work and stay in Canada.

Especial thanks to Dr. Alessandro Chiado, Dr. Stefano Ansaloni, Dr. Andrea Massa, Dr. Mouli Thalluri for their assistance in labs at Poli(TO).

Further, acknowledgment to the Higher Education Commission, Pakistan for providing me scholarship to pursue Masters and Doctorate studies. Sincere thanks to all the HEC colleagues and other friends from Pakistan, for their everlasting love and support, during stay in Italy.

Finally, I would like to thank my parents, my wife and kids Mayeda and Tabrez for their everlasting love and motivation.

Abstract

This Ph.D. thesis deals with the synthesis, immobilization of bismuth-based nanostructures and their photocatalytic evaluation for degradation of organic pollutants mainly dyes, with the aim to optimize synthesis and photo-evaluation conditions by focusing the practical application of heterogeneous photocatalysis. Initially, various bismuth based single structures α-Bi_2O_3, $Bi_5O_7NO_3$ and heterostructures α/β-Bi_2O_3, β-$Bi_2O_3/Bi_5O_7NO_3$ were synthesized by a simple and scalable route *i.e.* thermal decomposition of precursor salt. Properties such as crystallinity, composition, morphology and optical parameters were tuned by simply varying the calcination temperature. Heterostructures of α/β-Bi_2O_3, β-$Bi_2O_3/Bi_5O_7NO_3$ are well crystallized, formed stable composites (originated from single precursor salt) and eventually improved the stability of β-Bi_2O_3 (a metastable form) in the heterojunction structure. Single structures and heterostructures were evaluated for photodegradation of various dyes (differ in chemical structures and ionic behaviors) under visible and UV light. Test were conducted on single dyes or mixed solution of 2/3 dyes to assess the photocatalytic mechanism and kinetics when dealing the mixed effluent. From the obtained results, it was observed that α/β-Bi_2O_3 and β-$Bi_2O_3/Bi_5O_7NO_3$ heterostructures have higher photocatalytic response due to efficient cascade of electrons and holes within the tuned heterojunction and band alignments. Moreover, different dyes interact differently with the photocatalyst and resulted in changed kinetics, while mechanism of degradation depended upon their ionic behavior. Furthermore, during degradation of mixed solution; dyes that have higher interaction (with photocatalyst) and low absorptivity preferentially degraded earlier.

Afterwards, α/β-Bi_2O_3 were used to investigate and distinguish coexisting processes during photocatalysis: (i) intense adsorption, (ii) dye photobleaching and sensitization assisted photodegradation and (iii) partial or complete

mineralization. It was found that some dyes with Azo (N=N) and sulphonic groups have intense adsorption over photocatalyst surface and discoloration could occur without photocatalysis. Further, it was revealed that under controlled conditions, the other coexisted processes hardly occur during photocatalysis. Moreover, indigo carmine (IC) dye was found appropriate for preliminary photo-evaluation because its discoloration/removal process could be directly associated with photocatalytic oxidation by analyzing some identified spectral changes in UV-vis absorbance spectrum. Moreover, it was highlighted that dye chromophoric groups react readily and are easily attacked by the originated photocatalytic reactive species and partially mineralized, while further degradation of resulted intermediates containing phenyl groups, became more difficult to oxidize or reduce to achieve complete mineralization.

In addition, to investigate and identify the mechanism and the path of photodegradation of the investigated dyes, two approaches were used: 1) the photo-evaluation of dyes in presence of quenchers of hole, atomic oxygen and hydroxyl radical *i.e.* triethyl amine (TEA), P-benzoquinone (BQ) isopropanol (IP) and, respectively and 2) Evolution of O_2 after water oxidation. From the experimental results it was observed, that the photocatalytic activity eventually reduced in presence of quenchers as they quench the originated reactive radical species. Moreover, evolved O_2 during water splitting confirmed that electrons and holes are well separated and able to generate reactive oxygen and radical species for photodegradation and partial mineralization of dyes.

Thereafter, the work was focused to tackle the challenges of powder photocatalyst recovery and to explore a competing route, *i.e.* immobilized fixed support. Glass, steel mesh and sintered silica were used for photocatalyst immobilization to solve the problems associated to photocatalyst recovery, mass limitation and low interaction of pollutants with fixed photocatalyst supports. The immobilization/deposition of β-Bi_2O_3 over each support, was achieved by

pneumatic spray pyrolysis and subsequent calcination at 450 °C. During photo-evaluation of different β-Bi_2O_3 immobilized supports; deposited sintered silica exhibited higher activity and competing response to β-Bi_2O_3 powder. The improved activity of sintered silica was associated to the rough, porous and hydrophilic nature of silica that have facilitated in providing higher interaction of deposited β-Bi_2O_3 films with dye molecules. Furthermore, β-Bi_2O_3 deposited sintered silica exhibited improved performance for photodegradation and mineralization of various dyes of different chemical structures and ionic behaviors and cyclic stability up to 3 cycles.

Then, the work was focused to obtain single structure ferromagnetic bismuth ferrite ($BiFeO_3$) and its heterostructure ($BiFeO_3/Fe_2O_3/Bi_2Fe_4O_9$); as they have the advantage of easy magnetic separation from aqueous solution. The single structure $BiFeO_3$ and its heterostructures were obtained by using Sol-Gel method, in which precursor solution, containing dissolved $Bi(NO_3)_3{:}5H_2O$ and $Fe(NO_3)_3{:}9H_2O$ were preheated and calcined at 500°C with and without addition of Polyethylene Glycol (PEG) and NaOH in the precursor solution. From the XRD and UV-vis DRS analysis it was observed that addition of PEG and NaOH, assisted to obtain single nanostructure $BiFeO_3$, simply by enabling the particles polymerization and inhibiting the formation of other compounds like Fe_2O_3 and $Bi_2Fe_4O_9$. It was revealed that single phase $BiFeO_3$ is antiferromagnetic in nature and have very low photocatalytic response, due to the low energy band gap and high electron and holes recombination rate. On the other hand, $BiFeO_3/Fe_2O_3/Bi_2Fe_4O_9$ heterostructure displayed high magnetic saturation and exhibited improved photoactivity. This is due to a low electrons and holes recombination rate because of tuned band alignment and charge transfer within the heterojunction interfaces. Cyclic stability and photocatalytic performance of $BiFeO_3/Fe_2O_3/Bi_2Fe_4O_9$ were found almost similar during photodegradation of various dyes up to 3 cycles. At the end, detailed analyses of the efficient

heterostructure α/β-Bi_2O_3 and promising β-Bi_2O_3 immobilized silica were made, for the evaluation of bulk single and mixed dye solutions under natural sunlight and at varying IC dye concentrations. It was found that the mechanism and the photodegradation kinetics were almost similar amongst lab conditions and during sunlight irradiation and for bulk solutions of single and mixed dyes. Moreover, the experienced phenomena of the degradation and achieved kinetic rate at varying IC concentration were almost alike for both α/β-Bi_2O_3 and deposited β-Bi_2O_3 sintered silica. These results revealed that deposited β-Bi_2O_3 sintered silica could have the promising potential over α/β-Bi_2O_3 or any other powder photocatalyst under solar light irradiation. Moreover, cyclic stability and the photoactivity of both α/β-Bi_2O_3 and deposited β-Bi_2O_3 silica were almost identical up to 3 cycles.

Contents

1. Introduction and Background of the Study 1

1.1 Advanced oxidation processes (AOP) and heterogeneous photocatalysis 1

1.2 Challenges for Heterogeneous photocatalysis (HP) 3

1.3 Important aspects of photocatalysts and their synthesis 5

1.4 Important aspects of pollutants under investigation 6

1.5 Bismuth based materials as photocatalyst 8

1.5.1 Bismuth Oxide (Bi_2O_3) 9

1.5.2 Bismuth Oxy-Nitrates 10

1.5.3 Bismuth Ferrite ($BiFeO_3$ or BFO) 11

1.6 Objectives and structure of thesis 14

2. Solid-state Synthesis of $Bi_5O_7NO_3$, β-Bi_2O_3/$Bi_5O_7NO_3$ heterostructures and α-Bi_2O_3 and photocatalytic degradation of dyes under visible light 16

2.1 Introduction 16

2.2 Experimental..18

2.2.1 Synthesis 18

2.2.2 Characterization 18

2.2.3 Organic dyes photocatalytic degradation..20

2.2.4 Photocatalytic water oxidation..21

2.3 Results and discussion...21

2.3.1 TGA analysis 21

2.3.2 XRD 22

2.3.3 FESEM...24

2.3.4 Optical properties..25

2.3.5 Chemical composition (XPS) 27

2.3.6 Photocatalytic dyes degradation 30

2.4 Conclusion 36

3. α/β-Bi_2O_3 Heterostructure for Sequential Photodegradation of Single and Mixed Dye Solutions 38

3.1 Introduction 38

3.2 Experimental details 39

3.2.1 Synthesis of Bi_2O_3 powders 39

3.2.2 Characterization 40

3.2.3 Photocatalysis Tests 40

3.3. Results and discussion 41

3.3.1 Characterization of Bi_2O_3 41

3.3.2 Individual dye photodegradation 45

3.3.3 Mixed solution (IC and RhB) photodegradation 51

3.3.4 Mixed solution (all 3 dyes) photodegradation 53

3.3.4.1 As prepared mixed solution (pH-6.5) 53

3.3.4.2 Mixed solution at basic condition (pH-9.5) 54

3.3.5 Analysis of the degradation path 55

3.3.6 Photodegradation mechanism of single and mixed dyes 57

3.4 Conclusion 58

4. Distinguishing different Co-Existed Processes during Photocatalysis of Dyes: Adsorption, Photodiscoloration, Photodegradation and Mineralization..........59

4.1 Introduction 59

4.2. Photocatalysis Tests Methodology 63

4.2.1 Photolysis 64

4.2.2 Adsorption 64

4.2.3 Dye sensitization 64
4.2.4 Photodegradation 65

4.2.5 Mineralization 65
4.3 Results and Discussion 65
4.3.1 Photocatalysis 65
4.3.2 Photodegradation pathway 72
4.4 Conclusion 75
5. β-Bi_2O_3 Films Deposited on different Substrates by Pneumatic Spray Pyrolysis and their Photo-evaluation for Degradation of different types of Organic Dyes 77
5.1 Introduction 77
5.2 Experimental work 79
5.2.1 Characteristic of substrates 79
5.2.2 Films immobilization 79
5.2.3 Characterization of films 80
5.2.4 Photocatalysis Tests 80
5.3 Results and discussion 81
5.3.1 Characterization of the films 81
5.3.2 Photocatalysis 84
5.3.3 Photocatalytic mechanism for deposited silica 89
5.4 Conclusion 90
6. $BiFeO_3$ and $Bi_2Fe_4O_9$/Fe_2O_3/$BiFeO_3$ ferromagnetic heterostructures and their role in visible light driven photocatalysis for organic dyes degradation and O_2 evolution 92
6.1 Introduction 92
6.2 Experimental 94
6.2.1 Synthesis 94

6.2.2 Characterization 95
6.2.3 Photocatalysis 95
6.3 Results and Discussion 96

6.3.1 Crystalline Structure 96
6.3.2 Morphology 97
6.3.3 Magnetization 99
6.3.4 Optical Properties 100
6.3.5 Band edges positions 102
6.3.6 Photocatalysis 103
6.4 Conclusion 108
7. Photocatalytic Evaluation and Comparison of Heterostructure α/β-Bi_2O_3 and β-Bi_2O_3 Deposited Sintered Silica for Degradation of Single and Mixed Dyes in bulk solutions under natural sunlight 110
7.1 Introduction 110
7.2 Experimental 111
7.2.1 Synthesis 111
7.2.2 Characterization 112
7.2.3 Photocatalytic Evaluation 113
7.3 Results and Discussion 114
7.3.1 Characterization 114
7.3.2 Photocatalysis 118
7.3.3 Cyclic stability 123
8. References 125

List of Figures

Fig. 1.1 Basic Principle of heterogeneous photocatalysis, showing 1) interaction and transfer towards photocatalyst surface, 2) adsorption of primary (green) and secondary intermediates (yellow), 3) chemical reaction(s) between pollutants and photocatalyst and 4) detachment of by products from photocatalyst surface……. 2

Fig. 1.2 Photocatalytic schematic showing; A) the transfer of electron from valence band (VB) to conduction band (CB) and B) performing oxidation and reduction reactions on photocatalyst surface. …………………………………… 3

Fig. 1.3 Examples of A) slurry based rector and B) immobilized fixed support….4

Fig. 1.4. Scheme for photocatalyst redox potential vs normal Hydrogen electrode (NHE) in case of, a) single and b) coupled photocatalyst…………………………5

Fig. 1.5 Scheme for photocatalytic reaction when performed, A) only by photocatalyst, B-C) dye sensitization assistive, D) coupled photocatalyst, one with narrow energy band gap…………………………………………………………...7

Fig. 1.6 Redox potential vs normal electrode of various bismuth materials………8

Fig. 1.7 Crystalline structures; a) α-Bi_2O_3 (monoclinic), B) β-Bi_2O_3 (tetragonal) and c) δ-Bi_2O_3 (cubic)……………………………………………………………..9

Fig. 1.8 UV–vis DRS of the $BiNO_3$ precursor (a), α- and β-Bi_2O_3 (b-c); Inset the corresponding Tauc plots for energy band gap estimation………………………10

Fig. 1.9 Crystalline structures of $Bi_5O_7NO_3$ (rhombohedral)……………………11

Fig. 1.10 Crystalline structures of $BiFeO_3$ (rhombohedral); where Bi and Fe following the rotation of O octahedra……………………………………………12

Fig. 1.11 (a) Magnetization hysteresis loops of BFO samples, where one obtained at low temperatures (80, 100, 120) are pure BFO with very low magnetization, while others two with higher magnetization value contain γ-Fe_2O_3 impurity; inset shows Solgel-drying temperature dependent M_S……………………………… 13

Fig. 2.1 Bubbling reactor set-up; overall view (left) and top view (right)……….21

Figure. 2.2 TGA and DTG curves for Bi $(NO_3)_3$:$5H_2O$ thermal decomposition...22

Fig. 2.3 XRD patterns of samples prepared with different thermal treatments: B400, $B400_{RC}$, B425, B450 and B525. A) full-spectra and B) magnification in the range between 26 and 35°……………………………………………………… 23

Fig. 2.4 FESEM Images: A) B400: inset B) $B400_{RC}$ C) B425, D) B450 and E) B525…………………………………………………………………….. 24

Fig. 2.5 UV-Vis DRS spectra of samples: A) B400, $B400_{RC}$, B425 and B450 and B) B525 and COMB. Tauc plots of the corresponding samples are shown in the insets……………………………………………………………………. 26

Fig. 2.6 (A) XPS survey of all the samples. High resolution spectra of: Bi4f (B), O1s (C), N1s (inset in C) and Valence Band region (D)……………………… 28

Fig. 2.7 Band structures calculated from the VBM (from XPS measurements) and Eg (from UV-Vis spectroscopy analyses) for all the samples………………… 30

Figure. 2.8 Relative C/C_o curves for degradation of Rh-B (A) and IC (C) *vs.* irradiation time for all samples. Absorbance spectra of Rhodamine B (B) and Indigo Carmine (D) during the photodegradation with B450 sample. (E) Kinetic curves of BB dye degradation under different dye concentrations (ppm) and photocatalyst loadings (from 10 to 30 mg), with the determined K_{app} (min^{-1}) reported each curve. (F) Absorbance spectra of BB dye solution (30 ppm) during the photodegradation with 20 mg of B450 sample…………………………… 31

Fig. 2. 9 (A) Photocatalytic mechanism of dyes degradation on β-Bi_2O_3/$Bi_5O_7NO_3$ heterostructure. (B) cumulative O_2 evolution during water oxidation reaction with the B425 and B450 samples, under sunlight illumination and by using silver nitrate as sacrificial reagent……………………………………………………34

Fig. 3.1. XRD patterns of all Bi_2O_3 commercial (COMα, COMβ) and synthesized samples…………………………………………………………………...42

Fig. 3.2 A) UV-Vis DRS spectra and the optical band gap estimation (inset) of the Bi_2O_3 commercial (COMα, COMβ) and synthesized (B550 and B650) samples, and B) Emission spectrum of the UV and Visible Lamp………………………...43

Figure 3.3 Potentiometric titrations and its first derivative of each one indicating the pzc value of all Bi_2O_3 commercial (COMα, COMβ) and synthesized (B550 and B650) samples……………………………………………………………45

Fig. 3.4 Profile of relative concentration and kinetic curve plot of *IC* dye photodegradation under (A, B) UV light and (C, D) visible light, respectively, by using Bi_2O_3 photocatalysts……………………………………………………46

Fig. 3.5 A) Indigo carmine structure and absorbance spectra B) Rhodamine B structure and absorbance spectra during their photodegradation using B550 sample under UV light irradiation……………………………………………47

Figure 3.6. A) Profile of relative concentration and B) kinetic curve plot of *RhB* dye photodegradation under UV and visible light, respectively, by using B550 composite sample……………………………………………………………...48

Fig. 3.7 Apparent kinetic rate constant of pseudo first order reaction for all Bi_2O_3 samples in the; A) *IC* and B) *RhB* dye degradation under UV and visible light irradiation………………………………………………………………………...49

Fig. 3.8 UV-vis photoabsorption spectrum vs time of acid blue 113 (AB) at, A) neutral pH, B) basic pH and C) degradation kinetics and estimated K_{app} under UV and visible light for different pH…………………………………………………50

Fig. 3.9. Absorbance spectrum of the two-dyes mixture photodegradation by using B550 sample under visible light at: A) short and B) long time………………….52

Fig. 3.10. A) Kinetic curves and B) Apparent kinetic rate (K_{app}) of each dye in the mixed solution of indigo carmine (IC) and rhodamine-B (RhB) using B550 composite under UV and visible light…………………………………………53

Fig. 3.11 Three dyes Mix Solution neutral pH, UV-vis absorbance spectrum vs time……………………………………………………………………………….54

Fig. 3.12 Three dyes mix solution-basic pH UV-vis absorbance spectrum vs time……………………………………………………………………………….55

Fig. 3.13 Relative concentration A) IC, B) RhB and K_{app}: C) IC and D) RhB….56

Fig. 3.14 A) Diagram of electrons transfer cascade on α/β-Bi_2O_3 surface, B) Mechanism of photodegradation of single and mixed dyes……………………...57

Fig. 4.1 A-C) Change in UV-vis absorption spectrum in dark, for all dyes; inset chemical structure of dye and D) relative Concentration C/C_o for all dyes in dark……………………………………………………………………………….66

Fig. 4.2 Digital images before and after dark; A) AB dye solution and B) α/β-Bi_2O_3 powder……………………………………………………………….67

Fig. 4.3 UV-vis spectra of *Rh-B* in (A) Visible light and (B) UV light………....68

Fig. 4.4 UV-vis spectra of IC in (A) Visible light and (B) UV light……………68

Fig.4.5 UV-vis spectra of *AB* at pH 9.5 in (A) Visible light and (B) UV light…69

Fig. 4.6 A) Photodegradation kinetics of individual dyes at optimum conditions in UV and visible, B) TOC reduction % of dye solutions at different irradiation time under visible light………………………………………………………71

Fig. 4.7 Proposed scheme for the photodegradation and partial mineralization of IC dye…………………………………………………………………………. ...73

Fig. 4.8 Proposed scheme for photodegradation and partial mineralization of RhB dye…………………………………………………………………………………. 74

Fig. 4.9 Proposed scheme for photodegradation and partial mineralization of AB dye…………………………………………………………………………………75

Fig. 5.1 Schematic representation, i) pneumatic spray pyrolysis set-up and ii) photocatalytic reactor, where (A) is the lamp, (B) are the vials, (C) are the immobilized substrate, (D) is dye solution and (E) is the external casing……….80

Fig. 5.2 A) XRD patterns of the obtained β-Bi_2O_3 films, B) UV-Vis DRS spectra and band gap estimation in tauc plot (inset)…………………………………… 81

Fig. 5.3 Bare substrates (A-C), β-Bi_2O_3 deposited substrates at low magnification (D-F), at high magnification (G-I)……………………………………………… 83

Fig. 5.4 EDS elemental mapping of deposited glass (up), deposited silica (center) and deposited mesh (bottom) indicating bismuth (A, D, G), oxygen (B, E, H), silicon (C, F) and Iron (I)……………………………………………………… 84

Fig. 5.5 A) Adsorption %, B) Relative concentration C/C_o for IC dye with blank, grown substrates and bulk β-Bi_2O_3 C) photodegradation kinetic rate for *IC* dye with all substrate D) photodegradation absorbance spectrum vs time with Silica.86

Fig. 5.6 A) Absorbance spectrum vs different irradiation time with deposited silica A) Acid Blue 113 (*AB)*, B) Rhodamine-B (*RhB)*, C) relative C/C_0 vs time for all dyes with deposited silica and D) cyclic stability of deposited silica…….88

Fig. 5.7 TOC analysis of all dyes solution with deposited silica………………...89

Fig. 5.8 Photocatalytic mechanism: adsorption and photodegradation of all dyes…………………………………………………………………………………90

Fig. 6.1 XRD patterns of all the calcined samples………………………………97

Fig. 6.2 FESEM images of the calcined samples: A) BFO-SG, B) BFO-P, C) BFO-PN at 200 nm scale, D-F) at 100nm scale, respectively………………….98

Fig. 6.3 A-B) Magnetization at normal temperature for all samples and C) digital images of the water, showing magnetization of synthesized powder in presence of magnet……………………………………………………………………………99

Fig. 6.4 a) Reported UV-vis DRS results for Single phase $BiFeO_3$ and $Bi_2Fe_4O_9$ and their heterostructure, b) their estimated band gap and c) reported DRS for single phase α-Fe_2O_3 at different annealing temperatures…………………….. 101

Fig. 6.5 UV-Vis DRS for all the synthesized samples and inset showing Tauc plots and estimated energy band gap……………………………………….. 101

Fig. 6.6 A) XPS Valence band spectra of all samples. The valence band maximum (VBM) values have been determined by linear extrapolation of the leading edge to the base line. B) Band structures, determined after using estimated VBM and Eg……………………………………………………………………… 103

Fig. 6.7 Relative concentration A), kinetic curves B) and degradation absorption spectrum of IC C) for all BFO samples. D) kinetic curves of IC in comparison to other dyes; RhB and AB…………………………………………………… 104

Fig. 6.8 Photodegradation absorbance spectrum, A) AB and B) RhB with BFO-P sample; evolved cumulative O_2 for all BFO samples and D) performance of BFO-P sample for each dye up to 3 cycles………………………………………. 106

Fig. 7.1 Impregnation method used for β-Bi_2O_3 deposition on sintered silica substrate 111

Fig. 7.2 FESEM images α/β- Bi_2O_3 at different magnification scale…………. 113

Fig. 7.4 FESEM images A) bare silica and B-C) β-Bi_2O_3 deposited silica at different magnification scales………………………………………………… .114

Fig. 7.5 EDS elemental mapping A) whole acquired elemental map B) Bismuth map C) Oxygen map and D) Silicon map……………………………………115

Fig. 7.6 UV-vis DRS of bare and β-Bi_2O_3 deposited silica; inset Tauc plot along with estimated energy band gap……………………………………………...116

Fig. 7.7 C/C_o and kinetics of IC A-D), in case of α/β-Bi_2O_3 and β-Bi_2O_3 deposited silica and their respective, degradation absorbance spectrum *vs* time…………118

Fig. 7.8 IC bulk dye solution: A) before and B) after exposure under sunlight. C) β-Bi_2O_3 deposited silica before and after photocatalytic evaluation……………119

Fig. 7.9 A) C/C_o of RhB for α/β-Bi_2O_3, bare and β-Bi_2O_3 deposited silica and without photocatalyst B) photodegradation absorbance spectrum of RhB *vs* time ……….......120

Fig. 7.10 A-D) Absorbance spectra of mixed solution vs time, in case of α/β-Bi_2O_3 and β-Bi_2O_3 deposited silica for shorter and longer irradiation time. E-F) kinetics in case of α/β-Bi_2O_3 and β-Bi_2O_3 deposited silica……………………123

Fig. 7.11 Performance of both of α/β-Bi_2O_3 and β-Bi_2O_3 deposited silica up to 3 cycles, in case of IC dye………………………………………………………...124

List of Tables

Table. 2.1 Crystalline phases, energy band gap, BET surface area, N content (at. %) and kinetic apparent rate for all the samples………………………………...25

Table 2.2. XPS relative atomic concentration (atomic %) of the elements present in all the samples ……………………………………………………………..27

Table 3.1. Composition phase, average crystal size and band gap energy of the commercial (COMα, COMβ) and synthesized (B550 and B650) samples……...44

Table. 6.1 Calculated physical-chemical properties and photocatalytic results of the synthesized samples…………………………………………………………97

Chapter 1

Introduction and Background of the Study

1.1 Advanced oxidation processes (AOP) and heterogeneous photocatalysis

Clean water is one of the precious commodity for all living organisms, but it is getting scarce and contaminated day by day, due to its higher consumption and induced pollution by industrial and domestic activities by means of leaving untreated or semi-treated wastewater in natural aquifer. This has a direct impact on aquatic species and indirect influence on humans. Hence at present treatment of polluted water is essential in removing the pollutants or at least to reduce their toxicity before disposing to main natural streams. Conventional treatment of wastewater is carried by physical and biological methods, focusing on the adsorption, coagulation and filtration etc., but besides associated high cost, energy and time, their effectiveness still has not reached at standard level. On the other hand, these methods are not really ecofriendly, because by using them the waste is only transferred from one form to another form, and still is considered as waste *i.e.* 1) Adsorption of pollutants (dyes, phenolic compounds, heavy metals etc.) over adsorbents and transferring them from water to solid, which need further treatment for the removal of adsorbed pollutants from adsorbents; and such cyclic transfer remains continue: 2) the biological processes treat the water but generate toxic sludge, that further need to be treated before safe disposal.

In recent decades, advanced oxidation processes (AOPs) are found to be effectual, economical and ecofriendly in the degradation of toxic pollutants. AOPs is associated with aqueous phase in-situ generation of reactive species by using hydrogen peroxide (H_2O_2), ozone (O_3), photo-fenton reaction, heterogeneous photocatalysis etc., that oxidized and (or) reduced the parent compound (s) and decrease the level of toxicity by means of complete degradation or mineralization into CO_2 and H_2O, HCO_3 or other less toxic compounds.

In particular, heterogeneous photocatalysis (HP) has gained much interest because it simply employed the use of photocatalyst/semiconductor for the efficient generation of reactive species in aqueous media. The basic and continued principle of HP in degradation of organic pollutants can be summarize with the help of scheme given in Fig. 1.1. Initially the organic pollutants need to interact and transfer towards solid surface of photocatalyst by means adsorption, so as degradation reactions could occur at surface and finally the residual secondary pollutants detached from the photocatalyst surface for refreshing that interface, ready for newer interaction.

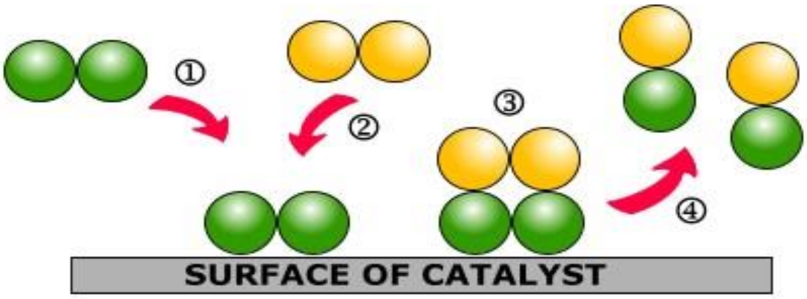

Fig. 1.1 Basic Principle of heterogeneous photocatalysis, showing 1) interaction and transfer towards photocatalyst surface, 2) adsorption of primary (green) and secondary intermediates (yellow), 3) chemical reaction(s) between pollutants and photocatalyst and 4) detachment of by products from photocatalyst surface.

To generate the reactive species, the photocatalyst need to be activated through irradiation of a light source (UV or visible/solar light), that could promote transfer of an electron from valence band (VB) to conduction band (CB). The basic principle of photocatalyst activation lies behind the successful electron transfer; provided with the photon energy (higher than the optical energy band gap (E_g) of the semiconductor) that can excite the localize electrons to move across the optical bands and play considerable role for enabling oxidation and reduction reactions in aqueous solution, as shown in the schemes in Fig. 1.2 suggested by

[1, 2]. These excited electrons (e^-) to CB and left holes (h^+) in the VB, after enabling water oxidation and (or) reduction, can generate reactive species in form of hydroxyl radical (OH^-) and atomic oxygen ($O^{\cdot}$) and can perform degradation and mineralization of the pollutants; as shown in schemes given Fig. 1.2 and general chemical reactions given in Eq. 1.1 - 1.3 [1-3].

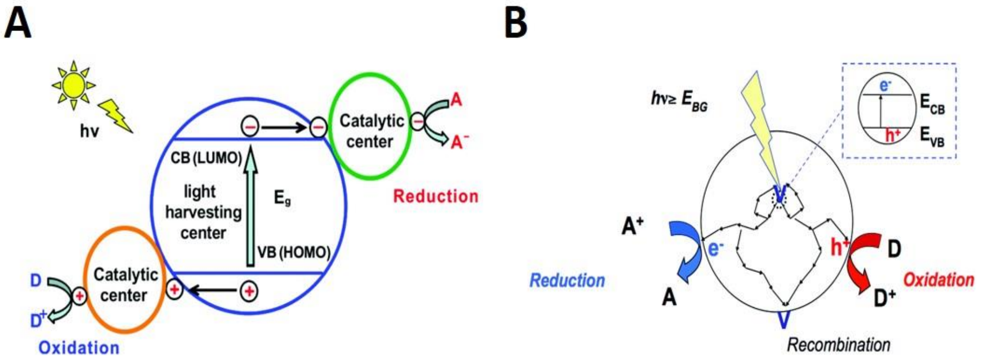

Fig. 1.2 Photocatalytic schematic showing; A) the transfer of electron from valence band (VB) to conduction band (CB) and B) performing oxidation and reduction reactions on photocatalyst surface [1, 2].

$$hv + (SC) \rightarrow e^- + h^+ \qquad Eq. 1.1$$

$$A_{(ads)} + e^- \rightarrow A^-_{(ads)} \qquad Eq.\ 1.2$$

$$D_{(ads)} + h^+ \rightarrow D^+_{(ads)} \qquad Eq.\ 1.3$$

1.2 Challenges for Heterogeneous photocatalysis (HP)

Suitability of the heterogeneous photocatalysis (HP) for the degradation of pollutants depends upon various aspects, and few of them are still challenging in way of bringing HP in real applications; which are:

1) Design of visible light active photocatalysts, which can be effectively activated by natural solar light and provide improved performance in degradation of the pollutants and further led their effective mineralization. Till date plenty of solar active photocatalysts are reported by various researchers and suggested as prominent for their large-scale use; doped TiO_2, doped ZnO, CdS, Bi_2O_3, BiOX (X= Br, I, Cl) [4-24].

2) Efficient and cost-effective recovery of small particles, their filtration and reuse. For improved photoactivity micro and nanometric particles are preferred, due to higher surface area, better dispersion in the solution and adequate passage

for activation of particles through irradiation source [25]; which on contrary impose trouble in recovering them and making them available for repeated cycles [26, 27]. Many researchers have adopted methods to tackle the problem of photocatalyst recovery and among them the promising is the magnetic separation by means of incorporating iron (Fe) in form of doping, coupling either on core or at shell, to recover the materials through use of external magnetic field; TiO_2/Fe_2O_3, $ZnO/Fe_2O_3/ZnFeO_3$ [28-30]. In addition, some photocatalytic materials being ferromagnetic are found good for photocatalytic properties along with an advantage of magnetic, like $BiFeO_3$ [31-34].

3) Selection of slurry based or fixed support based reactors; important because of dispersion/interaction of the photocatalyst with pollutant in bulk solution and to ensure the effectual photocatalysis process. For example, Nayereh Soltani *et. al*. used a reactor containing slurry of ZnS and CdS; scheme given in Fig. 1.3A, while Bahnemamm *et. al.* and Malato *et. al.* have used a fixed bed immobilized with TiO_2 (Degussa P25) shown in scheme Fig. 1.3B, for the degradation of organic pollutants using sun light irradiation [35, 36]. At one end slurry based system have the advantage of good dispersion and controlled interaction of photocatalyst and pollutants, but on contrary recovery of slurry is the problem. Secondly the use of fixed immobilized supports are lacking to maintain the optimized interaction of photocatalyst and pollutants and considerably lower the degradation kinetics than slurry.

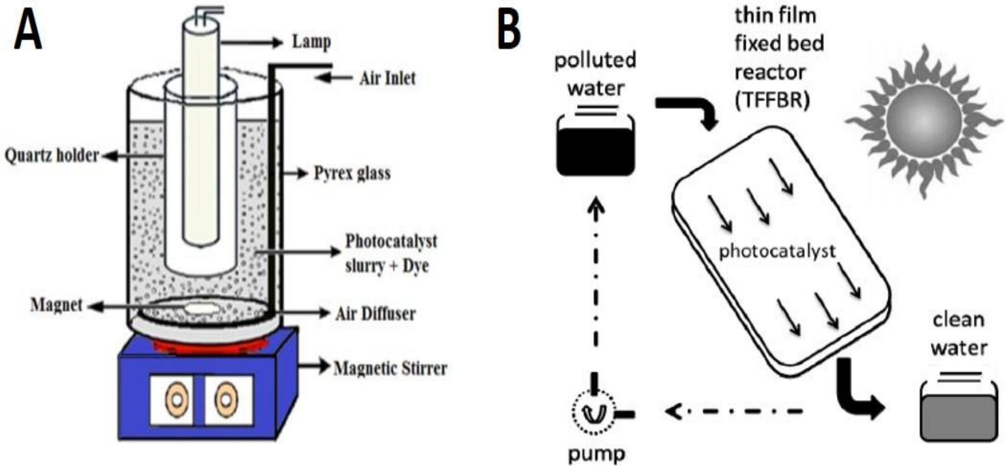
A
Lamp
Air Inlet
Quartz holder
Pyrex glass
Photocatalyst slurry + Dye
Magnet
Air Diffuser
Magnetic Stirrer
B
polluted water
thin film fixed bed reactor (TFFBR)
photocatalyst
clean water
pump

Fig. 1.3 Examples of A) slurry based rector [36], and B) immobilized fixed support [35].

1.3 Important aspects of photocatalysts and their synthesis

In this section, some important aspects of photocatalytic material are discussed considering the available literature and several issues from the point of view of physio-chemical properties and synthesis. Along with the importance of solar driven material, it is also significant to consider:

1) adequate bang gap of the photocatalyst in the range where optimum solar spectrum/energy could be utilized for activation, not too low to avoid recombination of e^- and h^+ for example as in case of CdS, BiOI, CdSe etc. that have reportedly very low band gap of 2.2 and 1.9 and 1.7 eV, respectively [22, 37, 38]. On the other hand, not too high for low/limited activation for example ZnO, TiO_2 in the range of 3- 3.2 eV [9, 37, 38]. Moreover, the appropriate band position in the region, where the CB edge must be at a higher energy than the reduction potential of hydrogen (determined at -0.28 eV), while the VB edge must be lower than the oxidation potential of water (determined at +1.23 eV) as shown in the reported scheme in Fig. 1.4a and 1.4b [39]; to efficiently perform the reduction and oxidation together or alone in case of coupled photocatalyst (one with oxidation potential and other with reduction potential; Fig. 4b) for water splitting or to degrade the organic pollutants; attacked by reactive species.

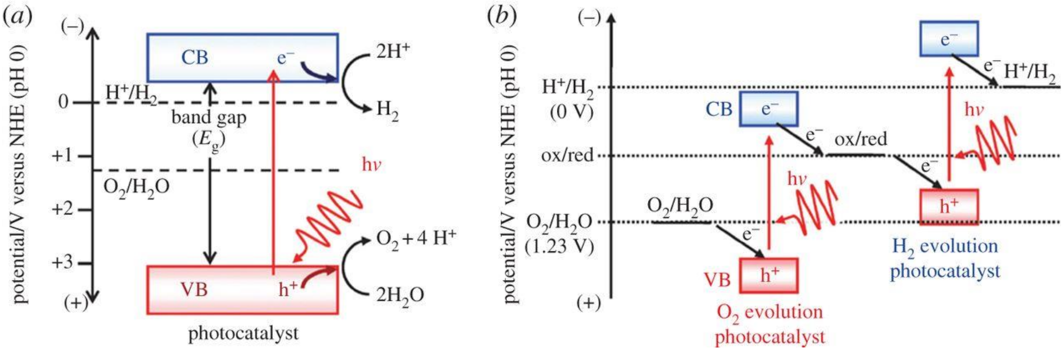
(a)
(–)
(+)
potential/V versus NHE (pH 0)
0
+1
+2
+3
CB
e⁻
H⁺/H₂
band gap
(E_g)
O₂/H₂O
hν
VB
h⁺
2H⁺
H₂
O₂ + 4 H⁺
2H₂O
photocatalyst
(b)
(–)
(+)
potential/V versus NHE (pH 0)
H⁺/H₂
(0 V)
ox/red
O₂/H₂O
(1.23 V)
CB
e⁻
e⁻
ox/red
hν
O₂/H₂O
e⁻
VB
h⁺
O₂ evolution
photocatalyst
e⁻
e⁻
H⁺/H₂
hν
e⁻
h⁺
H₂ evolution
photocatalyst

Fig. 1.4 Scheme for photocatalyst redox potential vs normal Hydrogen electrode (NHE) in case of, a) single and b) coupled photocatalyst [39].

2) chemical and cyclic stability to obtain similar performance in repeated cycles; various photocatalysts have an advantage of improved photocatalytic activity but have low stability in aqueous media. Different pH and concentration of pollutants, may cause chemical detoriation in terms of corrosion, dissolution of photocatalyst for example as the case with CdS, CdSe, ZnS, ZnO, Fe_2O_3 [40]. All these mentioned photocatalysts have the problem of corrosion and leaching in

aqueous media at mild acidic or low pH. Therefore, considering the mixed nature of effluent, such photocatalysts should not be considered for water treatment.

3) scalable and simple synthesis of the photocatalysts is vital, when considering the quick availability of the material with standard characteristics. Commonly different synthesis techniques are employed, such as sol-gel, hydrothermal, solvothermal and solid-state decomposition methods. Moreover, when maintaining alkaline solutions with the addition of either dispersing or polymerizing agents have made it tough to synthesize specific photocatalyst by controlling the complex chemistry of solvents, precursors and shape modifying agents. Furthermore, to improve photocatalytic performance (in visible light) of the materials with large energy band gap *i.e.* TiO_2 and ZnO, interstitial doping is an appropriate option, by which band structures could be tuned by including various dopants within the structures like: Fe [41, 42], Ce [43], N [9, 42, 44], Ag/Cu [40, 45]. Doping could improve the solar light photocatalytic performance by improving the photonic absorption in visible spectrum or avoiding the problem of electrons and holes recombination, due to assisted electron capture and transfer by introduced interstitial defects. However, the selective and standard doping methods are challenging, because of difficulties in maintaining the lattice refinement with standard characteristic due to lack in control over the complex chemistry of precursor solution and dopants [46].

1.4 Important aspects of pollutants under investigation

In HP, along with the consideration of the photocatalysts and their properties, it is also important to focus the selected model pollutants and conditions of their evaluation, because the proposition of one photocatalyst, should not be considered for one or a limited number pollutant. At one specific condition of evaluation, the performance should be unchallenged for most of the pollutants of different ionic behaviors and chemical compositions. For example, when considering photodegradation of organic dyes (colorants), there are many structural varieties with different ionic behaviors *i.e.* cationic, nonionic and anionic types, also the wastewater is extremely variable and mixed in composition, due to large number of dyes and other chemicals used in textile processing, the problem is further made complex by the thousands of dyestuffs commercially available for particular textile fibers. Nevertheless, enormous studies have concluded the photocatalytic performance after evaluating single dye and still the focus is on only exploring the potential photocatalyst by evaluating most common dyes like methylene blue and rhodamine B [47]. During selection of the model pollutants it would be significant to consider different ionic behaviors and structure, various concentrations and pH, single of mixed solution (different dyes in one solution. All these have strong influence on photocatalysis process; in terms of interaction, irradiation passage (slightly or highly depending upon dye intensity and concentration) and other related terms.

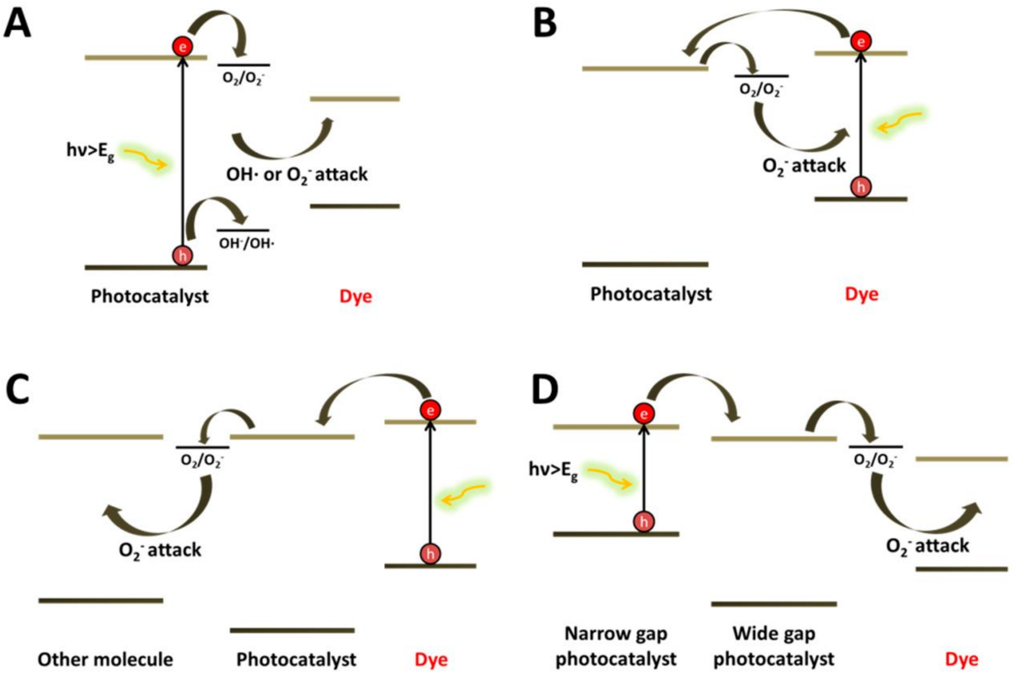
A
e
hv>E$_g$
O_2/O_2^-
OH· or O_2^- attack
OH^-/OH·
h
Photocatalyst
Dye
B
e
O_2/O_2^-
O_2^- attack
h
Photocatalyst
Dye
C
O_2/O_2^-
O_2^- attack
e
h
Other molecule
Photocatalyst
Dye
D
e
hv>E$_g$
h
O_2/O_2^-
O_2^- attack
Narrow gap photocatalyst
Wide gap photocatalyst
Dye

Fig. 1.5 Scheme for photocatalytic reaction when performed, A) only by photocatalyst, B-C) dye sensitization assistive, D) coupled photocatalyst, one with narrow energy band gap [47].

Moreover, the selectivity of dyes as pollutant model to evaluate the photocatalytic performance is challenged by many authors, because the photodegradation of dyes and its analysis are simpler than other organic pollutants *i.e.* phenolic compounds (like bisphenol, nitro or chloro-phenols etc.) and other pesticides or medicines; rarely investigated [27] [47]. It is reported that colorants being in the visible range of spectrum are easier to degrade and may undergo certain processes differ than photocatalysis and cause discoloration of the solution; such as dye self-sensitization and photolysis. In case of sensitization the electrons in dye molecule can excite at visible light exposure and could transfer to photocatalyst and overall influence the degradation process [47]; scheme given in Fig. 1.5 explains the process of photocatalysis in conjunction with other processes (sensitization-assisted in Fig. 1.5B and C) that could assist the photocatalyst in performing degradation which is different from real photocatalytic process. Moreover, during photolysis the dye colorants can be decolorized under visible light irradiation due to cleavage of chemical group responsible for color appearance for example, due to electronic transitions within molecule or due to breakage of some main chromophoric groups, like (N=N) of methyl orange, acid yellow [48]. Moreover, leuco dyes lose their color by changing the absorbance spectra from one wavelength to another after their oxidation or reduction; most common leuco dyes are rhodamine B and indigo carmine [49] [47, 50]. Therefore, along with other parameters of photocatalysis there should be careful consideration of the selection of the model pollutants, before suggesting the potentiality of any photocatalyst.

1.5 Bismuth based materials as photocatalyst

Bismuth-containing semiconductors have recently gained high interest and have been extensively studied and proposed as potential photocatalytic materials for solar driven water splitting and decomposition of organic molecules; such as, Bi_2O_3 (α, β and δ phases) [13, 18, 19, 51], BiOX (X = Cl, Br and I) [52-56], $BiFeO_3$ [31, 57, 58], $(BiO)_2CO_3$ [59-61], $BiVO_4$ [62, 63] and $Bi_5O_7NO_3$ [14, 64, 65]. The main features of bismuth based materials lie to their wide visible light absorption and their ability to generate superoxide and hydroxide radicals under sunlight irradiation. Redox potential vs normal Hydrogen electrode (NHE) for most of bismuth based materials is given in Fig. 1.6 [66], most of them have appropriate energy band gap and edge positioning, but few of them have reportedly strong potential for photodegradation of organic pollutants in solar light, including Bi_2O_3 [13, 18, 19, 51], $BiFeO_3$ [31, 57, 58]. In upcoming sections, the interesting candidates for photodegradation of organic pollutants are discussed in detail with the support of available literature.

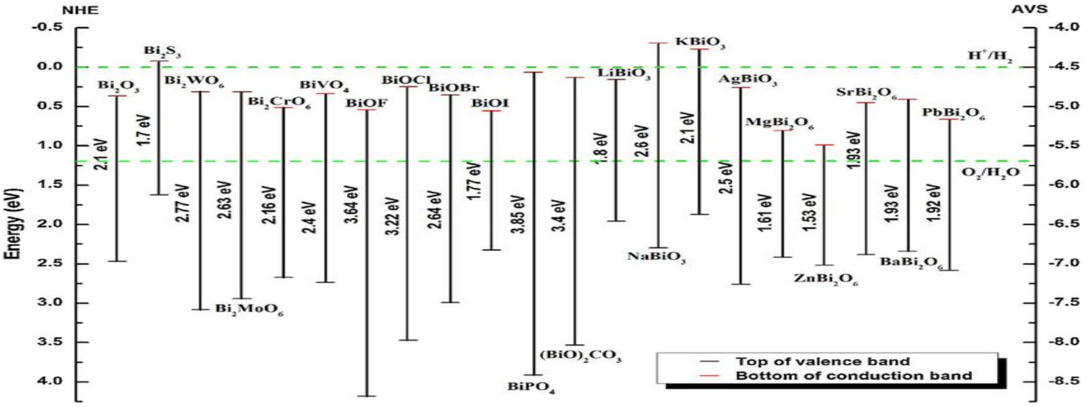

Fig. 1.6 Redox potential vs normal electrode diagram of various bismuth based materials in comparison to other semiconductors [66].

1.5.1 Bismuth Oxide (Bi_2O_3)

Bismuth oxide (Bi_2O_3) being in the optimum range of visible spectrum, has been suggested as a potential visible-light photocatalyst [13, 19, 67-71]. So far, six polymorphs are reported for Bi_2O_3: α-Bi_2O_3 (monoclinic), β-Bi_2O_3 (tetragonal), γ-Bi_2O_3 (body centered cubic), δ-Bi_2O_3 (cubic), ω-Bi_2O_3 (triclinic) and ε-Bi_2O_3 (triclinic) [72-74]; the widely known and most studied phases are α, β and δ-Bi_2O_3 and their crystal structures displayed in Fig. 1.7 [75]. Each phase pointedly display different optical and electrical properties [76]. The room temperature α-phase and the high-temperature (> 725°C) δ-phase are thermodynamically stable, while the others are metastable phases [16].

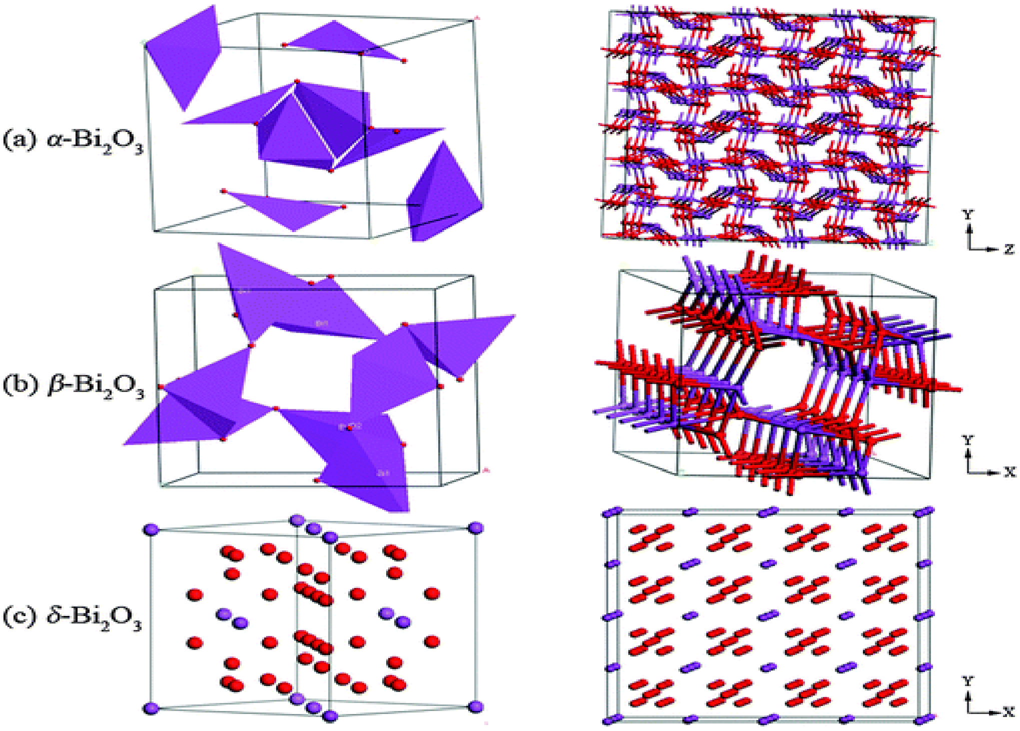

Fig. 1.7 Crystalline structures; a) α-Bi_2O_3 (monoclinic), B) β-Bi_2O_3 (tetragonal) and c) δ-Bi_2O_3 (cubic) [75].

For the photocatalytic applications, much attention has been paid on α- and β-phases, because both can be easily obtained during chemical and or solid synthesis of Bi_2O_3 with various morphologies and could be tuned for photocatalysis [15, 19, 69, 77, 78]. Visible light active photodegradation of dyes strongly represents the dominated effects by the crystalline phase, surface area and morphology. According to various researchers monoclinic α-Bi_2O_3 with an optical absorption edge at around 450nm wavelength exhibits direct optical band gap in the range of 2.7-2.9 eV [15, 79-82], while for tetragonal β-Bi_2O_3, the reported values are slightly lower *i.e.* 2.4 - 2.5 eV [13, 19, 68, 69]; for both phases, slight variation is due to difference in synthesis routes and present impurity. The reported UV-Vis DRS spectra of α and β-Bi_2O_3, shown in Fig. 1.8 [83], where it can be observed that both have appropriate absorbance in visible spectrum, however β-Bi_2O_3 depicts slightly better absorption until 550 nm with an advantage of better utilization of visible light for activation. However, some reports showed a good photocatalytic performance for the α-phase [15, 79-82], while others displayed much improved results for β-phase [13, 19, 68, 69] due to the lower energy gap, allowing high utilization of solar spectrum. Considering the significance of synthesis (highlighted in section 1.3) for large scale synthesis, it is noted that most of the synthesis methods reported by various researcher, to obtain α and β-Bi_2O_3 focused on chemical derived routes with complex formation of hydrothermal, solvothermal, solgel precursor solutions along with shape modifying agents and pH modifiers; clearly an obstacle in scaling up the production of the material.

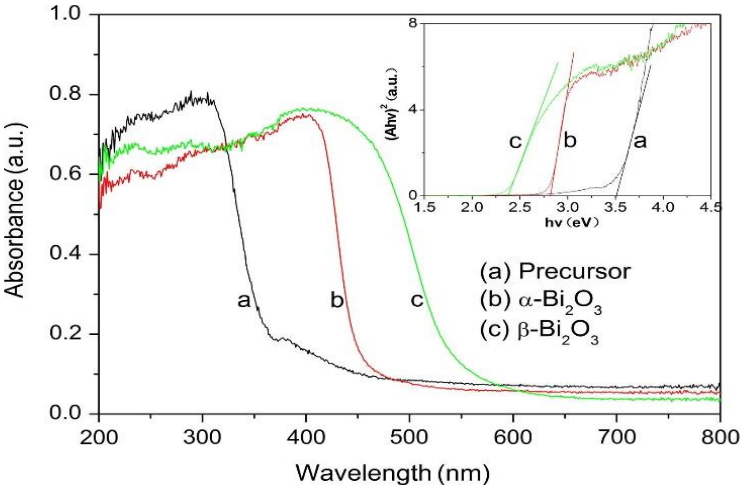

Fig. 1.8 UV–vis DRS of the $BiNO_3$ precursor (a), α- and β-Bi_2O_3 (b-c); Inset shows the corresponding Tauc plots for energy band gap estimation [83].

1.5.2 Bismuth Oxy-Nitrates

Recently, researchers have gained interest on bismuth oxy-nitrates, such as rhombohedral $Bi_5O_7NO_3$ with layered crystal structure (reported by Ziegler *et. al.* and shown in Fig. 1.9) [84], presented Bi and O atoms joins at the center and surrounded by Nitrates (NO_3). Therefore, $Bi_5O_7NO_3$ provides a high number of Oxygen as charge carrier assisted with Nitrogen and most significantly featured various morphologies *i.e.* fibers, rods, sheets, 3D flowers and bouquets, that could contribute in improving the photocatalytic performance [14, 65].

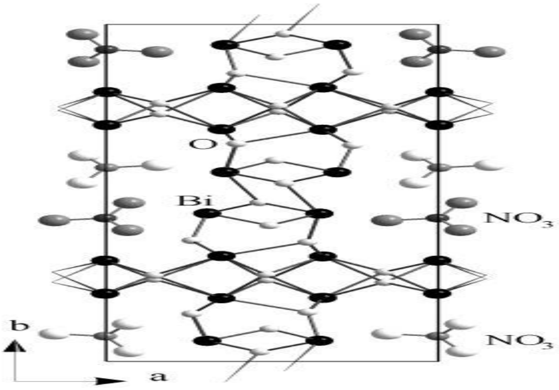

Fig. 1.9 Crystalline structures of $Bi_5O_7NO_3$ (rhombohedral) [84].

Various synthesis techniques are reported to obtain $Bi_5O_7NO_3$, such as sol-gel, hydrothermal, solvothermal and solid-state decomposition methods, or by using different synthesis media: alkaline solutions with the addition of either dispersing or polymerizing agents [14, 65, 70, 85]. For instance, Kodama *et. al.* [86] were the first to report the photocatalytic effect of $Bi_5O_7NO_3$, which was synthesized by thermal decomposition of bismuth nitrate pentahydrated ($Bi(NO_3)_3:5H_2O$) in basic media. Recently, Shu Gong *et. al.* [14] synthesized $Bi_5O_7NO_3$ nanosheets through an hydrothermally treated solution of $Bi(NO_3)_3:5H_2O$ at pH 9 followed by calcination [14]. Shujie Yu *et. al.* [65] also reported $Bi_5O_7NO_3$ nanosheets, but synthesized via a solvothermal method from a solution of $Bi(NO_3)_3:5H_2O$ at pH 12 containing a surfactant (Triton X-100) [65]. Both works confirmed the photocatalytic activity of $Bi_5O_7NO_3$ for the degradation of Rhodamine B dye (RhB) under visible light irradiation. As mentioned earlier for the issues related to synthesis, here again most of the reported methods for $Bi_5O_7NO_3$ synthesis required the use of surfactants and other reagents, like bases for alkaline solutions [14, 65, 70, 85], which limit the scale-up of the production of such materials due to increased cost associated to the use of additional chemicals, specialized systems for controlling the solution pH and after-treatment processes for removing eventual residues or by-products [15].

1.5.3 Bismuth Ferrite ($BiFeO_3$ or BFO)

Bismuth ferrite ($BiFeO_3$) possess an interesting feature from the point of quick and simplest recovery of photocatalyst after its application *i.e.* being ferromagnetic can be separated through applied magnetic field [31-34]. Recently

BFO, has attracted much attention due to potential applications for novel magnetoelectric devices and is also considered as an important visible-light responsive photocatalyst for degradation of organic pollutants and water splitting due to narrow band gap (~2.2 eV) with exceptional chemical stability compared to other less stable semiconductors like CdS, CdSe, ZnS. GaS [40]. It is reported that the distorted perovskite rhombohedral BFO possess G-type antiferromagnetism, which is dominantly controlled by ordering of [111] facet [16, 19, 54, 56, 70, 87-92], shown in Fig. 1.10 [93]; therefore, by modifying the ordering of this facet, the magnetization of BFO could be tailored from weak to higher [94, 95].

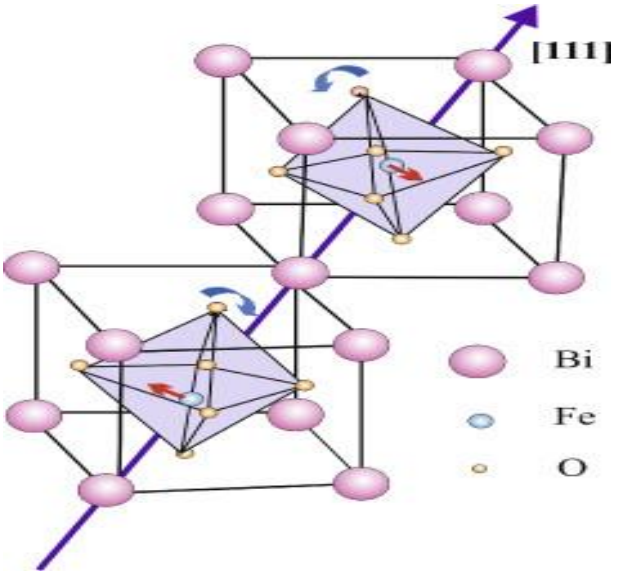

Fig. 1.10 Crystalline structures of $BiFeO_3$ (rhombohedral); where Bi and Fe following the rotation of O octahedra [93].

It is important from the point of recovery and reuse, that BFO should contains an adequate magnetism, to potentially consider it for photocatalysis and easy magnetic separation. Particularly for photocatalytic evaluation there are some studies confirming the effectiveness of $BiFeO_3$. For example, Gao *et. al.* and Li *et. al.* have applied hydrothermally synthesized BFO for the degradation of methyl orange and congo red under visible light [96, 97]. Huo et al. reported mesoporous hollow sphere of BFO with high surface area and its use in photocatalytic mineralization of Rhodamine B under visible-light [98]. Guo *et. al.* [33], synthesized single phase BFO and BFO-Fe_2O_3 using solgel method respectively and have shown improved visible light driven photocatalytic performance for the degradation of Rhodamine B. In addition, some researchers have revealed the use of BFO materials for clean energy supplies, for example, Lee *et. al.* reported that $SrTiO_3$-coated BFO core/shell nanostructures [99] and BFO nanocubes synthesized by Joshi *et. al.* [57] can generate H_2 under visible-light irradiation, which widens the versatility of BFO.

Furthermore, it has been recently explored that the ferromagnetic behavior in BFO is due to Fe_2O_3, while pure BFO is antiferromagnetic or only accounts weak saturated magnetization at room temperature [100]. As the photocatalytic reaction is commonly performed in a suspension of bulk/slurry of photocatalysis, which therefore inevitably encounter obstacle in separation and manipulation of pure single phase BFO material due to small particle size and weak saturated magnetization at room temperature; identified from both theoretical and experimental results about 0.05mB Fe^{-1}, too small to allow separation under applied external magnetic field; reported in Fig. 1.11 by Guo *et. al.* [33].To bring the characteristic of optimum ferromagnetism in BFO, the presence of Fe_2O_3, attained morphology and structural and optical appearance can play an important role from the point of views of magnetic separation and photocatalytic improvements [33].

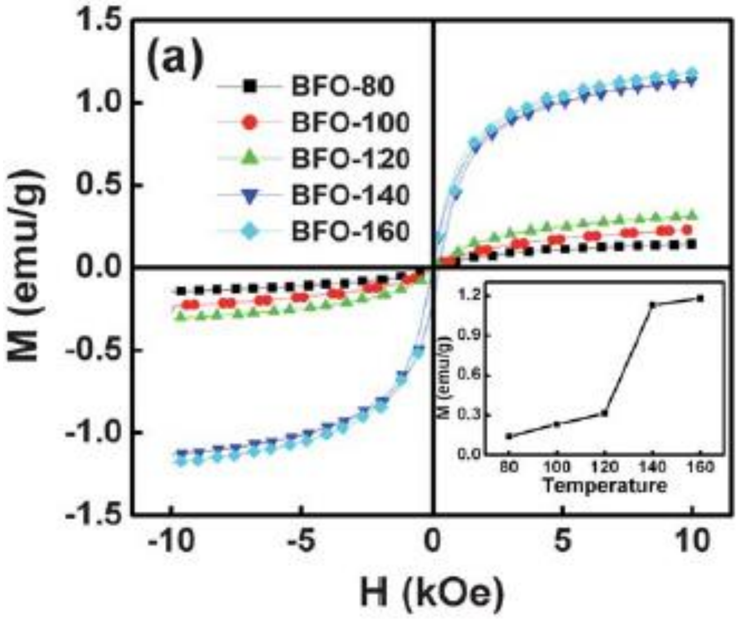

Fig. 1.11 (a) Magnetization hysteresis loops of BFO samples, where one obtained at low temperatures (80, 100, 120) are pure BFO with very low magnetization, while others two with higher magnetization value contain γ-Fe_2O_3 impurity; inset shows Solgel-drying temperature dependent Magnetic saturation [33].

1.6 Objectives and structure of thesis

After careful overview of the literature and basing earlier discussed challenges to HP, the objectives and outcomes of the whole work are summarized as:

1- Facile scalable synthesis to obtain various bismuth based single structures and heterostructures and further their photocatalytic evaluation of various dyes with different structure, ionic behaviors and interaction towards photocatalyst; reported in chapter-2.

2- Find the simple synthesis route in achieving two different crystalline structure of Bi_2O_3 (α and β) in a single material, featured with crystal stability and improved photoactivity in visible light; reported in chapter-3.

3- Photocatalytic evaluation of different dyes, each in single and mixed solution (of two or more dyes); to analyze the degradation kinetics and behavior of photocatalyst towards mixed regime of various dyes of different composition and ionic behaviors; reported in chapter-3.

4- Photocatalytic investigation in conjunction with series of coexisted and conflicted processes (intense adsorption, photobleaching, photolysis, dye sensitization, partial or complete mineralization), which have been rarely studied and discussed during the photocatalytic work mainly for the degradation of dyes. Proposed and explained the photocatalytic path and mechanism during, by adopting different approaches *i.e.* evolving O_2, total organic carbon analysis and addition of electrons and holes quenchers; summarized in chapter-4.

5- Find the suitable fixed support, facilitating the adequate mass transfer and interaction of pollutants with the immobilized photocatalyst films, to obtain similar/competing photocatalytic efficiency as in case of powder photocatalyst; presented in chapter-5.

6- Synthesis and systematic investigation of single structure $BiFeO_3$ and $BiFeO_3/Fe_2O_3/Bi_2Fe_4O_9$ heterostructures in terms of morphology, magnetism and band alignment favoring the photocatalytic activity towards degradation of dyes and water oxidation, along with the advantage of recovery by means of applied magnetism; reported in chapter-6.

7- Final investigation and comparison of efficient α/β-Bi_2O_3 heterostructure and β-Bi_2O_3 deposited silica, in terms of photocatalytic response and mechanism. For this purpose, different dyes as single or in mixed solutions were evaluated in smaller quantity at lab scale and of large quantities under natural sunlight; compiled in chapter-7.

In general, this thesis work aimed to provide the information on investigation of bismuth based materials, carefully designed by focusing the real challenges of HP such as scalable synthesis, economic recovery and reuse of photocatalyst and suitable fixed supports in targeting the pollutants. Moreover, the evaluation of different dyes as single or in mixed solution can provide help in understanding the photocatalytic mechanism when dealing single or mixed effluent and designing the photocatalyst in terms of its utilization not only for degradation of single pollutant but various pollutants of different chemical composition and type. Furthermore, using bismuth based materials (other than widely known $BiVO_4$) for water splitting and evolution of O_2 can be an indicator of designing multipurpose and versatile photocatalyst for various application; including pollutants degradation, H_2 and O_2 generation. In addition, the proposed materials could be interesting for other applications like: adsorption assisted photocatalysis of emerging organic and inorganic pollutants, antibacterial properties etc.

Chapter 2

Solid-state Synthesis of $Bi_5O_7NO_3$, β-Bi_2O_3/$Bi_5O_7NO_3$ heterostructures and α-Bi_2O_3 and photocatalytic degradation of dyes under visible light

2.1 Introduction

Bismuth-based semiconductors, such as, Bi_2O_3 (containing α, β and δ phases) [13, 18, 19, 51], BiOX (X = Br, Cl and I) [52-56], $BiFeO_3$ [31, 57, 58], $(BiO)_2CO_3$ [59-61], $BiVO_4$ [62, 63] and $Bi_5O_7NO_3$ [14, 64, 65], have been extensively studied as potential candidates for both water splitting and degradation of organic molecules. The main attributes of solar driven activity reside within their wide visible light absorption and ability to generate superoxide and hydroxide radicals through the optimum utilization of solar spectrum.

Recently, researchers have centered the attention on oxynitrides of bismuth for the possibility to obtain various nano and micro structured morphologies (*i.e.* fibers, rods, sheets, 3D flowers and bouquets) and to tune their energy band gap for improving the photoactivity; through various synthesis techniques, such as sol-gel, hydrothermal, solvothermal and solid-state decomposition methods, or by using different synthesis media: alkaline solutions with the addition of either dispersing or polymerizing agents [14, 65]. For instance, Kodama *et. al.* [86] were the first to report to synthesize $Bi_5O_7NO_3$ through thermal decomposition of bismuth nitrate penta-hydrate ($Bi(NO_3)_3$:$5H_2O$) and basic bismuth nitrate (BBN). Recently, Shu Gong *et. al.* [14] used chemical route to synthesize $Bi_5O_7NO_3$ nanosheets via hydrothermally treated solution of $Bi(NO_3)_3$:$5H_2O$ at pH 9 followed by calcination [14]. Shujie Yu *et. al.* [65] also obtained $Bi_5O_7NO_3$ nanosheets, via a solvothermal method from a highly alkaline solution of $Bi(NO_3)_3$:$5H_2O$ at pH 12 also containing a surfactant (Triton X-100) [65]. Both works displayed the photoactivity of $Bi_5O_7NO_3$ for the degradation of Rhodamine B (RhB) under visible light irradiation. As in all the reported cases, synthesis of $Bi_5O_7NO_3$ required the use of surfactants and alkaline solutions [14, 65, 70, 85], which bound the scale-up of the synthesis of such materials due to higher cost related to the use of additional chemicals, specialized systems for regulating the solution pH and after-treatment processes such as removal of eventual residues or by-products [15].

Moreover, the above-mentioned synthesis routes of $Bi_5O_7NO_3$ have led to the formation of one crystalline structure or its heterostructure with different phases of bismuth oxides, but the role of any of them on the photocatalytic activity have not been fully understood yet. Therefore, a good control of the scalable synthesis method to obtain specific target structures is of great importance for photocatalyst production and its application. To the best of our knowledge, after Kodama *et. al.* [86], there are no other reports in which $Bi_5O_7NO_3$ has been obtained via thermal decomposition of ($Bi(NO_3)_3$:$5H_2O$) and BBN without any further additives. As well, the photocatalytic degradation of dyes other than the Rh-B by $Bi_5O_7NO_3$ have been rarely investigated in the literature. Therefore, grounded in the previous study, α/β-Bi_2O_3 composite was synthesized via solid state route [101], therefore in current work, $Bi_5O_7NO_3$ nanostructures and heterostructures containing β-Bi_2O_3 and $Bi_5O_7NO_3$ have been synthesized through the similar route *i.e.* thermal decomposition under controlled heating and cooling of sample, without the use of alkaline solution and any other shape-directing chemical reagents. The obtained samples were evaluated for photocatalytic activity for the degradation of three unbiodegradable organic dyes, with different functional groups and ionic behaviors: cationic Xanthene type (Rhodamine B (RhB)), an anionic Indigoid type (Indigo Carmine (IC)) and a refractory anthraquinone type (Remazol Brilliant Blue B (BB)), which are representative of colorants used in biology and textile industries, have been investigated and compared with those of pure α-Bi_2O_3 and β-Bi_2O_3 powders. The specific role of the Bi_2O_3 and $Bi_5O_7NO_3$ physio-chemical properties in the photocatalytic activity of the single or heterostructured materials, under simulated sunlight irradiation are analyzed and discussed in detail.

2.2 Experimental

2.2.1 Synthesis

$Bi(NO_3)_3$:$5H_2O$, precursor salt and commercial β-Bi_2O_3 of analytical grade were purchased from Sigma Aldrich and used as received. In a typical method, $Bi(NO_3)_3$:$5H_2O$ salt was initially heated in furnace at 200 °C for 1 h to evaporate the water content, then the temperature was increased up to 300°C and kept constant for 2 h. Then after subsequent calcination was followed at four target temperatures: 400, 425, 450 and 525°C for 2 h. After calcination, all the samples were allowed for natural cooling inside the furnace. The obtained samples were labelled as B400, B425, B450, B525, respectively; following calcination temperature. For comparison purpose, another sample was calcined at 400 °C for 2 h and rapidly cooled down in about 2 min, and labelled as $B400_{RC}$. The commercial β-Bi_2O_3 sample was named as COMB.

2.2.2 Characterization

2.2.2.1 Morphology and Elemental Mapping

Field emission scanning electron microscopy (FE-SEM, Zeiss Merlin) integrated with an OXFORD INCA ENERGY 450 energy-dispersive X-ray spectroscopy (EDS) detector was used to observe the morphology of the obtained samples, by means of investigating the molecular surface and electronic properties of respective sample. Typically, this analysis followed the interaction of an incident electron beam and the solid specimen, which can generate a variety of emissions from the specimen surface, including secondary electrons, backscattered electrons, Auger electrons, X-rays, visible photons and other related. With this, high quality images could be obtained at low voltage with negligible electrical charging of sample. Using FESEM-EDS, focus was to obtain secondary electron imaging and X-ray spectroscopy for elemental composition. Total organic carbon

(TOC) analysis was carried out using a Shimadzu TOC-L analyzer with a high sensibility column.

2.2.2.2 X-ray Diffraction (XRD)

X-Ray diffraction (XRD) is an analytical method to identify the crystal structure of single and polymorphs materials, for the single crystal or powder samples. Typically, a diffractogram records the diffraction pattern by measure the intensity against the diffraction angle (Bragg's angle); generates intensity vs diffraction plot. Obtained XRD patterns, can be analyzed to classify the crystalline structure and phase(s) of single or hetero-material, in relation with the database given by Joint Committee on Powder Diffraction Standards (JCPDS); by means of analyzing the patterns in programmed software with JCPDS database.

The calcined powders were analyzed by using an X'Pert Phillips diffractometer, with Cu Kα radiation, under the following conditions: $2\theta = 15°-60°$, 2θ step size = 0.02° at 40 kV and 30 mA. The XRD spectra were analyzed by using X'Pert High Score Plus software [17].

2.2.2.3 X-Ray Photoelectron Spectroscopy (XPS)

X-ray photoelectron spectroscopy (XPS) is a sensitive technique for the analysis of surface chemical composition, by irradiating a sample's surface, to eject the occupied electrons from valence and core levels; under ultra-high-vacuum. The kinetic energies in ejecting these photoelectrons can provide the information of the chemical states from the atoms, which were irradiated and resulted these photoelectrons. For emitted electrons from lower orbitals, their binding energy must be overcome, to further reduce their kinetic energy. In XPS, the kinetic energy of ejected photoelectrons is measured by an analyzer and then translated into a binding energy for the precise atomic orbital of an electron. In this way, each element with unique set of binding energies, can be recognized respective to its electronic states.

Here, a PHI 5000 Versa-Probe Scanning X-ray Photoelectron Spectrometer (XPS), with an Al k-alpha source at 1486.6 eV, was used to investigate the surface chemical composition of each sample. The spectra obtained from the XPS analysis was corrected by referencing the C1s line to 284.5 eV.

2.2.2.4 UV-Vis Diffused Reflectance Spectroscopy (DRS)

UV-Vis diffuse reflectance spectroscopy (DRS) is a method to evaluate the absorption and optical properties of the material. For photocatalyst, the spectra recorded by DRS, can be used to estimate absorption coefficient and band gap (E_g). DRS spectra were recorded on a UV-Vis Varian's Cary 5000 spectrophotometer, equipped with an integration sphere and analyzed after using

$BaSO_4$ as a reference; the obtained spectra were then converted to tauc plot using Kubelka–Munk method [15] and band-gap energy (E_g) was determined considering an allowed direct transition for the sample, by estimating the linear portion of the $(F(R)\times hv)^2$ *vs hv* curve to $F(R)=0$ [102].

2.2.2.5 Specific Surface Area

For analyzing the porosity of as calcined samples, specific surface area was measured by means of N_2 sorption at 77 K on a Micromeritics Tristar-II Brunauer−Emmett−Teller (BET) instrument.

2.2.2.6 Thermogravimetric analysis (TGA)

Thermogravimetric analysis (TGA) can be useful in analyzing the material stability and incurred losses at temperature increase. For thermal decomposition of $Bi(NO_3)_3{:}5H_2O$ (precursor salt), it would be interesting to analyze the subsequent losses with respect to increase temperature. For TGA analysis, a Mettler Toledo TGA/SDTA851 instrument was used, under ambient atmosphere at flow rate of 100 ml/min and 5 °C/minute heating rate, from 25 to 600 °C.

2.2.3 Organic dyes photocatalytic degradation

In order to evaluate the photocatalytic response of the synthesized samples, initially, the degradation of Rhodamine B (RhB) and Indigo Carmine (IC) were evaluated. To do that, 10 mg of each photocatalyst powder were added in 20 ml of RhB or IC dyes solutions, at a concentration of 5 mg/l (1.04×10^{-2} mmol) and 10 mg/l (2.144×10^{-2} mmol), respectively, which were initially stirred in darkness for 30 min. Then, the dispersions were irradiated with cold fluorescent light (in 400-700nm spectrum) by means of a visible lamp Flexilux-650, which was set at a very small irradiance of 40 W/m^2 in order to avoid any dye-sensitization phenomena. 3 ml solution was extracted at different time sequence and centrifuged at 10000 rpm for 5 min and the absorbance spectra was recorded using UV-vis spectrophotometer (Agilent Cary 60 UV-Vis). Furthermore, the photocatalytic response of the most performing sample was investigated for refractory dye Remazol Brilliant Blue R (BB) and degradation behavior was evaluated at various dye concentrations (*i.e.* 10, 20 and 30 ppm) and at different photocatalyst loadings (*i.e.* 10, 20, 30 mg).

2.2.4 Photocatalytic water oxidation

The most performing materials were evaluated for their photocatalytic water oxidation activity in the presence of an electron scavenger. A custom device that was previously developed and used in the reported work [17, 103], also shown in the Fig. 2.1. This device consists of a closed and stirred bubbling reactor made of quartz, was used for the photocatalytic water oxidation experiments. For each test, the reactor was filled with 110 ml of 50-mM aqueous $AgNO_3$ solution prepared with deionized water, leaving a 40% of the total volume of the reactor unfilled. Then, 100 mg of photocatalyst powder were added to the solution, resulting in a suspension of 0.91 $g_{catalyst}/l_{solution}$. Tests were performed in a temperature range between 15 and 17 ^{o}C at neutral pH. Argon inlet flow rate was fixed at 12 Nml/min, controlled by a Bronkhorst Mass Flow Controller. After setting dissolved oxygen at baseline (zero), the reactor was irradiated with simulated solar-light, by means of a plasma lamp provided by Solaronix (model LIFI STA-40) with a 420nm cut-on filter (to cut the UV portion of the spectrum), at an irradiance of 100 $mW.cm^{-2}$.

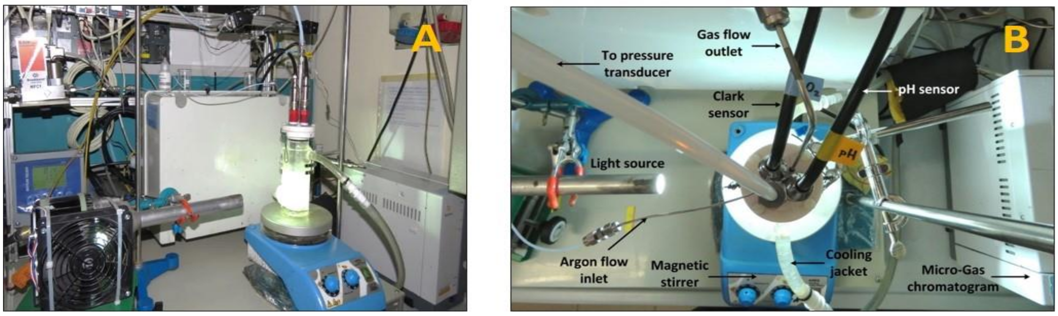

Fig. 2.1 Bubbling reactor set-up; overall view (left) and top view (right).

2.3 Results and discussion

2.3.1 TGA analysis

Fig. 2.2 shows the TGA curve for $Bi(NO_3)_3{:}5H_2O$ analysed from 25 to 600 °C and its first derivative (DTG) plot. It is observed that weight loss started at 60 °C and was followed up to about 160 °C, with three prominent noted peaks in the DTG spectra at 78 °C, 132 °C and 156 °C. In this interval, the total weight loss of about 36 % could be related to water removal. A further weight loss (~8 wt. %) was noticed in the temperature range 250-330 °C, which is displayed by another leading peak at 278 °C in DTG plot, probably due to the breaking of of the bismuth nitrate into decomposition intermediates, identified as $Bi_5O_7NO_3$ and other volatile products, such as NO and O_2 [86]. An additional weight loss of around 4 %, with no considerable peaks in DTG, was observed from 330 °C to 471 °C, which could be related to the migration of O_2 and NO to the solid surface and their removal. Further, two minor peaks appeared in the DTG at 471 °C and 510 °C, mainly ascribed to the dissociation of $Bi_5O_7NO_3$ into stoichiometric Bi_2O_3, accompanied by a continued loss of O_2 and NO [86]. Above 540 °C, no notable changes in both TGA and DTG plots were observed; suggesting the complete dissociation of $Bi_5O_7NO_3$ to a stable Bi_2O_3 phase comprised by 49 wt% of the original weight of precursor salt [86, 104, 105].

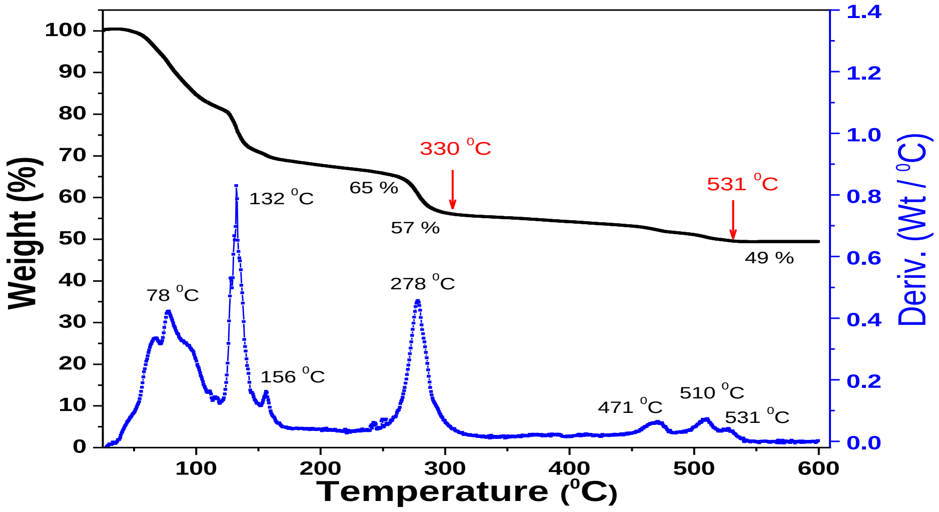

Figure. 2.2 TGA and DTG curves for Bi $(NO_3)_3$:$5H_2O$ thermal decomposition.

2.3.2 XRD

XRD patterns of all samples are shown in Fig. 2.3A (normal scale) and 2.3B (magnified scale). All the diffraction peaks of the B400 sample ascribed to orthorhombic $Bi_5O_7NO_3$ (JCPDS card no. 00-051-0525). A large broadening of the main peaks at 27.60 and 30.67°suggested that the achieved $Bi_5O_7NO_3$ at 400 °C is less crystallized or is not completely stabilized, however Kodama *et. al.* [86] reported that structural improvements could be obtained at elevated calcination temperature or by a rapid quench after the calcination.

After calcination at 425 °C, the $Bi_5O_7NO_3$ peak at 27.60° observed for the B425 sample is well pronounced and a bit stretched; however, additional peaks appeared at 27.80, 31.18, 32.7, 45.82, 55.42° that evidence the presence of some β-Bi_2O_3 (JCPDS card no. 01-076-0147), as clearly observed in the magnified XRD patterns in Fig. 2.3B. This suggest that, at 425 °C, the losses of NO and O_2 as discussed in TGA analysis, introduced the formation of a $Bi_5O_7NO_3$/β-Bi_2O_3 heterostructure. The XRD spectrum of the B450 sample (calcined at 450°C) also confirmed the existence of a $Bi_5O_7NO_3$/β-Bi_2O_3 heterostructure, even richer in β-Bi_2O_3 proportion than the B425 sample, as witnessed by the leading β-Bi_2O_3 peaks height. Moreover, this can be linked to a further decomposition of the $Bi_5O_7NO_3$ by increasing the temperature, with a consequent loss of NO and O_2 and generation of β-Bi_2O_3.

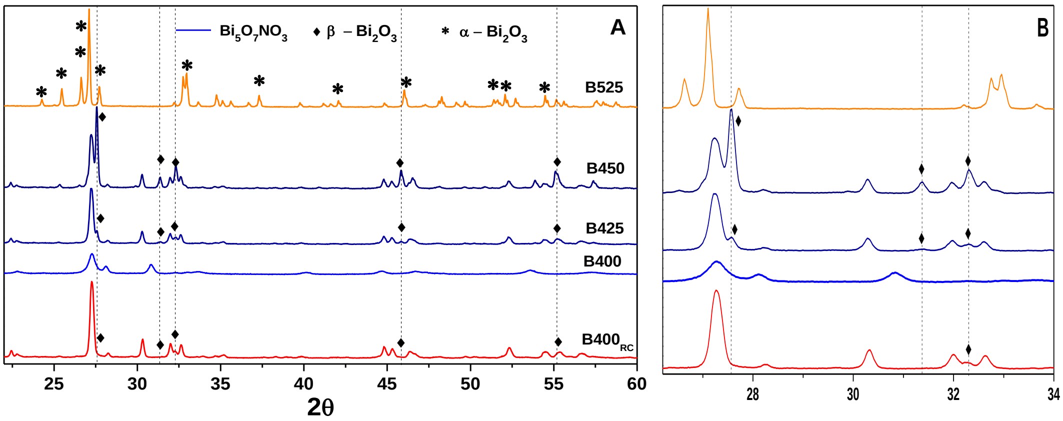

Fig. 2.3 XRD patterns of samples prepared with different thermal treatments: B400, $B400_{RC}$, B425, B450 and B525. A) full-spectra and B) magnification in the range between 26 and 35º.

It is unveiled in many studies that, the metastable β-Bi_2O_3 phase is usually transformed into α- Bi_2O_3 during ambient cooling to room temperature; unless some dopants, such as tantalum or niobium, are introduced and stabilize the metastable β-phase at room temperature [106-108]. In the present case, it is noteworthy that stabilization of β-Bi_2O_3 is caused by the N present in the precursor. Additionally, this stabilizing role of N is supported by the XRD spectrum of the sample calcined at 525 °C, which evidenced all the diffraction peaks of the monoclinic α-Bi_2O_3 phase and reveals that, after a complete loss of N, the β-Bi_2O_3 phase was then transformed into α-Bi_2O_3 during the cooling process [86, 104, 105]. Another proof came from the indicated results in the Table 1, the N atomic % (obtained from EDS analysis) of the B525 sample is only in traces level than the other samples. In the XRD pattern of $B400_{RC}$ sample, the $Bi_5O_7NO_3$ peaks became sharper and more pronounced than for the B400 sample, as anticipated due to the rapid cooling after calcination resulted higher crystallinity of the $Bi_5O_7NO_3$. However, in sample $B400_{RC}$ some other peaks also appeared together with the $Bi_5O_7NO_3$ structure (see Fig. 2.3B), which could be ascribed to a small amount of β-Bi_2O_3 at very low intensity, but due to XRD sensitivity for concentration below it was difficult to be confirmed by relating only with XRD analysis. It is worth mentioning that Shu Gong *et. al.* and Shujie Yu *et. al.* [14, 65] reported XRD patterns similar presented here for materials prepared like the $B400_{RC}$ sample, but they only identified the $Bi_5O_7NO_3$ structure without classifying the low intensity peaks. Considering that presence of any Bi_2O_3 in $Bi_5O_7NO_3$ structure could influence the photocatalytic performance of the $B400_{RC}$ sample if compared to other materials; intense analysis of other characterization was followed and discussed in detail in coming sections.

2.3.3 FESEM

Relevant differences in morphology and degree of agglomeration were observed, due to different calcination temperature. The FESEM image of the sample calcined at 400 °C (Fig. 2.4A) showed flat overlapped nanosheets, identical to previously reported morphology of $Bi_5O_7NO_3$ [14, 64]. While these overlapped sheets in progress to grow and detached at higher temperatures (*i.e.* 425 °C), as noticed in sample B425 in Fig. 2.4C. A further increase of the temperature to 450 °C allowed these sheets to separate more, with the origination of tiny channels and then transformation into a porous network of nanoflakes (Fig. 2.4D); ascribed to typical structure that has been reported for various bismuth based oxides [14, 53].

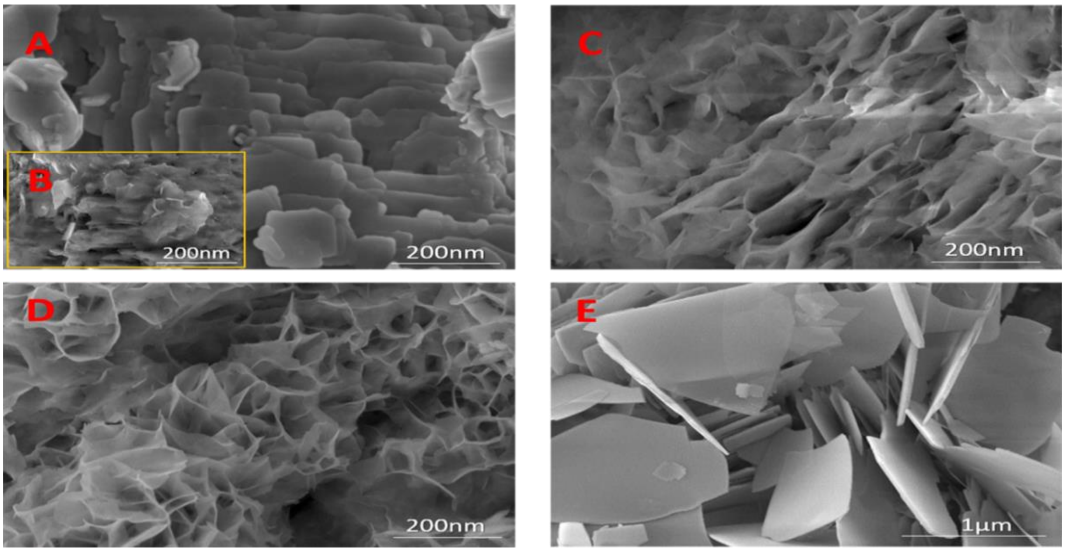

Fig. 2.4 FESEM Images: A) B400: inset B) $B400_{RC}$ C) B425, D) B450 and E) B525

At elevated temperature to 525 °C the formation of larger and unconnected micrometric sheets (Fig. 2.4E) was found, possibly because of the crystals sintering induced at such conditions. The B400$_{RC}$ sample shown in Fig. 2.4B (inset in Fig. 2.4A) displayed misaligned and distorted sheets because of rapid cooling after calcination; change than B400 sample in which the nanosheets were conclusively aligned and overlapped.

It is known that the formation of layered nanostructure and the presence of nano and micro pores could improve the photocatalytic active area and activated sites. To observe that, BET surface areas of all the samples were measured, by means of N_2 adsorption and values are given in Table 2.1. It was confirmed that the B450 sample with interconnected nanoflakes structure has a larger surface area than the other samples with flat layers or nanosheets *i.e.* B400, B425 and B400$_{RC}$. In case of sample B525, decrease in the surface area is associated with agglomeration of large plates due to increased calcination temperature.

Table. 2.1 Crystalline phases, energy band gap, BET surface area, N content (at. %) and kinetic apparent rate for all the samples

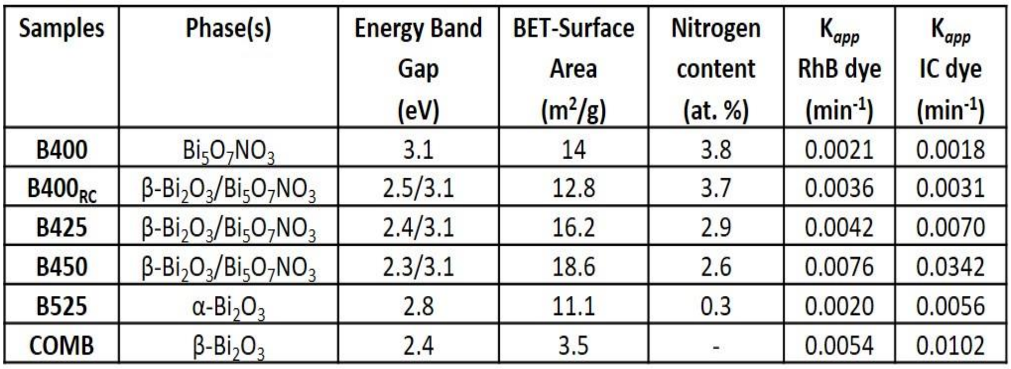

Samples	Phase(s)	Energy Band Gap (eV)	BET-Surface Area (m^2/g)	Nitrogen content (at. %)	K_{app} RhB dye (min^{-1})	K_{app} IC dye (min^{-1})
B400	$Bi_5O_7NO_3$	3.1	14	3.8	0.0021	0.0018
B400$_{RC}$	β-$Bi_2O_3/Bi_5O_7NO_3$	2.5/3.1	12.8	3.7	0.0036	0.0031
B425	β-$Bi_2O_3/Bi_5O_7NO_3$	2.4/3.1	16.2	2.9	0.0042	0.0070
B450	β-$Bi_2O_3/Bi_5O_7NO_3$	2.3/3.1	18.6	2.6	0.0076	0.0342
B525	α-Bi_2O_3	2.8	11.1	0.3	0.0020	0.0056
COMB	β-Bi_2O_3	2.4	3.5	-	0.0054	0.0102

2.3.4 Optical properties

Fig. 2.5A and 2.5B display UV-Vis DRS spectra of all samples while insets show the corresponding Tauc plots used for the band gap estimation [15, 101]. In Fig 2.5A the absorption in the region 250 – 420 nm of samples: B400, B425, B450 and B400$_{RC}$ consistent to electron transitions from valence band to conduction band that are characteristic of $Bi_5O_7NO_3$ [64, 65, 104]. However, another appeared plateau associated to absorption edges above 380 nm in the B425, B450 and B400$_{RC}$ samples evidenced the presence of an additional β-Bi_2O_3 phase; as confirmed when compared with the one of the commercial β-Bi_2O_3 (COMB) shown in Fig. 2.5B and reported in previous studies [14, 18, 101]. An increasing of the visible absorption up to 550 nm in the order $B400_{RC}$ < B425 < B450 is in accordance with the XRD results, featuring that B425 and B450 samples are constituted by β-Bi_2O_3/$Bi_5O_7NO_3$ heterostructures, while the $B400_{RC}$ sample is mainly composed of $Bi_5O_7NO_3$ with a few amounts of impurity associated to β-Bi_2O_3. This finding for $B400_{RC}$ sample is important since the presence of a broadening in UV-VIS spectra from 370 nm to 520 nm has been previously reported for $Bi_5O_7NO_3$ only; by Shu Gong *et. al.* and Shujie Yu *et. al.* [14, 65], without classifying β-Bi_2O_3 within the $Bi_5O_7NO_3$ structure, although the XRD and UV-VIS absorbance spectra reported by them were similar to that are presented here. In their studies role of β-Bi_2O_3 impurities was not highlighted during the photocatalytic performance of $Bi_5O_7NO_3$. For B525 sample, typical absorption from 380 nm to 450 nm observed in Fig. 2.5B corresponds to the α-Bi_2O_3 [14, 101].

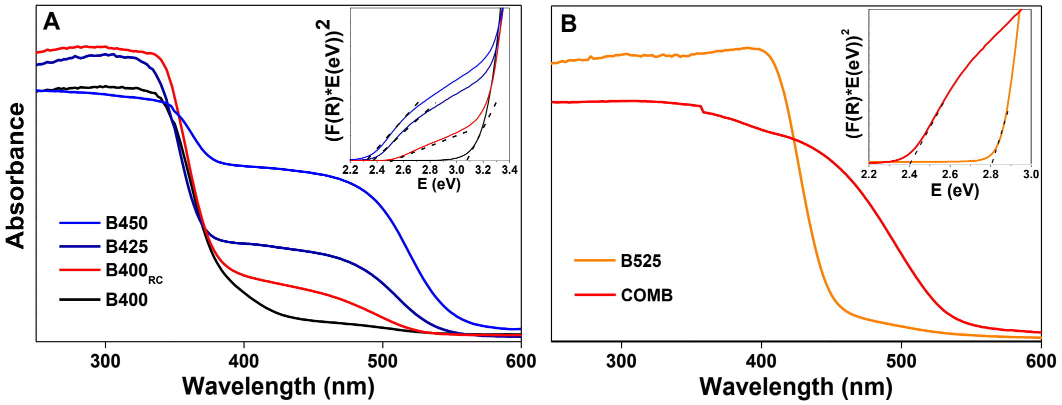

Fig. 2.5 UV-Vis DRS spectra of samples: A) B400, $B400_{RC}$, B425 and B450 and B) B525 and COMB. Tauc plots of the corresponding samples are shown in the insets.

The estimated band gap energy values for all samples are given in Table 2.1. In the case of heterostructures, the obtained values for each transition are mentioned separately *i.e.* contribution of β- Bi_2O_3 and $Bi_5O_7NO_3$. In previous work by Shu Gong *et. al.* and Shujie Yu *et. al.* [14, 65], $Bi_5O_7NO_3$ has been stated as visible light driven photocatalyst with a narrow band gap energy: as 2.51 or 2.7 eV, respectively. However, here obtained results demonstrate that the $Bi_5O_7NO_3$ has an absorbance spectrum near UV-region with a band gap of about 3.1 eV (sample B400), as found in other works [64, 65, 104]. Another confirmation of narrowing in energy band gap of $Bi_5O_7NO_3$ can be seen in Tauc plot, in which contribution of the β-Bi_2O_3 phase could be clearly observed for samples: B400$_{RC}$, B425 and B450, which narrowed the band gap values between 2.3 and 2.5 eV. For the B525 samples, the estimated band gap was of 2.8 eV, higher than that of the β-Bi_2O_3 portion of the heterostructures, is in accordance to the β-Bi_2O_3 transformation into α-Bi_2O_3, when N was completely lost at increased temperature.

2.3.5 Chemical composition (XPS)

XPS analysis has been conducted to analyze the chemical composition of the samples surface, since the knowledge of the chemistry of the first layers of a material is of fundamental importance for understanding its catalytic properties. Survey scans (see Fig. 2.6A) have been acquired for all the samples to know the relative atomic concentration of the chemical elements and the results are reported in Table 2.2.

Table 2.2. XPS relative atomic concentration (at%) of the elements present in all the samples

Samples	C	O			N	Bi	O/Bi in Bi oxide
B400	35.7	40.3	10.3	30.0	0.9	23.0	1.3
B400$_{RC}$	44.7	33.9	11.2	22.7	0.8	20.6	1.1
B425	35.2	40.0	16.0	24.0	1.0	23.9	1.0
B450	36.6	38.9	9.4	29.5	1.1	23.5	1.3
B525	51.6	26.6	6.5	20.1	-	21.8	0.9
		Total amount of O	O involved in C—O bonds	O involved in Bi oxides			

As can be seen, all the samples show the presence of C, O and Bi, while N has been detected in all the samples apart from B525 one (Fig. 2.6C, inset), which confirms the previous EDS results. The presence of C should be ascribed to surface contamination from the environment (adventitious carbon) The amount of O involved in C—O bonds was inferred from the deconvolution of the high resolution (HR) C1s spectra (not reported). Thus, the remaining O amount should be ascribed to the formation of Bi oxynitride or Bi oxides (both $Bi_5O_7NO_3$ or Bi_2O_3); as discussed in the XRD section. However, the O/Bi ratio is lower than expected, both for the $Bi_5O_7NO_3$ (O/Bi = 2) or Bi_2O_3 (O/Bi = 1.5) for all the samples. This means that there is a lack of O on the surface (O vacancy), which has to be ascribed to structural defects and/or sub-stoichiometric forms of Bi oxides [109].

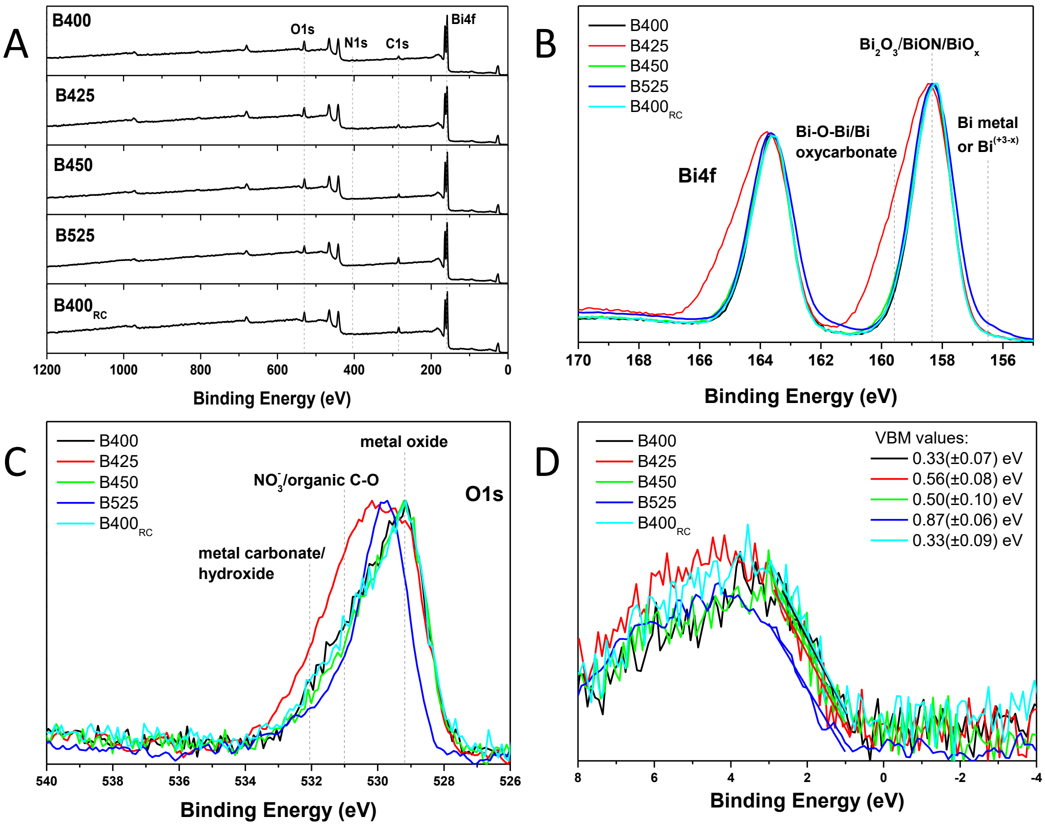

Fig. 2.6 (A) XPS survey of all the samples. High resolution spectra of: Bi4f (B), O1s (C), N1s (inset in C) and Valence Band region (D).

To evaluate the bismuth chemistry, the HR spectra of the Bi4f doublet ($4f_{7/2}$ and $4f_{5/2}$) was acquired and is reported in Fig. 2.6B. All the samples show the main $4f_{7/2}$ peak at 158.3 eV, which corresponds to the Bi^{3+} oxidation state [110] in accordance to the presence of either $Bi_5O_7NO_3$ or Bi_2O_3 phases. Moreover, the spectrum of the B425 sample shows an enlargement of the peaks towards higher binding energies: from the deconvolution procedure, not shown, an extra component at 159.4 eV for $Bi4f_{7/2}$ peak (and another one separated by +5.31 eV for the $Bi4f_{5/2}$ component) should be added to correctly fit the experimental curve. This chemical shift has been already reported in literature and has been ascribed to an amorphous material (e.g. Bi oxalate, carbonate or hydroxide) [111]. This hypothesis could be reasonable since from the O1s HR spectra (see Fig. 2.6C), the B425 sample's oxygen peak has an enlargement towards higher binding energy: probably a chemical shift due to a metal carbonate or hydroxide [112], because of oxygen deficiency at surface. Previously, from the XRD and TGA analyses, it was observed that the formation of β-Bi_2O_3/$Bi_5O_7NO_3$ heterostructure was initiated during calcination at 425 °C (B425) due to loss of N and O. XPS analyses confirmed that calcination at 425 ^oC induced a lower amount of available O and a high quantity of structural O defects that could lead to the formation Bi hydroxide at the surface, which being amorphous in nature was not detected by XRD. Moreover, from Table 2.2, the B425 sample shows a higher amount of O bonded with C, which could be associated to CO_2 adsorbed on the O defective sites and thus, the presence of other C-containing amorphous structures such as Bi-oxalate or Bi-carbonate could not be excluded. The B525 sample, the one without N on the surface, instead shows a chemical shift towards lower binding energies (extra peak at 156.3 eV for $Bi4f_{7/2}$). This peak is usually related to the presence of oxidation states lower than +3 (Bi-O- non-bridging oxygens) or 0 (for metallic Bi) [113].

Using XPS analysis, valence band maximum (VBM) energy level was also estimated (see Fig. 2.6D). According to the literature [114], it was made a linear fit on the descending part of the signal towards the 0 eV value, which corresponds to the Fermi Energy (EF) level. The distance between the X-intercept and the EF corresponds to the VBM. As can be inferred from Fig. 2.6D, all the N containing samples have similar curves. The VBM values of the B400 and B525 samples were of 0.33 eV and 0.87 eV, respectively, which thus correspond to bare $Bi_5O_7NO_3$ and α-Bi_2O_3. The difference in VBM values of B425 and 450 samples *i.e.* 0.56 and 0.5 eV, respectively, is expected due to the presence of β-Bi_2O_3. Since the amount of β-Bi_2O_3 in the $B400_{RC}$ sample is too low, it has shown similar VBM as of sample B400.

VBM obtained from the XPS analysis and band gaps calculated from the UV-Vis spectroscopy measurements, were used to draw a simplified scheme of the energy levels for each sample [115], which is shown in Fig. 2.7. For both the B400 and $B400_{RC}$ samples, the $Bi_5O_7NO_3$ band gap was used since it is the most representative crystalline phase in these photocatalysts. As expected, the band levels of the B525 sample are representative of the α-Bi_2O_3. In the case of B425 and B450, the change in VBM values was reasonably due to the bismuth oxide and not to the bismuth oxynitride phase due to existence of β-Bi_2O_3. From the figure Fig. 2.7, it is clear that the positions of the CB and VB levels of the β-Bi_2O_3 are lower in energy than such of $Bi_5O_7NO_3$ (sample B400) and, therefore, an enhanced charge carrier separation in the β-Bi_2O_3/$Bi_5O_7NO_3$ heterojunctions is expected (samples: $B400_{RC}$, B425 and B450) due to the proper alignment of the energy levels of these two crystalline materials, while the higher band gap of bare $Bi_5O_7NO_3$ and α-Bi_2O_3 is expected to play against their photocatalytic behavior.

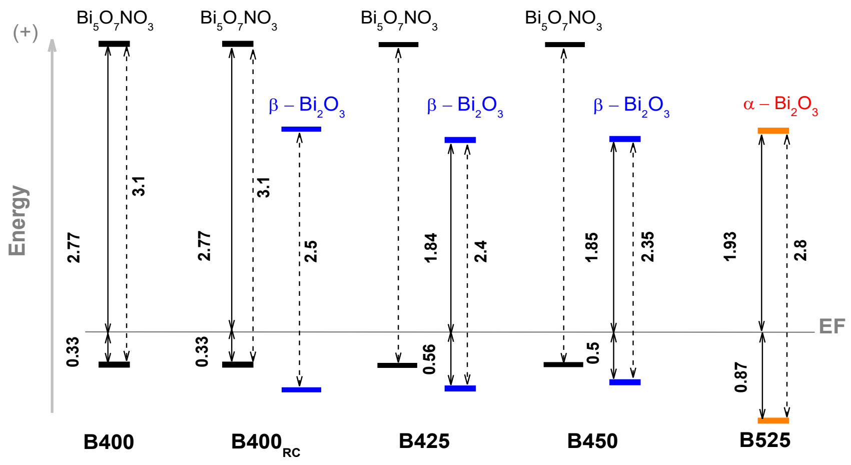

Fig. 2.7 Band structures calculated from the VBM (from XPS measurements) and Eg (from UV-Vis spectroscopy analyses) for all the samples.

2.3.6 Photocatalytic dyes degradation

All the prepared samples as well as the commercial β-Bi_2O_3 were evaluated for photodegradation of cationic RhB and IC dye. Initially, the dye solution along with photocatalyst was kept in dark for 30 min under stirring; identified as adequate time for adsorption-desorption equilibrium. Afterwards, the dye solution was irradiated under simulating sunlight and aliquots were taken, at different time intervals; in order to record the change in the absorption spectrum with respect to time and to assess photodegradation process. Fig. 2.8A and C shows the relative concentration (C/C_o) curves versus the irradiation time, where C is the dye concentration at different times and C_o is the initial one, but were obtained by using the intensity of the main absorption peak of each dye at time t. Moreover, the apparent photodegradation kinetic rates (K_{app}), correspond to each sample and for both dyes, were determined by using Eq. 1 and are reported in Table 2.1.

$$\ln(A_t/A_o) = K_{app} * t \qquad \text{(Eq. 2.1)}$$

where, A_o is the initial dye absorbance maxima, A_t is the final dye absorbance maxima at irradiation time t (min) and K_{app} is the rate constant (min^{-1}). The above equation is typical for pseudo first order of reaction kinetics [101]. As shown in Fig. Fig. 2.8A, adsorption rate (between 10 and 20 %) of the cationic Rh-B dye molecule was observed for all samples under dark conditions. This could be due to a preferential chemisorption of either carboxylic ($COOH^-$) [101] or diethylamine ($(C_2H_5)_2NH^+$) groups, which are present in the chain of the Rh-B dye molecule, and interacted with the surface of the photocatalysts [116-118].

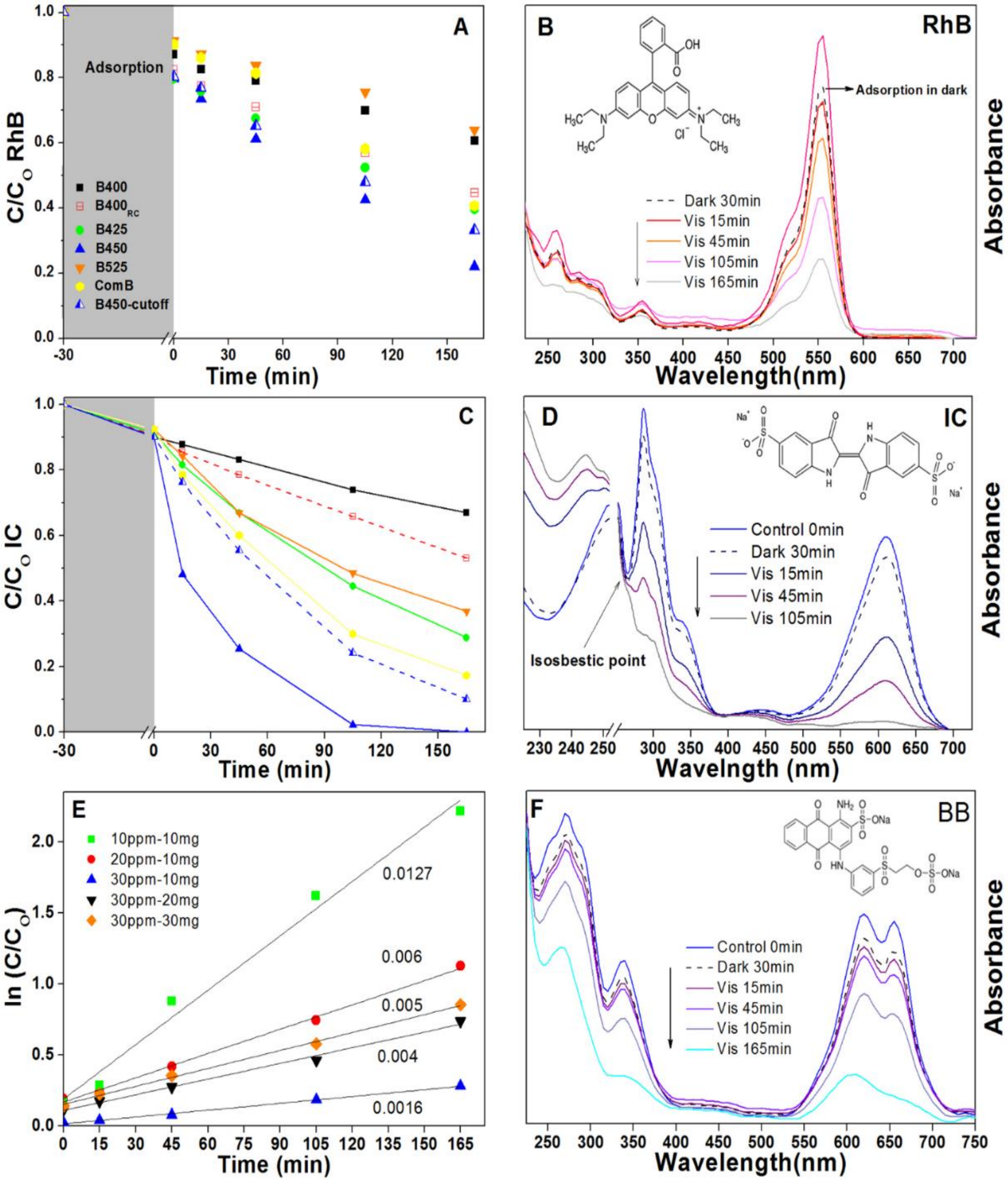

Figure. 2.8 Relative C/C₀ curves for degradation of Rh-B (A) and IC (C) *vs.* irradiation time for all samples. Absorbance spectra of Rhodamine B (B) and Indigo Carmine (D) during the photodegradation with B450 sample. (E) Kinetic curves of BB dye degradation under different dye concentrations (ppm) and photocatalyst loadings (from 10 to 30 mg), with the determined K_{app} (min^{-1}) reported each curve. (F) Absorbance spectra of BB dye solution (30 ppm) during the photodegradation with 20 mg of B450 sample.

The Rh-B dark-adsorption behavior is in good correlation with the photocatalysts surface area and increased from the B400 sample, which is constituted by $Bi_5O_7NO_3$ flat nanosheets, to the B425 and B450 samples, which are based on a more porous structure made of interconnected nanoflakes (as seen above in FESEM images of Fig. 2.4) that provably enhanced the number of reactive sites. Under simulated sunlight illumination, the B400 and B525 samples have shown some activity for the Rh-B degradation, but it did not reach 40 % and was lower than those of the β-$Bi_2O_3/Bi_5O_7NO_3$ heterostructured samples: $B400_{RC}$, B425 and B450. These results are in contrast to the high activity of $Bi_5O_7NO_3$ for the degradation of Rh-B under visible light earlier reported by Shu Gong *et. al.* and Shujie Yu *et. al* [14, 65]. As explained above, in their works, the authors reported on $Bi_5O_7NO_3$ powders that have similar characteristic as obtained for $B400_{RC}$ sample and had similar optical properties to it, which suggest that the visible light response (and low band gap, *i.e.* 2.5 to 2.7 eV) of their samples was due to the presence of some β-Bi_2O_3, as demonstrated by the above presented results. The time-course photodegradation process of the Rh-B solution is followed as the UV-Vis absorbance spectra at different irradiation time (Fig. 2.8B), which shows a continuous decrease of the main Rh-B peak at 554 nm and of the whole spectrum. Such result indicated that the effective photodegradation of Rh-B could be associated with a strong interaction of the dye molecule with β-$Bi_2O_3/Bi_5O_7NO_3$ surface, provided by a preferential adsorption of carboxylic and diethylamine groups, that could be subsequently oxidized by reactive oxygen species (*i.e.* $O_2^{\cdot-}$ and $OH^{\cdot}$ radicals) [101]. In literature is reported that hypsochromic shifts in the absorbance spectrum of Rh-B are observed when dye-sensitization of the photocatalyst with Rh-B are observed [47]. Thus, since no hypsochromic shifts were evidenced here, suggesting that the degradation of Rh-B followed a photocatalytic mechanism using the heterostructured samples. Similar results for Rh-B were also obtained in previous studies which used α/β-Bi_2O_3 composites and α-Bi_2O_3 [16, 101].

In the case of the anionic IC dye, the dark-adsorption rate on the photocatalysts was of about 10 % for all samples (Fig. 2.8C), due to a preferential adsorption of sulphonic (- SO_3) groups over photocatalyst indicating a negligible impact of morphology and surface area on adsorption phenomena; the obtained adsorption rate was in accordance to previous studies [16, 101, 119]. After exposing to light, a faster decrease of the dye concentration was observed for all the β-$Bi_2O_3/Bi_5O_7NO_3$ heterostructured samples, *i.e.* $B400_{RC}$, B425 and B450, evidenced a faster kinetics than for Rh-B, but the kinetic rate was remained higher for B450 sample; also indicating the improved performance compared to other samples. The decrease in IC absorbance spectra is the result of photocatalytic degradation of the IC as confirmed by the UV-Vis spectra changes (shown in Fig. 2.8D); as a result of oxidation of the Indigoid (HNC=CNH) group of IC by generated $O_2^{\cdot -}$ and $OH^{\cdot}$ radical species, with a subsequent dissociation into Isatin sulfonic acid and 2-amine-5-sulfo-benzoic acid intermediates, which were identified due to their UV adsorption peaks at 220 and 260 nm, respectively [16, 101, 119-121].

Though, α-Bi_2O_3 (*i.e.* B525) and the pure $Bi_5O_7NO_3$ sample (*i.e.* B400) for both Rh-B and IC dyes, displayed very low performance: for α-Bi_2O_3 (besides having band gap of 2.8 eV) could be due to unfavorable morphology that not permitted adequate interaction with dye molecule, while for pure $Bi_5O_7NO_3$ sample being high band gap of 3.1 eV not efficiently activated under visible light. Overall, from the analyses of the K_{app} rates (Table 2.1) and relative concentration plots of both dyes (Fig. 2.8), it was found that the B450 sample exhibits the best performance; In fact, the B425 and $B400_{RC}$ samples displayed lower photocatalytic activity than the B450, revealing a provably limited availability of free electrons and holes in the heterostructures for being lower in β-Bi_2O_3 proportion.

The improved activity of the B450 sample could be ascribed to an optimal proportion between β-Bi_2O_3 and $Bi_5O_7NO_3$ in heterostructure that leads to a wider absorption spectrum range, porous morphology in favor of higher surface area, lower amount of O defects and better crystallinity than the other heterostructured samples (*i.e.* B425 and $B400_{RC}$). However, this improved activity could be additionally related to the suitable alignment between β-Bi_2O_3 and $Bi_5O_7NO_3$ (as reported in Fig. 2.6), which allows synergy and an improved charge carriers separation at the β-$Bi_2O_3/Bi_5O_7NO_3$ heterojunction interphase. Fig. 2.9A shows a scheme representing the photocatalytic mechanism of the β-$Bi_2O_3/Bi_5O_7NO_3$ heterostructure surface during the degradation of the investigated dyes. That is, photogenerated electrons are transported from the CB of $Bi_5O_7NO_3$ to the CB of β-Bi_2O_3, while the holes move from the VB of β-Bi_2O_3 to the VB of $Bi_5O_7NO_3$, which allowed to a higher amount of free e^- and h^+ to be transported to the photocatalyst surface. As a consequence, the rates of oxidation and reduction reactions at the powder-solution interphase was improved enabling the formation of reactive oxygen species (OH radicals, $OH^{\cdot}$, and superoxide ions, $O_2^{\cdot -}$) that are responsible for the dyes degradation. This synergetic effect is also confirmed by the superior photodegradation activity of the β-Bi_2O_3/$Bi_5O_7NO_3$ heterostructures with respect to the commercial β-Bi_2O_3 (COMB), as shown in Fig. 2.8A and 2.8C. Moreover, in order to quantify in what extend photogenerated e^-/h^+ in $Bi_5O_7NO_3$ contributed to the catalytic performance, the B450 sample was also investigated by using a 420nm cut-off filter that removed UV light. Indeed, results shown in Fig. 2.8A and 2.8C (for B450 cut-off), revealed that the UV activation of $Bi_5O_7NO_3$ played an important role in the photocatalytic process, since a decrease in the overall activity of the B450 sample was observed with respect to the results obtained without the UV cut-off filter: the kinetic rate decreased from 7.6×10^{-3} to 5.4×10^{-3} min^{-1} (29 %) during the Rh-B photodegradation and from 34.2×10^{-3} to 13.2×10^{-3} min^{-1} (61 %) during the IC photodegradation.

In order to confirm that h^+ (responsible of the formation of OH radicals) are well separated from the free e^- during photocatalytic performance and playing their role in photodegradation; water oxidation tests were also carried with the most performing heterostructured samples *i.e.* B400 and B450. In fact, since the VB position of both $Bi_5O_7NO_3$ and β-Bi_2O_3 are suitable for the light-induced water oxidation reaction by those semiconductors (*i.e.* $2H_2O + 4h^+ \rightarrow O_2 + 4H^+$), the O_2 evolution on these materials could be used as a mean to quantify the number of holes able to reach the catalyst surface and to estimate the relative efficiency of h^+/e^- separation between two photocatalyst materials.

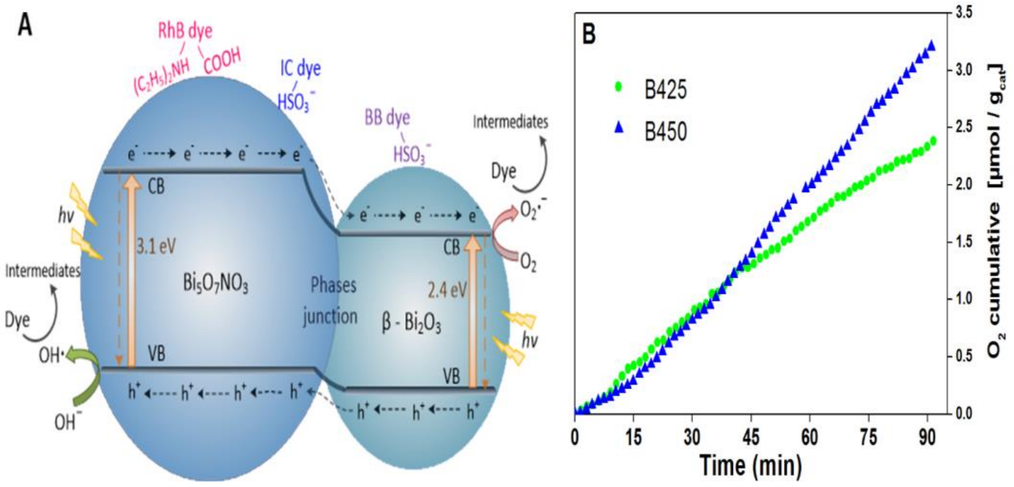

Fig. 2. 9 (A) Photocatalytic mechanism of dyes degradation on β-Bi_2O_3/$Bi_5O_7NO_3$ heterostructure. (B) cumulative O_2 evolution during water oxidation reaction with the B425 and B450 samples, under sunlight illumination and by using silver nitrate as sacrificial reagent.

As shown in Fig. 2.9B, the B450 sample evidenced a higher O_2 evolution ability than the B425 one, which confirm the previous hypothesis of the optimum β-$Bi_2O_3/Bi_5O_7NO_3$ ratio in the B450 material.

Since, B450 sample exhibited high photocatalytic response during degradation of RhB and IC and for O_2 evolution, therefore further investigation was continued with B450 sample, for the degradation of refractory anionic dye Remazol Brilliant Blue R (BB), at different concentrations. This dye was selected because it contains an anthraquinone group that renders it more stable and difficult to remove than dyes like Rh-B and IC [47].

Dark-adsorption rates of BB in a high concentrated solution (30 ppm) over the β-$Bi_2O_3/Bi_5O_7NO_3$ heterostructured sample was found to be very low (~ 3 %) with a photocatalyst amount of 10 mg, but it was improved up to 17 % with 20 mg and remained almost the same by increasing the loading to 30 mg of material. Fig. 2.8E reports the kinetic curves of degradation experiments under UV-Vis light illumination and shows that at a low concentration of BB dye, *i.e.* 10 ppm, the rate of degradation (12×10^{-3} min^{-1}) was higher than such at concentrations of 20 and 30 ppm, which had reaction rates of 6×10^{-3} and 1.6×10^{-3} min^{-1}, respectively. The exponential decrease in the photocatalytic performance could be related to the limited number of active sites of photocatalyst per number of dye molecules. This decreased kinetic rate is consistent to previously obtained results [122-124], which indicated that higher dyes concentrations reduced light penetration, decreased the path length of photon entering to the solution and reduced the light-exposure of the photocatalyst, which affected the generation of $O_2^{\cdot-}$ and $OH^{\cdot}$ Species lowering the overall photocatalytic activity.

In order to assess the optimal loading of photocatalyst when dealing with dye solutions at higher concentrations, *i.e.* up to 30 mg/l, the photocatalytic evaluation was also carried by adding 20 and 30 mg of photocatalyst in the dye solution. Plots in Fig. 2.8E show that the kinetic constant (K_{app}) for the BB dye degradation at 30 ppm was improved more than two-fold by doubling the photocatalyst loading. It changed from 1.6×10^{-3} min^{-1} with 10 mg of photocatalyst to 4×10^{-3} min^{-1} with 20 mg, while a further increase of the photocatalyst amount to 30 mg barely contributed to a further increase in the kinetic rate. This suggested that the optimum photocatalyst / BB dye weight ratio is of around 33, which is about 2-3 times lower than previous results found in the literature [125, 126]. As for the IC dye, also in the case of BB dye is adsorbed on the catalyst surface through sulphonic groups that allowed the interaction of this anthraquinone-based chromophore with the photogenerated reactive oxygen species ($OH^{\cdot}$ and $O_2^{\cdot-}$

radicals). Representative absorbance spectra of BB dye degradation with 20 mg of photocatalyst during the time course of the experiment are shown in Fig. 2.8F. It is shown that, initially, photodegradation occurred slowly due to the high dye concentration (30 ppm), but after about 45 min the main absorbance peaks at 620 nm and 655 nm decreased faster and reached a minimum at about 165 min. In order to find if BB dye underwent mineralization, total organic carbon (TOC) was measured before and after the photocatalytic test and those results confirmed a 55 % of BB mineralization after 165 min of irradiation exposure. Such result was also confirmed by a shift of the peak at 338 nm to 320 nm, which indicates the formation of some degradation intermediates.

2.4 Conclusion

$Bi_5O_7NO_3$, α-Bi_2O_3 and $Bi_5O_7NO_3$/β-Bi_2O_3 heterostructures were synthesized by means of a simple and low-cost thermal decomposition of $Bi(NO_3)_3$:$5H_2O$, at different calcination temperatures, avoiding the use of other solvents or chemicals. TGA and DTG experiments revealed that an instable $Bi_5O_7NO_3$ phase can be formed from 278 °C that undergoes a gradual loss of volatile gases up to 471 °C, which was observed as a threshold temperature for the decomposition of $Bi_5O_7NO_3$ that transforms into β-Bi_2O_3. XRD revealed that a low-crystalline $Bi_5O_7NO_3$ is obtained after calcination at 400 °C with a slow cooling, while at higher temperatures (425 and 450 ^oC) its crystallinity is improved, but some β-Bi_2O_3 is formed in the lattice creating β-Bi_2O_3/$Bi_5O_7NO_3$ heterostructures, due to the presence of N that was found to stabilize the β-Bi_2O_3 polymorph at room temperature. The amount of β-Bi_2O_3 increased with temperature rises and at even higher temperatures, *i.e.* 525 °C, the $Bi_5O_7NO_3$ completely decompose and β-Bi_2O_3 is transformed into α-Bi_2O_3, due to the complete loss of N. The morphology evolution was monitored from FESEM characterization: initially, tightly overlapped nanosheets were obtained at 400 °C, while temperature increase up to 425 or 450 ^oC allowed them to transform into porous nanoflakes with an improved specific surface area, which modified into micrometric and well-separated sheets at 525 ^oC. By following a fast cooling after calcination at 400 ^oC, a small amount of β-Bi_2O_3 was also formed within $Bi_5O_7NO_3$, which induced a broadening of the UV-Vis spectrum of this sample towards higher wavelength, *i.e.* up to 550 nm, and light induced transition with a band gap energy of about 2.4 eV, like it was observed for the other β-Bi_2O_3/$Bi_5O_7NO_3$ heterostructured samples. XPS analysis revealed the presence of oxygen vacancies on the photocatalysts surface, which can be ascribed to structural defects and/or sub-stoichiometric forms of Bi_2O_3 due to continuous loss of O during calcination at higher temperatures, which might play a role in the photocatalytic performance.

Among all the synthesized samples and in comparison, with a commercial β-Bi_2O_3 sample, the best photocatalytic degradation of Rh-B and IC dyes under simulated sunlight illumination was found with the β-$Bi_2O_3/Bi_5O_7NO_3$ heterostructured sample obtained at 450 °C. The heterojunction formed between $Bi_5O_7NO_3$ and β-Bi_2O_3 caused an improved reactivity with respect to the pure phases by enabling an effective charge carrier separation, which is supported by the experimental determination of the band levels by means of VBM, XPS and UV-Vis spectroscopy analyses. Indeed, a cascade effect of well-separated electrons and holes at the surface of β-$Bi_2O_3/Bi_5O_7NO_3$ heterostructures permitted an efficient generation of superoxide ($O_2^{\cdot-}$) and hydroxyl ($OH^{\cdot}$) radicals in the solution, which was also confirmed by the water splitting and O_2 evolution ability of this material. Additionally, this $Bi_5O_7NO_3$/β-Bi_2O_3 heterostructure showed a good performance for the photocatalytic mineralization of a refractory dye, *i.e.* BB that contains anthraquinone group, at low concentrations (*i.e.* 10 ppm) or at higher ones (*i.e.* 30 ppm) with an optimum photocatalyst/dye weight ratio of 33, which is 2-3 times lower than previously reported results. From the here reported results, it was demonstrated that $Bi_5O_7NO_3$, α-Bi_2O_3 and β-$Bi_2O_3/Bi_5O_7NO_3$ heterostructures can be easily synthesized by solid-state route and that the visible light driven photocatalytic activity of bismuth oxynitrides can be boosted by forming heterostructures with β-Bi_2O_3, for the development of sustainable technologies for both degradation of organic pollutants in water or water splitting applications.

Chapter 3

α/β-Bi_2O_3 Heterostructure for Sequential Photodegradation of Single and Mixed Dye Solutions

3.1 Introduction

As earlier stated that, for photocatalysis using bismuth oxide (Bi_2O_3), widely investigated phases are α-Bi_2O_3 (monoclinic) and β-Bi_2O_3 (tetragonal) with an optimum bang gap energy *i.e.* around 2.4 - 2.8 eV. Both α and β- Bi_2O_3 phases are normally obtained during chemical route synthesis of Bi_2O_3 with various micro and nanostructures [15, 19, 69, 77, 78]. Some reports showed a good activity for α-Bi_2O_3 [15, 79-82], while others have found the β-Bi_2O_3 as the most effective [13, 19, 68, 69] in visible light, due to the narrow energy band gap, that allows to utilize a large portion of the solar spectrum. More recently, two studies have reported higher photocatalytic performance of α/β-Bi_2O_3 heterostructure; but the relevant information about the proportion of each phase was not given [102, 106]. Hou *et. al.* displayed the degradation of anionic methyl orange (*MO*) and cationic rhodamine B (*RhB*) under visible light by β/α- Bi_2O_3 composite in comparison to β-Bi_2O_3 sheets [106]. The results in their study revealed an optimal degradation of both dyes with α/β heterojunction obtained at 210°C, around 90% removal was quickly achieved for anionic *MO* in 15 min, while for cationic *RhB* dye in 60 min.

Shan *et. al.* obtained α/β- Bi_2O_3 heterojunction using two step synthesis method in which α-Bi_2O_3 and β- Bi_2O_3 were separately synthesized; they mixed them proportionally to make α/β-Bi_2O_3 heterojunction and further evaluated for the photodegradation of *RhB* under visible light; they showed 95% photodegradation was quickly achieved in 30 min [102]. The results were compared with single phases α-Bi_2O_3 and β-Bi_2O_3 and the description of better photoactivity of α/β heterojunction was depicted in terms of efficient charge carrier separation and bulk of free electrons and holes in the solution due to the proper alignment of α/β-Bi_2O_3 electronic bands allowed superior activity than obtained with single phases of α and β. The mentioned studies summarized improved performance of the α/β-Bi_2O_3 heterojunction, however some points need to be verified: as high amount of dye (s) were adsorbed on the photocatalyst surface, during the dark conditions that led high decrease in optical absorbance of the dye solution even before exposing under the irradiation and is not considered as the photodegradation. Moreover, Hou *et. al.* wrongly interpreted the relative dye concentration, C/C_0 plot; reported the dye intensity decrease in dark (of about 0.76) as 24% and not mentioned as the correct 76% adsorption; being very high on the α/β-Bi_2O_3 surface and was not supposed to be included in the estimation of the reaction kinetic rate of photocatalytic process, because this not involved the photoactivity and is only related with the dye intensity decrease due to adsorption over the photocatalyst surface [127, 128]. Nevertheless, both works of Hou *et. al.* and Shan *et. al.* have suggested the concept of using mixtures of phases in taking the benefit of the Bi_2O_3 different polymorphs to improve the photoactivity.

The current study comprised on a facile scalable synthesis method to obtain α/β-Bi_2O_3 composite with major characterization analyses and evaluation of photoactivity, under UV and visible light on laboratory conditions. In order to approach the real situation, in which wastewater contains more than a single dye, the photocatalytic evaluation was individually made on three different single dyes (cationic and anionic), as well as a mixture of these dyes; which have been rarely done in the past.

3.2 Experimental details

3.2.1 Synthesis of Bi_2O_3 powders

Precursor salt $Bi(NO_3)_3·5H_2O$ salt was purchased from Sigma-Aldrich and used as received. Bulk powders were synthesized using previously reported method [101]: that employed thermal decomposition of $Bi(NO_3)_3·5H_2O$. In brief, initially at 150 °C for 30 min to evaporate the water content, then the temperature was increased to 250 °C (lower than the previously stated in chapter-2; used to obtain single and heterostructure of Bi_2O_3 and $Bi_5O_7NO_3$) and kept for 2 hours. This pre-obtained sample then further calcined at 550 and 650 °C for 2 hours and then allowed for ambient cooling inside furnace. For comparison, commercial powders: α- Bi_2O_3 obtained from Farmaquimia and β- Bi_2O_3 from Sigma-Aldrich were used without any treatment. The calcined samples were labelled as B550 and B650 respective to their calcination temperatures, while COMA referred to commercial α- Bi_2O_3 and COMB to commercial β- Bi_2O_3.

3.2.2 Characterization

The crystalline structure of calcined and commercial samples was examined by X-ray diffraction (XRD) using a SIEMENS D500 X-ray diffractometer (Cu-Kα X-ray source). The obtained diffraction patterns were analyzed by using PDXL2 software to classify each phase, defining the grain size (Halder-Wagner method) and the relative amount of each crystalline phase in case of sample with more than one phase (Relative Intensity Ratio, RIR method) [129]. The point of zero charge (pzc) was measured by potentiometric titration method, using 0.01 M KCl salt as the background electrolyte for the stabilization of ionic strength in the solution, considering that the cations and anions of the background electrolyte (KCl) do not compete/react with photocatalyst surface during absorption process and do not allow formation of complexes in the solution [101]. The initial pH of 50 ml solution with 0.01 M KCl and 50 mg photocatalyst was adjusted to 2 by adding 0.01 M of HCl. The titration was followed by increasing the pH from 2 to 12 pH by gradually adding NaOH solution (0.01 M). Finally, data of the change in the pH as a function the NaOH addition were plotted and the PZC value was determined as the interception point crossing both plots [130] or estimation by using the differential technique suggested by Bourikas *et. al.* [131].

3.2.3 Photocatalysis Tests

The photoactivity of synthesized samples and commercially available samples were evaluated for degradation of anionic Indigo Carmine (*IC*), Acid Blue 113 (*AB*) and cationic rhodamine B (*RhB*) dyes under either fluorescent UV or white light 9 Watt (with irradiance intensity of 26 Wm^{-2}, and 9 Watt with irradiance intensity of 33 Wm^{-2}, respectively); investigating 20 mL of each dye solution at around neutral pH and with dye concentration of 10 mg/L. The photocatalyst load in the dye solution was 0.8 mg/mL and the resulted suspension was stirred for 30 min in the dark; adequate time for adsorption-desorption equilibrium. The absorbance spectra of each dye solution (3 mL) was measured as a function of time through Shimadzu 1800 UV-vis spectrophotometer, after dye solution withdrawal and centrifuge at 8000 rpm for 5 min. After UV-Vis analysis withdrawn aliquot were returned to the vial to preserve the same amount of powder and solution. After choosing the sample with the best photoactivity characteristics, it was assessed for the degradation of a mixed solutions one including two dyes *IC* and *RhB* dye and other including all three dyes i.e. *IC, AB* and *RhB*. These mixed solutions were prepared with 1.5×10^{-6} M concentration of each dye to ensure the same number of molecules in the solution. The powder loading for mixed solution was similar as 0.8 mg/mL and for photocatalytic investigation pH for one solution containing two dyes *IC* and *RhB* dyes was close to neutral. While for the mixed solution containing all three dyes evaluation were made at neutral, acidic and basic pH conditions; to understand the effect of pH on the kinetic rate and mineralization of dyes in mixed solution.

3.3. Results and discussion

3.3.1 Characterization of Bi_2O_3

3.3.1.1 Crystalline structure

The XRD patterns of the commercial and calcined samples are shown in Fig. 3.1. The commercial α-Bi_2O_3 COMA exhibited all the diffracted peaks correspond to monoclinic-α-Bi_2O_3, with principal peaks at 27.06, 27.52, 33.9° (JCPDS card no. 01-071-0465). Similarly, for commercial β-Bi_2O_3 (COMB) the diffracted peaks at 27.96, 31.78, 32.72, 46.22 and 55.48° ascribed to tetragonal-β-Bi_2O_3 (JCPDS card no. 01-078-1793) [13, 68]. The narrow pattern of diffracted peaks of both commercial α- and β-Bi_2O_3 samples suggested higher crystallinity with an average grain sizes of 91 and 53 nm respectively, determined after applying Halder-Wagner method [129]. While in case of the synthesized samples B550 and B650, most of the diffracted peaks correspond to the α-Bi_2O_3, but also some β-Bi_2O_3 peaks (at 27.96, 32.72, 46.22°) can be identified in sample B550; which revealed that sample B550 composed of two different phases *i.e.* α and β and exhibiting a α/β-Bi_2O_3 composite; with around 20% in proportion of β-phase; indicated in the Table 3.1.

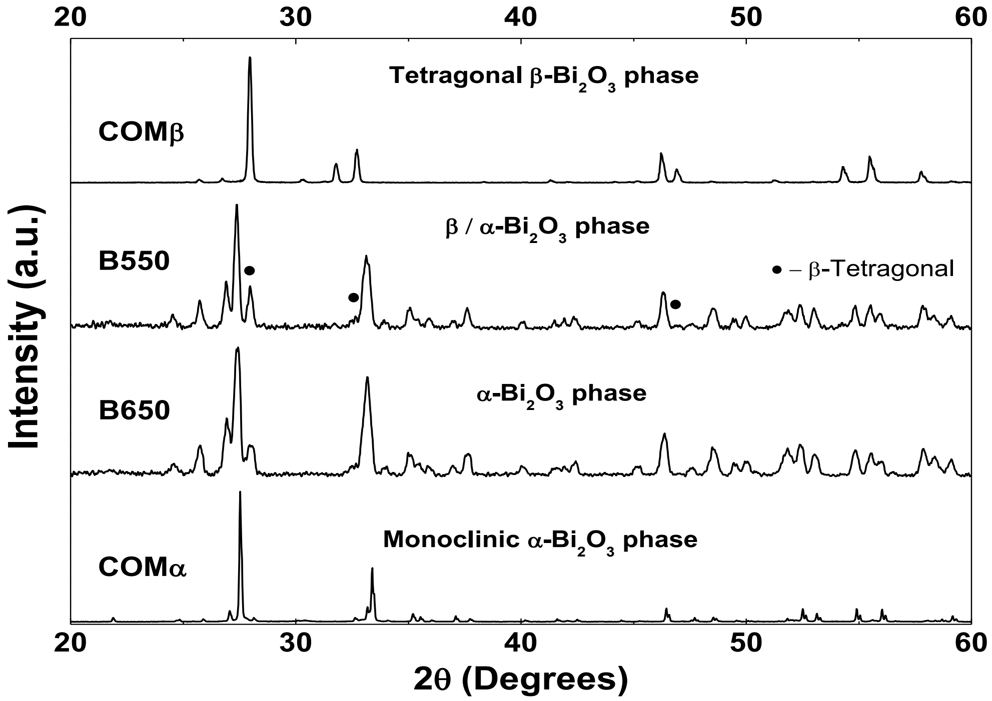

Fig. 3.1. XRD patterns of all Bi_2O_3 commercial (COMα, COMβ) and synthesized samples.

The average size of nanocrystallites α/β-Bi_2O_3 composite was around 30 nm, estimated from the behavior of diffracted peaks width. The presence of β within the lattice of α-phase in the composite (originated from single precursor) is reported as the stable interface of a heterojunction [106, 132]. Moreover, for B650 samples as all the diffracted peaks corresponding to single α-Bi_2O_3 phase with the estimated average grain size of 27 nm; revealed that metastable β phase after high temperature calcination is completely transformed to α-phase without affecting the average grain size; this phenomenon is already explained in section 2.3.2 of chapter 2, in which it was discussed that due to complete loss of Nitrogen at high temperature, β phase cannot be stabilized any more during cooling to room temperature and is completely transformed into α.

3.3.1.2 Optical property

Fig. 3.2A shows the UV-Vis DRS analysis of all the samples and inset showing tauc plot, obtained after using Kubelka-Munk method [15]. The commercial samples exhibited wide absorption edge: from 400 to 450 nm for sample COMA and from 470 to 550 nm for COMB. These absorption edges are typical characteristic of the α-Bi_2O_3 and β-Bi_2O_3, respectively, and are commonly associated to the electronic transition from the valence band to the conduction band [101].

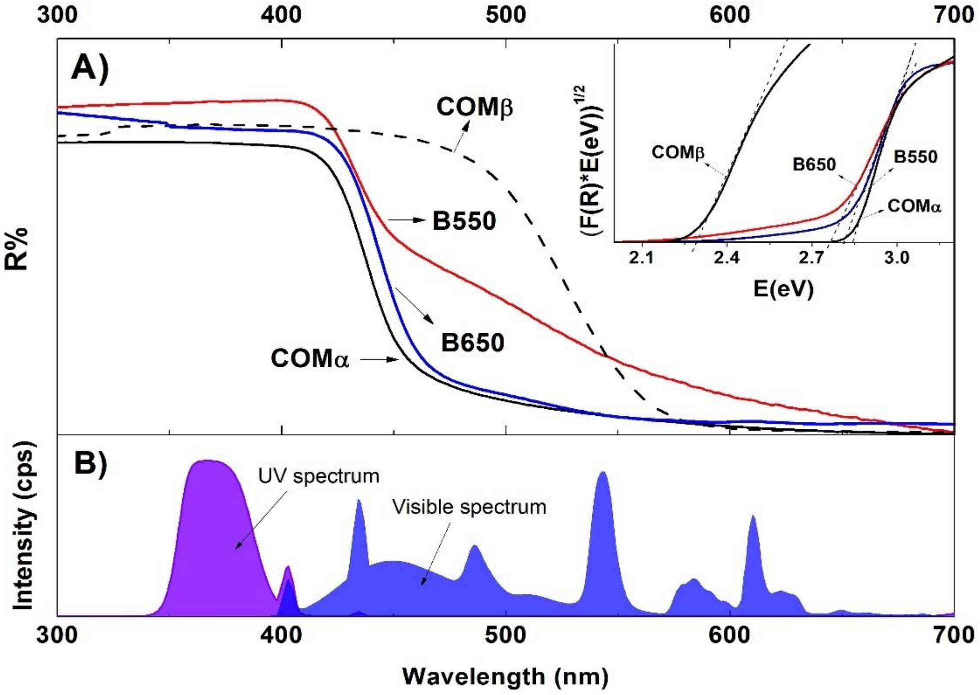

Fig. 3.2 A) UV-Vis DRS spectra and the optical band gap estimation (inset) of the Bi_2O_3 commercial (COMα, COMβ) and synthesized (B550 and B650) samples, and B) Emission spectrum of the UV and Visible Lamp.

As discussed in previous chapters, that lower energy band gap and the optimum absorption in the visible region, like for β-Bi_2O_3, represents a great benefit for a better utilization of solar light and effective photocatalytic reactions [13]. In Fig. 3.2A the sample B650 (α-Bi_2O_3), representing similar characteristic of absorption as obtained in case of COMA; the absorption edge in the region between 410 to 450 nm. However, for sample B550, absorption curve towards wide region up to 550 nm, was due to the contribution of the β-Bi_2O_3 phase. The estimated band-gap energy for the COMB is around 2.3 eV while for COMA and sample B650 are in the range 2.8-2.9 eV (Table 1). For the α/β-Bi_2O_3 composite (B550), presence of β-phase (at 20%) influenced the visible-light absorption within the β/α-heterojunction [132] and resulted a decrease in the band-gap energy around 2.75 eV. Observing the absorption properties of all the samples in comparison to emission spectra of fluorescent UV and white light lamp (Fig. 3.2B), it can be assessed that all the samples can fully utilize UV light; however, the COMA and B650 cannot fully absorb visible spectrum and therefore can have lower photoactivity.

Table 3.1. Composition phase, average crystal size and band gap energy of the commercial (COMα, COMβ) and synthesized (B550 and B650) samples.

Sample	**Composition Phase (%)**		**Energy Band Gap (eV)**	**BET surface Area m²/grams**
	α	**β**		
COMβ	00	100	2.3	2.1
B550	80	20	2.75	4.3
B650	100	00	2.9	2.9
COMα	100	00	2.8	1.8

3.3.1.3 PZC property and surface area

The point of zero charge (PZC) is a significant property of photocatalyst, helps in assessing the pH value, that have an influence on the adsorption and interaction of anionic or cationic molecules when dispersed in the aqueous solution. When the solution pH is below the PZC value, the solid surface becomes protonated [133], and anionic molecule are likely to adsorbed. While if pH is above PZC value then photocatalyst surface is less protonated and could adsorb cationic molecules. First derivative was applied to the data obtained after performing titration *i.e.* increasing the pH from 2 to 12 in presence of background electrolyte; obtained PZC for the α, β and for α/β-Bi_2O_3 composite samples (Fig. 3.3) were found in the range of 6.8 to 7.8, lower than previously reported as 9.4 [130]. The Lower PZC of α/β-composite and commercial α-Bi_2O_3 than that of other samples, suggests that they can achieve higher protonation at the neutral pH of solution and enable improved interaction with anionic dyes. The obtained values of specific BET surface areas are given in Table. 3.1; lower in case of commercial samples *i.e.* up to 2 m^2/g, while average for synthesized samples i.e. up to 4.3 m^2/g.

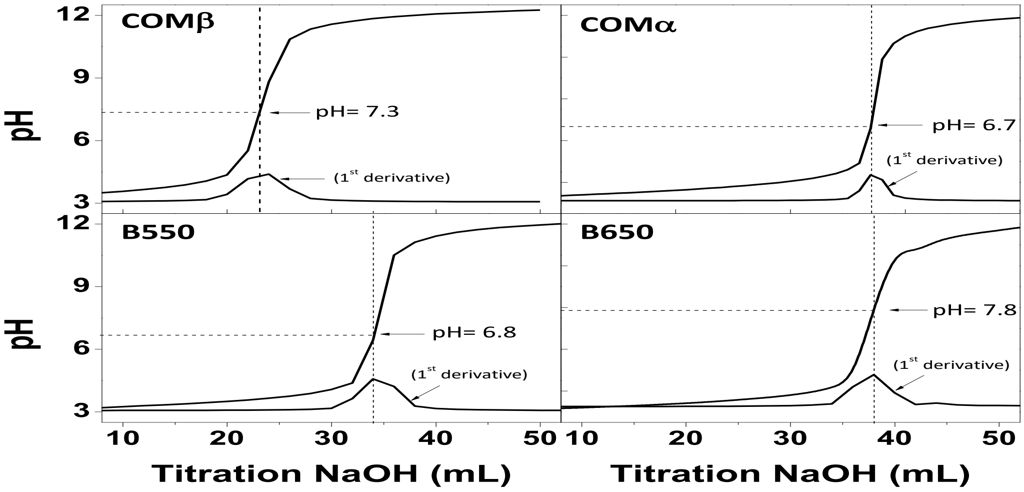

Figure 3.3 Potentiometric titrations and its first derivative of each one indicating the pzc value of all Bi_2O_3 commercial (COMα, COMβ) and synthesized (B550 and B650) samples.

3.3.2 Individual dye photodegradation

To evaluate the photoactivity of synthesized and commercial samples, initially indigo carmine (*IC*), Acid Blue 113 (*AB*) and rhodamine-B (*RhB*) were individually investigated; in order to choose the sample with best photocatalytic response. The Fig. 3.4 show relative concentration (C/C_0) plots (Fig. 3.4A and 3.4C) and the kinetic curves of photodegradation of the *IC* (Fig. 3.4B and 3.4D), respectively, during dark and exposure under UV and visible light irradiation, for all samples. pH of *IC* dye solution was found as 6.8, that is near to PZC values of most of the samples and depicts that the surface charge of all samples is poorly protonated, therefore small amount of *IC* dye could have adsorbed on amphoteric sites; that have allowed poor interaction of the anionic dye with poorly protonated surface and is associated to hydrogen bonds present in the *IC* dye molecule [134]. Afterwards, under irradiation in UV light the C/C_0 of *IC* dye decreased (Fig. 3.4A), reaching at (60-65%) removal at 45 min, in case of COMA and COMB samples. While in the case of B550 and B650, higher and effective removal up to 85 and 96% were observed, respectively. For all samples, behavior of linear kinetic curves obtained after plotting $\ln(C_0/C)$ *vs* the reaction time (*t*) showed a straight line (Fig. 3.4B), depicting that the *IC* dye degradation followed pseudo first order kinetic reaction [135]. The highest apparent kinetic rate under UV irradiation was found for α/β- Bi_2O_3 ($k_{app} = 10.5\times10^{-2}$ min^{-1}). When the *IC* dye photodegradation was carried under visible light (Fig. 3.4C), the rate of degradation was decreased as compared to the rate obtained under UV light. Both commercial (COMA) and synthesized α- Bi_2O_3 samples presented low removal up to 25 and 10%, respectively.

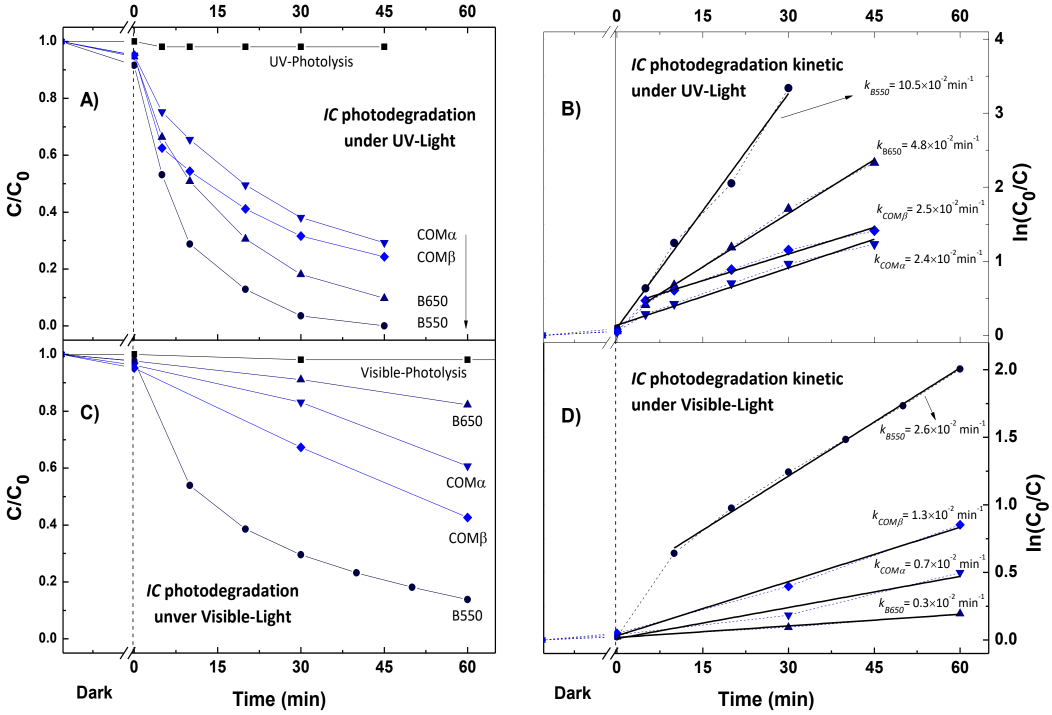

Fig. 3.4 Profile of relative concentration and kinetic curve plot of *IC* dye photodegradation under (A, B) UV light and (C, D) visible light, respectively, by using Bi_2O_3 photocatalysts.

In contrast, for the samples B550 and COMB that contain β-phase the conversion was of 90% and 50%, respectively and the pattern is quite similar to the results obtained under UV light, but at lower rate (Figure 3.4C). The kinetic curves of IC dye degradation in visible light, again showed a straight line (Fig. 3.4D) and the apparent kinetic constant were determined as: a low $k_{app} = 0.3\times10^{-2}$ min^{-1} for B650 sample). The α/β-Bi_2O_3 composite (B550) exhibited the highest photoactive response for both UV and visible light irradiation, where the k_{app} under UV light (k_{app}=10.5×10^{-2} min^{-1}) was 3.7 times higher than obtained under visible light (k_{app} =2.6×10^{-2} min^{-1}, Figure 3.4D); revealing the fact that both α and β phases in the composite fully utilize the spectral energy of UV light and provided the high amount of reactive species during degradation process.

The absorbance spectra of *IC* in course of time is presented in Fig. 3.5A, showing the characteristic peak of *IC* dye at 610 nm [136]. The main peak slightly reduced (10%) during the dark condition, as very small amount of *IC* dye was adsorbed on sample B55O surface. Afterwards, the immediate subsequent decrease in absorbance peak of the *IC* dye is associated to the photodegradation of *IC* dye molecule with the destruction of the indigoid group (NHC=CNH) of *IC* via oxidation, originating intermediate products as appeared in the UV-vis absorbance spectra in the UV-region (210-260 nm); communally ascribed to benzene and carboxylic groups.

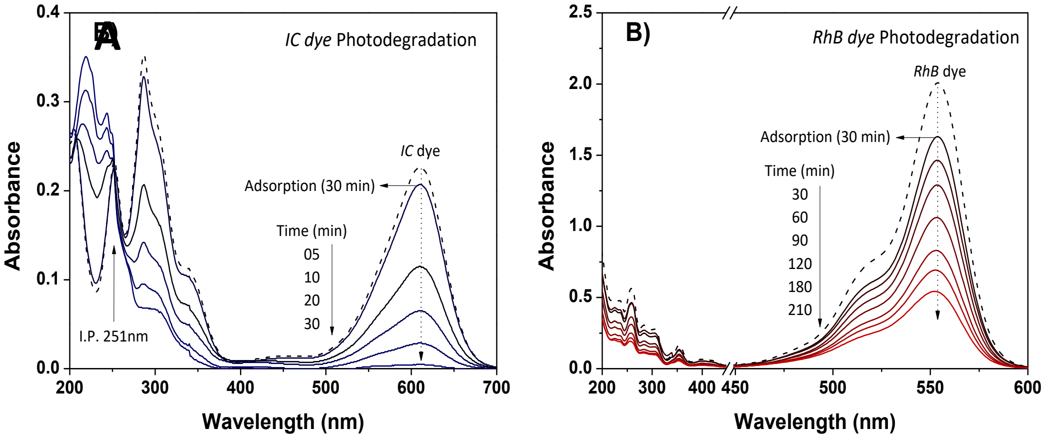

Fig. 3.5 Absorbance spectra during their photodegradation using B550 sample under UV light irradiation, A) Indigo carmine (IC) B) Rhodamine B (RhB).

As discussed earlier in chapter-2, these intermediates are identified as *Isatin sulfonic acid* and *2-amine-5-sulfo-benzoic acid* [137-139], additionally exhibiting isosbestic absorption point (I.P.) at 251 nm and revealing the fact that these changes in the *IC* spectrum occurred due to photodegradation process [137], without any mineralization that could be achieved after longer irradiation exposure.

Fig. 3.5B shows the photodegradation absorbance spectra of the *RhB* dye under UV light using the B550 sample. The principle absorbance peak of *RhB* at 554 nm [140], was reduced by 20% in dark due to its adsorption on α/β-Bi_2O_3 surface [141]. Afterwards, the *RhB* dye concentration was slowly decreased in longer time UV irradiation (210 min). It is known that the *RhB* photodegradation generates several intermediary products [142]; with hypsochromic shifts could be due to self-sensitization of *RhB* during photodegradation, reported by M. Rochkind [47] and mentioned in earlier chapters. However, using α/β-Bi_2O_3 for degradation *RhB* no additional or hypsochromic shift in UV-vis absorbance spectra was seen, revealing that degradation of *RhB* was achieved without formation of intermediates. The pH of *RhB* dye solution was near to 6.8, that could have allowed poor protonation on all samples and the surface of the samples could be partially hydroxylated when *RhB* dye is preferentially adsorbed over amphoteric sites. Nevertheless, high adsorption *RhB* dye (20%) were seen on the α/β- Bi_2O_3 surface, but the interaction of cationic *RhB* dye with hydroxylated surface is via oxygen bonds of the carboxylic groups in the dye structure; stronger than the interaction with hydrogen bond of *IC*. Moreover, it is also reported that *RhB* dye could also follow partial adsorption on the protonated Bi_2O_3 surface, via diethylamino group [140, 143]; also present in the molecular chain of *RhB* dye.

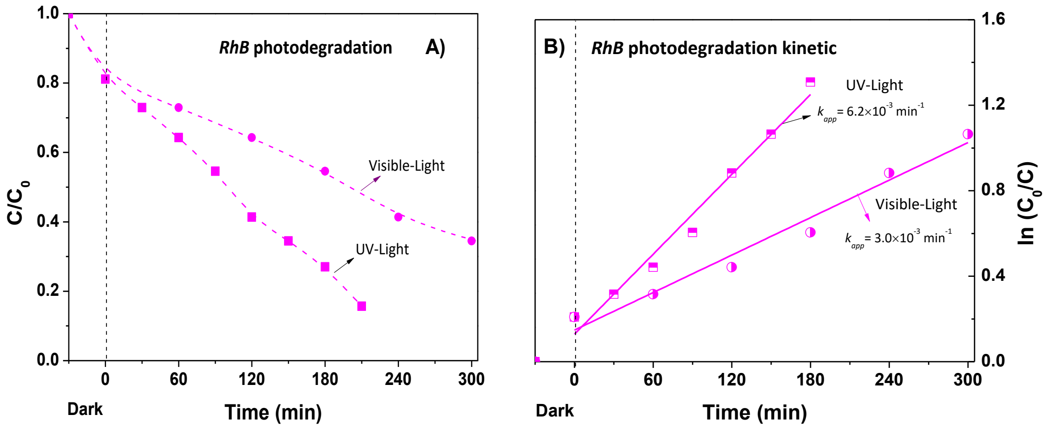

Fig. 3.6 A) Profile of relative concentration and B) kinetic curve plot of *RhB* dye photodegradation under UV and visible light, respectively, by using B550 composite sample.

Fig. 3.6 displays photodegradation kinetics of *RhB* dye under UV and visible light only for B550, as it again displayed best performance than other samples. Fig. 3.6A shows the C/C_o of the *RhB* dye during different irradiation time, while Fig. 3.6B highlights the corresponding kinetic analysis (preceding from dark conditions). Difference in the rate of degradation of *RhB* under UV and visible light was quite similar that observed with *IC* dye *i.e.* at 210 min, the removal efficiency was 80% (UV) and 40% (visible). The kinetic curves resulted straight lines (Fig. 3.6B), confirming that *RhB* dye degradation also followed pseudo first order kinetic reaction [144]. For B550 (α/β-Bi_2O_3) sample, the k_{app} values were 6.2×10^{-3} and 3×10^{-3} min^{-1} under UV and visible light, respectively; 2 times higher for UV. Dealing with *RhB*, it is identified that the self-sensitization of *RhB* dye could be possible and promote the transfer of excited electrons (from HOMO to LUMO under visible spectrum) from RhB to the photocatalyst surface and could assist the photocatalyst process [145, 146]; however, here using UV light at 367 nm (Fig. 3.2B), the self-sensitization of *RhB* dye is negligible. While using visible light with low intensity (33 watts/m^2), sensitization could have facilitated in increasing the rate of degradation similar or higher to UV light [47], but obtained lower k_{app} under visible light proved that, RhB sensitization was not occurred and confirmed that the degradation of RhB only followed photocatalysis process by α/β-Bi_2O_3 under both conditions *i.e.* UV and visible light.

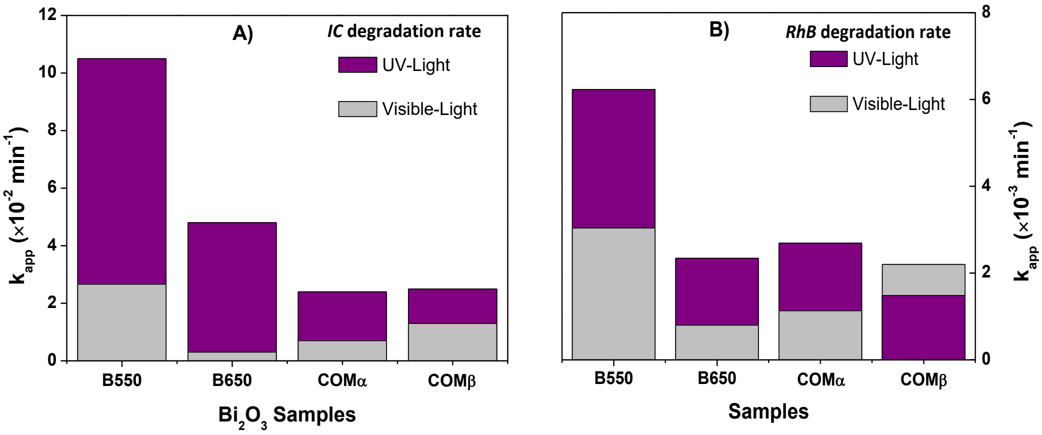

Fig. 3.7 Apparent kinetic rate constant of pseudo first order reaction for all Bi_2O_3 samples in the; A) *IC* and B) *RhB* dye degradation under UV and visible light irradiation.

Finally, for the selection of best material for further studies, the obtained k_{app} values were considered. Fig. 3.7A and 7B give the achieved k_{app} for photodegradation of *IC* and *RhB*, respectively; under UV and visible light. With a clear indication that, α/β-Bi_2O_3 (B550 sample) exhibited better performances than other materials and commercial β-Bi_2O_3 (COMB), which has been proposed as the most photoactive phase [19, 147]. The high photoactivity of α/β-Bi_2O_3 can be associated to the heterojunction interface between α and β phases, which led the better charge distribution in achieving effective degradation.

In addition, from the obtained results of photodegradation of *IC* and *RhB* dyes, it can be observed that the degradation rate strongly depends upon the type (ionic nature) and chemical structure (main coloring and branched groups) of the dye and further its adsorption rate over photocatalyst. The weak interaction/adsorption of anionic *IC* dye with α/β-Bi_2O_3 surface could be responsible for the high photodegradation rate; favored by refreshing and maintaining the active site on α/β-Bi_2O_3 surface and allowing subsequent interaction with *IC* dye molecules. In order to investigate, if the dye of the same ionic behavior but of different chemical structure followed the same order of degradation (influenced by the interaction), other anionic dye Acid Blue 113 (*AB*) was investigated using B550 sample (α/β-Bi_2O_3) under UV light and visible light, at neutral pH (as prepared solution) and basic pH. Fig. 3.8A shows the adsorption rate of AB dye at neutral and basic pH; it can be observed that, at neutral pH the adsorption rate was very high up to 52% and the degradation kinetics is very low. As from the previous analysis with IC dye, it was revealed that low adsorption could facilitate in refreshing the sites of photocatalytic surface and allowed maximum irradiation passage. Therefore, high adsorption of AB could be reduced by changing the solution pH to basic *i.e.* 9.5 (with anionic inhibition by OH^-).

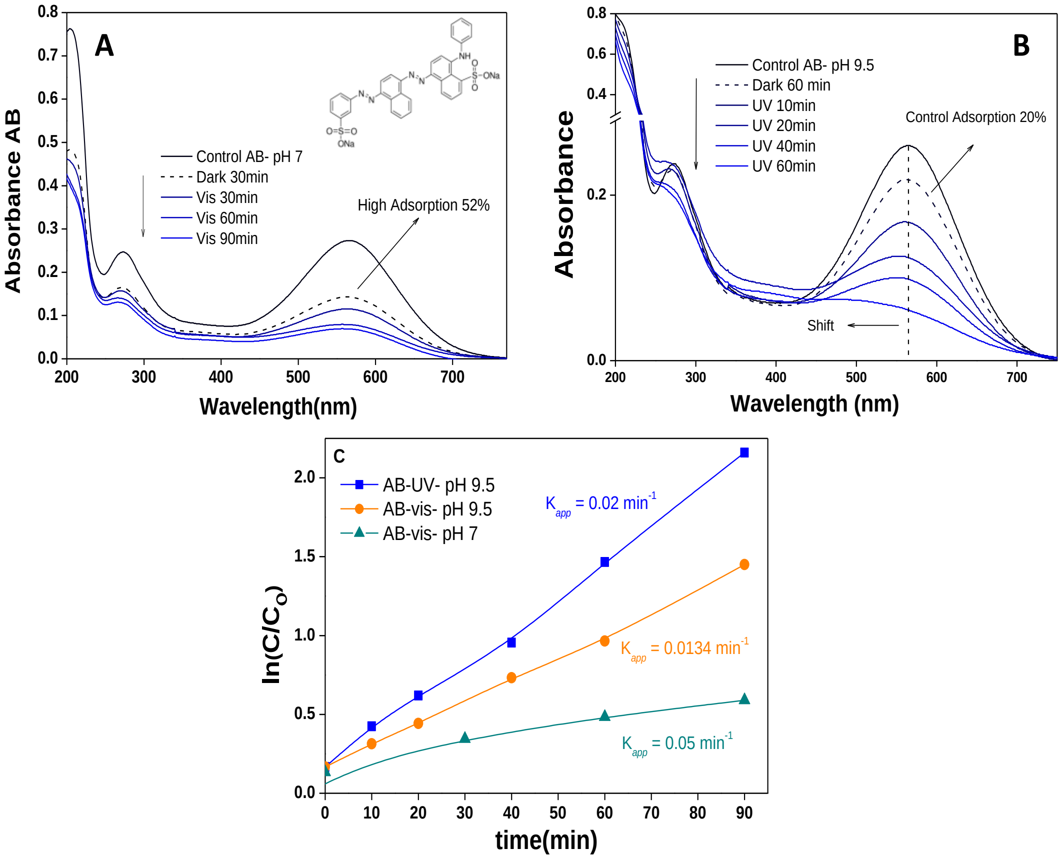

Fig. 3.8 UV-vis photoabsorption spectrum vs time of acid blue 113 (AB) at, A) neutral pH, B) basic pH and C) degradation kinetics and estimated K*app* under UV and visible light for different pH using B550 sample.

It can be observed in Fig. 3.8B that the adsorption of AB was reduced to 20% at basic pH. Moreover, degradation kinetics of AB under UV and visible light was improved; can be observed from the determined K_{app} rates in plots Fig. 3.8C. Moreover, the k_{app} values obtained under UV light are higher than obtained under visible light, which are in accordance with the previous obtained results in case of

IC and RhB dyes. Inset in Fig. 3.8A shows the chemical structure of AB dye; besides being anionic type with sulphonic groups ($^{-}SO_3$) alike to IC, the encountered high adsorption rate at neutral pH probably due to the difference in coloring group *i.e.* azo (N=N) and the resulted neutralization of protonated sites of α/β-Bi_2O_3 surface by interacted branched sulphonic groups; which allowed attraction/adsorption of additional dye molecules; such cases are extensively reviewed for dyes containing azo coloring group [148]. While in case of modifying pH the competing ^{-}OH ions hindered dye molecules in rushing over the α/β-Bi_2O_3 surface and allowed them to stay in the bulk solution. Moreover, in parallel to decrease in the UV-vis absorbance spectrum of AB (Fig. 3.8B), shift of the main peak from 564 nm towards left of the spectrum suggest a spectral change related to photodegradation process and probably an indication of the formation of intermediate(s).

3.3.3 Mixed solution (IC and RhB) photodegradation

For the evaluation of mixed dyes solutions, molar concentration of each dye (*IC* and *RhB)* was kept at 1.5×10^{-6} M, to make sure similar number of dye molecules, representing each dye in the solution. The recorded total absorption spectrum of the mixed solution is shown in Fig. 3.9A, exhibited the contribution of both *IC* and *RhB* dyes, with two principle absorbance peaks at 610 and 554 nm; of each respective dye. The photodegradation of mixed solution was investigated by using the α/β-Bi_2O_3 sample (B550) under visible light. The degradation absorbance spectra of mixed solution are displayed in two-time scales: one showing first 90 min of observation, 30 min in dark and 60 min of irradiation (Fig. 3.9A) and other showing longer time irradiation from 60 to 240 min (Fig. 3.9B). During dark condition, both *IC* and *RhB* dyes were preferentially adsorbed on α/β-Bi_2O_3 surface (at 10 and 15%, respectively), over protonated sites; originated due to mixed solution pH= 6, slightly lower than PZC value of α/β-Bi_2O_3 *i.e.* 6.7 [149]. Afterwards during irradiation, primarily the absorbance spectra of the *IC* dye subsequently reduced in first 60 min (Fig. 3.9A), in parallel at the same time, intermediate products (discussed previously) were appeared in UV-region. However, at that time the absorbance spectra representing RhB hardly decreased. Once the dye *IC* degradation was completed after 60 min, the degradation of *RhB* dye is initiated (Fig. 3.9) and remained continue in longer run up to 240 min, where dramatically a hypsochromic blue-shift was observed at 540 nm along with appearance of isosbestic absorption point at 502 nm, indicating the formation of an secondary products linked to RhB; identified as *N,N-diethyl-N-ethyl-*

rhodamine [142], which mainly appears when carboxyl group (-COOH) of RhB preferentially adsorbed on the semiconductor surface rather than diethylamino group (CH_3-NH-CH_3) and as a result the reactive species mostly attacked the conjugated chromophore in the dye structure [90, 143]. The *RhB* dye adsorption via -COOH probably assisted by the change in pH *i.e.* toward acidic (pH < 6), due to formation of secondary products *Isatin sulfonic acid* and *2-amine-5-sulfo-benzoic acid* in the mixed solution after photodegradation of *IC* dye. It was experimentally confirmed that pH of the solution reduced from 6 to 5.2 after first 60 min exposure *i.e.* after degradation of *IC*. The overall investigation revealed that the *IC* dye was selectively degraded along with formation of its intermediates products and afterwards *RhB* dye underwent for degradation and formed *N,N-diethyl-N-ethyl-rhodamine*, in assistance of intermediates of the *IC* dye.

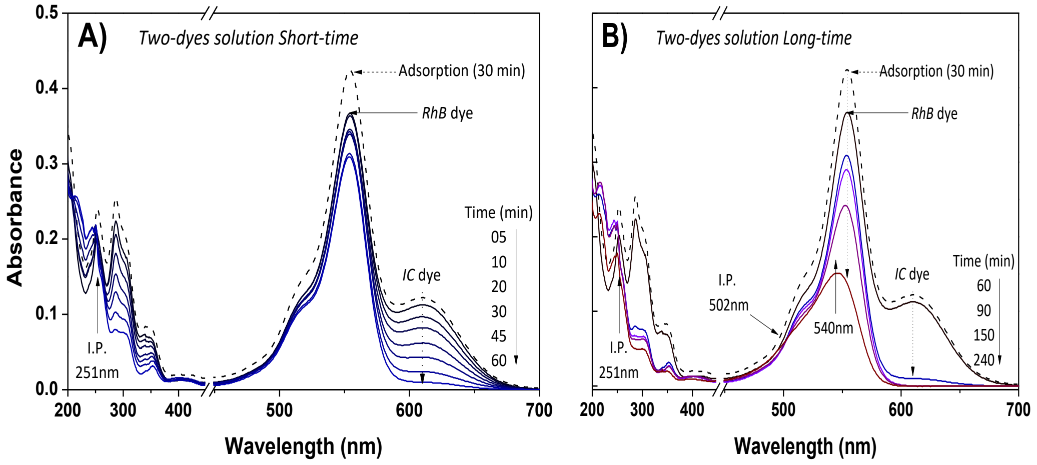

Fig. 3.9. Absorbance spectrum of the two-dyes mixture photodegradation by using B550 sample under visible light at: A) short and B) long time.

In case of mixed solution, the estimated k_{app} for *IC* degradation in first 60 min was 3.5×10^{-2} min^{-1} and at that time *RhB* dye was just adsorbed (Fig. 3.10A); and from 60 to 240 min, the k_{app} for the *RhB* was increased a bit: estimated 0.85×10^{-2}min^{-1}; but was lower than *IC*. Similar behavior of degradation was observed when investigation of mixed solution was performed under UV irradiation (spectra not shown), but compared to visible light the photodegradation rate of both dyes was about 10 times higher under UV irradiation (Fig. 3.10B).

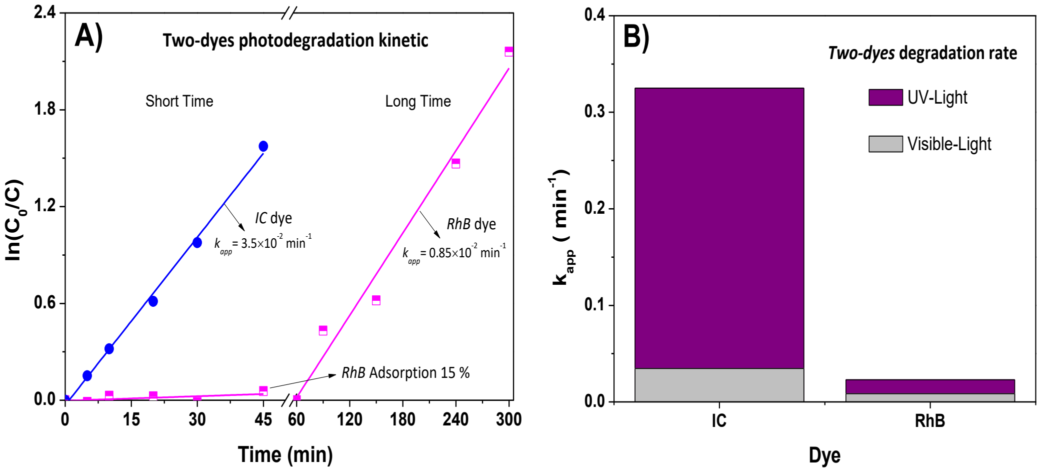

Fig. 3.10. A) Kinetic curves and B) Apparent kinetic rate (K_{app}) of each dye in the mixed solution of indigo carmine (IC) and rhodamine-B (RhB) using B550 composite under UV and visible light.

3.3.4 Mixed solution (all 3 dyes) photodegradation

3.3.4.1 As prepared mixed solution (pH-6.5)

Fig. 3.11 shows the recorded absorbance spectra of mixed solution containing all three dyes at different irradiation time at neutral pH. The absorbance spectra at 0 min (control) shows the representation of all three dyes with principle peaks at 554 nm (for *RhB*) including a widened shoulder exhibiting the contribution of both *IC* and *AB* dyes. At neutral pH during dark conditions, all three dyes (respective absorbance peaks) almost equally decreased due to the adsorption over α/β-Bi_2O_3 surface; on average of 32% from the initial intensity/absorbance maxima; estimated from Fig. 3.11A. This high adsorption is linked with the competing dye ions, particularly here sulphonic groups of *IC* and *AB* and carboxylic group of *RhB* allowed their respective dye molecules to be adsorbed over the solid α/β-Bi_2O_3 surface and not allowing one another to stay in bulk solution. Afterwards, under visible light irradiation, parallel decrease was observed in the all absorbance peaks, again the absorbance peak *IC* and *AB* decreased faster than reduction of *RhB*, revealing the same phenomena of sequential and random degradation as was observed in case when *IC* and *RhB* mixed solution. Furthermore, once their degradation was achieved, the degradation kinetics of *RhB* was accelerated. However, no prominent secondary peaks were observed except one at 251 nm indicating the isosbestic point of IC after 90 min irradiation and a small shift at 550 nm (from actual 554 nm) after 150 min, suggesting that degradation was subsequently followed without any formation of major intermediates. After 240 min, final solution was analyzed for TOC; and 44% decrease in the TOC was achieved; 12% related to actual mineralization after excluding 32% decrease due to initial adsorption on α/β-Bi_2O_3 surface.

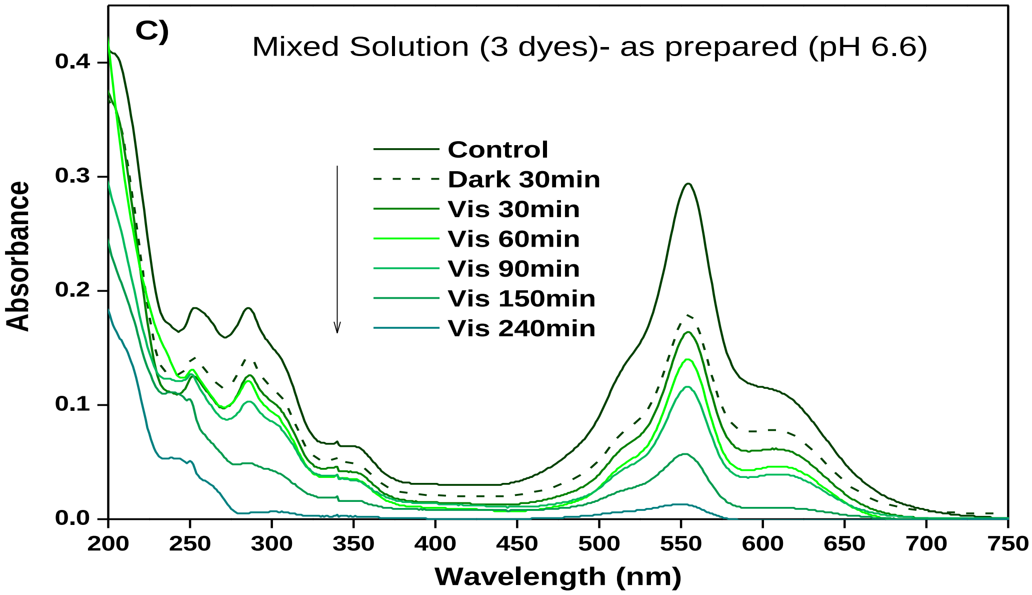

Fig. 3.11 Three dyes Mix Solution neutral pH, UV-vis absorbance spectrum vs time.

3.3.4.2 Mixed solution at basic condition (pH-9.5)

To observe if the rate of degradation and degree of mineralization could be improved further by changing the solution pH to basic; photodegradation of mixed solution (containing all three dyes) at basic pH was performed. Fig. 3.12 shows the time course absorbance spectra of mixed solution at basic pH (without any prominent changes in the overall spectra by changing the pH to basic). During adsorption process in dark, all dyes were equally adsorbed over α/β-Bi_2O_3 surface, but in overall decrease in adsorption rate (25%), indicating that adsorption can be controlled by adding one competing anion (here is ^-OH). Under exposure to visible light, similar pattern in degradation behavior was observed: first, selective and preferential decrease to the absorbance peak of *IC* and *AB* and respective formation of unidentified intermediates in 90 min, then after decrease in *RhB* absorbance peak at low rate. However, in case of basic pH, no prominent secondary peaks were observed except the unidentified changes and increase in spectrum from 250 to 400nm, could be due to that partial degradation of *AB* and *IC*, while possibly *RhB* was only decolorized due to limited available active sites on α/β-Bi_2O_3 surface. After 240 min, final solution was analyzed for TOC and 30% decrease in TOC was recorded mainly associated to only adsorption not the mineralization; revealing the fact that at basic pH nevertheless the adsorption was controlled from 35 to 25%, but it allowed formation of such unidentified secondary product that not favored to achieve their mineralization, and only allowed discoloration of the mixed solution.

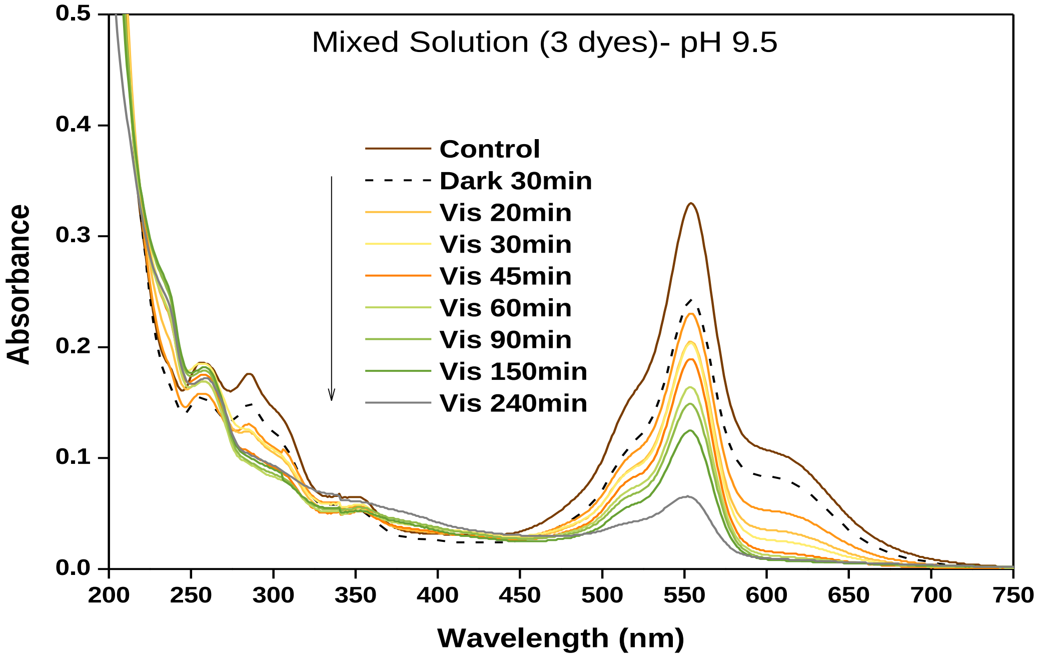

Fig. 3.12 Three dyes mix solution-basic pH UV-vis absorbance spectrum vs time.

3.3.5 Analysis of the degradation path

To explore the adopted degradation path during photodegradation of each dye *i.e.* either oxidation and (or) reduction, recently some researchers have suggested the use of reagents for the quenching of holes, hydroxyl radicals and atomic oxygen [14, 150, 151], to observe any significant change in the degradation kinetics due to their presence in the dye solution. For example, Triethylamine (TEA) can be used for quenching of holes (h^+), P-benzoquinone for (BQ) the atomic/reactive oxygen (O^*) and Iso-propanol (IP) for the hydroxyl radicals (OH^-) [14, 150, 151]. Their presence in the dye solution could influence on the photocatalysis process and can reduce the kinetic rate of degradation because of the quenching of generated reactive species or holes on the photocatalytic surface. In this regard, *IC* dye solution (at 20 mg/l concentration) and *RhB* dye solution (at 5 mg/l concentration) were investigated using α/β-Bi$_2$O$_3$, with and without the presence of these quenchers *i.e.* TEA, BQ and IP; under visible light. Fig. 3.13A-D show the C/C_o plots, kinetics curves and determined K_{app} of IC and RhB dye solution with and without presence of quenchers. It can be observed that the degradation rate is strongly reduced with the presence of each quencher, revealed that both the O^*, OH^- radicals are responsible for the degradation of *IC* and *RhB* dyes; originated after oxidation and reduction. Moreover, the information given in Fig. 3.13, confirmed that the electrons are well separated from the h^+ in generating the reactive species, which have been affected with the presence of any quencher.

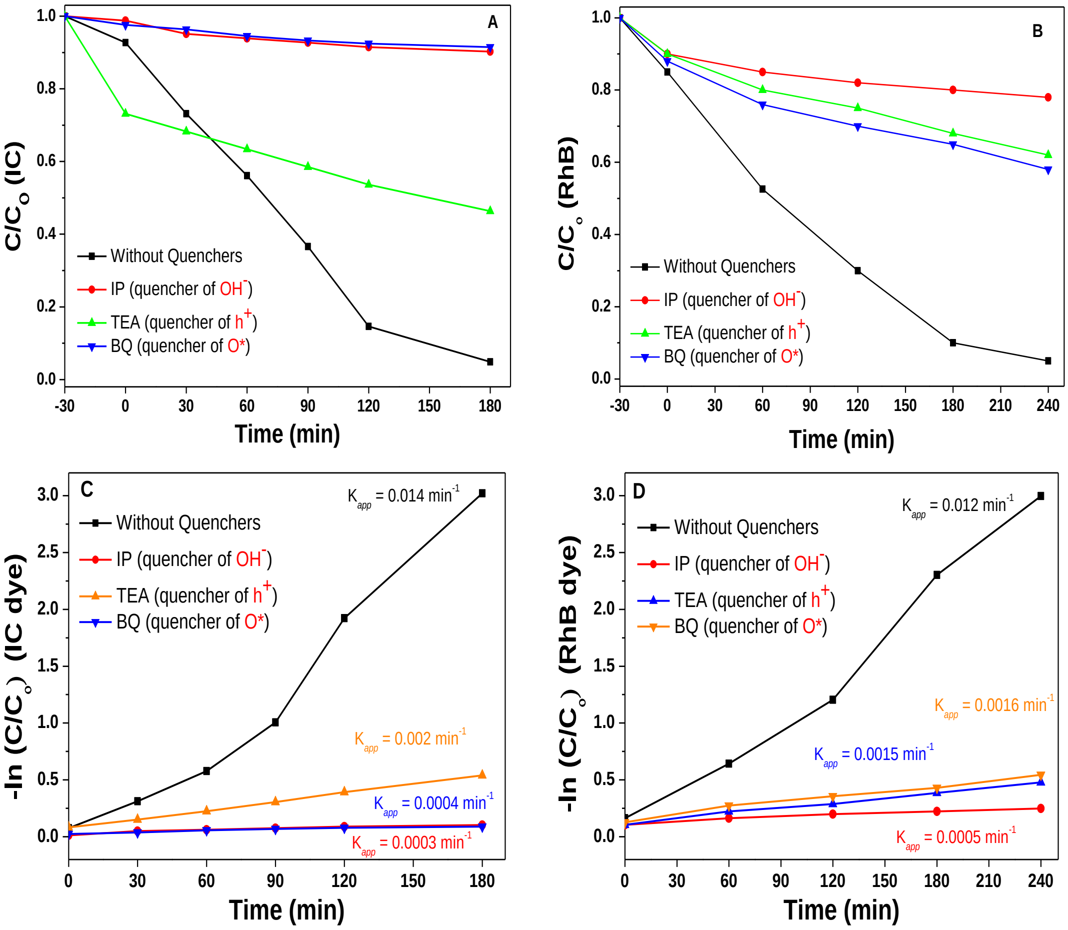

Fig. 3.13 Relative concentration in presence of quenchers A) IC, B) RhB and kinetic curves and K_{app}: C) IC and D) RhB

3.3.6 Photodegradation mechanism of single and mixed dyes

The mechanism of photo induced degradation in case of using single phase or heterostructures has been well known, in which any dye is degraded via oxidation and reduction path enabled after generation of reactive species on semiconductor surface [138, 139]. Following the information assessed from Fig. 3.13A-D, the illustration of photodegradation mechanism can be proposed as scheme (Fig. 3.14A). Strongly interconnected heterostructure of α/β-Bi_2O_3 have provided more reactive species ($O_2^{\cdot}$ and $OH^{\cdot}$), because of well separated e^- and h^+ and better charge transport within the phase junction (Fig. 3.14B), by which photogenerated e^- at the conduction band of the α-Bi_2O_3 could move to β-Bi_2O_3, while the h^+ could be transferred from β-phase to α-phase and eventually attacked each dye, first for discoloration and then mineralization [101, 106].

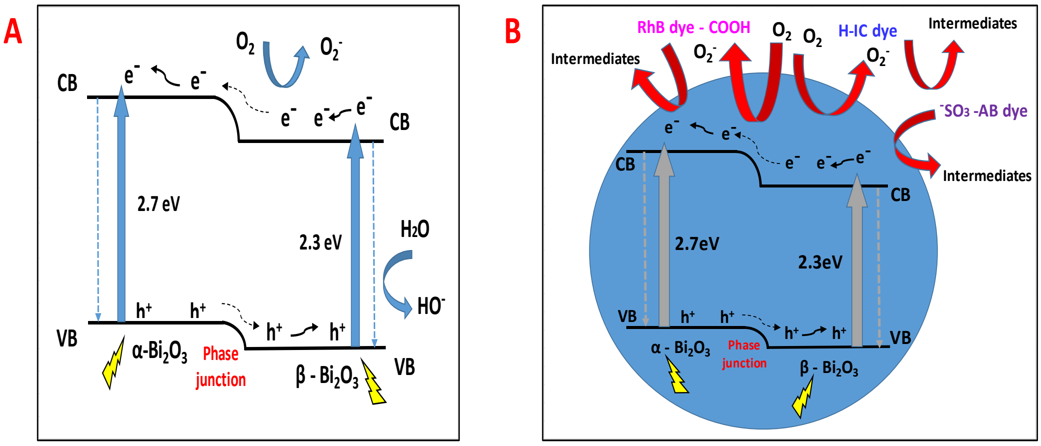
A
CB
e⁻
e⁻
O2
O2⁻
e⁻ e⁻ e⁻
CB
2.7 eV
2.3 eV
H2O
HO⁻
h⁺ h⁺
h⁺ h⁺
VB
α-Bi2O3
Phase junction
β-Bi2O3
VB
B
RhB dye - COOH
Intermediates
O2⁻
O2 O2
H-IC dye
O2⁻
Intermediates
⁻SO3 -AB dye
Intermediates
e⁻ e⁻
e⁻ e⁻ e⁻
CB
CB
2.7eV
2.3eV
VB
h⁺ h⁺
h⁺ h⁺
VB
α - Bi2O3
Phase junction
β - Bi2O3

Fig. 3.14 A) Diagram of electrons transfer cascade on α/β-Bi_2O_3 surface, B) Mechanism of photodegradation of single and mixed dyes.

However, rare information can be found in literature, related to the mechanism for degradation of mixed dyes. Here in particular case, following the obtained results from the absorbance spectra, C/C_o profiles and the kinetic rates degradation mechanism can be proposed. During degradation of two dyes mixture (anionic *IC* and cationic *RhB*), the generated reactive species on the α/β- Bi_2O_3 surface, preferentially react with anionic *IC* dye, enabling its immediate photodegradation (Fig. 3.14B) due to interaction through of the hydrogen bond attached with the main coloring indigoid group of *IC*. Once the *IC* dye degraded and its intermediates were formed, afterwards reactive species around the adsorption sites reacted with cationic *RhB* dye attached through the carboxylic group (Fig. 3.14B) and as a result de-ethylation of *RhB* occurred due to photodegradation by α/β- Bi_2O_3 [143]. In case of mixed solution with three dyes (anionic IC, AB and cationic RhB), the followed mechanism was similar by which anionic dyes *IC* and *AB* were preferentially attacked first by generated $O_2^{\cdot}$ and $OH^{\cdot}$ and formed respective intermediates, afterwards degradation of *RhB* was followed and resulted some unidentified intermediates.

3.4 Conclusion

The α/β-Bi_2O_3 heterostructure was successfully synthesized by facile solid-state route via thermal decomposition of $Bi(NO_3)_3 \cdot 5H_2O$ and subsequent calcination at 550°C. The obtained heterostructure comprised on 20% of β-Bi_2O_3 in proportion, which facilitated the photoactivity in visible light. In case of individual degradation of each dye by α/β-Bi_2O_3, the achieved kinetic rates with *IC* were higher for *AB* and the *RhB*; influenced by the adsorption and interaction of each dye by their ionic type and molecular structures. In case of mixed solutions: one containing IC and RhB dyes and other with all three dyes, random and sequential degradation was observed, in which anionic *IC* and AB dyes were degraded first at faster kinetic rate and afterwards degradation of the cationic *RhB* dye was begun and accelerated. In mixed solution, the originated secondary products (in form of organic acids) after degradation *IC* dye, induced the adsorption of *RhB* dye through carboxylic groups and resulted deethylation of RhB. The efficient photoactivity of α/β-Bi_2O_3 under visible light is probably due to the improved electron-hole separation and transfer of electrons and holes between the strongly interconnected phase junction of α and β phases.

Chapter 4

Distinguishing different Co-Existed Processes during Photocatalysis of Dyes: Adsorption, Photodiscoloration, Photodegradation and Mineralization

4.1 Introduction

Following the results and discussion in previous chapters, it has been highlighted that heterogeneous photocatalysis could be considered as a sustainable option: as it utilizes solar energy for photoactivity and enables oxidation and (or) reduction reactions allowing the degradation and mineralization of organic pollutants. To further deepen the study, the main aim of heterogeneous photocatalysis should be focused *i.e.* degradation of the parent pollutant and of their originated intermediate(s) and finally their mineralization into CO_2 and H_2O, NO_2 etc. without any residual secondary pollutants or transformation into nontoxic compounds [47, 152]. If such outcomes can be achieved simply using solar energy, then heterogeneous photocatalysis will be a viable alternative for water treatment. The evaluation of the photocatalysts performance as discussed before, usually performed by measuring the degradation of organic compounds; mostly the use of dyes (as model pollutants) is widespread due to the ease of the method, by which the kinetics of the process can be easily estimated using a spectrophotometric technique. The "photocatalytic activity" is evaluated by measuring the color removal/decoloration of the dye solution as a function of irradiation time, *i.e.* the decrease in the intensity of the main absorbance peak; usually expressed in terms of the dye relative concentration (C(t)/C(t=0); C/C_0). However, during such evaluation, a series of competing and coexisted processes must be considered, particularly when investigation is done under visible light. More often working with dyes, these processes (to be discussed later) are not considered to an extent and their selection as model pollutant (to evaluate new photocatalysts) has been questioned by the experts [47, 153]. In addition, it has been comprehensively verified by various authors that decoloration or partial degradation is not equivalent to dye mineralization and complete removal of color can be attained without mineralization**.**

Realizing the fact, that the traditional photocatalytic evaluation method using dyes are conflicted even when enormous literature is available and still going on; portraying the selection of suitable photocatalyst (s) based on decoloration of dye(s) solution. There is a need to understand and examine some additional processes, which somehow linked with the photocatalytic evaluation and could influenced the overall process and therefore must be resolved to avoid the mentioned conflicts. The co-existed processes are:

1) The initial adsorption of the dye over the photocatalyst surface, caused substantial or may be continuous decrease of the dye concentration in the solution; often misinterpreted as result of the “photocatalytic activity” of the semiconductor; as was the case in these studies [6, 23]. In a typical experiment, the suspension containing the dye solution and the photocatalyst is stirred in the dark conditions to allow the adsorption-desorption equilibrium. Depending upon the ionic behavior, type and chemical composition of dye, as well as the pH of the solution, the adsorption rate varies; while in some cases, high adsorption of the dye over the photocatalyst surface could be due to porous morphology, larger surface area and strong affinity towards dye molecules could significantly decrease the relative concentration of the dye and wrongly perceived as color removal due to photocatalysis/mineralization [154]. Since the total organic carbon (TOC) in the solution is also decreased because the dye which was in the solution, now adsorbed over the photocatalyst and is no longer present in the solution used for TOC analysis [155]. Indeed, adsorption of the dye onto a material with large surface area is a widespread technique to treat the polluted water but is not a

catalytic process. Therefore, the amount of dye adsorption as a function of time must be followed in dark and separated from photocatalysis.

2) Secondly, consideration of photolysis of the dye: photo-decomposition or photo induced chemical reaction in which a chemical compound is broken into smaller units through the self-absorption of photons by the dye molecule from irradiation source, favorably under visible light, because coloring compounds present absorbance in the visible spectrum. The light absorption may cause homolytic cleavage of the dye functional group (mainly responsible for giving the visible color to the solution), like for example, the double bond in the indigoid group (NH-C=C-NH) in indigo carmine [50] or the C-O=C group in the rhodamine B [156] or the azo group in methyl orange [157]. Therefore, photolysis should also be accounted under the defined experimental conditions of the irradiation source (lamp type, wavelength, intensity, etc.), without the presence semiconductor, and the degree of photolysis experienced by dye must be recognized and separated from the real photocatalytic activity achieved only by semiconductor.

3) It has been stated above and discussed in literature that, the subsequent decrease in the relative concentration (C/C_0) measured at a single wavelength should not be only considered to assess degradation of the pollutant dye into non-organic carbon or mineralization. So, let’s focus the various competing processes that could lead this decrease in the absorbance spectra or dye intensity and summarize the useful information for selection of dyes as model pollutants:

3A. The decrease in the dye intensity can be the outcome of charge transfer (oxidative or reductive process) between the photo-generated carriers in the semiconductor and the dye molecule, which only changes the distribution of the π-conjugated bonds responsible of the visible color absorption, but not the breaking of bond; here we named this phenomenon as photo-bleaching rather relating it as photodegradation. Typical examples of such phenomenon are the leuco dyes; dyes representing two molecular forms where one of them is colorless. The transformation between these two forms is due to oxidation-reduction reactions is generally irreversible, while if transformations related to heat, light or pH are reversible. Some of the dyes used in various studies actually belong to the family of leuco dyes, such as crystal violet, indigo carmine, malachite green and rhodamine B, so the decoloration observed during a photocatalytic experiment could be possible due to reduction reaction and subsequent transformation of dye molecule, but is not due to photocatalysis.

Therefore, it is important to monitor the whole absorbance spectrum instead of a single wavelength or narrow region; this could allow to observe changes in the whole spectrum along with decrease of the principle absorbance peak. For example, indigo carmine dye and rhodamine B have characteristic peaks at 610 and 554 nm, respectively, while their leuco-forms do not show absorption in the red, but they display slight yellow color with main absorbance maxima at 396 nm and 420 nm, respectively [156, 158]. By a confined examination of the dye absorbance spectra as a function of time, the phenomena of photo-bleaching can be distinguished from photodegradation process [47, 49].

3B. It is also possible that dye molecule itself is working as a photosensitizer, as indicated in chapter-1; absorbing resonantly the visible light and transferring electrons (the one excited from HOMO to LUMO) to the conduction band of the semiconductor, leaving the dye unstable with cation radical, which in parallel promote the active specie to the semiconductor surface and as a consequence attack the destabilized dye molecule; as revealed by M. Rochkind [47]. It is a synergetic process between the adsorbed dye molecule and the semiconductor, that probably can occur when the incident light source contains the adequate wavelength and intensity to be absorbed by the dye and promoting the charge transfer from dye to semiconductor. Since, in this case strong attachment of dye molecule and semiconductor for dye-sensitization, therefore adsorption plays critical role in charge transport and assisting the degradation process [159]. This eventually could lead to the mineralization of the organic molecule as revealed in case of RhB that degrades by means of N-deethylation sensitization under visible light by using BiOCl [47] or TiO_2 [160] photocatalysts. Nevertheless, main aim of mineralization is achieved even with assistance of dye sensitization, so it should not be considered as negative, but if there is sensitization, then it would be rather difficult to reach any conclusion about the efficiency, solely associated with semiconductor material and proposing visible-light activeness of a photocatalyst.

3C. Photodegradation: breaking of parent molecule into secondary intermediate(s); after attacked by oxidation and reduction by oxygen reactive species (superoxides or hydroxyl radicals) under stirring or aerated conditions. Photodegradation can be observed using UV-vis spectrophotomer: along with gradual decrease in the dye absorbance spectra, in parallel if there is any spectral changes in the whole absorption envelope due to the contribution from secondary intermediates at certain wavelengths, or fortunately the substantial increase of other absorption peaks, exhibiting indistinctive intermediates [152]. However, such changes are not observed for most of the dyes and in general more sophisticated techniques are needed to identify and confirm the formation and presence of the intermediates; for example, high performance liquid chromatograph, HPLC [157, 161, 162], but then there is problem to recognize and differentiate various intermediates associated with each dye. Previously, it was explored that indigo carmine (*IC*) dye is suitable to detect intermediate(s) using UV-VIS spectroscopy [101, 121, 163, 164], because when the indigoid group (NHC=CNH) of the IC breakdown via oxidation, originated some secondary products corresponding to isatin sulfonic at 210–260 nm in the UV-vis spectral region. However, detection of the secondary intermediates still not guaranteed the partial or total mineralization but can give information about the reaction and photo-induced interactions between the semiconductor and the probe pollutant.

4) Mineralization is the final aim of the photocatalytic degradation of organic pollutants into water and CO_2 [47, 49, 152] which can only be achieved by the formation of powerful oxidizing species; superoxides and hydroxyl radicals. One cannot evaluate the mineralization by using spectrophotometric analysis. The final step during the authentic investigation of photocatalytic material simply should be the measurement of the total organic carbon (TOC) analysis, but since TOC is measured only for solution, it is vital to consider the quantity of molecules that were adsorbed on the photocatalyst surface or on photocatalyst immobilized fixed support [155].

After highlighting above stated coexisted processes, the current study focused some key measurements to distinguish that obtained discoloration if achieved due photocatalytic response of a semiconductor material or due to other mentioned processes. Some of the discussion related to these processes are already included in many papers, but not necessarily a good interpretation of the results is given and still leading towards misinterpretations and false evaluations. The selected photocatalyst for this study was α/β-Bi_2O_3, because it gave improved results under visible and UV light; some of the already discussed results in chapter-3 are repeated in the current chapter, but their discussion was followed related to the above stated processes.

4.2. Photocatalysis Tests Methodology

Three dyes were selected: the cationic dye Rhodamine-B (RhB) at a concentration of 5 mg/L and two anionic dyes Acid Blue 113 (AB) and Indigo

Carmine (IC) at concentration of 10 mg/L. For each experiment, 15 mg of the α/β-Bi_2O_3 powder were added in 20 mL of the dye solution. Stirring rate was kept constant at 1200 rpm and experiment was performed either under irradiation of a fluorescent 9 W UV blue lamp (at wavelength 350nm-420nm) having an irradiance of 27 watt/m^2 or of a fluorescent 9 W white lamp (at 420-630 nm) having an irradiance of 33 watt/m^2 [101].

4.2.1 Photolysis

The photolysis of all dyes was examined placing the dye solution at the corresponding concentration inside the reactor under magnetic stirring and irradiated for two hours. The absorbance of the solution was monitored every 30 minutes extracting a 3mL aliquot from the solution. The experiment was performed using both UV and fluorescent white lamps.

4.2.2 Adsorption

To investigate the adsorption behavior of the different dyes onto the α/β-Bi_2O_3 powder, 20 mL of each dye solution at pH = 6.6 ± 0.2 were stirred in dark in presence of the α/β- Bi_2O_3 powder sample. The absorbance of the solution was monitored every 30 minutes until no further changes were observed. In case of AB, where a high adsorption rate onto the catalyst was observed, additional experiments were conducted at alkaline pH (9.5), to single out the role of adsorption from that of the other processes.

4.2.3 Dye sensitization

According to previous reports by Kuo *et. al. [165] and* M. Rochkind *[47]* in case of sensitization, rate of discoloration rate is higher for the visible light than for the UV. In order to determine the possible contribution of the sensitization process, the experiments were performed and compared using both UV and visible light for each dye. Photocatalyst load and solution volumes were the same as previously mentioned. The absorption bands of the various dyes are centered at 554 nm (RhB), 610 nm (IC) and 565 nm (AB) and the white lamp used emits in the whole range between 420 and 640 nm. Therefore, it is possible to excite the dye molecule by resonant absorption.

4.2.4 Photodegradation

To investigate the process of photodegradation, the IC dye was chosen, to easily observe the origination of the secondary intermediates, using UV-Vis spectroscopy [101, 121, 163, 164]; previously identified as *isatin sulfonic* by measuring the spectral region between 210–260 nm.

4.2.5 Mineralization

To assess mineralization, the adopted procedure is widely known: evaluation of the total organic carbon (TOC) content before and after irradiation as a function of irradiation time. The reduction in the TOC, after considering possible contributions from the adsorption of the dye molecule onto the photocatalyst surface, is directly proportional to the mineralization of the dye functional groups through the formation of CO_2 and H_2O. TOC analysis was carried out using a Shimadzu TOC-L analyzer with a high sensibility column.

4.3 Results and Discussion

4.3.1 Photocatalysis

In order to distinguish the contribution of the early stated processes *i.e.* adsorption, photolysis, photo-bleaching, photodegradation and mineralization and their influence on photocatalysis, investigation of as annealed α/β-composite sample was precisely followed for each dye and will be separately discussed in upcoming sections.

4.3.1.1 Adsorption

Fig. 4.1A-C show the whole absorbance spectra of all three dyes as a function of time in the dark-stirred conditions. A slight decrease in the intensity of the whole spectra without any change in the peak position can be observed. When the adsorption is very weak after the spectrum looks similar to the original solution, as was the case with IC. The adsorption effect was followed up to 60 minutes and the results indicated that the adsorption-desorption equilibrium was attained after 30 minutes for each of the 3-dyes. This can be clearly observed in Fig. 4.2D that shows the decrease in the relative concentration ($C/C_{\circ}$) *vs* time in dark for all dyes at pH = 6.6 ±0.2. From this reduction, the fraction of adsorbed dye is evaluated as

$(1 - C/C_o)$. For cationic RhB at neutral pH, the adsorption was 16%, in agreement with what has been reported previously [166] and observed in earlier chapters.

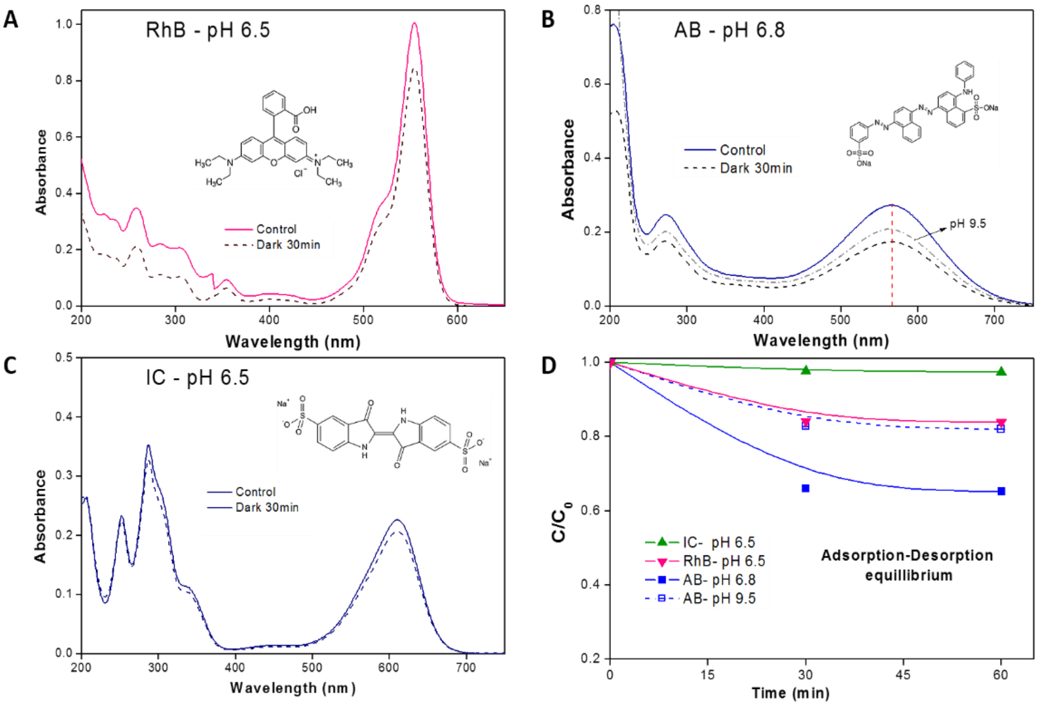

Fig. 4.1 A-C) Change in UV-vis absorption spectrum in dark, for all dyes; inset chemical structure of dye and D) relative Concentration C/C_0 for all dyes in dark.

For IC and AB anionic dyes at neutral pH, the maximum decrease due to adsorption was 3% and 46% respectively. In both dyes, the anionic behavior is related with sulphonate groups (inset of Fig. 4.1B and 4.1C) that interacts with the photocatalyst. At neutral pH, the Bi_2O_3 surface is partially protonated (H^+), and in the region of the amphoteric sites, the anionic dye could be adsorbed by hydrogen bonds [101]. Explanation of high adsorption of the AB dye is already given in chapter-3; in which the contribution of electrostatic attraction associated to azo-dyes on the deprotonated α/β-Bi_2O_3 surface was briefed. The uncontrolled adsorption at neutral pH can be seen in digital image (Fig. 4.2A and 4.2B) of the dye solution and recovered powder before and after investigation under dark; the AB solution almost lost color by means of high adsorption over α/β-Bi_2O_3. High adsorption was reduced to 19% by modifying the solution pH to alkaline media, exploiting the inhibition provided by OH^-, as can be observed in Fig. 4.1B and 4.1D (dotted line refers to pH = 9.5). Adsorption occurs via electrostatic or hydrophobic-hydrophobic interactions or hydrogen bonding, so the effect of the solution pH is important because it directly influences the electrostatic interaction. The response of the system depends on the anionic properties of molecule and the point of zero charge of the semiconductor, so it is always important to evaluate the adsorption under different conditions.

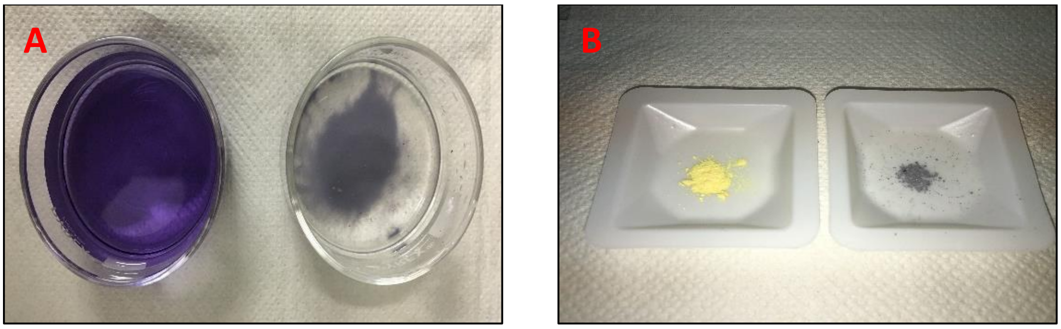

Fig. 4.2 Digital images before and after dark; A) AB dye solution and B) α/β-Bi_2O_3 powder

4.3.1.2 Dye Sensitization

The sensitization process was monitored by comparing the kinetic rate and absorbance spectra under visible and UV light. The absorbance spectra of the RhB dye solution (pH = 6.5) during irradiation using both visible and UV light are presented in Fig. 4.2A-B. The RhB solution exhibited a characteristic absorbance peak at 554 nm. During the visible irradiation, no peak shifts were observed but the intensity of the main absorbance peak slowly decreased over 180 min of irradiation. Similarly, the color removal of the RhB under UV light (350-420 nm) irradiation is shown in Fig. 4.2B, where the dye cannot be sensitized (due to unavaibility of visible spectrum). Under UV light RhB degradation exhibited a subsequent decrease in the intensity of all peaks, but at higher degradation rate, up to 2 times to visible light; revealed that sensitization process under visible light was negligible due to similar degradation spectra in visible and UV irradiations.

Moreover, in case of RhB, the sensitization can also be observed through the hypsochromic shift of the main absorbance peak from 554 nm to 498 nm related to the N-dethylation of RhB to Rhodamine [47]. Watanabe et al [167] reported efficient photochemical N-deethylation accompanied by acetaldehyde formation through the electron-transfer from the adsorbed dye molecule (on cadmium sulphide semiconductor) in its single excited state to the conduction band of the semiconductor. However, no shifts were observed in our case (Fig. 4.3A), suggesting that RhB was photodegraded mainly due to photoactivity of α/β-Bi_2O_3.

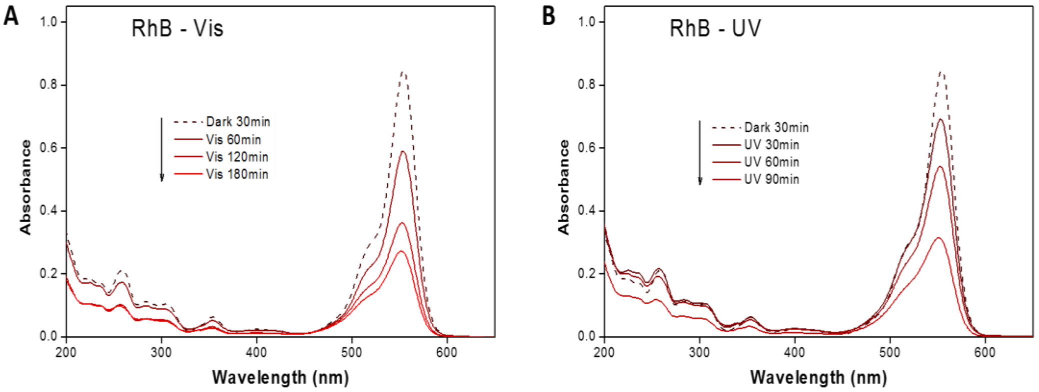

Fig. 4.3 UV-vis spectra of *Rh-B* in (A) Visible light and (B) UV light.

The absorbance spectra of the IC solution (pH-6.8) during the–irradiation process under visible and UV light are presented in Fig. 4.4A-B. The IC solution exhibited a characteristic absorbance peak at 610 nm. The sensitization process is negligible because the IC dye is poorly adsorbed onto the photocatalyst and the changes in the spectra are similar under visible and UV light. The kinetic rate was high under the UV.

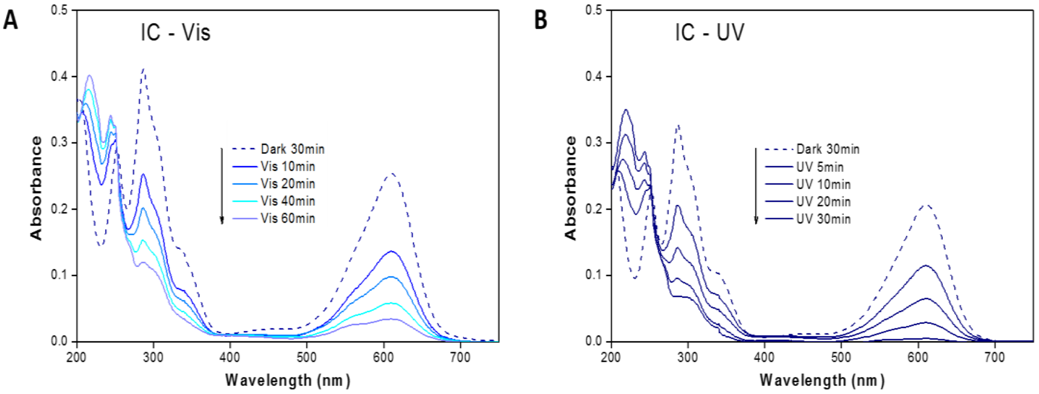

Fig. 4.4 UV-vis spectra of IC in (A) Visible light and (B) UV light.

For the anionic AB dye solution (at pH = 9.5), comparing the time course absorbance spectra (see Fig. 4.5A-B), slight shift during visible light exposure (not observed in case of UV light) suggest that the photodegradation process could accompanied by the sensitization process. During visible light irradiation this main absorbance peak was shifted from 565 to 550 nm with the rise of an apparent isosbestic point at 460 nm peak in the first 40 min (Fig. 4.5A), suggesting the presence of two compounds in single solution of AB. In addition, the degradation rate was very similar for both visible and UV irradiations, suggesting that the sensitization process took place under visible light. As mentioned above the secondary products formed absorbs at nearly the same wavelength, but with different absorptivity values. In this case the final spectrum (90 min) of the AB solution irradiated by visible light evidenced substantial higher absorbance in the 450 to 650 nm region, comparison to that observed under UV (Fig. 4.5B). The high adsorption rate, shift in the absorbance spectrum and similar kinetics in UV and Visible light proved that sensitization of AB has occurred that have promoted charge transfer from AB to conduction band of α/β-Bi_2O_3 and have assisted the photocatalysis in achieving faster degradation of AB.

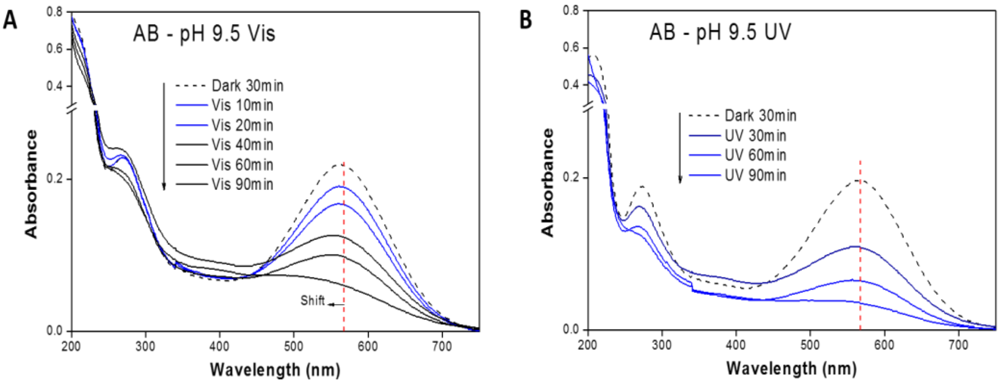

Fig.4.5 UV-vis spectra of *AB* at pH 9.5 in (A) Visible light and (B) UV light.

4.3.1.3 Photobleaching

The photobleaching process is related to the formation of the leuco forms of the dyes (leuco indigo carmine or leuco Rhodamine) due to oxidation-reduction reactions which commonly occur for instance in the controlled oxygen diffusion rate. However, here, the photodegradation of the three dyes was performed at higher stirring rate *i.e.* 1200 rpm, generating oxidizing conditions. Analyzing the whole absorption spectrum of each dye solution after the visible light irradiation with and without photocatalyst (Fig. 4.3-4.5), the isosbestic points of leuco-IC [119, 158] and of leuco-RhB dyes [156] were not observed. As mentioned earlier that leuco-forms of IC and RhB do not show absorption in the red, but they display slight yellow color with main absorbance maxima at 396 nm and 420 nm, respectively [156, 158]. However, the results obtained in our case, indicating that the photo-bleaching process of the dyes did not occur, confirming that the changes in the spectra are only related to photocatalysis by α/β-Bi_2O_3.

4.3.1.4 Photodegradation by Spectral Changes

As mentioned earlier, RhB presented neither photobleaching nor sensitization, therefore the color removal (photodiscoloration) observed in Fig. 4.3 can be attributed to the photodegradation of the dye molecule through the formation of intermediates; after when attacked by photogenerated carriers of the semiconductor. It is known that the RhB photodegradation generates several intermediary products [142] and goes through the formation of triethyl-rhodamine, diethyl-rhodamine, ethyl-rhodamine and rhodamine, having different λ_{max} at 555, 539, 522, 510, 498 nm, respectively. But in our case the photodegradation of RhB followed without formation of such intermediates, which can be identified in UV-Vis spectra, similar observation was reported in various cases of RhB degradation by using Bi_2O_3 [101, 168].

Considering that the IC dye suffered neither photobleaching nor sensitization, the photodiscoloration observed for the IC dye during the photocatalytic experiments can be attributed to photodegradation. Fig. 4.4A-B show that the main absorbance peak of IC dye fully decreased when exposed to either visible or UV light. The changes in the whole spectrum are associated to the destruction of the indigoid group (NHC=CNH) of the IC dye structure, leading to absorbance peaks in the 210-240 nm region originating from the benzene and carboxylic groups of the secondary products. The identified secondary species in the final absorbance spectrum was already discussed as the typical formation of *Isatin sulfonic acid* and *2-amine-5-sulfo-benzoic acid* [101, 121, 163, 164], which are formed when the superoxide radicals (oxygen reactive species) attack the indigoid group and destroy the IC structure, carrying out the photodegradation process [163]. In addition, the persistent absorption and the additional isosbestic point at 251 nm indicates that the photodegradation process of the secondary products was neither complete under UV light nor under visible light irradiation. This result was expected because the generated superoxide radicals are oxygen reactive species with middle oxidizing power [169].

The anionic AB dye was highly absorbed onto the photocatalyst surface and during the visible illumination; it is possible that electron transfer processes occurred between the excited dye molecule and the semiconductor *i.e.* it is likely that part of the color removal was due to the sensitization process. However, under UV light irradiation, the absorption spectra of AB was slightly changed, suggesting the formation of secondary products arising from the destruction of the azo-group (N=N) of the AB dye structure by the generated superoxide radical. This result suggests that superoxide radicals are also generated under visible light and therefore other secondary products of the AB photodegradation process could be formed. Unfortunately, it is impossible to quantify the percentage of the sensitization and photodegradation processes because the formed secondary products masked the real absorbance from the original AB dye. The partial photodegradation of the AB dye could be associated with the limited number of generated oxidizing radicals since the active sites on the photocatalyst were occupied by the adsorbed dye.

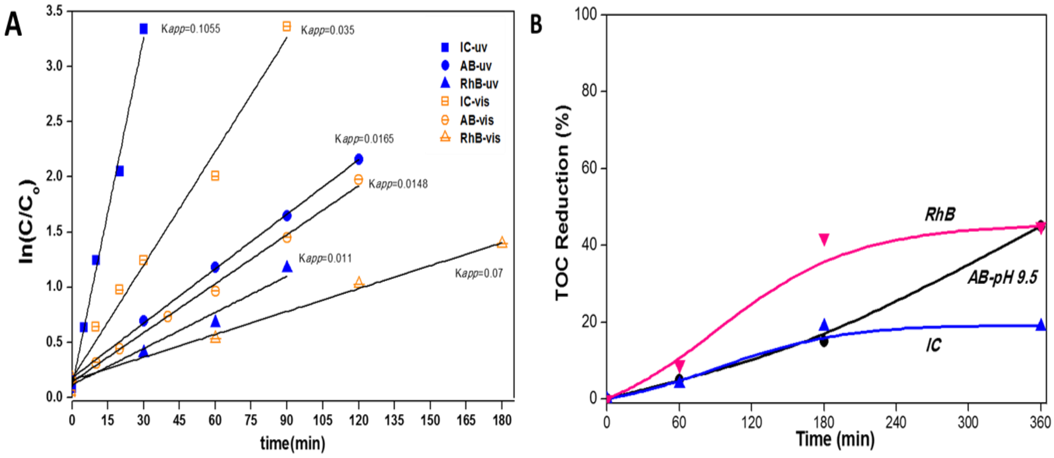

Fig. 4.6 A) Photodegradation kinetics of individual dyes at optimum conditions in UV and visible, B) TOC reduction % of dye solutions at different irradiation time under visible light.

When evaluating a photocatalytic material, the kinetics of the reaction is usually analyzed. In many cases the change in the dye relative concentration (C/C_0) follows a pseudo first order reaction where k_{app} is the slope of the straight line of the $\ln(C/C_0)$ *vs* time (t) plot, according to the Langmuir-Hinshelwood model. Fig. 4.6A shows that the reactions with the three dyes under UV and visible light follow a pseudo first order reaction. The k_{app} value of the reactions performed under UV light is larger than those obtained under visible light for the IC and RhB dyes, indicating the absence of the sensitization process. On the other hand, the apparent reaction rates under UV and visible light for the AB were almost similar. The rates of reactions under both illumination for the different dyes were IC > AB > RhB, with k_{app} values of 0.036 min^{-1}, 0.01482 min^{-1} and 7×10^{-3} min^{-1} with visible light and 0.1055 min^{-1}, 0.0165 min^{-1} and 0.011 min^{-1} with UV light respectively.

4.3.1.5 Mineralization

Fig. 4.6B shows the TOC reduction % of the different dye solutions at different times of visible light. For RhB, a reduction of 9% of the organic carbon content was observed after the first 60 min of irradiation, a percentage like that obtained by adsorption (Fig. 4.2D). Nevertheless, the decrease of TOC reached 45% after 360 min exposure, suggesting the presence of stable secondary products. In case of IC dye, the 4% reached at 60 min is related to the poor absorption onto photocatalyst, and a maximum TOC diminution of 19% was obtained after 180 min exposure with no further increase at longer exposure time (up to 360 min). This result suggests that the persistence of typical intermediates (*Isatin sulfonic acid* and *2-amine-5-sulfo-benzoic acid;* see Fig. 4.4) does not lead to further mineralization; similar results were reported by D. Sánchez-Martínez *et. al.* [16], in which complete mineralization was not achieved by using α-Bi_2O_3. For AB at alkaline pH the TOC decrease reached 5% at 60 min. and further decreased to to 45% after 360 min, again suggesting that these secondary products still remain in the solution. The pattern of TOC *vs* irradiation time, revealed that the decrease of TOC by the mineralization process occurred steadily and not instantaneously after sensitization/photodegradation of each dye.

4.3.2 Photodegradation pathway

4.3.2.1 IC

As stated earlier that, for the synthesized bismuth oxide based heterostructures, the electrons and holes are well separated and originate oxidative and reductive species, that can target the pollutants and caused them to oxidize and reduce into intermediate secondary products and further complete or partial mineralization of these intermediates. For example, in case of IC dye, is stated earlier that the indigoid group attacked by the photocatalytic oxidation and initially split into isatin sulphonic, which further oxidized into *2-amino-alpha-oxo-5-sulfo-benzeneacetic acid* and finally oxidized into *2-amine-5-sulfo-benzoic acid* [121, 170, 171] [172]. This path of photodegradation of IC is given in Fig. 4.7, which is already suggested by many researchers, basing on the spectral changes in the UV-vis absorption spectrum and obtained results using high-performance liquid chromatography (HPLC) and LC-MS (Liquid Chromatography-Mass Spectroscopy [121, 170, 171]. The proposed path in Fig. 4.7 and TOC analysis (Fig. 4.6B), revealed that after the formation of *2-amine-5-*

sulfo-benzoic acid further mineralization of this compound was not achieved, probably because of their low interaction with the α/β-Bi_2O_3 and higher stability.

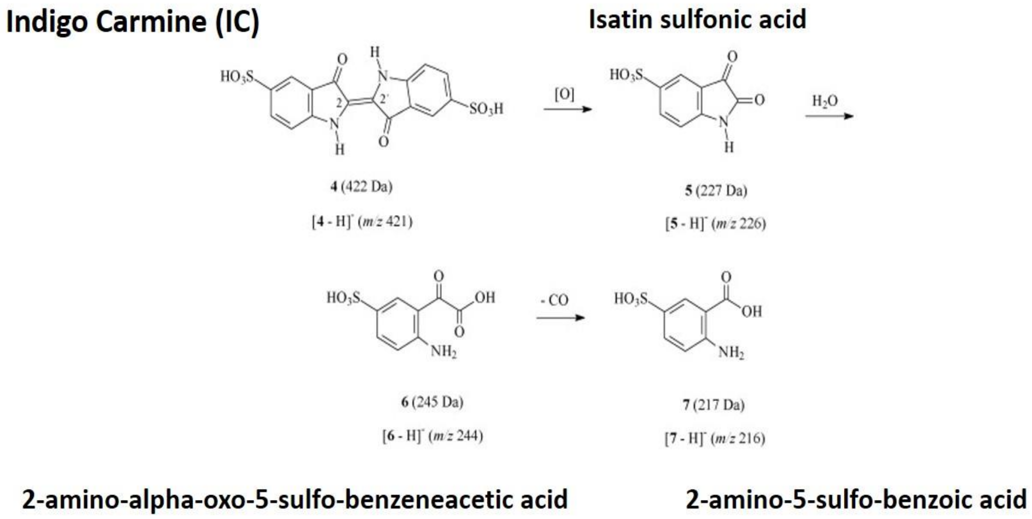
Indigo Carmine (IC)
Isatin sulfonic acid
HO₃S
SO₃H
[O]
H₂O
4 (422 Da)
[4 - H]⁻ (m/z 421)
5 (227 Da)
[5 - H]⁻ (m/z 226)
- CO
NH₂
OH
6 (245 Da)
[6 - H]⁻ (m/z 244)
7 (217 Da)
[7 - H]⁻ (m/z 216)
2-amino-alpha-oxo-5-sulfo-benzeneacetic acid
2-amino-5-sulfo-benzoic acid

Fig. 4.7 Proposed scheme for the photodegradation and partial mineralization of IC dye

4.3.2.2 RhB

In case of RhB, photodegradation was achieved without any hypsochromic shifts in UV-vis absorption and alike cases were also reported by some researchers. Basing on these outcomes those researchers have suggested two-way processes route: N-demethylation and destruction of the conjugated structure for the formation of intermediate by-products of RhB; identified by using HPLC, GC-MS and LC-MS [173-176]. Various products (e.g., N,N-diethylrhodamine and N-ethylrhodamine) were detected along with 3-hydroxybenzoic acid, oxalic acid, malonic acid, succinic acid, glutaric acid and adipic, given in proposed scheme in Fig. 4.8; following the reported work [173-176]. After forming these intermediates, additional cleavage of the chromophore and the aromatic ring opening could have occurred that allowed subsequent mineralization of RhB, by which it was converted to smaller organic species and ultimately mineralized to inorganic products (e.g., CO_2 and water).

The possible path of RhB degradation resulted in 45% mineralization and suggests that it underwent irreversible chemical changes, probably due to oxidation reactions originated by photocatalyst. However, it seems that chromophoric groups are easily reacted and attacked by the originated reactive species, but further degradation of RhB intermediates contain phenyl groups, which becomes more difficult to oxidized or reduced in order to achieve complete mineralization [172].

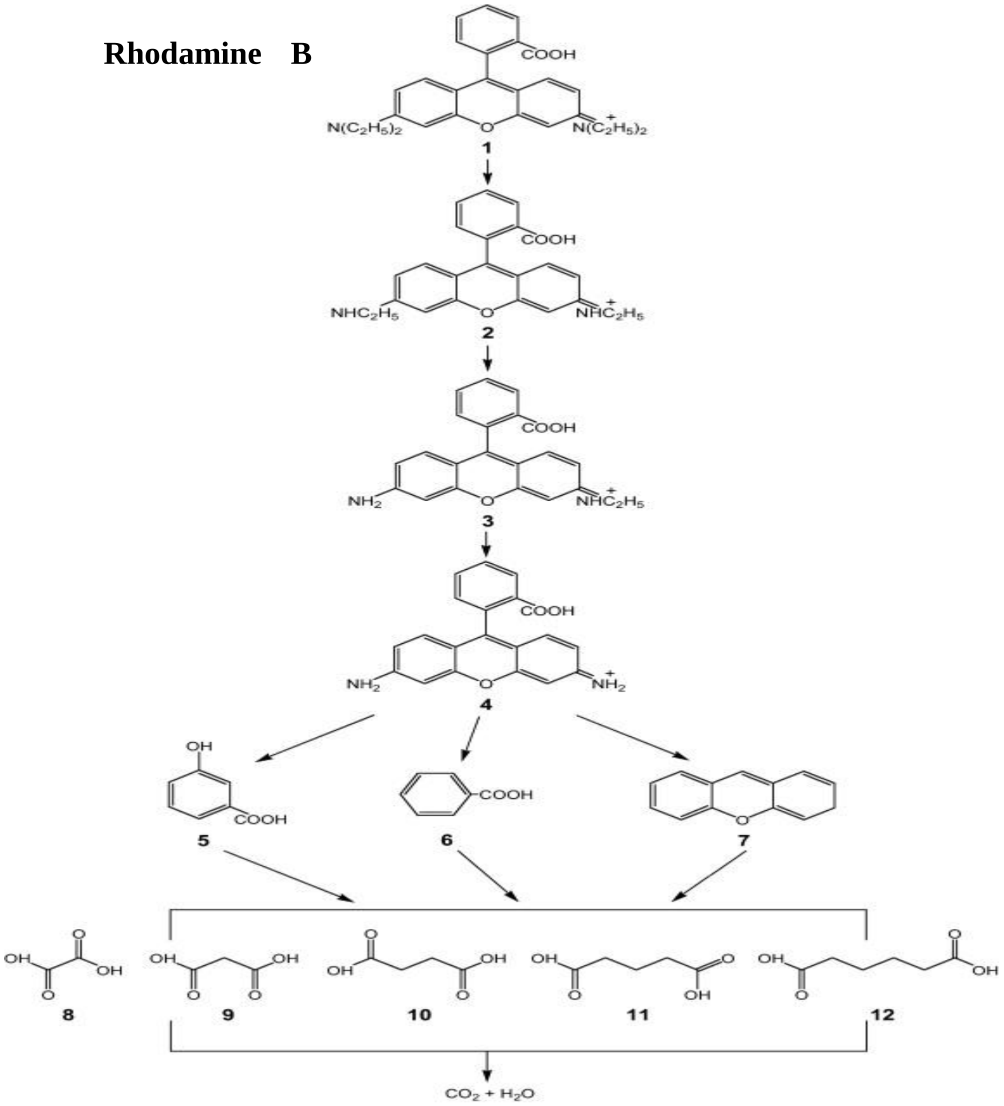
Rhodamine B
COOH
N(C2H5)2
N(C2H5)2
1
NHC2H5
NHC2H5
2
NH2
3
NH2
4
OH
5
6
7
8
9
10
11
12
CO2 + H2O

Fig. 4.8 Proposed scheme for photodegradation and partial mineralization of RhB dye; [173-176]

4.3.2.3 AB

For AB dye initially dye molecule could underwent azo reduction (chromophoric group) in which several amino containing aromatic compounds could be formed as intermediate products and leaving the dye solution colorless.

The proposed degradation scheme of AB is given in Fig. 4.9 based on the result obtained by A. Garg *et. al.* and S. Sekar *et. al.* [177, 178], both research groups have studied degradation of AB dye using HPLC, GCMS and LC-MS analyses and reported that, supplementary intermediates formed due to desulfunation and dethylation via oxidation reaction by the reactive species. Further they have analyzed that, after the formation of these intermediates, aromatic ring cleavage was achieved that resulted the formation of dibutyl phthalate and phthalic acid and some aliphatic hydrocarbons; based on the identification using HPLC, GCMS and LC-MS [177, 178]. These originated intermediates products subsequently followed partial mineralization (resulted TOC reduction up to 46%) and formed stable organic compounds. Here again complete mineralization was not achieved, because of the same reasons mentioned earlier *i.e.* intermediates stability and their lack of interaction with α/β-Bi_2O_3.

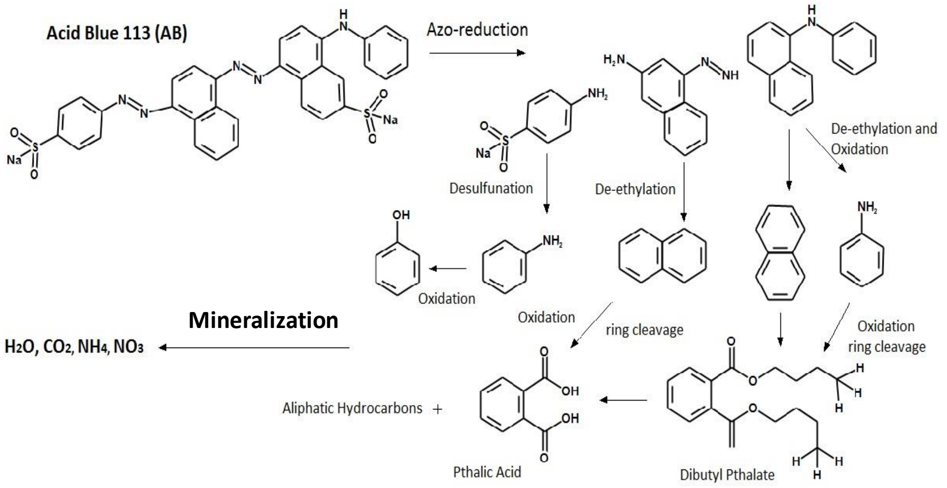
Acid Blue 113 (AB)
Azo-reduction
De-ethylation and Oxidation
Desulfunation
De-ethylation
Oxidation
Mineralization
H2O, CO2, NH4, NO3
Oxidation
ring cleavage
Oxidation
ring cleavage
Aliphatic Hydrocarbons +
Pthalic Acid
Dibutyl Pthalate

Fig. 4.9 Proposed scheme for photodegradation and partial mineralization of AB dye

4.4 Conclusion

During photocatalytic investigation of three different dyes rhodamine-B (RhB), acid blue 113 (AB) and indigo carmine (IC) using α/β-Bi_2O_3 photocatalyst various coexisted process were highlighted and discussed in detail *i.e.* adsorption, photobleaching, dye sensitization in conjunction to actual photocatalytic degradation and mineralization processes. It was observed that AB faced uncontrolled adsorption up to 46% at neutral pH and resulted partial discoloration, which was controlled up to 19% by changing the pH to alkaline media, where OH^-

provided inhibition towards high adsorption. Moreover, Photodegradation of AB was assisted with sensitization process due to strong interaction of dye and photocatalyst that have promoted charge transfer from AB to α/β-Bi_2O_3 surface; confirmed from the observed spectral changes in absorbance spectrum and the identical degradation kinetic rate under UV and visible light. Moreover, achieved mineralization of AB was around 45% mineralization. While RhB dye neither faced photobleaching nor dye sensitization and photodegraded without formation of intermediates and reached to 45% mineralization at 360 min irradiation exposure. In case of IC, photodegradation was achieved due to photocatalytic response of α/β-Bi_2O_3 without following photodiscoloration due to photobleaching, sensitization or higher adsorption, and resulted in 19 % removal in TOC value due to small adsorption and less mineralization. Furthermore, during the IC photodegradation, appearance of additional spectral changes in absorbance spectra, provided an indication to assess the photocatalytic process by using simple UV-vis analysis. From the overall study, it was concluded that during photocatalytic response of α/β-Bi_2O_3, only discoloration and partial mineralization was obtained due to breaking of coloring group of each dye, that resulted in formation of unidentified stable intermediates, which were not able to mineralize further.

Chapter 5

β-Bi_2O_3 Films Deposited on different Substrates by Pneumatic Spray Pyrolysis and their Photo-evaluation for Degradation of different types of Organic Dyes

5.1 Introduction

So far, heterogeneous photocatalysis faced many practical challenges and amongst them the most significant is dealing with the effective recovery of nanoparticles, their filtration and recycling in economical way [179-184]. For high photoactivity, micro and nanometric scales are preferred with the advantage of prominent surface area, higher dispersion in the bulk solution and suitable passage for particles activation via irradiation source [25]. However, in bulk, these small particles are hard to recover, and the filtration required for recharge and reuse of the catalysts, is the additional operational costs for water purification. Moreover, during the photocatalytic process, small particles may experience coagulation and agglomeration and their catalytic activity is reduced [26, 27]. These problems have brought attention towards the development of non-slurry systems in which the photocatalyst can be immobilized on certain fixed supports. In addition, it is also accounted that the photocatalyst immobilized supports should satisfy certain requirements like: chemically inertness, transparency to the irradiation source *i.e.* UV or visible light, and reasonable specific surface area favoring the capture or interaction of pollutants in the bulk solution [27, 180]. A lot of work was already done, suggesting diverse materials as supports. Focus was put on carbon, silicon and mineral based porous supports which have advantage of larger surface area, which allows a good contact between the pollutants and photocatalyst needed for continued degradation. Examples of such supports are silica based [88, 181, 182, 185-196], activated carbon [197-201], synthetic clay laponite [202] glass, steel mesh [51, 203-207] and recently some polymers such as polyimide [208]. Most of the mentioned studies have presented approaches for the immobilization of TiO_2 on various substrates, but in overall, the photocatalytic response was considerably lower than the bare TiO_2 powder, mainly due to low dispersion, decreased transparency, limited mass transfer and poor interaction of the photocatalyst with pollutants. Thus, supported photocatalysts are still considered as unsuitable for the advancement of non-slurry systems alternative.

The current work was aimed to identify potential supports for immobilization of photocatalyst, which may prove as effective in resolving the challenges of mass transfer limitation, optimum irradiation passage and better interaction with the pollutants. Chosen supports were porous sintered silica discs, steel mesh and corning glass; selection is based on the idea of their easy integration within the water treatment system. The sintered silica discs along with an advantage of uneven roughness, porosity and the intrinsic hydrophilicity could be resulted as an interface in targeting the pollutants for effectual photoactivity. The principle of using steel mesh is to target the pollutants in tiny holes and its flexibility could allow easy integration within the water treatment system. The selection of corning glass is based on the comparison of overall photoactivity amongst the other chosen supports, because the photocatalyst deposited films on glass has been extensively studied for the photocatalytic evaluation of dyes using TiO_2, ZnO and Bi_2O_3 [51, 87, 183, 204-206, 209, 210]. The pneumatic spray pyrolysis (PSP) method was initially used for thin films deposition because it is found as simple and cost effective method, that allow uniform film growth and particles distribution [87, 211-213], in comparison to other methods such as, sol-gel, CVD or MOCVD, dip coating [201, 209, 214-219]. Along with analyzing different substrates, attention was also given to photocatalytic evaluation in visible light; focusing to identify visible-active photocatalyst immobilized on competitive support. Therefore, tetragonal bismuth oxide (β-Bi_2O_3) films were immobilized on the mentioned supports; since β-Bi_2O_3 were found promising for activity in visible-light [18, 19, 87, 127, 220-224]. The photocatalytic investigation of the deposited films was based on the highest kinetic rate of discoloration of various organic dyes: differing in ionic behavior and chemical structure; considering their evaluation in terms of adsorption capacity and interaction of each with immobilized substrates and mineralization capability of the prominent substrate,

5.2 Experimental work

5.2.1 Characteristic of substrates

Sintered silica discs (made of borosilicate glass) with diameter of 20 mm and of porosity grade-3, having an average pore size of 10-15 µm, were obtained from Pyrex®. Plain corning glass and steel mesh (50 microns plain weave) were rectangularly cut at dimension of 12 x 25 mm (length x width).

5.2.2 Films immobilization

The precursor solution was prepared by dissolving bismuth(III) acetate $Bi(CH_3CO_2)_3$ from Sigma-Aldrich in deionized water and acetic acid at a proportion of 75 and 25 Vol%, respectively, at 45 °C under continuous stirring until a transparent homogeneous solution was obtained [155]. Before deposition, selected supports/substrate were separately sonicated in acetone and isopropanol for 10 min. Fig. 5.1A shows the scheme of PSP system [225], displaying the sprayed nozzle on top and deposition chamber containing heating plate and tin bath; used for temperature and holding the substrate, moreover the rate of precursor solution and pneumatic air is controlled by two rotameters. For deposition of β-Bi_2O_3 films, precursor solution was sprayed on each substrate from a maintained distance of 27 cm and at a constant rate of 2.15 ml/min. Before placing the substrate on tin bath; temperature of that chamber was kept constant at 450 °C; similar conditions were previously used and reported to obtain β-Bi_2O_3 [87].

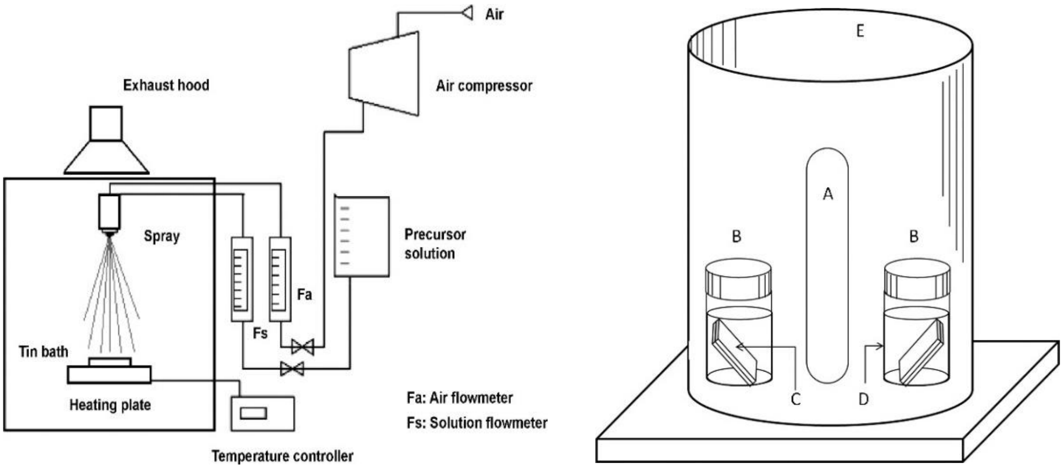

Fig. 5.1 Schematic representation, i) pneumatic spray pyrolysis set-up and ii) photocatalytic reactor, where (A) is the lamp, (B) are the vials, (C) are the immobilized substrate, (D) is dye solution and (E) is the external casing [225].

5.2.3 Characterization of films

During films deposition along with each substrate, a 1 cm x 1 cm piece of corning glass was also put, to be used for X-ray diffraction (XRD) and UV–vis diffused reflectance spectra (DRS); as a representation of the similar films that also deposited on the substrates, to avoid the background and the effect of the substrates. The phase composition of immobilized samples was characterized by XRD, using SIEMENS D500 X-ray diffractometer (Cu-Kα X-ray source). The diffraction patterns were analyzed through the PDXL2 software to identify the crystalline structure and particle size [51, 87, 210, 212]. The DRS were recorded using the same method as indicated in chapter-2. Morphology of the deposited and blank substrates was examined by field-emission scanning electron microscopy. Energy-dispersive X-ray spectroscopy (EDS) was used to assess elemental mapping and distribution over the deposited substrates.

5.2.4 Photocatalysis Tests

For photocatalytic investigation a reactor given in Fig. 5.1B [225],was used in which each immobilized substrate inside the dye solution was laid inclined facing towards the irradiation source [226]. The photocatalytic response of bare and immobilized substrates was initially evaluated by determining the photodegradation under standard fluorescent white lamp (with an irradiance of 33 Wm^{-2} and spectral range from 400 nm to 700 nm), using 15 mL of anionic indigo carmine (*IC*) dye solution at neutral pH and at concentration of 5 mg/L. For each observation, dye solution was initially stirred for 45 min in the dark to attain adsorption-desorption equilibrium. The stirring rate was kept constant at 600 rpm in both dark and irradiated conditions. The absorbance spectra of the dye solution as a function of time was recorded, using a UV-vis spectrophotometer (Shimadzu 1800) after analyzing the withdrawn aliquots of 3 mL and putting it back to the vial after measurement. After selecting the best substrate with improved photocatalytic performance was further analyzed for photodegradation cationic Rhodamine B (*RhB*) solution at 3 mg/L concentration of and anionic Acid blue 113 (*AB*) solution at 5 mg/L concentration, to analyze the photocatalytic behavior, mechanism and photodegradation kinetics when experiencing with dyes of diverse functional groups, structures and ionic behaviors. The total organic carbon (TOC) analysis were made by using a TOC-L Shimadzu Total Organic Carbon analyzer via NPOC method in a high sensibility mode. Furthermore, the photocatalytic evaluation was repeated with the best substrate, up to three cycles to assess the suitability of the substrate and stability of deposited films.

5.3 Results and discussion

5.3.1 Characterization of the films

5.3.1.1 Crystalline structure

As mentioned earlier that, during films deposition on each substrate, a piece of corning glass was also placed. The obtained XRD pattern on deposited glasses is displayed in Fig. 5.2A.

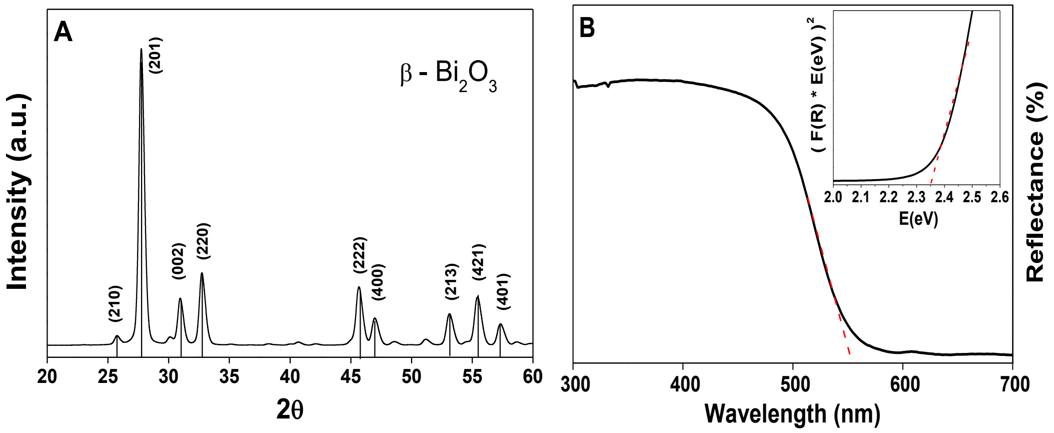

Fig. 5.2 A) XRD patterns of the obtained β-Bi_2O_3 films on glass substrate and B) UV-Vis DRS spectra of β-Bi_2O_3 films and band gap estimation in tauc plot (inset).

Diffracted peaks indicate a tetragonal-β-Bi_2O_3 crystalline structure with major peaks at 2θ: 27.78, 32.62, 45.52 and 55.39° (JCPDS card no. 01-076-0147) attributed to (201), (220), (222) and (421) planes respectively. Alike XRD patterns were reported earlier, in which β-Bi_2O_3 films were attained on silica wafers and corning glass by using PSP [87]. With alike results of XRD, it was observed under strict standard conditions, the achieved crystalline structure of thin films is always tetragonal-β, even for different types of substrates.

5.3.1.2 Optical band gap

Fig. 5.2B shows the UV-Vis DRS spectra of one β-Bi_2O_3 deposited witness glass. The obtained films displayed a wide absorption plateau ranging from 300 to 550 nm, the absorption edge above 550 nm representing electron transitions from the valence band to the conduction band, and activation could be efficiently achieved in the visible light. The obtained Tauc plot applying Kubelka-Munk method is given in the inset of Fig. 5.2B and estimated band gap energy of the films is around 2.4 eV; close to previously reported β-Bi_2O_3 films and powders [19, 87, 101, 209, 220-222, 227].

5.3.1.3 Morphology

The FESEM and optical images of the bare and deposited substrates are shown in Fig. 5.3A-I. Fig. 5.3A shows a flat surface of bare glass, while after deposition (Fig. 5.3D and 3G), a random and non-compact distribution of crystalline sub-micrometric particles can be clearly noticed. The random distribution of β-Bi_2O_3 particles on glass substrate could be associated to quick evaporation of the sprayed droplets after arriving on the surface [87, 211-213]. The bare steel sown in Fig. 5.3B also presented flat morphology, while after deposition similar sub-micrometric particles can be seen on deposited steel (Fig. 5.3E and 5.3H), but distributed in a more compact way than in the case of glass. The compactness of particles in case of steel mesh could be related to the difference in geometry and appearance than glass and allowed different behavior in aligning of sprayed droplet over the mesh surface. In addition, tiny channels (inside circular thin steel wires) possibly have some influence in getting such compact morphology, by allowing wrapping of sprayed droplets and particles before evaporation. In case of sintered silica, bare sample rather presented large silica particles with uneven but regularly placed holes (Fig. 5.3C), however the deposited film morphology was different for glass and mesh (Fig. 5.3F and 5.3I). It appeared as overlaid sheets; one after one. This could be related to roughness, hydrophilicity and uneven porosity of silica that have allowed even distribution and slow evaporation of sprayed droplets during deposition.

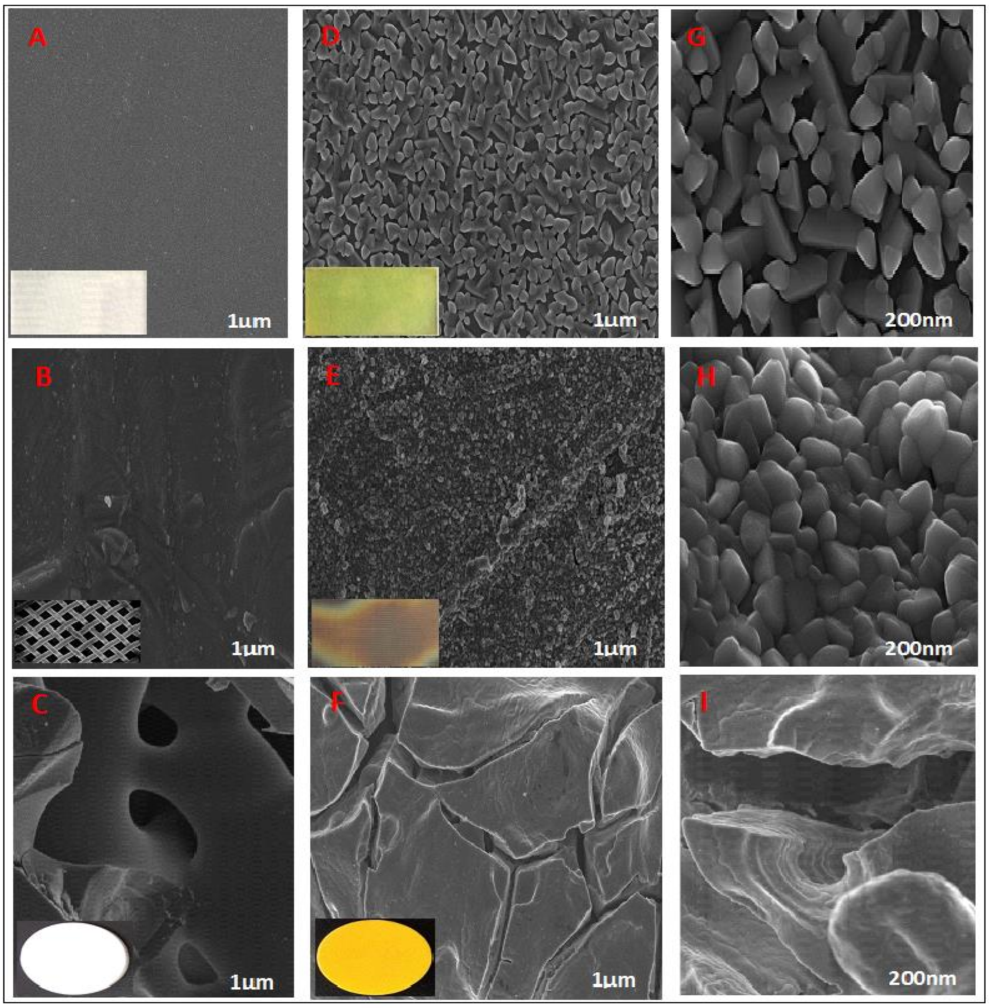

Fig. 5.3 Bare substrates (A-C), β-Bi_2O_3 deposited substrates at low magnification (D-F), at high magnification (G-I).

The EDS analysis was performed for the elemental composition and mapping of the deposited films on each substrate. The obtained elemental maps of deposited glass, sintered silica and mesh are shown in in Fig. 5.4A-I and suggest that β-Bi_2O_3 films are uniformly distributed and nearly cover the entire surface of glass, mesh and sintered silica substrates.

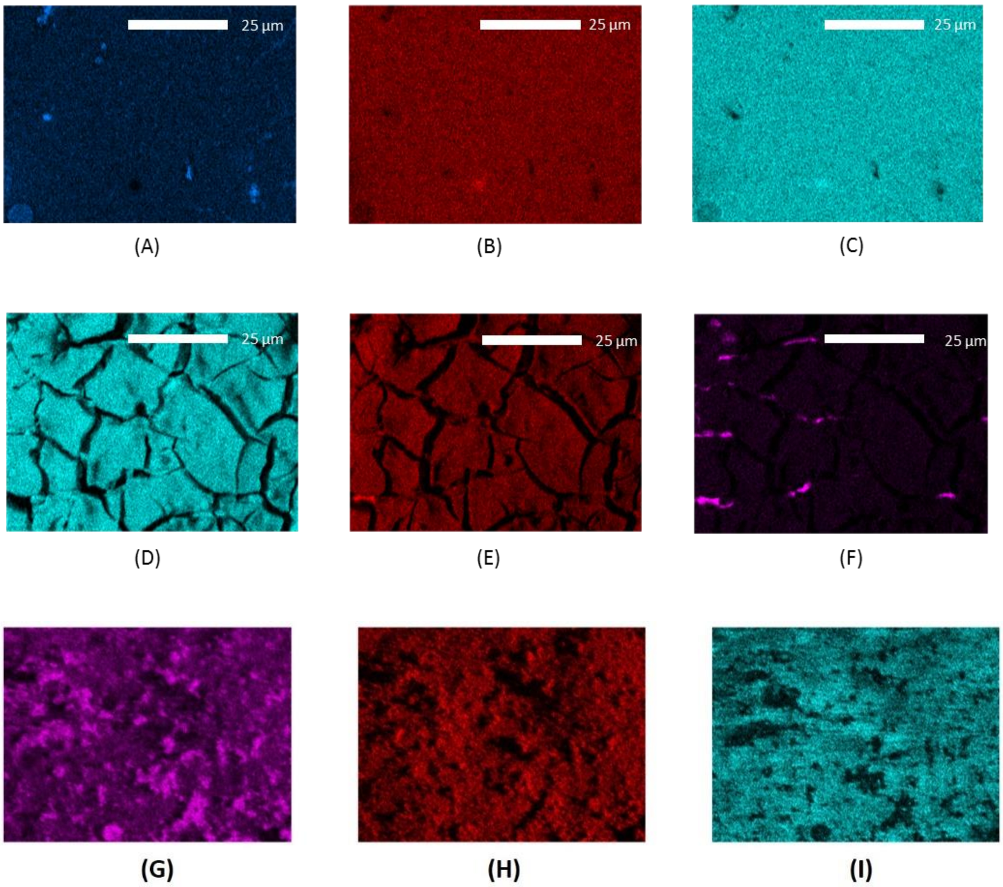

Fig. 5.4 EDS elemental mapping of deposited glass (up), deposited silica (center) and deposited mesh (bottom) indicating bismuth (A, D, G), oxygen (B, E, H), silicon (C, F) and Iron (I).

5.3.2 Photocatalysis

5.3.2.1 Indigo Carmine

Primarily, anionic Indigo Carmine (*IC*) was used to determine the photoactivity of β-Bi_2O_3 deposited substrates in comparison to bare substrates and commercial β-Bi_2O_3 powder (Sigma Aldrich). At start, *IC* dye solution with each substrate and powder was kept under dark for around 45 min to attain adsorption-desorption equilibrium. Afterwards, dye solution was irradiated using white fluorescent lamp to initiate and analyze photoactivity of the deposited films and commercial powder. The adsorption rate of the *IC* over bare, deposited substrates and powder, obtained in each case are shown in Fig. 5.5A; with deposited silica adsorption rate was around 16%, higher than bare silica (up to 12%), β-Bi_2O_3 powder (up to 5%) and other bare and deposited substrates (up to 3%), which indicated good interaction of dye molecules with β-Bi_2O_3 films due to porous, rough and hydrophilic nature of silica [228-231]. Bare and deposited glass and steel, hardly adsorbed IC dye, due to limited roughness and availability of active sites permitted by β-Bi_2O_3 films; inadequate interaction with dye molecules. In case of β-Bi_2O_3 powder the adsorption was low, because the IC dye only interact with Bi_2O_3 by limited hydrogen bonds in the chemical structure; as discussed earlier in chapter-2 and 3. Fig. 5.5B displays the profile of relative concentration (C/C_o), where C_o is the initial concentration (after adsorption) and C is the final concentration of dye at an irradiation time (t) for bare and β-Bi_2O_3 deposited substrates. In Fig. 5.5B the obtained relative C/C_o shows that bare substrates hardly changed the concentration after irradiation, however considerable reduction can be observed for the deposited β-Bi_2O_3 substrates in comparison to previously obtained result in case of evaluation with commercial β-Bi_2O_3 powder (chapter-3); confirmed that photodegradation of the *IC* dye occurred due to photocatalytic response of the β-Bi_2O_3; not due to other processes such as: intense adsorption, photobleaching, sensitization etc.; discussed in earlier chapters.

Perceiving the behavior of C/C_o, photodegradation of the IC dye was attributed to pseudo 1st order reaction and further apparent kinetic rate (k_{app}) was calculated by using $\ln(C/C_o)$ vs irradiation time [232]. Kinetic curves for deposited substrates and powder are shown in Fig. 5.5C. Observing the K_{app}, the photocatalytic efficiency for degradation of the *IC* dye can be assigned as: powder β-Bi_2O_3 > deposited silica > deposited mesh > deposited glass. It was obvious that powder β-Bi_2O_3 displayed highest activity due to good dispersion in bulk dye solution, but fixed β-Bi_2O_3 deposited silica also shown competing response, mainly due to efficient interaction of grown films with dye molecules, provided by the uneven porosity of silica and voids in the thin films sheets that braced and maintained capturing of dye molecules for effective photodegradation compared to deposited mesh and glass.

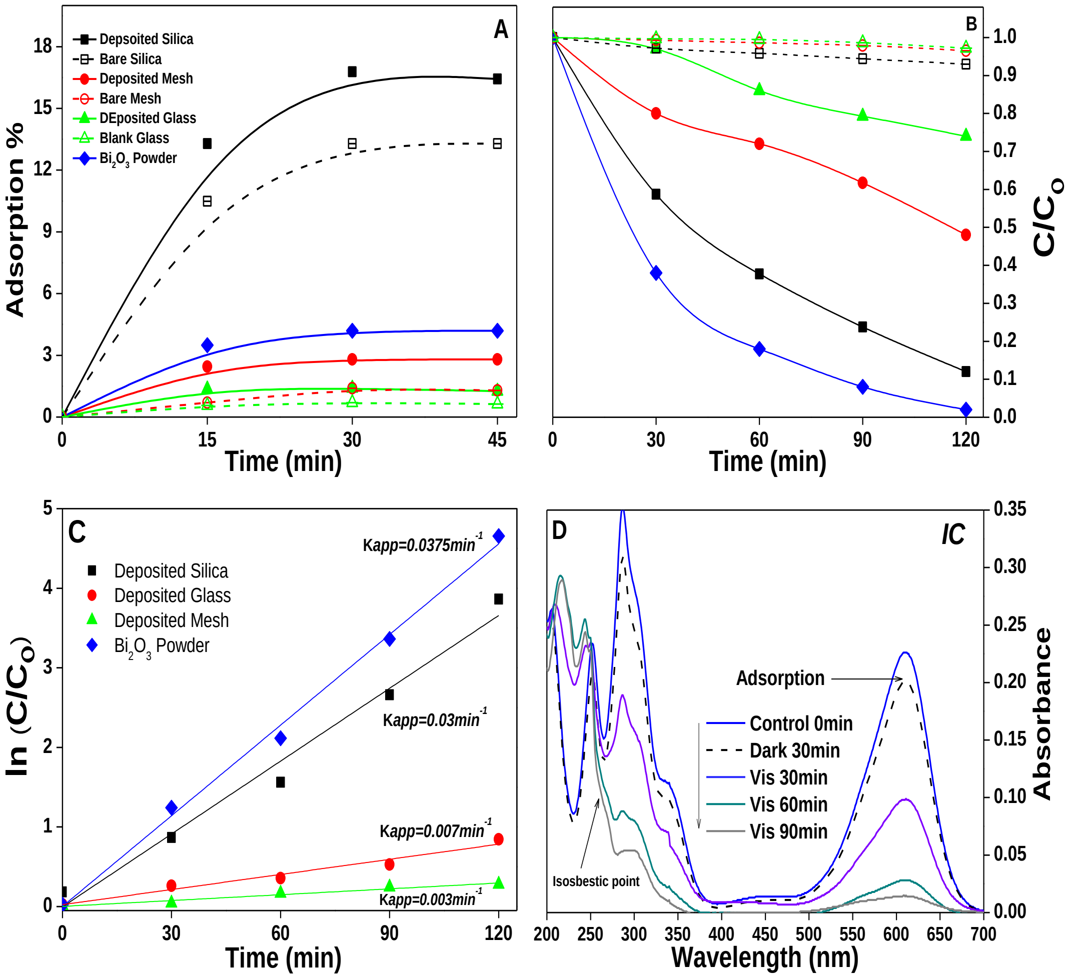

Fig. 5.5 A) Adsorption %, B) Relative concentration C/C_o for IC dye with blank, grown substrates and bulk β-Bi_2O_3 C) photodegradation kinetic rate for *IC* dye with all substrate D) photodegradation absorbance spectrum vs time with deposited silica.

The K_{app} was higher with deposited silica: around 10 and 7 times higher than deposited glass and mesh, respectively. The relatively high response in case of deposited silica, is related to the large surface area of the deposited silica, which provides a better interaction of the dye molecules with the catalyst and leads to a more efficient photodegradation.

Parallel to clear photodiscoloration, time course spectral changes in absorbance spectra of IC (Fig. 5.5D), suggested that color removal is due to photodegradation by deposited β-Bi_2O_3. The substantial increase in absorbance at 218 nm and appearance of isosbestic point at 251 nm, revealed that secondary products were formed, which are known as isatin sulfonic acid and 2-amine-5-sulfo-benzoic acid [101, 121, 233]; as reported in earlier chapters. The absorption peaks in the range of 210-240 nm are an indication of persistent formation of benzene and carboxylic groups as secondary intermediates, while the vanishing of the absorption at 610 nm suggests that structure of the *IC* was attacked by photocatalytic oxidation and indigoid group (NHC=CNH) was broken [101].

5.3.2.2 Evaluation of other dyes

Since the β-Bi_2O_3 deposited silica showed a high photocatalytic activity for degradation of *IC*, therefore the further evaluation of *RhB* and *AB* dye solutions was only performed using deposited silica. Fig 5.6A and 5.6B show the time-course absorbance spectra of *RhB* and AB dye solutions in presence of deposited silica, moreover Fig. 5.6C shows the relative C/C_o of *AB* and *RhB* dyes in comparison to *IC*. K_{app} calculated using pseudo 1st order kinetic equation [232], were: 4 x 10^{-2}, 3.2 x 10^{-2}, 3 x 10^{-2} min^{-1} for *AB*, *RhB* and IC dyes respectively. The increased kinetic rate in case of *RhB* and *AB* dyes could be related to improved interaction of dye molecules with β-Bi_2O_3 films than in case *IC*. The improved interaction of *RhB* and *AB* can be observed, from the obtained adsorption shown in Fig. 5.6C *i.e.* 32% and for 35%, respectively, almost twice than in case with *IC i.e.* 16%. In case of *RhB* and *AB*, good protonation of β-Bi_2O_3 and high amount of active sites, allowed attraction of diethylamino groups in *RhB* molecular chain to preferentially adsorb over β-Bi_2O_3 thin films [101]. Whereas, with anionic *AB* azo-dye (same type as *IC* dye), the high adsorption could be linked to anionic species *i.e.* sulphonic groups (H^+ - SO^{-3}) in the solution, which deprotonated (neutralized) β-Bi_2O_3 deposited films; similar cases of high adsorption because of such azo dyes (with attached anionic species) are found for basic yellow 28 and acid orange G dyes; using TiO_2 [148].

Finally, to assess the information of the stability of the deposited films and viability of silica as an alternate support for photocatalysts, photocatalytic activity was carried up to three cycles. Fig. 5.6D shows the photodegradation performance of the three dyes up to three cycles. It was observed that the photodegradation rate for each dye was almost similar for first two cycles, but was reduced in the third cycle. This reduction in efficiency could be connected to drop in the adsorption rate due to altered porosity and decreased in active sites of the films, that previously have sustained the capturing of dye molecules. However, the two first cycles have shown compatibility for successive cycles and efficacy of the utilization of β-Bi_2O_3 deposited silica for heterogeneous photocatalysis. Morever, recharging/refreshing of silica and β-Bi_2O_3 films after two cycles, by means of rinsing with hot water or thermal treatment at low temperature (up to 100 °C) can remove the residuals from the surface and could sustain the same performance as achieved in first cycles.

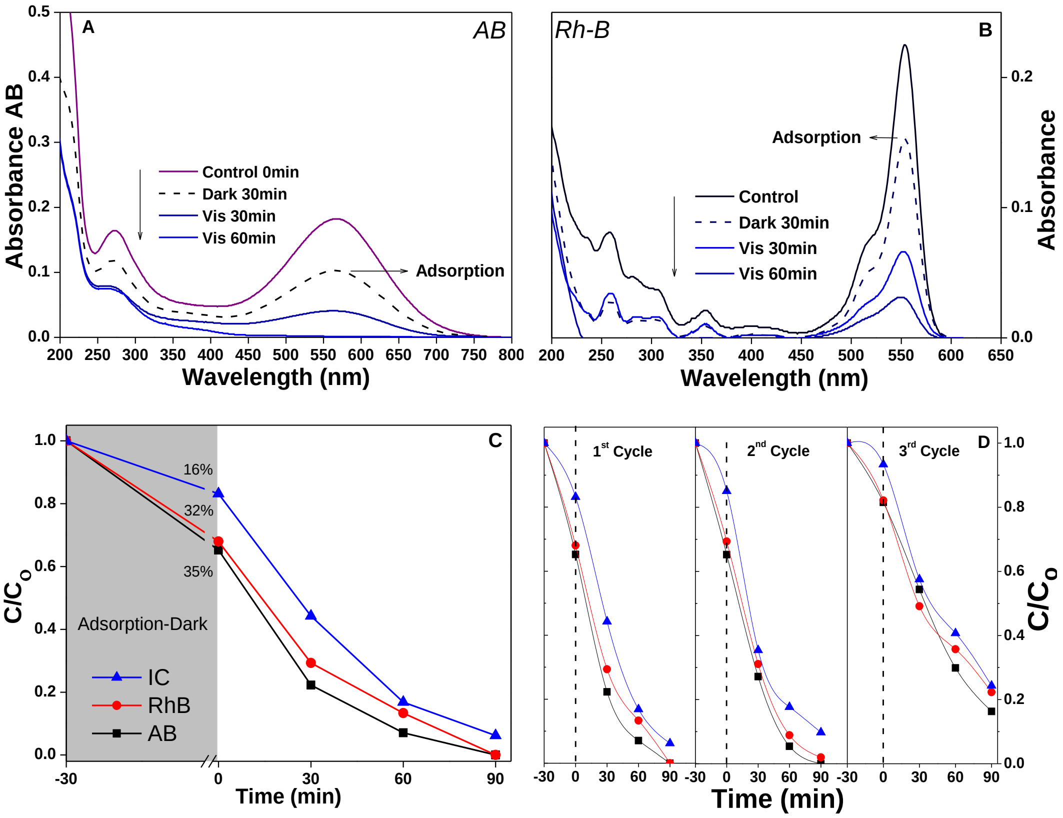

Fig. 5.6 A) Absorbance spectrum vs different irradiation time with deposited silica A) Acid Blue 113 (*AB*), B) Rhodamine-B (*RhB*), C) relative C/C_0 vs time for all dyes with deposited silica and D) cyclic stability of deposited silica.

5.3.2.3 TOC analysis

To analyze, if the β-Bi_2O_3 deposited films are also able to mineralize the secondary intermediate formed after initial degradation of each dye; TOC analysis of irradiated dye solutions was performed. It was summarized in earlier chapters, that degradation and mineralization of dyes are not simultaneous, so it was reasonable to consider TOC analysis after longer irradiation; after 2 and 4 h. Fig. 5.7 shows a substantial decrease in the amount of total organic carbon for all dyes: removal capacity was of 22% for IC, 49% for RhB and 55% for AB dye solutions respectively. Keeping in mind, the high dye adsorption capability on the β-Bi_2O_3 deposited silica substrate (Fig. 5.6C), the apparent decrease in TOC have to be adjusted, in order to compensate the decrease in concentration, not only due to dye molecules degradation but also due to adsorption (referring Fig. 5.6C). Therefore, the realistic contribution associated to mineralization process is estimated as: 6%, 17% and 23% for IC, RhB and AB, respectively. This suggests that β-Bi_2O_3 deposited silica could efficiently mineralize the formed secondary intermediates by RhB and AB dyes, at 4 h exposure. While for IC, again the formed secondary intermediates were not mineralized further due to their high stability and lack of interaction with β-Bi_2O_3 deposited silica.

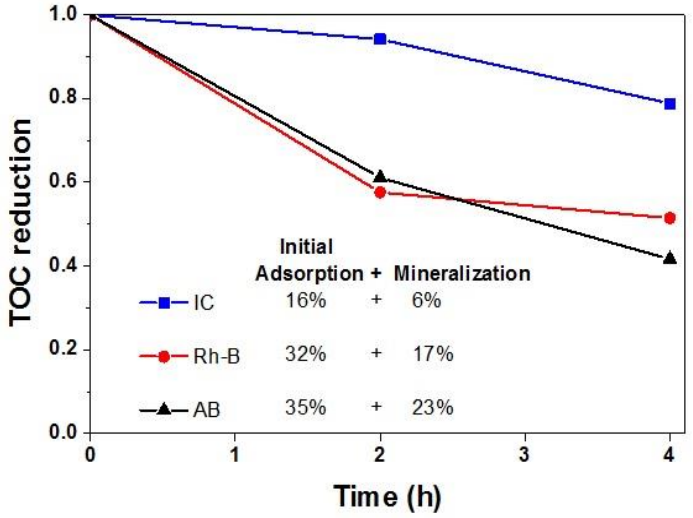

Fig. 5.7 TOC analysis of all dyes solution with deposited silica.

5.3.3 Photocatalytic mechanism for deposited silica

Fig. 5.8 shows the possible mechanism followed during photocatalysis by using β-Bi_2O_3 deposited silica. Enhanced photoactivity is related with the suitable adsorption and improved interaction of the dye with β-Bi_2O_3 films assisted by characteristics of silica. For *IC* dye, attached sulphonic group and hydrogen bonds preferentially interacted with deposited silica, where the activated reactive species attacked the indigoid group and decomposed into isatin sulfonic acid and 2-amine-5-sulfo-benzoic acid secondary products [101, 121, 233]. For *AB* azo-dye, the adsorption linked sites were preferentially the sulphonic groups, but improved adsorption than *IC* dye was associated to electrostatic attraction on deprotonated β-Bi_2O_3 films due to their neutralization by sulphonic groups of *AB*. Another significant influence could be linked to negative charge of silica [148, 231, 234, 235]. that could have repelled the sulphonic groups (negatively charge) of *AB* dye and subsequently moved them towards β-Bi_2O_3 films. All these combined effects allowed high interaction of AB dye with the originated reactive species ($^{-}O_2\cdot$ and $^{-}OH\cdot$) for efficient degradation. For cationic *RhB* dye, improved degradation rate is also related to its better interaction with the β-Bi_2O_3 due to suitable adsorption: primarily due to the presence of diethyloamine groups (positively charged) in *RhB* molecular chain, attracted by negatively charge silica at one end, while on the other hand negatively charged carboxylic group was pushed/repelled by silica towards β-Bi_2O_3 films. As already stated in earlier chapters and reported in many studies, that photodegradation of *RhB* originates several intermediates due to hypsochromic shifts that could be observed in the UV-vis absorbance spectrum and mainly occurred when photocatalytic process assisted with sensitization of *RhB* [47]. However, here again *RhB* photodegradation occurred without formation of secondary intermediates in case of β-Bi_2O_3 deposited films; alike to previously reported results while using α/β-Bi_2O_3 and α-Bi_2O_3 by various groups [16, 101].

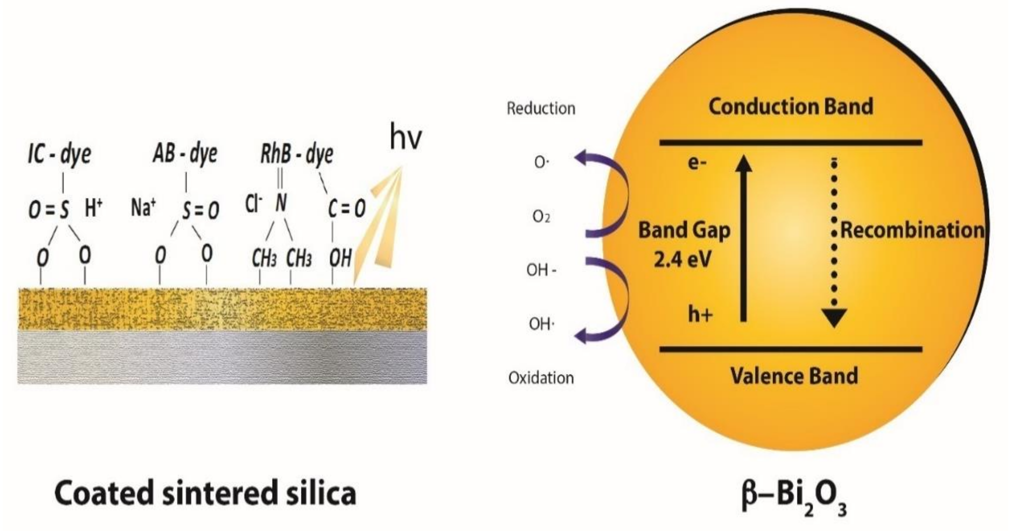

Fig. 5.8 Photocatalytic mechanism: adsorption and photodegradation of all dyes.

5.4 Conclusion

The β-Bi_2O_3 films were immobilized over glass, steel mesh and sintered silica through a facile and economical pneumatic spray pyrolysis method by using bismuth acetate as a precursor. XRD patterns suggested that crystalline structure of the obtained films was tetragonal β-Bi_2O_3, moreover the UV-Vis DRS spectra exhibited the broad absorption edge in visible region with an estimated energy band gap of 2.4 eV, that could facilitate for effective activation in visible light. Furthermore, FESEM images displayed significantly different morphologies of obtained β-Bi_2O_3 films for each substrate: random and non-compact microparticles with regular distribution on glass due to quick evaporation of sprayed droplets, compact microparticles on mesh due to geometry and appearance of tiny channels of the mesh and overlaid sheets deposited on silica due to difference in adhesion behavior and slow evaporation of sprayed droplets; influenced by the characteristics of silica such as uneven porosity, roughness and hydrophilicity of silica. EDS elemental mapping revealed regular distribution of β-Bi_2O_3 particles on each substrates surface. The best and competitive photocatalytic response in degradation of IC dye under visible light was found with β-Bi_2O_3 deposited silica, detected after relating the kinetic rate of photodegradation with deposited mesh and glass. Efficiency of β-Bi_2O_3 deposited silica was related to rough, uneven and porous nature of silica and cavities within the overlaid β-Bi_2O_3 sheets, that helped in providing high interaction with dye molecules for efficient photoactivity. Kinetic rate and mineralization capability was higher in case of *AB* and *RhB* dyes than *IC* dye, due to good interaction with β-Bi_2O_3 deposited silica. In case of *AB* the high interaction is facilitated by electrostatic attraction towards β-Bi_2O_3 films linked to branched sulphonic groups, though in case of RhB dye principally because of positively charged diethyloamine groups in the chemical structure that preferentially have attracted towards deprotonated β-Bi_2O_3 films and silica, and seized for photoactivity. Photocatalytic activity evaluation of these dyes suggested that interaction of dye molecules with bismuth oxide is mediated by the functional and branched groups in the molecular structure, moreover porosity and roughness of the selected substrate played vital role in sustaining the interaction of β-Bi_2O_3 films with dye molecule for competitive photoactivity. Finally, the efficacy of β-Bi_2O_3 deposited silica in frequent cycles for photodegradation of these dyes confirmed that the sintered silica could be suitable option as a fixed support and further application in heterogeneous photocatalysis with an advantage of achieving enhance degradation efficiency, without the cost of separation, filtration and reuse of photocatalyst.

Chapter 6

$BiFeO_3$ and $Bi_2Fe_4O_9/Fe_2O_3/BiFeO_3$ ferromagnetic heterostructures and their role in visible light driven photocatalysis for organic dyes degradation and O_2 evolution

6.1 Introduction

As stated earlier, among various obstacles for bringing heterogeneous photocatalysis into real application, principal challenge is the availability of photocatalyst for repeated cycles *i.e.* effective recovery or separation of photocatalyst from already treated bulk solution. To reuse the photocatalyst for consecutive cycles micro/nano-particles are needed to recover and filtered, which increased the operational costs of water treatment. Nevertheless, the use of immobilized or fixed supports are better alternative to slurry based, but overall, the photocatalytic activity was lower than the bare powder, because of low dispersion, reduced transparency for irradiated light and less mass transfer between fixed photocatalyst and pollutants. Therefore, supported photocatalysts are still in contest for the progress of alternative non-slurry based systems. Moreover, many researchers have revealed magnetized photocatalytic materials with the ability to separate them from the aqueous phase using external magnetic field. Widely known are single phase ferromagnetic $BiFeO_3$ and others composite materials like Fe_2O_3/TiO_2, Fe_2O_3/ZnO, γ-$Fe_2O_3/SiO_2/TiO_2$, $BiFeO_3/SrTiO_3$, $BiFeO_3/Fe_2O_3$ [28-30, 33, 236-238]. Most of the mentioned magnetized materials have displayed good photolytic activity for various dyes and other pollutants and somehow managed to provide the practical solution of quick recovery from the suspension. Particularly $BiFeO_3$ alone has attracted much attention due to potential applications for novel magnetoelectric devices and is also considered as an important visible-light responsive photocatalyst for degradation of organic pollutants and water splitting due to narrow band gap (~2.2 eV) with exceptional chemical stability compared to other less stable semiconductors like CdS, ZnS. GaS [40]. Considering the utilization of magnetized $BiFeO_3$ for environmental remediation, it is important to control the shape, size and crystal purity. For the preparation of multiferroic micro-/nano-structure with significant features, it is difficult to obtain a single phase multiferroic $BiFeO_3$ without impurity through conventional solid-state and soft chemical routes carried at high sintering temperatures [33]. Currently, extensive efforts were employed to synthesize $BiFeO_3$ considering the determining role of scale, morphology and magnetism. Many studies have reported notable changes in the magnetic, electrical and optical properties by varying morphologies such as nanocubes, nanowires, sub-microspindle, nanotubes [33, 57, 239, 240]. However, to obtain single crystal structure $BiFeO_3$ some parasitic impurities/phases like Fe_2O_3 and $Bi_2Fe_4O_9$ could not be avoided and strongly affected by spatial geometry and structural defects [33, 239, 241, 242]. In spite, many studies demonstrated substantial photocatalytic properties of $BiFeO_3$, but still the performance is lower than that of other visible-light photocatalysts containing bismuth element, such as, Bi_2O_3 [13, 19, 67-71], $BiVO_4$ [62, 63], for the main reasons of electrons and holes recombination due to very narrow band gap and inappropriate optical band position [33, 239, 241, 242]. In order to solve these problem, some researchers focused on the scale and morphology of $BiFeO_3$ *i.e.* microspheres or mesoporous hollow spheres and highly exposed facets of $BiFeO_3$ pills or rods with high surface area could achieve high photocatalytic performance [16, 19, 54, 56, 70, 87-92]. On the other hand, some researchers have investigated that pure/single phase $BiFeO_3$ is antiferromagnetic or having very low saturated magnetization at room temperature (around 0.05mB Fe^{-1}) [33], that was wrongly interpreted in many studies, that have reported single phase $BiFeO_3$ as ferromagnetic and it has been revealed that presence of small impurities such as: Fe_2O_3 and $Bi_2Fe_4O_9$ in $BiFeO_3$ structure was responsible for the high magnetic saturation [243]. Finally, it has been summarized and confirmed that pure $BiFeO_3$ possess very low magnetism, which is too small to allow separation in the aqueous phase [33] [243]. However, in the conflict that pure $BiFeO_3$ is ferromagnetic or not, the additional effect due to presence of either Fe_2O_3 or $Bi_2Fe_4O_9$ on photocatalytic performance have been rarely investigated. Therefore, to examine that besides increasing magnetic field if presence of Fe_2O_3 and $Bi_2Fe_4O_9$ could influence photocatalytic performance, current study was aimed to evaluate single phase $BiFeO_3$ and $Bi_2Fe_4O_9/Fe_2O_3/BiFeO_3$ ferromagnetic heterostructures, for degradation of cationic Rhodamine-B (RhB), anionic Indigo Carmine (IC) and Acid Blue 113 (AB). Moreover, both single phase $BiFeO_3$ and $Bi_2Fe_4O_9/Fe_2O_3/BiFeO_3$ were also evaluated for photocatalytic water splitting to evolve O_2, in relation to the presence of $Bi_2Fe_4O_9/Fe_2O_3$.

6.2 Experimental

6.2.1 Synthesis

Precursor salts bismuth nitrate-pentahydrate ($Bi(NO_3)_3{:}5H_2O$), iron nitrate-nonahydrate ($Fe(NO_3)_3{:}9H_2O$) and reagent poly ethylene glycol (PEG) were obtained from Sigma Aldrich and were used without any modification. Typically, 1 mmol of ($Bi(NO_3)_3{:}5H_2O$) was initially dissolved in 100 ml of 0.5 M HNO_3 solution and continuously stirred until crystal clear solution was achieved, then after 1mmol of ($Fe(NO_3)_3{:}9H_2O$) was added and stirring remained continue to obtain the clear solution. The obtained solution was divided in three flasks. In one flask, 0.5ml of PEG was slowly added and continuously stirred, while in second flasks after addition of PEG, 5 ml of NaOH (0.5 M) was added, while in the third flask synthesis was followed without any additives or reagents. All precursor solution in flasks were continuously stirred on hot plate at fixed temperature of 60 °C, until thick reddish-brown Sol-Gel was obtained. The obtained thick gels were placed in the furnace and initially heated up to 300 °C for 30 min and final calcination was followed at 500 °C for 1 hr. After calcination obtained powders were first rinsed in ethanol then in water, centrifuged and finally dried at 60 °C in an oven for 5 hr. The obtained samples were labelled as: BFO-SG for one without any reagents and NaOH, BFO-P: in which only PEG was added and BFO-PN: contained both PEG and NaOH in precursor solution.

6.2.2 Characterization

Morphology of the as-calcined powders was investigated by means of a MERLIN ZEISS field-emission scanning electron microscopy (FE-SEM) with a high-resolution. The calcined powders were analyzed by means of X-ray diffraction (XRD), to investigate both crystalline structure and phases composition. UV−Vis diffuse reflectance spectra were recorded by using Varian Cary 500 spectrophotometer. Tauc plots of the Kubelka Munk function were used to calculate the energy band gap (E_g) value. Specific surface area was measured by means of N_2 sorption at 77 K on a Micromeritics Tristar-II Brunauer−Emmett−Teller (BET) instrument. The magnetic measurements were taken by a vibrating sample magnetometer (VSM) at room temperature, all curves were normalized to nanoparticles mass to make an easier comparison among samples. Furthermore Magnetization vs. temperature measurements were also performed on both samples starting from 25 °C until 700 °C. XPS analysis was done for the estimation of valence band maximum (VBM), which were further used along with estimated E_g to determine the bands positions of all samples.

6.2.3 Photocatalysis

In order to evaluate the photocatalytic response of the synthesized samples, the degradation of cationic Rhodamine B (RhB), anionic Indigo Carmine (IC) and Acid Blue 113 were evaluated. Initially, 40 mg of each photocatalyst powder were added in 50 ml of IC solution, at a concentration of 10 mg/l and at neutral ph; obtained slurry was initially stirred in dark for 30 min. Then, the dispersions were irradiated with white fluorescent lamp of 9 watt; at a very small irradiance of 33 W/m^2. Furthermore, the best photocatalyst chosen after evaluation of IC dye, was investigated for photodegradation of RhB (at neutral pH) and AB (at pH 9.5, to control the intense adsorption rate) dyes at concentrations of 5 and 10 mg/l, respectively, to analyze the suitability and rate of kinetics in dealing multiple dyes of different characteristics. Total organic carbon (TOC) analysis was carried out using a Shimadzu TOC-L analyzer with a high sensibility column.

To evaluate the potential of single phase $BiFeO_3$ and its heterostructures for photocatalytic water oxidation, experiments were performed with each photocatalyst in the presence of an electron scavenger. For water oxidation experiment, a device explained earlier in chapter-2 was used under similar conditions.

6.3 Results and Discussion

6.3.1 Crystalline Structure

Fig. 6.1 displays XRD patterns of all the obtained samples after calcination. It can be observed that, when the gel-drying and subsequent calcination was followed without PEG and NaOH then a heterostructure of $Bi_2Fe_4O_9$/α-Fe_2O_3/$BiFeO_3$ is obtained, in which $Bi_2Fe_4O_9$ dominates with a high proportion of 78% and revealed that without addition of chemical reagent the formation of single structure $BiFeO_3$ could not be guaranteed; because at the time of pre drying of gel at 300 °C, the formation of stochiometric compounds like $Bi_2Fe_4O_9$ and $Bi_{25}FeO_{40}$ and parasitic α-Fe_2O_3 could not be ensured without any shape modifiers reagents such as, PEG, citric or tartaric acid and anion inhibitors like NaOH [94, 244-246].

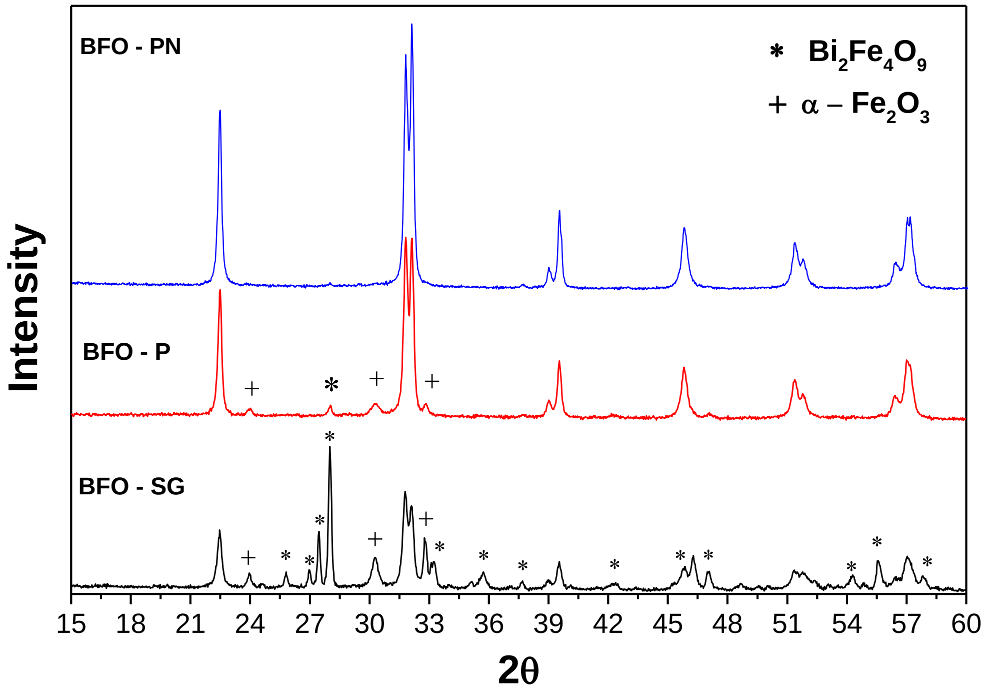

Fig. 6.1 XRD patterns of all calcined samples. Non-labelled peaks are associated to $BiFeO_3$.

For the sample BFO-P, in which only PEG wad added in the precursor solution, somehow formation of $BiFeO_3$ is controlled, but the appearance of very small impurities of $Bi_2Fe_4O_9$ could not be avoided. However, for this sample $BiFeO_3$ is in higher proportion in the heterostructure up to 90%, with commonly known facets of (104), (110) and with principle peaks at 31.75° and 32°, however the previously dominated structures of $Bi_2Fe_4O_9$ and α-Fe_2O_3 still can be observed in the normal spectra. It is worth to mention that some studies have suggested that very small presence of $Bi_2Fe_4O_9$ and α-Fe_2O_3, could not be avoided during the solgel synthesis and sometime is hard to detect by XRD or present in very small intensity and has been ignored by many researchers; however, an additional step of leaching/washing with low concentrated HNO_3 can be used to remove $Bi_2Fe_4O_9$ and α-Fe_2O_3 from the $BiFeO_3$ structure [243]. For sample BFO-PN (contained PEG and NaOH), XRD patterns ascribed to single $BiFeO_3$ structure, revealing that ionic inhibition by NaOH [247], have not allowed or limited the formation of $Bi_2Fe_4O_9$ and Fe_2O_3. The average grain sizes were calculated by considering the most intense principle peak of each sample by using the Scherrer's equation [33] and are 63 nm, 52 nm and 48 nm for the BFO-SG, BFO-P and BFO-PN samples, respectively; given in Table. 6.1.

Table. 6.1 Calculated physical-chemical properties and photocatalytic results of the synthesized samples.

Sample	Crystalline Phase(s) and Phase %	Avg. Particle Size (nm)	Magnetic Saturation (emu/g)	Energy Band Gap (eV)	Specific Surface Area (m^2/g)	K_{app} (10^{-2} min^{-1})	TOC removal (%)
BFO-SG	**$BiFeO_3$-14** **$Bi_2Fe_4O_9$-78** **α-Fe_2O_3-8**	63	0.1	1.92	12	IC: 0.2	
BFO-P	**$BiFeO_3$-90** **$Bi_2Fe_4O_9$-4 α-Fe_2O_3-6**	52	9.8	1.97	7.5	IC: 1 AB: 1.3 RhB: 1.7	26% 31% 48%
BFO-PN	**$BiFeO_3$**	48	0.05	2.05	15.2	IC: 0.16	

6.3.2 Morphology

Morphology of all the calcined samples are shown in Fig. 6.2A-C and Fig. 6.2D-F, at 200 and 100nm scales, respectively. Significant difference in the morphological structure can be observed for all samples. Sample BFO-SG (Fig. 6.2A and D) exhibited microplates of different length and width, but of average thickness around 20nm; reported as the typical structure of $Bi_2Fe_4O_9$ [248-251], and is in accordance with the XRD results, which revealed a high proportion of $Bi_2Fe_4O_9$ in that sample. At a higher magnification (see Fig. 6.2D) a porous surface of these plates and an irregular ordering are evidenced. For the BFO-P sample (Fig. 6.2B and E), the morphological structure is made of spheroids and microplates. These spheroids (formed by nano grains) could be associated to the morphological structure of $BiFeO_3$. In addition, a wide distribution of microplates suggests a considerable presence of $Bi_2Fe_4O_9$ in this sample that, however, polymerize and assembled vertically in a regular manner due to the addition of PEG. The BFO-PN sample showed a significantly different morphology of interconnected nanocubes, which are identical to previously reported $BiFeO_3$ structures [252, 253]. The obtained single and well-ordered $BiFeO_3$ nanostructure in this sample demonstrated that the addition of NaOH provided ionic inhibition [247] and avoided the formation of intermediate compounds: $Bi_2Fe_4O_9$ and α-Fe_2O_3. Moreover, obtained values for specific surface area given in Table. 6.1, higher in case of BFO-PN sample, suggested an improvement in the surface area due to decrease in the particle size and well-ordered morphology of nanocubes.

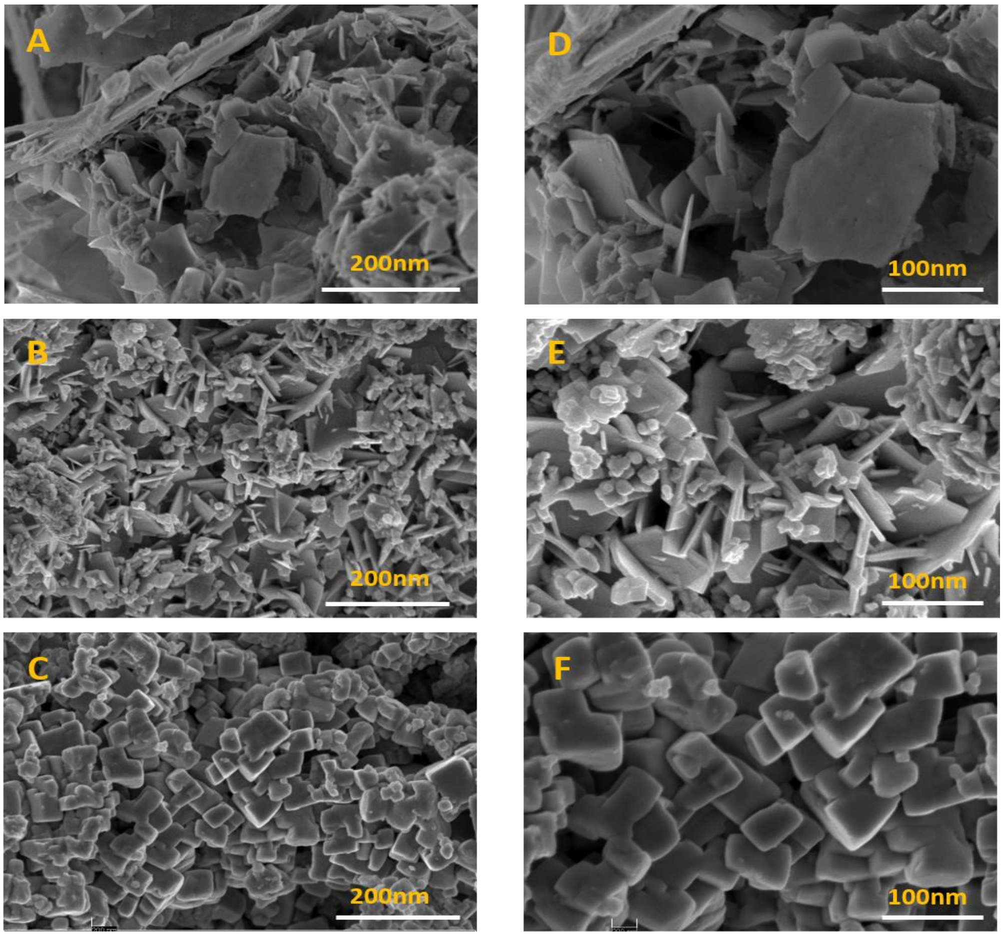

Fig. 6.2 FESEM images of the calcined samples: A) BFO-SG, B) BFO-P, C) BFO-PN at 200 nm scale, D-F) at 100nm scale, respectively.

6.3.3 Magnetization

Fig. 6.3A shows the room temperature magnetic hysteresis (M–H) loops for all the calcined samples with a magnetic field up to 15 kOe. For samples BFO-SG and BFO-PN the magnetic signal is very low compared to the M-H loop observed in sample BFO-P. Therefore, a separate plot is shown for BFO-SG and BFO-PN in Fig. 6.3B, revealing that both samples (the one with high content of $Bi_2Fe_4O_9$ and the other containing the single $BiFeO_3$ phase) exhibit a non-saturating magnetism, with high-field magnetization (M_{HF}) of about 0.12 and 0.05 emu g^{-1}, respectively; as reported in Table. 6.1.

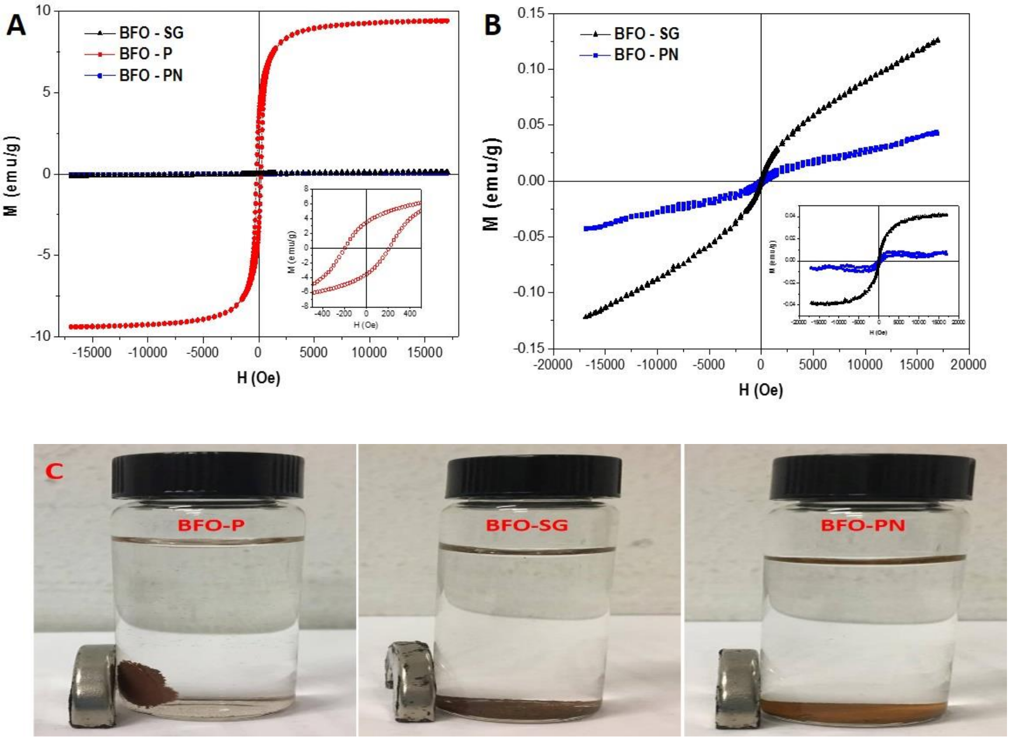

Fig. 6.3 A-B) Magnetization at normal temperature for all samples and C) digital images of the water, showing magnetization of synthesized powder in presence of magnet.

Almost identical values of M_{HF} have been reported for both $Bi_2Fe_4O_9$/ $BiFeO_3$ heterostructures and single phase $BiFeO_3$ [33, 239, 241, 242]. Moreover, it is also mentioned in many studies that the magnetic behavior of these compounds is strongly dependent on size, crystal facets and morphology. To have a sufficiently high M_{HF}, a particle size lower than 57nm, well-ordered (001) and (111) facets and a regular morphology are needed [33, 239, 241, 242]. The high M_s (of about 9.8 emu g^{-1}) in BFO-P sample is mainly due to the presence of α-Fe_2O_3, which is alike to other reported cases of $BiFeO_3$/α-Fe_2O_3 heterostructures. This means that magnetism in $BiFeO_3$ is dominated by the Fe_2O_3 presence. However, the BFO-SG sample that also contains some α-Fe_2O_3 clearly shows a non-saturating behavior, indicating an antiferromagnetic contribution that is stronger in this sample than in the BFO-P, one for which the ferromagnetic phase is dominating and possibly responsible for the sigmoidal shape of the loop. The inset in Fig. 6.3B shows the M(H) curves after subtraction of the antiferromagnetic signal; a weak ferromagnetic signal is indeed observed in sample BFO-SG, while the subtracted signal of sample BFO-PN is virtually zero. Finally, the separation ability of each sample by effect of an applied magnetic field was investigated in water by putting a small permanent magnet near the glass vial. The digital image shown in Fig. 6.3C confirmed that the BFO-P sample (left) can be magnetically separated from solution more easily than the other samples: BFO-SG (center) and BFO-PN (right).

6.3.4 Optical Properties

The obtained optical absorption spectra of all the samples are shown in Fig. 6.5. All samples have displayed wide visible light spectrum, which is correlated to most of the reported UV-Vis spectra of materials includes single phase $BiFeO_3$ and its heterostructures. Sun *et. al.* [254], wang *et. al.* [255, 256] Zhang *et. al.* [242] and *Ryan et. al*. [257] have stated that, there are two typical absorption edges for $Bi_2Fe_4O_9$, one in the region in between 600-632 nm, while another at around 800-820 nm, moreover edge at 600 nm can be ascribed to electronic transitions from valence band to conduction band and the edge at 800 nm is related to the d-d transitions of Fe [33]. In case of $BiFeO_3$ It is also reported by Zhang *et. al.* [242] that pure single phase $BiFeO_3$ nanofibers have photoabsorption at 576 nm and estimated band gap value 2.15 eV, while for pure $Bi_2Fe_4O_9$, an photoabsorption edge at ~632 nm links to an optical band gap of 1.96 eV; their reported results are given in Fig. 6.4(a) and (b) [242]. For α-Fe_2O_3, Guo *et. al* [33] and Mallick *et. al.* [258] have suggested that, out of its three divided optical zones: in 250-300 nm, 400-600 nm and 600-800 nm regions, electronic transition of α-Fe_2O_3 could be assigned in the range 580–620 nm. In the present case, the BFO-SG and BFO-P samples, *i.e.* heterostructures of $BiFeO_3/Fe_2O_3/Bi_2Fe_4O_9$, the contribution of each compound is evident in the UV-Vis spectra (see Fig. 6.5). For all samples, absorption edges displayed a minimum at around 750 nm, which is less marked as the purity of $BiFeO_3$ increases. In fact, in the BFO-SG sample, the optical absorption plateau of $Bi_2Fe_4O_9$ is stretched from 700 nm until 750 can be clearly observed (exhibiting a wide contribution of $Bi_2Fe_4O_9$), along with an additional transition from 550 nm to 580 nm related to the contribution of α-Fe_2O_3 and $BiFeO_3$. This could be further confirmed for the BFO-P and BFO-PN samples, where the absorptions shifted towards left *i.e.* in the region 580-700 nm, due to increase in the proportion of $BiFeO_3$.

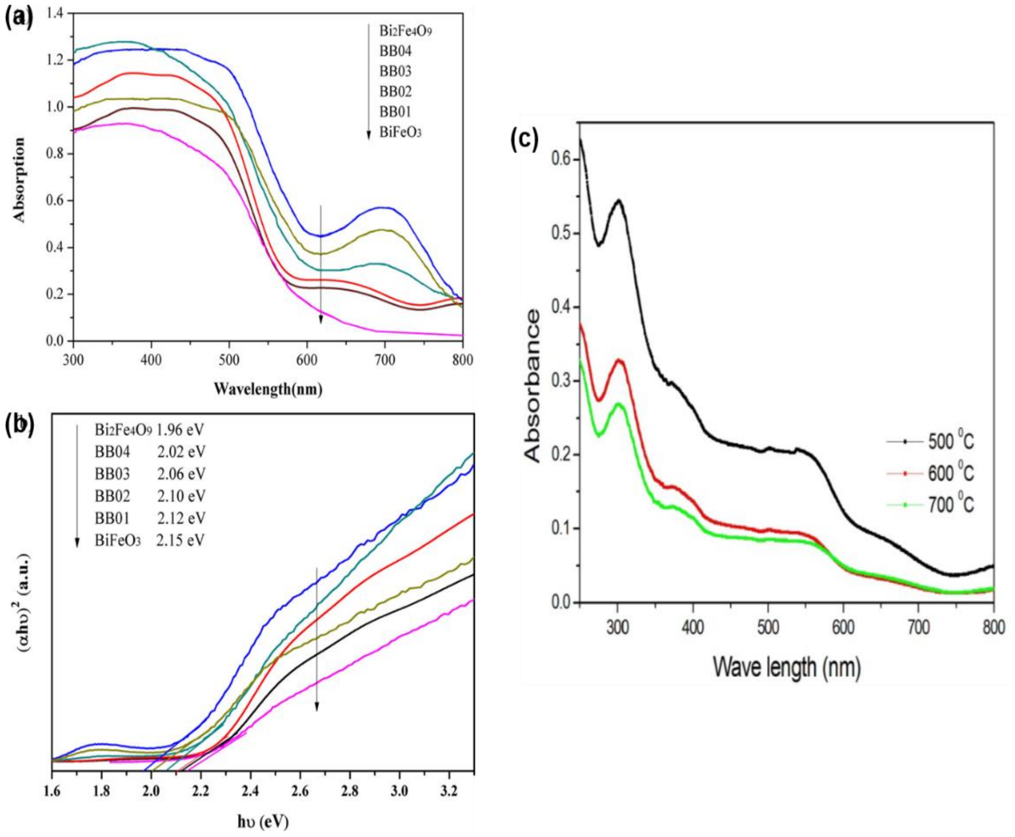

Fig. 6.4 a) Reported UV-vis DRS results for Single phase $BiFeO_3$ and $Bi_2Fe_4O_9$ and their heterostructure, b) their estimated band gap [242] and c) reported DRS for single phase α-Fe_2O_3 at different annealing temperatures [258].

Moreover, for single $BiFeO_3$ (BFO-PN), decreased absorbance in the region 600-750 nm, revealing negligible presence of $Bi_2Fe_4O_9$ and α-Fe_2O_3 (indicated in Fig. 6.5). The estimated band gap values are given in Table. 6.1 (tauc plots in inset of Fig. 6.5), *i.e.* 1.92, 1.97 and 2.05 eV, for samples BFO-SG, BFO-P and BFO-PN, respectively, and evidence an increased visible light absorption on the heterostructured samples due to the presence of $Bi_2Fe_4O_9$ and α-Fe_2O_3 in conjunction with $BiFeO_3$.

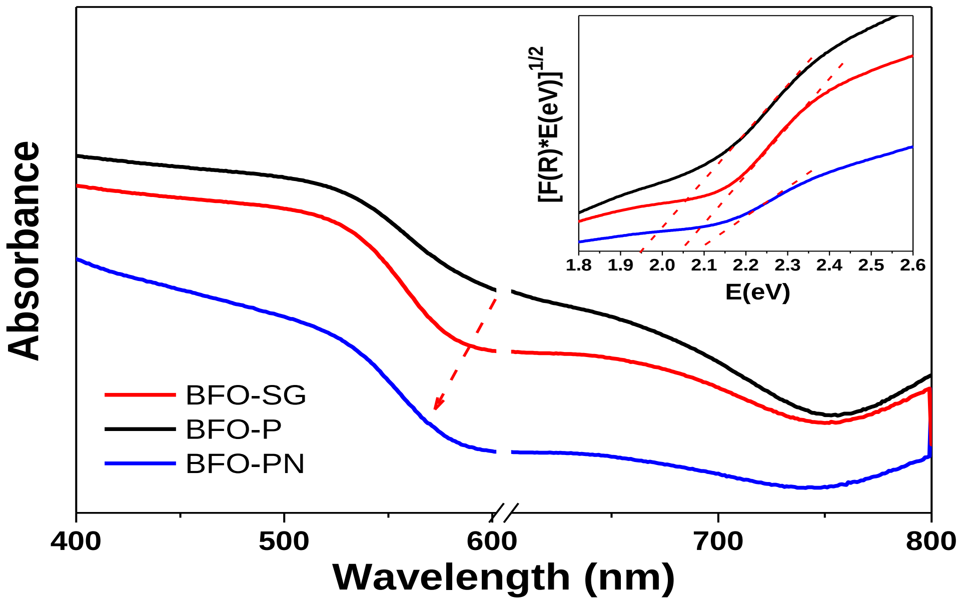

Fig. 6.5 UV-Vis DRS for all the synthesized samples and inset showing Tauc plots and estimated energy band gap.

6.3.5 Band edges positions

The VBM values for the three samples were determined by finding the intersection of a regression line that spans the linear portion of the X-ray photoelectron valence band leading edge with the background between the valence band maximum and the Fermi energy level (which corresponds to 0 eV in the binding energy axes) [259]. By means of CasaXPS software, a “step-down” background function was used to obtain the intersection between the linear fit of the descending edge of the VB and the linear fit of the background signal. Since the VBM positions are sensitive to the choice of points of the regions chosen to calculate the step-down function, at least three sets of points were selected for each sample to perform the fitting procedure. The average uncertainty has been found to be lower than 0.05 eV. The obtained VBM values are: 0.91 eV, 0.69 eV and 0.30 eV for BFO-SG, BFO-P and BFO-PN, respectively (see Fig. 6.6A). The decrease in the VBM could be associated to the increase in the purity of $BiFeO_3$. These VBM values and estimated energy band gaps (inset Fig. 6.5) were used to draw the edges of the bands with respect to Fermi energy level (E_F) [115], shown in Fig. 6.6B. Thus, the edges of the CB and VB of the single $BiFeO_3$ are higher in energy than those of the BFO-SG sample (with highest proportion of $Bi_2Fe_4O_9$). Therefore, a charge carrier separation in the heterostructure is expected due to difference in the alignments of the CB and VB thresholds, since the position of single $BiFeO_3$ is slightly higher than $Bi_2Fe_4O_9$ presents in the BFO-SG heterostructure (see Fig. 6.6B). Moreover, the change in CB and VB edges and increase in $BiFeO_3$ have increased the reduction potential of BFO-P and BFO-PN samples. However, the role of α-Fe_2O_3 in varying band position is not clearly defined, due to suppression either by $Bi_2Fe_4O_9$ or by $BiFeO_3$ in both BFO-SG and BFO-PN samples. Though, the difference in the VBM values of sample BFO-SG and BFO-P in comparison to BFO-PN sample, and previously indicated optical transition of α-Fe_2O_3, *i.e.* in the range of 580–620 nm (Fig. 6.5), suggest that like $Bi_2Fe_4O_9$ CB and VB band edges of α-Fe_2O_3 also could have a lower energy position than $BiFeO_3$ and have jointly contributed to the band structure obtained for both heterostructures. Nevertheless, the difference in the bands in the heterostructure, could mitigate the electron and holes separation and could influence the photocatalytic behavior [33, 101, 260-264].

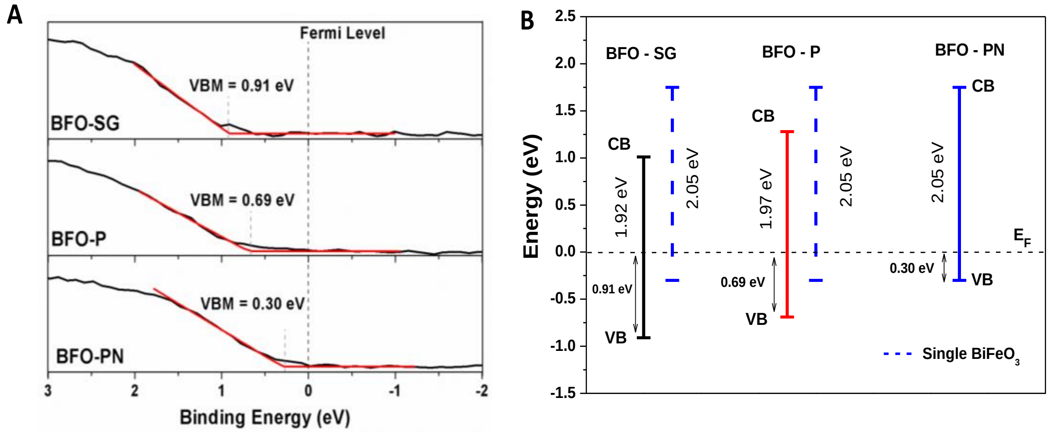

Fig. 6.6 A) XPS Valence band spectra of all samples. The valence band maximum (VBM) values have been determined by linear extrapolation of the leading edge to the base line. B) Band structures, determined after using estimated VBM and Eg.

6.3.5 Photocatalysis

6.3.5.1 Dyes photodegradation

To analyze the photocatalytic response of all samples, initially anionic Indigo Carmine (*IC*) dye solution was analyzed, because in earlier chapters it was observed that *IC* dye has the distinguish feature to observe the UV-Vis absorption spectral changes permitted by photocatalysis process. *IC* dye solution at a concentration of 10 mg/l was kept under dark in presence of each photocatalyst for 30min. Then after, dye solution was irradiated using white fluorescent lamp to observe the photoactivity.

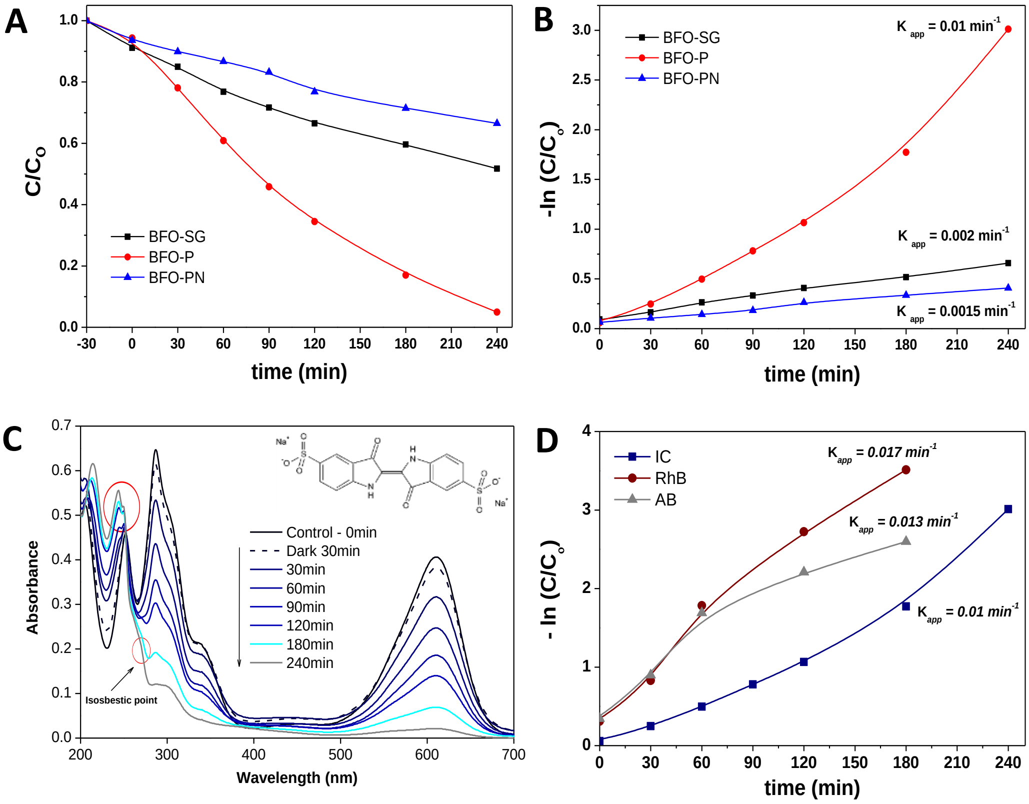

Fig. 6.7 Relative concentration A), kinetic curves B) and degradation absorption spectrum of IC C) for all BFO samples. D) kinetic curves of IC in comparison to other dyes; RhB and AB.

Fig. 6.7A shows relative concentration (C/C$_o$) with respect to time in dark and under irradiation, the noted adsorption for all sample is around 7%, as IC dye hardly adsorbed on any sample, which is in correlation with previously stated observation in earlier chapters. Furthermore, under irradiation, single phase $BiFeO_3$ hardly shows photocatalytic response for the degradation of IC. Earlier it has been revealed that single phase $BiFeO_3$ has the poor photocatalytic activity due to electrons and holes recombination, because of vary narrow energy band gap *i.e.* 2.1-2.2 eV [33, 239, 241, 242]. Some studies have suggested that the activity of $BiFeO_3$ could be improved either by tuning the structures with the addition of either Fe_2O_3 or $Bi_2Fe_4O_9$ within its lattice, or by adding H_2O_2 in the dye solution that could allow capturing of holes to avoid their recombination with excited electrons on $BiFeO_3$ surface [33]. On the other hand, other two samples with heterostructures of $BiFeO_3/Bi_2Fe_4O_9/\alpha\text{-}Fe_2O_3$ have shown higher photocatalytic response than synthesized single phase $BiFeO_3$. The best response obtained with sample BFO-P could be due to the optimum proportion of $Bi_2Fe_4O_9$ and $\alpha\text{-}Fe_2O_3$ in the heterostructure, which combines a low band gap (2.05 eV, hence exploiting the photon flux in the best way) to a reduced electron-hole recombination rate due to efficient charge separation. Analyzing the photodegradation curves with a pseudo 1^{st} order equation (Fig. 6.7B) it was found that the apparent kinetic rates (K_{app}) of BFO-P, BFO-PN and BFO-SG were 1, 0.2 and 0.16 x 10^{-2} min^{-1} (given in Table. 6.1), respectively, i.e. BFO-P value was more than 5 times higher than the others. The achieved K_{app} is higher than the previously reported single $BiFeO_3$ and $Bi_2Fe_4O_9$ [242, 248] and $BiFeO_3/Fe_2O_3$ [33], revealing that $BiFeO_3/Fe_2O_3/Bi_2Fe_4O_9$ heterostructure allowed better charge separation and transfer within interfaces of each material. The time-course degradation absorbance spectra of IC dye solution in case of BFO-P shown in Fig. 6.7C, in which appeared spectral changes at longer exposure revealed that the removal of IC dyes followed photodegradation. The originated increase in absorbance (encircled at 218 nm) and appearance of isosbestic point at 251 nm, reaffirm the phenomena of formation of secondary intermediates (as isatin sulfonic acid and 2-amine-5-sulfo-benzoic acid), in accordance to the stated results in previous chapters and in correlation to previous studies [101, 121, 233]. Moreover, the total organic carbon (TOC) analysis have shown a decrease of 33% in 4 h, from the actual value, which suggests that overall 26% IC dye underwent for mineralization (after removing the contribution of adsorption).

Following the discussion made in earlier chapters, that different dyes have different behavior of interaction with photocatalysts, therefore here sample BFO-P was evaluated for the degradation of another anionic dye AB and cationic RhB, to record any change in kinetic rate, adsorption and degradation behavior in comparison to IC dye. Fig. 6.7D depicting the obtained degradation kinetics and K_{app} for AB and RhB dyes in comparison to IC. The obtained K_{app} dramatically increased for both dyes than IC; determined as 1.3 and 1.7 x 10^{-2} min^{-1} for AB and RhB, respectively; higher than 1.7 x 10^{-2} min^{-1} in case of IC. The improved kinetics for these dyes is strongly related to the improved interaction of the dye molecule with the $BiFeO_3/Bi_2Fe_4O_9/\alpha\text{-}Fe_2O_3$, permitted by the rate of adsorption of dye molecules. In addition, improved interaction (by means of adsorption over $BiFeO_3/Bi_2Fe_4O_9/\alpha\text{-}Fe_2O_3$ surface) can be observed in Fig. 6.8A and 8B; associated to the decrease in absorption intensity during dark conditions *i.e.* up to 29% in case of AB and 26% in case of RhB, higher than 7% in case of IC. The high adsorption influenced anionic or cationic groups in the dye structure such as:

sulphonic groups in case of AB and diethyloamine groups in case of RhB, to adequately attract on the $BiFeO_3/Bi_2Fe_4O_9/\alpha\text{-}Fe_2O_3$ surface. Meanwhile this high interaction resulted in higher photoactivity and improved kinetic rate. Moreover, some identified spectral changes (encircled in Fig. 6.8A) at around 260nm in the UV-Vis spectra could be related to the photodegradation process, but their identification is not found in the literature; while TOC analysis revealed 60% decrease in AB dye solution after 3 hours and confirmed that 31% mineralization has occurred in conjunction to 29% of adsorption over the $BiFeO_3/Bi_2Fe_4O_9/\alpha\text{-}Fe_2O_3$ surface. In case of RhB, here again no hypsochromic shift or any spectral changes in the UV-vis spectrum were observed, reaffirming that degradation of RhB followed without any intermediate(s) formation with an overall decrease of 74% in TOC; 48% related to mineralization and other 26% to the adsorption over $BiFeO_3/Bi_2Fe_4O_9/\alpha\text{-}Fe_2O_3$ surface.

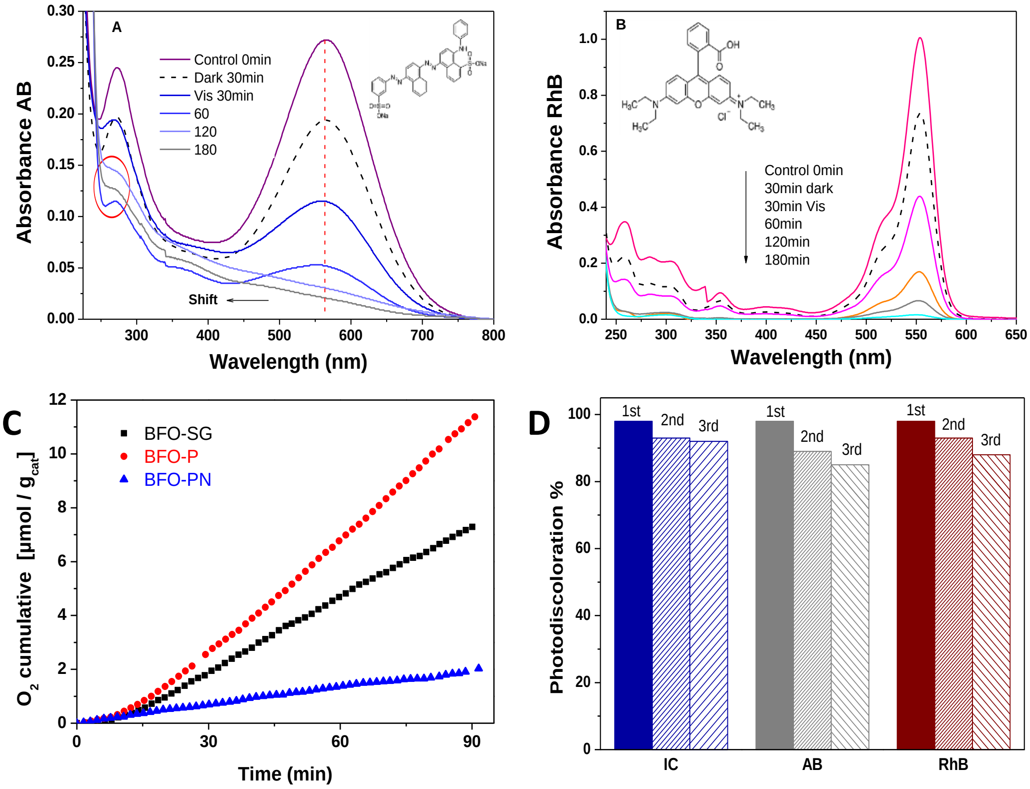

Fig. 6.8 Photodegradation absorbance spectrum, A) AB and B) RhB with BFO-P sample; evolved cumulative O_2 for all BFO samples and D) performance of BFO-P sample for each dye up to 3 cycles.

6.3.5.2 Evolution of O2

Some studies have proposed $BiFeO_3$ as the potential visible active material for water splitting [57]. Therefore, water oxidation tests were performed under visible light for all samples, to confirm: i) water splitting capability of single phase $BiFeO_3$ and its heterostructures and ii) the charge separation of h^+ (responsible of the formation of OH radicals) from the free e^-, during photocatalysis. Obtained results shown in Fig. 6.8C, evidenced O_2 evolution ability of each sample, but the evolved O_2 rate was higher in case of BFO-P sample than BFO-SG and BFO-PN. This confirmed the earlier stated hypothesis of having optimum $Bi_2Fe_4O_9/\alpha\text{-}Fe_2O_3$ proportion in the BFO-P heterostructure. During O_2 evolution the lowest rate in case of single phase $BiFeO_3$ could be related to the similar problem of e^- and h^+ recombination.

Finally, to conclude the study, sample BFO-P, magnetically separated after each test and repeatedly evaluated up to 3 cycles to confirm its suitability and performance for consecutive cycles for all three dyes. Results shown in Fig. 6.8D revealed that $BiFeO_3/Bi_2Fe_4O_9/\alpha\text{-}Fe_2O_3$ is stable enough to treat dye solution like IC at the same performance up to 3 cycles, due to its low adsorption and prolong availability of photoactive sites. However, in case of RhB and AB dyes, a little decrease in performance in third cycle is strongly due to blockage and hindrance caused by the adsorbed dye molecules/intermediates or other residues, but almost identical performance (in case of dyes with high adsorption capacity) could be ensured by recharging the $BiFeO_3/Bi_2Fe_4O_9/\alpha\text{-}Fe_2O_3$ surface by means of washing or low temperature heating, in order to remove the organic residues from surface.

6.3.5.3 Photodegradation mechanism.

Based on the information on CB and VB positions reported in Fig. 6.6A and 6B and the high photoactivity shown by $BiFeO_3/\alpha\text{-}Fe_2O_3/Bi_2Fe_4O_9$ heterostructure, the photodegradation mechanism can be proposed. The strongly interconnected interfaces between $BiFeO_3$ and $\alpha\text{-}Fe_2O_3$, $Bi_2Fe_4O_9$ materials allow photoexcited electrons (e^-) and the holes (h^+) to move within these interfaces; due to slight difference in the CB and VB edges, as was the case of previously reported heterostructures [106, 261, 265], in which simultaneous photoexcitation and transfer of e^- and h^+ within interfaces were suggested. As each material in $BiFeO_3/\alpha\text{-}Fe_2O_3/Bi_2Fe_4O_9$ heterostructure can contribute in providing the photoexcited electrons and holes (due to narrow Eg), therefore can promote efficient oxidation and reduction reactions and provide higher number of reactive species ($O_2^{\bullet -}$ and $OH^{\bullet}$). The attached IC dye is attacked by these reactive species and indigoid group is dissociated into isatin sulfonic acid and 2-amine-5-sulfo-benzoic acid and further mineralized up to 26% at 5 h irradiation [101, 121, 233]. The AB dye was attacked via adsorbed sulphonic groups (SO_3^-) at $BiFeO_3$/α-Fe_2O_3/$Bi_2Fe_4O_9$ surface, where the originated reactive species oxidized and/or reduced AB, to form intermediates like: dibutyl phthalate and phthalic acid and some aliphatic hydrocarbons (based on the identification made by some researchers [177, 178]), which further mineralized up to 31%. While the RhB dye is anchored to the catalyst surface via carboxylic groups, after which it is photodegraded and mineralized up to 48%, without originating secondary intermediates. It is reported in various studies [16, 47, 101, 155] that RhB dye degradation could results some hypsochromic shifts in the UV-Vis absorption spectrum, when the photocatalysis is assisted with dye-sensitization of RhB. However, since in the present case the RhB photodegradation occurred without any hypsochromic shift, it can be assumed that no dye-sensitization process underwent that, together with the visible light activity demonstrated for water oxidation, confirms the visible light activity of the here developed heterostructured photocatalyst.

6.4 Conclusion

Single $BiFeO_3$ and $BiFeO_3$/α-Fe_2O_3/$Bi_2Fe_4O_9$ heterostructures were obtained via simple sol-gel route and subsequent calcination by using PEG as shape modifier and NaOH as ionic inhibitor. XRD analysis revealed that the addition of both PEG and NaOH inhibits the formation of intermediate impurities phases, *i.e.* α-Fe_2O_3 and $Bi_2Fe_4O_9$. The addition of PEG alone allows to obtain a high proportion of $BiFeO_3$ in the heterostructure along with the presence of a low amount of α-Fe_2O_3 and $Bi_2Fe_4O_9$. Further addition of NaOH improved the crystallinity and purity of single $BiFeO_3$. The morphologies displayed significant differences: the BFO-SG sample exhibited large microplates of various lengths; the BFO-P sample was formed by spheroids together with well-ordered microplates; the BFO-PN sample exhibited interconnected nanocubes of single $BiFeO_3$. The specific surface areas increased when decreasing the particle size and increasing the purity of $BiFeO_3$. Magnetic analysis confirmed that a high magnetic saturation is generated by the presence of α-Fe_2O_3 and sample with high proportion of $BiFeO_3$ and $Bi_2Fe_4O_9$ are antiferromagnetic in nature. UV-Vis DRS evidenced a wide absorption spectrum divided in various zones, highlighting the presence of α-Fe_2O_3 and $Bi_2Fe_4O_9$ in the heterostructures, while their absorption spectrum was almost lowered after obtaining single $BiFeO_3$ phase. Valence band maximum and optical analyses together with water oxidation tests demonstrated that the presence of α-Fe_2O_3 and $Bi_2Fe_4O_9$ in optimum proportion can reduce the electron and holes recombination rate, leading to an improved photocatalytic activity of the BFO-P sample. The O_2 evolution capacity of this photocatalyst was the highest among the tested materials. Moreover, an efficient separation of electrons and holes at the surface of $BiFeO_3$/α-Fe_2O_3/$Bi_2Fe_4O_9$ could allow an improved generation of superoxide ($O_2^{\cdot -}$) and hydroxyl ($OH^{\cdot}$) radicals in the dyes solutions.

During degradation of IC dye, the best photocatalytic response was found with the BFO-P sample, *i.e.* $BiFeO_3$/α-Fe_2O_3/$Bi_2Fe_4O_9$ heterostructure with the highest proportion of $BiFeO_3$. Additionally, degradation kinetic rate was improved for AB and RhB dyes most probably due to the presence of ionic groups in their chemical structure that increased the interaction with the heterostructure surface. Finally, the $BiFeO_3$/α-Fe_2O_3/$Bi_2Fe_4O_9$ heterostructure has shown (i) stability in dye degradation performance up to 3 cycles and (ii) an easy magnetic separation. These outcomes show the high potentiality of $BiFeO_3$/α-Fe_2O_3/$Bi_2Fe_4O_9$ as a magnetically separable heterostructure for the development of visible-light driven photocatalytic powder-suspended systems for the degradation of organic pollutants and water splitting applications.

Chapter 7

Photocatalytic Evaluation and Comparison of Heterostructure α/β-Bi_2O_3 and β-Bi_2O_3 Deposited Sintered Silica for Degradation of Single and Mixed Dyes in bulk solutions under natural sunlight

7.1 Introduction

When proposing a visible active photocatalyst for heterogeneous photocatalysis (HP), it is significant to evaluate the photocatalytic response using outdoor natural sunlight, because it is obvious that intensity of natural sunlight varies depending on the weather, therefore the experience of performing photocatalysis would be changed when compare to fixed conditions of lab *i.e.* fixed irradiation intensity that led to maintained kinetic rate of degradation.

One other factor related to practical approach of HP, is the investigation of bulk solution; because there are plenty of studies in which a limited amount of dye solution is treated for photocatalytic evaluation, and have proposed as efficient photocatalysts basing on the results obtained after analyzing considerably lower amount of solution. Therefore, it would be important to consider the photocatalytic evaluation based on the observation on bulk dyes solution; to mitigate the problems, that encountered when there is large variation between the results obtained during lab conditions and large scale (during real applications) [231, 266]. On the other hand, a high dye concentration could have influence by hindering the irradiation passage and availability of limited active/reactive sites (originated by photocatalyst) could take more time in considerable photodiscoloration and degradation of this more concentrated solution.

From the previously obtained results the best photocatalytic response and improved kinetic rate was achieved with α/β-Bi_2O_3 heterostructure and β-Bi_2O_3 deposited sintered silica (described in chapter 3 and 5, respectively). Therefore, α/β-Bi_2O_3 heterostructure and β-Bi_2O_3 deposited sintered silica were selected for the final investigation of single and mixed organic dyes bulk solutions under outdoor natural sunlight; in order to compare the photoactivity with the results achieved in lab conditions *i.e.* the kinetics and mechanism of photodegradation. Some observations, were also made by varying the concentration of the dye solution to analyze the photocatalytic behavior and optimum kinetic rate at varying dye concentration.

7.2 Experimental

7.2.1 Synthesis

7.2.1.1 α/β-Bi_2O_3 heterostructure

Synthesis of α/β-Bi_2O_3 heterostructure was done, as explained in chapter-3. In brief, direct thermal decomposition of $Bi(NO_3)_3{:}5H_2O$, was followed initially at 150 °C for 1 h, then the temperature was raised up to 250 °C and hold there for 2 hr. Finally, annealing was followed at 550 °C for 2 hr and sample was allowed for ambient furnace cooling.

7.2.1.2 β-Bi_2O_3 deposited sintered silica

Here, the followed deposition method was different than the previously used method of pneumatic spray pyrolysis for the deposition of β-Bi_2O_3 deposited sintered silica (stated in chapter-5). This time impregnation method was used for the deposition of β-Bi_2O_3 on sintered silica. Initially, the precursor solution was prepared by dissolving 2 mmolar $Bi(NO_3)_3{:}5H_2O$ salt in 100 ml of deionized water containing 0.5 M HNO_3, then 1 ml of Triton X-100 non-ionic surfactant was slowly added in that solution under stirring conditions and at ambient temperature. The purpose of surfactant is to reduce the surface tension of the precursor solution and allowing uniform distribution of the solution throughout the sintered silica substrate. Before deposition sintered silica substrates of grade-2 with 40 mm diameter (average indexed pores size 40 – 100 µm) were first sonicated in ethanol sonicated and then in water, and further dried at 60 °C for 1 hr. In a typical method (step by step shown in Fig. 7.1), 10 ml of the precursor solution was poured in flat porcelain petri dish, the dried substrate was put in that and allowed for 30 min to soak the precursor solution; afterwards the petri dish was placed inside the furnace and initially heated to 150 °C for 2 hr, to evaporate the water and to allow pre-drying. Final annealing of the substrate was done at 450 °C for 1 hr and then substrate was allowed for slow ambient cooling inside the furnace.

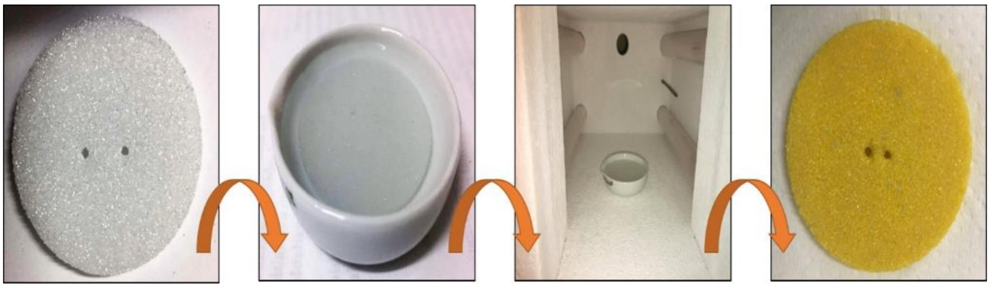

Fig. 7.1 impregnation method used for β-Bi_2O_3 deposition on sintered silica substrate

7.2.2 Characterization

7.2.2.1 α/β-Bi_2O_3 heterostructure

As the characterization details of α/β-Bi_2O_3 heterostructure were already given and explained in chapter-3. This time α/β-Bi_2O_3 heterostructure was only analyzed for FESEM images to assess the morphology; investigated on high resolution equipment MERLIN ZEISS field-emission scanning electron microscopy (FE-SEM).

7.2.2.2 β-Bi_2O_3 deposited sintered silica

The obtained substrate after deposition was characterized without any further treatment or modification. Morphology of the bare and deposited silica was investigated on the same instrument mentioned above, in addition elemental composition and mapping were obtained by using integrated OXFORD INCA ENERGY 450 energy-dispersive X-ray spectroscopy (EDS) detector. The X-ray diffraction (XRD) analysis of the bare and deposited silica was analyzed for crystalline structure and phase composition, on an X'Pert Phillips diffractometer at same operating conditions discussed earlier. UV−Vis diffuse reflectance spectra (DRS) of the bare and deposited silica were recorded by using Varian Cary 500 spectrophotometer, further Tauc plots were determined after using Kubelka Munk function and the energy band gap (E_g) of the obtained films was estimated.

7.2.3 Photocatalytic Evaluation

For photocatalytic investigation of α/β-Bi_2O_3 powder and deposited silica under lab conditions, the evaluation was followed as explained in earlier chapters. In brief, initially the photocatalytic response of α/β-Bi_2O_3 powder, bare and deposited silica was determined for the photodegradation under standard fluorescent white lamp of 25 watts (spectrum range from 400 nm to 700 nm), using 100 mL of anionic indigo carmine (*IC*) dye solution at neutral pH. The different sequence of IC concentration used for each photocatalyst sample were: 10, 20, 30 mg/L. The added quantity of α/β-Bi_2O_3 was 50 mg (fixed for different concentrations) in 100 ml dye solution, while one β-Bi_2O_3 deposited silica substrate of 40 mm was used. The proportion of α/β-Bi_2O_3 powder to IC dye solution was 0.5 mg/1ml and for deposited silica substrate was 0.4 mm/1ml. For each observation, dye solution was firstly stirred for 30 min in the dark to attain adsorption-desorption equilibrium. The stirring rate was kept constant at 600 rpm in both dark and irradiated conditions. The absorbance spectra of the dye solution as a function of time was recorded, using a UV-vis spectrophotometer (Shimadzu 1800) after analyzing the withdrawn aliquots of 3 mL (in case of α/β-Bi_2O_3 powder after centrifuged at 8000 rpm for 5 min) and putting back to the vial after measurement. After determining the optimum IC concentration to investigate; further evaluation of the 1 Liter bulk solution of IC (at identified optimum concentration) were followed under natural sun light in presence of deposited silica and α/β-Bi_2O_3 powder. Moreover, the evaluation of cationic Rhodamine B (RhB) dye, was followed under natural sun light using 1 Liter bulk solution of RhB at a fixed 5 mg/L concentration in presence of deposited silica and α/β-

Bi_2O_3 powder. The proportion of photocatalyst to dye solution was similar that was followed for IC dye. To observe the process of photolysis, blank dye solutions were also investigated, along with the solutions containing deposited silica and α/β- Bi_2O_3 powder.

Furthermore, the photocatalytic performance of mixed 1-liter bulk dye solution under natural sun light, was performed in presence of both deposited silica and α/β-Bi_2O_3 powder; mixed solution was prepared with 2×10^{-6} M concentration of IC and RhB dyes to ensure the same number of molecules in the solution, while the proportion of photocatalyst to dye solution was similar *i.e.* α/β-Bi_2O_3 powder to IC dye solution was 0.5 mg/1 ml and for deposited silica substrate was 0.4mm /1 ml. Finally, to conclude the study, the photocatalytic evaluation under natural sunlight was repeated up to three cycles for both deposited silica and α/β- Bi_2O_3 powder, to assess their suitability for the photocatalyst stability and long-term usage. The irradiation intensity of the standard white lamp and of the sun was continuously recorded through lux meter (Delta OHM photo-radiometer) by using different probes for UV and visible spectral regions: UVB – 280 – 315 nm, UVA – 315 – 400 nm and Visible light – 400 nm – 800 nm.

7.3 Results and Discussion

7.3.1 Characterization

7.3.1.1 α/β-Bi_2O_3 heterostructure

7.3.1.1.1 Morphology

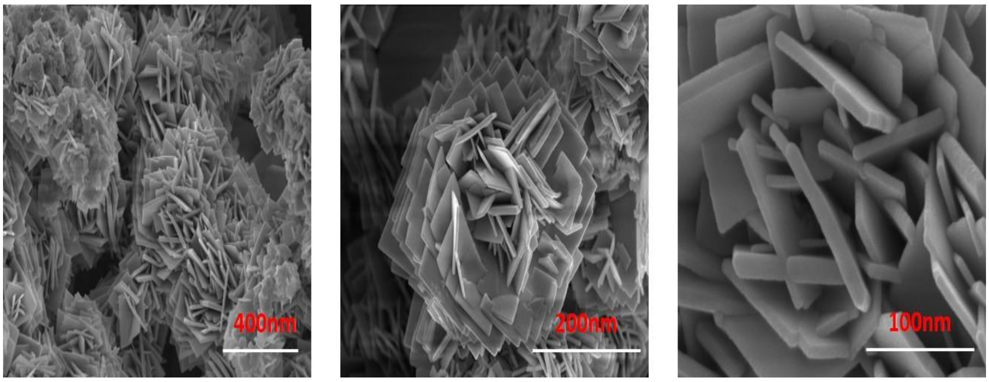

Fig. 7.2 FESEM images α/β- Bi_2O_3 at different magnification scale.

In Fig. 7.2 FESEM images are shown; depicting typical morphology of Bi_2O_3 materials containing layered interconnected flower like microstructure. Alike morphology is also reported in various studies [14, 53]. As observed from these images the thickness of the interconnected layers is ranging from 30-45 nm. The tiny voids and gaps between these layers providing some porosity to the material and could have facilitated when different dyes were evaluated earlier and discussed in chapter 3 and 4; exhibited the improved photocatalytic performance.

7.3.2.2 β-Bi_2O_3 deposited sintered silica

7.3.2.2.1 Crystalline Structure

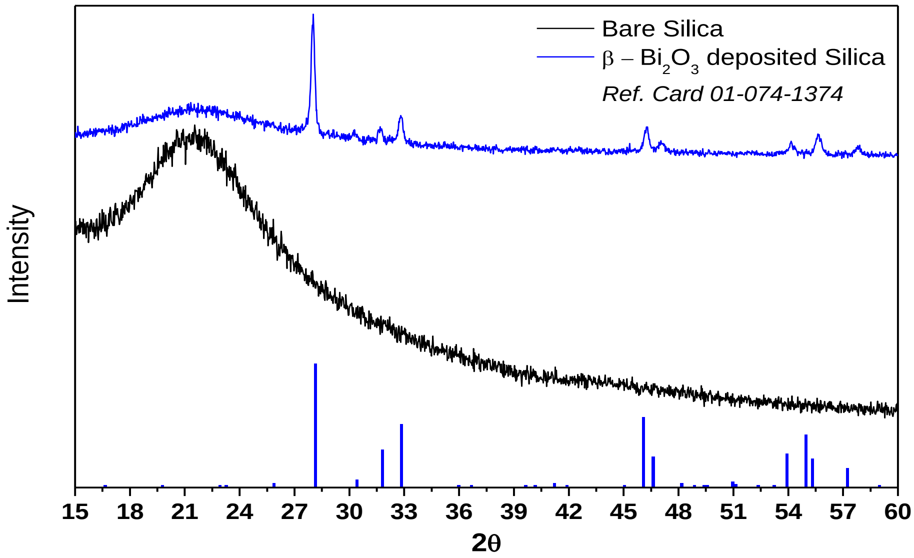

Fig. 7.3 XRD patterns of bare and deposited silica

Fig. 7.3 shows the obtained XRD patterns of bare and deposited silica, for the bare silica widen peak in the region from 16-25° ascribed to SiO_2 (JCPDS card no. 01-079-1913), while after deposition the mentioned widen peak is suppressed along with appearance of additional main peaks at 28, 31.82, 32.75, 46.99 and 55.6°, attributed to β-Bi_2O_3 (JCPDS card no. 01-074-1374) accredited to (221), (002), (400), (440) and (621) planes, respectively. The average particle size and the crystallinity could not be confirmed due to some suppression incurred by silica, but the appearance of well aligned peaks confirmed the presence of β-Bi_2O_3 over silica surface; identical to the already discussed XRD patterns over glass using spray pyrolysis technique (discussed in chapter-5).

7.3.2.2.2 Morphology

FESEM and digital images of bare and deposited silica are shown in Fig 7.4A-D. Bare silica in Fig. 7.4A shows irregular large grains of silica with unevenness porosity and roughness. After deposition, the random decoration of β-Bi_2O_3 over these large grains can be observed at lower scale in Fig. 7.4B, while at a bit higher magnification porous β-Bi_2O_3 interlayers can be clearly observed inside the cavities/pores of the silica (Fig. 7.4D). The structural appearance and co-joining of these β-Bi_2O_3 interlayers is almost similar as earlier observed in case of α/β-Bi_2O_3 heterostructure in Fig. 7.2. However, the morphology of deposited films obtained here (by employing impregnation method) is different than previously discussed morphology obtained over the sintered silica when using spray pyrolysis technique; in which overlaid sheets of β-Bi_2O_3 were seen. The main difference in morphology when encountering different deposition method is obvious. In case of spray pyrolysis, the continuous sprayed droplets allowed the formation of sheets one by one, which overlaid each other. While in case of impregnation method, the silica was surrounded by the precursor solution allowing the more contact and impregnation inside the irregular pores and permitted particles to grow and align together. Moreover, Fig. 7.5A-D shows the elemental mapping of the deposited films over silica, where Fig. 5A display the overall acquired elemental mapping while Fig. 7.5B-D displayed the map of each element *i.e.* Bi, O and Si, respectively. It can be observed that β-Bi_2O_3 particles are well distributed and followed growth over the surface and inside the pores of silica.

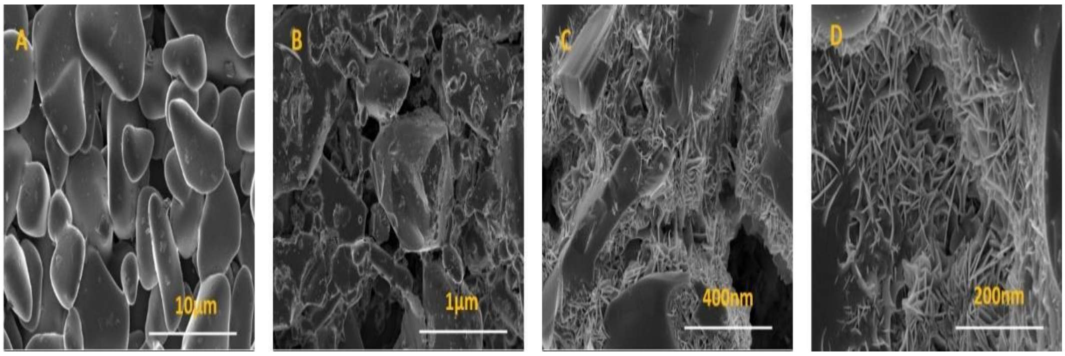

Fig. 7.4 FESEM images A) bare silica and B-C) β-Bi_2O_3 deposited silica at different magnification scales.

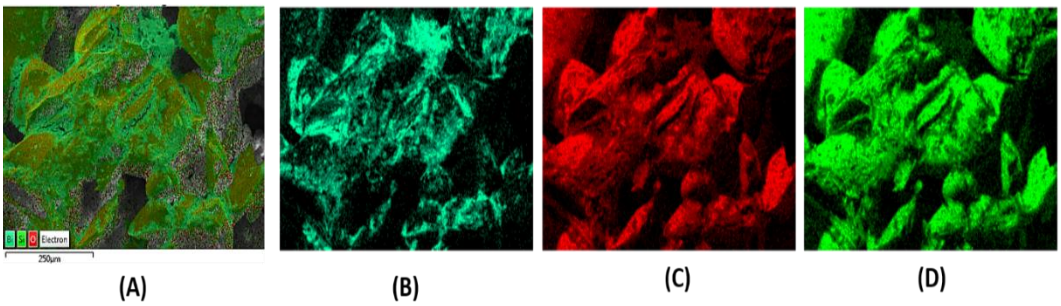

Fig. 7.5 EDS elemental mapping A) whole acquired elemental map B) Bismuth map C) Oxygen map and D) Silicon map.

7.3.2.2.3 Optical properties

Fig. 7.6 shows the UV-Vis photoabsorption of bare and β-Bi_2O_3 coated silica and inset shows the tauc plot with the estimated band gap energy of obtained β-Bi_2O_3 films. This can be clearly observed that bare silica has absorption edge in the UV-region, while after deposition, additional electronic transition can be observed in wide visible spectrum from 400-550nm, can be associated to transition from valence band to conduction band for β-Bi_2O_3, with an estimated energy band gap of 2.38 eV; alike to previously obtained results in chapter-5 with β-Bi_2O_3 deposited silica by using spray pyrolysis technique.

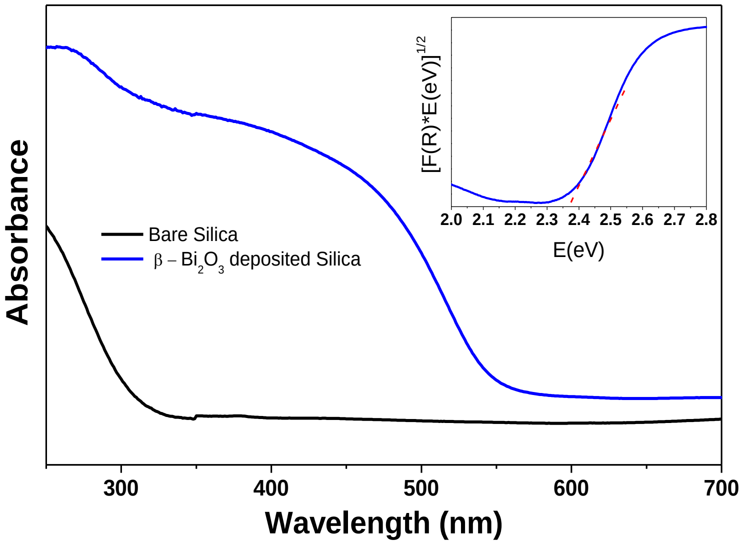

Fig. 7.6 UV-vis DRS of bare and β-Bi_2O_3 deposited silica; inset Tauc plot along with estimated energy band gap.

Moreover, in relation to XRD, Morphology and UV-Vis DRS results, it can be observed that along with β-Bi_2O_3, silica has contributed in each analysis, which suggest that surface of the silica is jointly shared with β-Bi_2O_3; this certainly will have influence on photocatalytic performance.

7.3.2 Photocatalysis

7.3.2.1 Indigo Carmine dye

Primarily anionic Indigo Carmine (*IC*) dye solution was investigated under lab conditions at varying concentration using both α/β-Bi_2O_3 and β-Bi_2O_3 deposited silica. 50ml of IC dye solution at concentration: 10, 20 and 30ml were used for the photoactivity of α/β-Bi_2O_3 and β-Bi_2O_3 deposited silica under fluorescent white lamp of 25watt, in order to analyze the rate of degradation and behavior of kinetics for both α/β-Bi_2O_3 and β-Bi_2O_3 deposited silica in comparison and together. The relative concentration (C/C_o) plots of α/β-Bi_2O_3 and β-Bi_2O_3 deposited silica are shown in Fig. 7.7A and B, while their kinetic curves and estimated K_{app} are shown in Fig7.7C and D, respectively. It can be clearly observed that the rate of kinetics when varying the IC concentration followed the alike trend for both *i.e.* simultaneous decrease in the kinetic rate with increased concentration for α/β-Bi_2O_3 and β-Bi_2O_3 deposited silica. Moreover, the photocatalytic response of β-Bi_2O_3 deposited silica is competing to α/β-Bi_2O_3; with an average small difference of only 0.006min^{-1} in K_{app} than α/β-Bi_2O_3, which is very promising considering the fixed support in comparison to bulk powder (which is highly dispersed in the solution). The improved and continued performance β-Bi_2O_3 deposited silica is mainly because of the roughness and porosity of silica, that have maintained the interaction of β-Bi_2O_3 films and IC dye molecules; discussed earlier in detail in chapter-5. Initially at 10ppm concentration, the K_{app} were 0.032 and 0.026 min^{-1} for α/β-Bi_2O_3 and β-Bi_2O_3 deposited silica, respectively, while decreased to 0.016 and 0.014 min^{-1} at dye concentration of 30ppm, respectively. In addition, in order to differ the removal of IC dye if encountered by sintered silica substrate only, evaluation was also followed using a bare and undeposited sintered silica for only 20ppm dye concentration. It was confirmed that after initial adsorption up to 10% the intensity of IC dye solution hardly changed with bare silica and suggesting that prior removal/degradation of IC was due to presence of β-Bi_2O_3, deposited on the surface and inside the pores.

The experiment for the evaluation of bulk IC dye solution (1 liter) under natural sun light irradiation were performed using dye solution of 20ppm concentration only. 500mg of α/β-Bi_2O_3 powder was added in the 1 liter of IC dye solution and in the separate experiment ten (in numbers) β-Bi_2O_3 deposited silica substrates. The similar proportion of α/β-Bi_2O_3 powder and deposited silica substrate to IC dye solution was followed *i.e.* 0.5 mg/1 ml and 0.4 mm/1 ml, respectively. The average noted irradiation intensity in the afternoon was around 600-650 watts/m^2, while average irradiation intensity during sun-set and cloudy condition was around 150-200 watts /m^2.

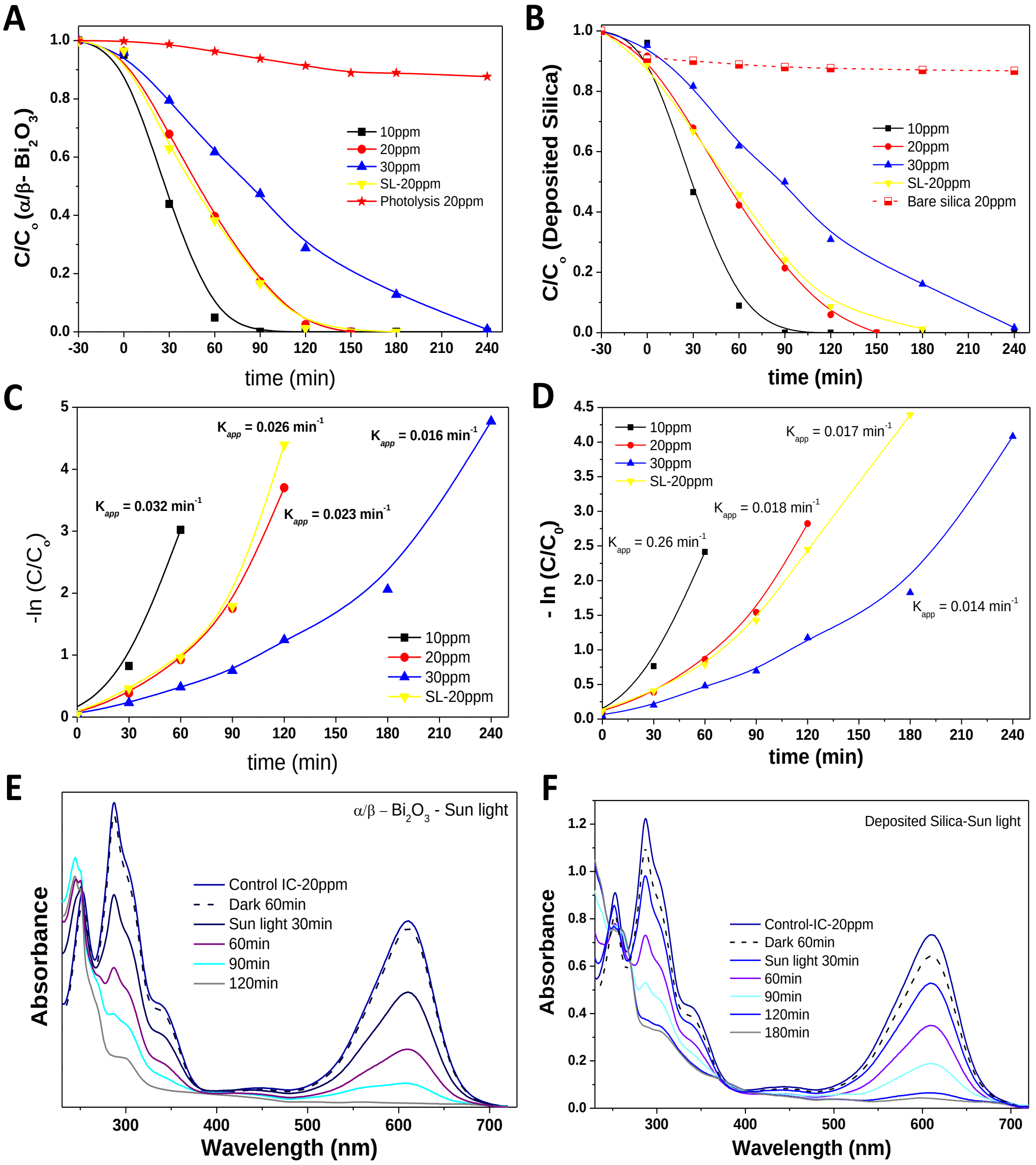

Fig. 7.7 C/C_o and kinetics of IC A-D), in case of α/β-Bi_2O_3 and β-Bi_2O_3 deposited silica and their respective degradation absorbance spectrum *vs* time.

The K_{app} under sunlight is almost identical to the achieved results in lab using simulated visible light at 20ppm concentration (Fig. 7.7C and D), in both cases of α/β-Bi_2O_3 and β-Bi_2O_3 deposited silica. The estimated K_{app} for α/β-Bi_2O_3 powder were 0.023:0.026 min^{-1} (visible light/sun light), while 0.018:0.017 min^{-1} (visible light/sun light) in case of β-Bi_2O_3 deposited silica; revealed that both α/β-Bi_2O_3 and β-Bi_2O_3 deposited silica have solar light driven visible activity at the similar performance as achieved in lab conditions. Moreover, 100 ml IC dye solution under sun light was also evaluated without photocatalyst, for photolysis; relative concentration in Fig. 7.7A suggest almost negligible decrease in intensity of IC have occurred due to photolysis for longer time.

It is worth to mention that besides having a lot of variation in irradiation intensity of sun light hardly influenced the photocatalytic response of both α/β-Bi_2O_3 and β-Bi_2O_3 deposited silica, however sometime low degradation kinetics was observed when some clouds appeared in front the sun light. In Fig. 7.7E and 7.7F, the time course absorption spectrum is shown for both α/β-Bi_2O_3 and β-Bi_2O_3 deposited silica under natural sun light, affirming the same phenomena of photocatalytic oxidation of IC dye by α/β-Bi_2O_3 and β-Bi_2O_3 deposited films; as discussed in earlier chapters *i.e.* spectral changes in the UV-Vis absorbance spectra of IC dye, associated to destruction of indigoid group and origination of isatin sulfonic acid and 2-amine-5-sulfo-benzoic acid in the UV- region (220-240 nm). In addition, Fig. 7.8A and 7.8B show the bulk IC dye solution before and after photocatalytic experiment under sun light using β-Bi_2O_3 deposited silica, while in Fig. 7.8C shows the deposited silica before and after photocatalysis test; hardly changes in appearance and can be efficiently utilized for subsequent cycles.

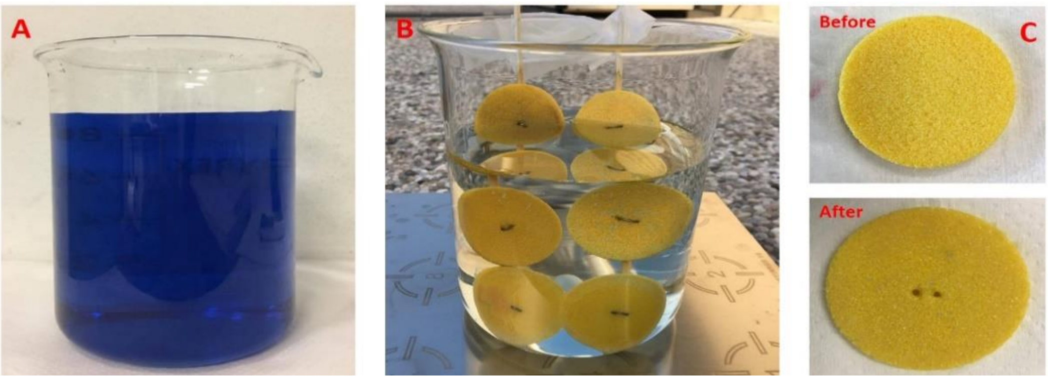

Fig. 7.8 IC bulk dye solution: A) before and B) after exposure under sunlight. C) β-Bi_2O_3 deposited silica before and after photocatalytic evaluation.

7.3.2.2 Rhodamine-B dye sunlight

The evaluation of *RhB* dye was only performed under sunlight and with only using 5ppm (5mg/l) concentration for both α/β-Bi_2O_3 powder and β-Bi_2O_3 deposited silica. The proportion of photocatalyst and dye solution was similar that was used before in case of IC. Fig 7.9A show the C/C_o respect to time, confirming the performance of α/β-Bi_2O_3 and β-Bi_2O_3 deposited silica at almost similar low difference, as observed for IC. The determined K_{app} of RhB were lower than IC dye for both α/β-Bi_2O_3. The lower in kinetics is related to the higher absorbance intensity of RhB dye, as the absorbance intensity of 5ppm concentration of RhB is equivalent to 30ppm concentration of IC and possibly the irradiation passage for the activation of α/β-Bi_2O_3 and β-Bi_2O_3 films was reduced due to high intensity of RhB color. Moreover, this could be confirmed when comparing the obtained kinetics for degradation of RhB (Fig. 7.9A) with kinetics for 30ppm of IC (Fig. 7B and D), the attained K_{app} are almost similar *i.e.* 0.012: 0.016 min^{-1} (5 ppm RhB: 30ppm IC) in case of α/β-Bi_2O_3, revealing the fact that dye molecules even at low concentration but of high coloring intensity can influence the kinetic rate, simply by effecting the passage of photocatalyst activation [266]. By analyzing C/C_o plots of RhB in Fig. 7.9A, the observed rate of adsorption over α/β-Bi_2O_3 was up to 15%, while a bit higher in case of β-Bi_2O_3 deposited silica, mainly associated to more interaction of RhB to the deposited silica; with an advantage of the roughness and porosity, that have assisted to maintain the competing response of degradation compared to α/β-Bi_2O_3 powder.

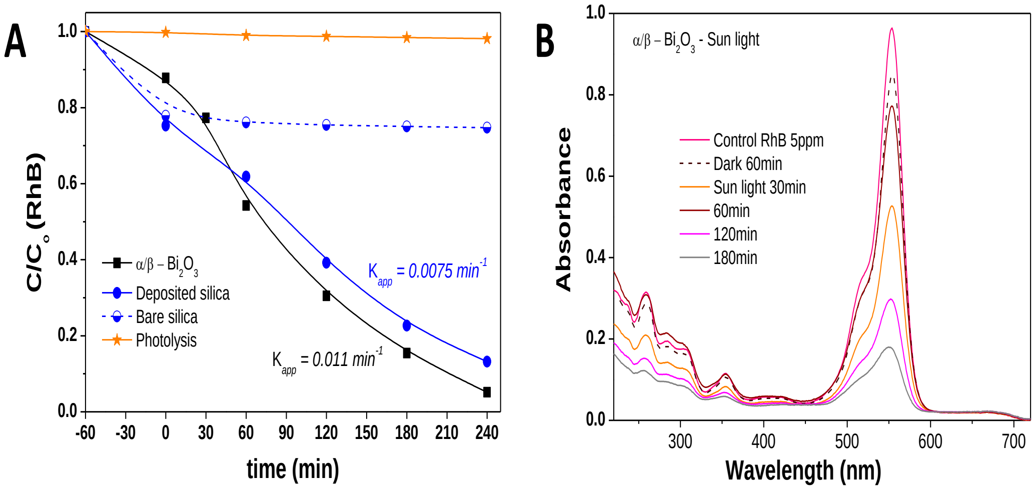

Fig. 7.9 A) C/C_o of RhB for α/β-Bi_2O_3, bare and β-Bi_2O_3 deposited silica and without photocatalyst B) photodegradation absorbance spectrum of RhB *vs* time.

In addition, the bare undeposited silica, after initial decrease due to adsorption have hardly influenced the removal of RhB from the solution, moreover, the process of photolysis was negligible during evaluation of RhB under sunlight (Fig. 7.9A). The degradation absorption spectra of RhB *vs* time in case of α/β-Bi_2O_3 is displayed in Fig. 7.9B; revealed that photodegradation of RhB have followed that similar pattern of degradation as obtained in earlier chapters *i.e.* without forming any intermediates, and without leading sensitization process.

7.3.2.3 Mixed solution sunlight

Mixed dye bulk solution at equal molar concentration of both IC and RhB dye (2×10^{-6} M) was evaluated for both α/β-Bi_2O_3 powder and deposited silica substrates under sun light. Initially, the separate bulk dye solution (1 liter) along with 500mg α/β-Bi_2O_3 powder and ten deposited silica substrates were stirred in dark for 60 min, then the bulk solution were irradiated under natural sunlight and 3 ml of solution were drawn timely to analyze the change in absorption spectra; in case of powders the analysis was done after centrifuge at 8000 rpm for 5 min. Fig. 7.10A-D display the time course absorption spectra of mixed solution. Observing the control solution at 0 min, the UV-Vis spectra of mixed dye represents the contribution of both RhB and IC dyes, with major peaks at 554 and 610 nm, respectively, revealing that when dyes were mixed together, the new absorbance spectra followed the representation of each dye [101]. Fig. 7.10A and 10C show the first 90 min of the exposure under sunlight, in which IC dye is favorably degrading at higher kinetic rate than RhB, the determined K_{app} were 0.019: 0.002 min^{-1} (IC: RhB) in case of α/β-Bi_2O_3 and 0.011: 0.003 min^{-1} (IC: RhB) in case of deposited silica for first 90 min (given in Fig. 7.10E and 10F). However, it could be observed from Fig. 10B, D, E and F, that the kinetics of RhB degradation increase after 90 min; once the degradation of IC completes *i.e.* enhanced to 0.006 and 0.0046 min^{-1} in case of α/β-Bi_2O_3 and deposited silica, respectively, (given in Fig. 10E and F). This affirms the same behavior of degradation which was observed and discussed in detail in chapter-3, when achieved only for α/β-Bi_2O_3 powder with this mixed solution under lab conditions and reported in our work [101]. Moreover, the time-course decrease in UV-vis absorbance spectra, K_{app} and change in the spectral peaks in UV-region were almost identical for both α/β-Bi_2O_3 powder and deposited silica and the rate, suggesting that the deposited silica is as efficient as the α/β-Bi_2O_3 powder, towards the sequential degradation of mixed solution of IC and RhB.

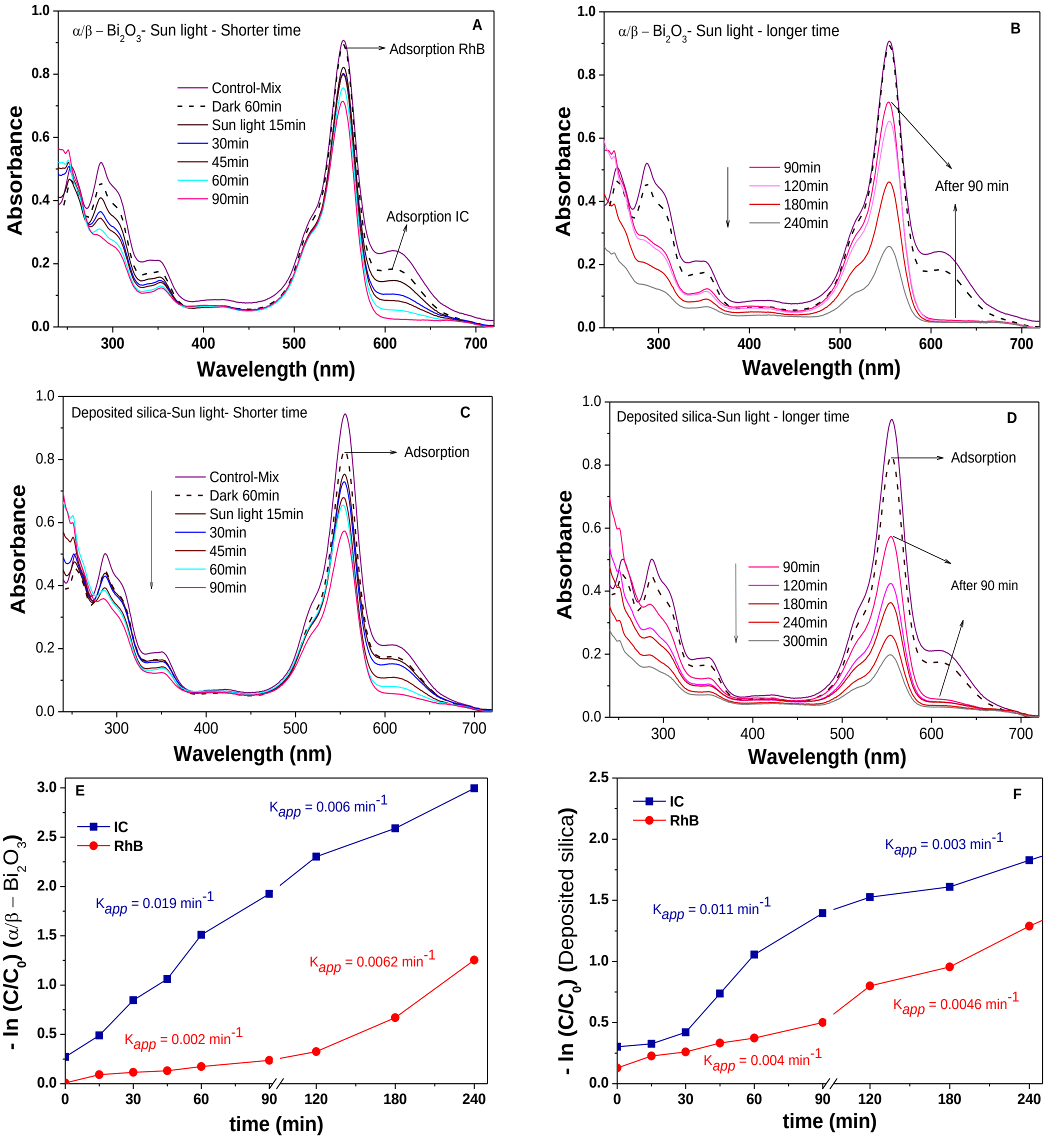

Fig. 7.10 A-D) Absorbance spectra of mixed solution vs time, in case of α/β-Bi_2O_3 and β-Bi_2O_3 deposited silica for shorter and longer irradiation time. E-F) kinetics in case of α/β-Bi_2O_3 and β-Bi_2O_3 deposited silica.

7.3.3 Cyclic stability

Cyclic stability of both α/β-Bi_2O_3 powder and deposited silica were investigated for photodegradation of 20ppm IC 100ml solution under sunlight, using 50mg of the recovered α/β-Bi_2O_3 powder and one recovered deposited silica substrate. Before using for next cycle, rinsing of the recovered powder and substrate was followed in hot water, at temperature of 80 °C and then after drying at the same temperature for 2 hr. Fig. 7.11 shows the photodiscoloration % of the α/β-Bi_2O_3 powder and deposited silica up to 3 cycles; it can be observed that both are stable for consecutive cycles, however the photodiscoloration % in case of α/β-Bi_2O_3 reduced to 77% and in case of deposited silica reduced to 81%. The reduction in discoloration in case of α/β-Bi_2O_3 may be due to agglomeration of the powder and in case of deposited silica probably due to change in the porosity and roughness of the silica and some loss of the β-Bi_2O_3 films [155]. Nevertheless, still the performance of both α/β-Bi_2O_3 and deposited silica are up to mark, suggesting their stability and longer usage for repeated cycles.

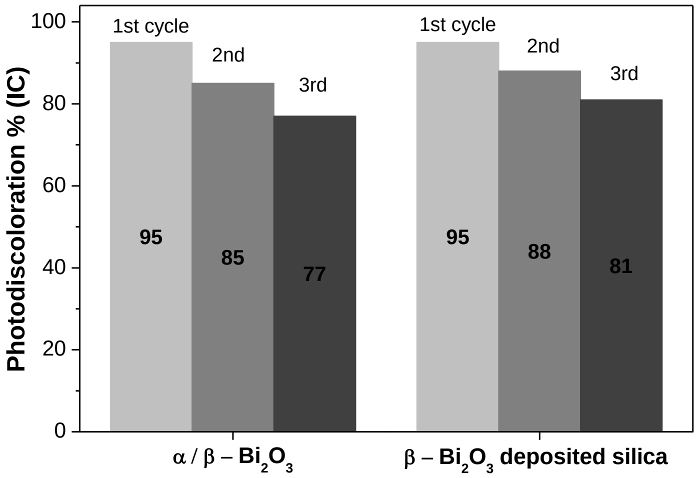

Fig. 7.11 Performance of α/β-Bi_2O_3 and β-Bi_2O_3 deposited silica up to 3 cycles, in case of IC dye.

8 References

[1] C. Gao, J. Wang, H. Xu, Y. Xiong, Coordination chemistry in the design of heterogeneous photocatalysts, Chemical Society Reviews, 46 (2017) 2799-2823.

[2] D. Friedmann, A. Hakki, H. Kim, W. Choi, D. Bahnemann, Heterogeneous photocatalytic organic synthesis: state-of-the-art and future perspectives, Green Chemistry, 18 (2016) 5391-5411.

[3] O. Ola, M.M. Maroto-Valer, Review of material design and reactor engineering on TiO2 photocatalysis for CO2 reduction, Journal of Photochemistry and Photobiology C: Photochemistry Reviews, 24 (2015) 16-42.

[4] R. Asahi, T. Morikawa, T. Ohwaki, K. Aoki, Y. Taga, Visible-light photocatalysis in nitrogen-doped titanium oxides, science, 293 (2001) 269-271.

[5] H. Irie, Y. Watanabe, K. Hashimoto, Carbon-doped anatase TiO2 powders as a visible-light sensitive photocatalyst, Chemistry Letters, 32 (2003) 772-773.

[6] T. Ohno, T. Mitsui, M. Matsumura, Photocatalytic activity of S-doped TiO2 photocatalyst under visible light, Chemistry letters, 32 (2003) 364-365.

[7] L. Zhao, X. Chen, X. Wang, Y. Zhang, W. Wei, Y. Sun, M. Antonietti, M.M. Titirici, One-Step solvothermal synthesis of a carbon@ TiO2 dyade structure effectively promoting visible-Light photocatalysis, Advanced Materials, 22 (2010) 3317-3321.

[8] S. Kumar, A. Baruah, S. Tonda, B. Kumar, V. Shanker, B. Sreedhar, Cost-effective and eco-friendly synthesis of novel and stable N-doped ZnO/gC 3 N 4 core–shell nanoplates with excellent visible-light responsive photocatalysis, Nanoscale, 6 (2014) 4830-4842.

[9] S. Rehman, R. Ullah, A. Butt, N. Gohar, Strategies of making TiO 2 and ZnO visible light active, Journal of hazardous materials, 170 (2009) 560-569.

[10] G.-S. Li, D.-Q. Zhang, J.C. Yu, A new visible-light photocatalyst: CdS quantum dots embedded mesoporous TiO2, Environmental science & technology, 43 (2009) 7079-7085.

[11] Q. Li, B. Guo, J. Yu, J. Ran, B. Zhang, H. Yan, J.R. Gong, Highly efficient visible-light-driven photocatalytic hydrogen production of CdS-cluster-decorated graphene nanosheets, Journal of the American Chemical Society, 133 (2011) 10878-10884.

[12] X. Zong, H. Yan, G. Wu, G. Ma, F. Wen, L. Wang, C. Li, Enhancement of photocatalytic H2 evolution on CdS by loading MoS2 as cocatalyst under visible light irradiation, Journal of the American Chemical Society, 130 (2008) 7176-7177.

[13] Z. Ai, Y. Huang, S. Lee, L. Zhang, Monoclinic α-Bi2O3 photocatalyst for efficient removal of gaseous NO and HCHO under visible light irradiation, Journal of Alloys and Compounds, 509 (2011) 2044-2049.

[14] S. Gong, Q. Han, X. Wang, J. Zhu, Controlled synthesis of bismuth-containing compounds (α-, β-and δ-Bi 2 O 3, Bi 5 O 7 NO 3 and Bi 6 O 6 (OH) 2 (NO 3) 4· 2H 2 O) and their photocatalytic performance, CrystEngComm, 17 (2015) 9185-9192.

[15] S. Iyyapushpam, S.T. Nishanthi, D. Pathinettam Padiyan, Photocatalytic degradation of methyl orange using α-Bi2O3 prepared without surfactant, Journal of Alloys and Compounds, 563 (2013) 104-107.

[16] D. Sánchez-Martínez, I. Juárez-Ramírez, L.M. Torres-Martínez, I. de León-Abarte, Photocatalytic properties of Bi2O3 powders obtained by an ultrasound-assisted precipitation method, Ceramics International, 42 (2016) 2013-2020.

[17] S.M. Thalluri, C. Martinez Suarez, S. Hernández, S. Bensaid, G. Saracco, N. Russo, Elucidation of important parameters of $BiVO_4$ responsible for photo-catalytic O_2 evolution and insights about the rate of the catalytic process, Chemical Engineering Journal, 245 (2014) 124-132.

[18] X. Xiao, R. Hu, C. Liu, C. Xing, C. Qian, X. Zuo, J. Nan, L. Wang, Facile large-scale synthesis of β-Bi2O3 nanospheres as a highly efficient photocatalyst for the degradation of acetaminophen under visible light irradiation, Applied Catalysis B: Environmental, 140–141 (2013) 433-443.

[19] Y. Yan, Z. Zhou, Y. Cheng, L. Qiu, C. Gao, J. Zhou, Template-free fabrication of α- and β-Bi2O3 hollow spheres and their visible light photocatalytic activity for water purification, Journal of Alloys and Compounds, 605 (2014) 102-108.

[20] Z. Ai, W. Ho, S. Lee, L. Zhang, Efficient photocatalytic removal of NO in indoor air with hierarchical bismuth oxybromide nanoplate microspheres under visible light, Environmental science & technology, 43 (2009) 4143-4150.

[21] S. Shenawi-Khalil, V. Uvarov, S. Fronton, I. Popov, Y. Sasson, A novel heterojunction BiOBr/bismuth oxyhydrate photocatalyst with highly enhanced visible light photocatalytic properties, The Journal of Physical Chemistry C, 116 (2012) 11004-11012.

[22] Y. Wang, K. Deng, L. Zhang, Visible light photocatalysis of BiOI and its photocatalytic activity enhancement by in situ ionic liquid modification, (2011).

[23] X. Xiao, C. Liu, R. Hu, X. Zuo, J. Nan, L. Li, L. Wang, Oxygen-rich bismuth oxyhalides: generalized one-pot synthesis, band structures and visible-light photocatalytic properties, Journal of Materials Chemistry, 22 (2012) 22840-22843.

[24] H. Zhang, L. Liu, Z. Zhou, Towards better photocatalysts: first-principles studies of the alloying effects on the photocatalytic activities of bismuth oxyhalides under visible light, Physical Chemistry Chemical Physics, 14 (2012) 1286-1292.

[25] C. Minero, D. Vione, A quantitative evalution of the photocatalytic performance of TiO2 slurries, Applied Catalysis B: Environmental, 67 (2006) 257-269.

[26] B. Gao, P.S. Yap, T.M. Lim, T.-T. Lim, Adsorption-photocatalytic degradation of Acid Red 88 by supported TiO 2: effect of activated carbon support and aqueous anions, Chemical Engineering Journal, 171 (2011) 1098-1107.

[27] U.I. Gaya, A.H. Abdullah, Heterogeneous photocatalytic degradation of organic contaminants over titanium dioxide: a review of fundamentals, progress and problems, Journal of Photochemistry and Photobiology C: Photochemistry Reviews, 9 (2008) 1-12.

[28] Y. Fu, X. Wang, Magnetically separable ZnFe2O4–graphene catalyst and its high photocatalytic performance under visible light irradiation, Industrial & Engineering Chemistry Research, 50 (2011) 7210-7218.

[29] T.A. Gad-Allah, S. Kato, S. Satokawa, T. Kojima, Treatment of synthetic dyes wastewater utilizing a magnetically separable photocatalyst (TiO2/SiO2/Fe3O4): Parametric and kinetic studies, Desalination, 244 (2009) 1-11.

[30] S. Xuan, W. Jiang, X. Gong, Y. Hu, Z. Chen, Magnetically separable Fe3O4/TiO2 hollow spheres: fabrication and photocatalytic activity, The Journal of Physical Chemistry C, 113 (2008) 553-558.

[31] C.M. Cho, J.H. Noh, I.S. Cho, J.S. An, K.S. Hong, J.Y. Kim, Low-Temperature Hydrothermal Synthesis of Pure BiFeO3 Nanopowders Using Triethanolamine and Their Applications as Visible-Light Photocatalysts, Journal of the American Ceramic Society, 91 (2008) 3753-3755.

[32] P. Fischer, M. Polomska, I. Sosnowska, M. Szymanski, Temperature dependence of the crystal and magnetic structures of BiFeO3, Journal of Physics C: Solid State Physics, 13 (1980) 1931.

[33] R. Guo, L. Fang, W. Dong, F. Zheng, M. Shen, Magnetically separable BiFeO 3 nanoparticles with a γ-Fe 2 O 3 parasitic phase: controlled fabrication and enhanced visible-light photocatalytic activity, Journal of Materials Chemistry, 21 (2011) 18645-18652.

[34] W. Ramadan, P.A. Shaikh, S. Ebrahim, A. Ramadan, B. Hannoyer, S. Jouen, X. Sauvage, S. Ogale, Highly efficient photocatalysis by BiFeO3/α (γ)-Fe2O3 ferromagnetic nano p/n junctions formed by dopant-induced phase separation, Journal of nanoparticle research, 15 (2013) 1848.

[35] A. Oliveira, E.M. Saggioro, T. Pavesi, J.C. Moreira, L.F.V. Ferreira, Solar Photochemistry for Environmental Remediation-advanced oxidation processes for industrial wastewater treatment, in: Molecular Photochemistry-Various Aspects, InTech, 2012.

[36] N. Soltani, E. Saion, M.Z. Hussein, M. Erfani, A. Abedini, G. Bahmanrokh, M. Navasery, P. Vaziri, Visible light-induced degradation of methylene blue in the presence of photocatalytic ZnS and CdS nanoparticles, International journal of molecular sciences, 13 (2012) 12242-12258.

[37] K. Natarajan, T.S. Natarajan, R.I. Kureshy, H.C. Bajaj, W.K. Jo, R.J. Tayade, Photocatalytic H2 Production Using Semiconductor Nanomaterials via Water Splitting–An Overview, in: Advanced Materials Research, Trans Tech Publ, 2015, pp. 130-156.

[38] M.Z. Rahman, C.W. Kwong, K. Davey, S.Z. Qiao, 2D phosphorene as a water splitting photocatalyst: fundamentals to applications, Energy & Environmental Science, 9 (2016) 709-728.

[39] T. Hisatomi, J. Kubota, K. Domen, Recent advances in semiconductors for photocatalytic and photoelectrochemical water splitting, Chemical Society Reviews, 43 (2014) 7520-7535.

[40] Q. Chen, J. Li, X. Li, K. Huang, B. Zhou, W. Cai, W. Shangguan, Visible-light responsive photocatalytic fuel cell based on WO3/W photoanode and Cu2O/Cu photocathode for simultaneous wastewater treatment and electricity generation, Environmental science & technology, 46 (2012) 11451-11458.

[41] J. Yu, Q. Xiang, M. Zhou, Preparation, characterization and visible-light-driven photocatalytic activity of Fe-doped titania nanorods and first-principles study for electronic structures, Applied Catalysis B: Environmental, 90 (2009) 595-602.

[42] A. Zaleska, Doped-TiO2: a review, Recent Patents on Engineering, 2 (2008) 157-164.

[43] A.-W. Xu, Y. Gao, H.-Q. Liu, The preparation, characterization, and their photocatalytic activities of rare-earth-doped TiO2 nanoparticles, Journal of Catalysis, 207 (2002) 151-157.

[44] Y. Cong, J. Zhang, F. Chen, M. Anpo, Synthesis and characterization of nitrogen-doped TiO2 nanophotocatalyst with high visible light activity, The Journal of Physical Chemistry C, 111 (2007) 6976-6982.

[45] K. Kanade, B. Kale, J.-O. Baeg, S.M. Lee, C.W. Lee, S.-J. Moon, H. Chang, Self-assembled aligned Cu doped ZnO nanoparticles for photocatalytic hydrogen production under visible light irradiation, Materials Chemistry and Physics, 102 (2007) 98-104.

[46] M. Pelaez, N.T. Nolan, S.C. Pillai, M.K. Seery, P. Falaras, A.G. Kontos, P.S. Dunlop, J.W. Hamilton, J.A. Byrne, K. O'shea, A review on the visible light active titanium dioxide photocatalysts for environmental applications, Applied Catalysis B: Environmental, 125 (2012) 331-349.

[47] M. Rochkind, S. Pasternak, Y. Paz, Using dyes for evaluating photocatalytic properties: a critical review, Molecules, 20 (2014) 88-110.

[48] I.K. Konstantinou, T.A. Albanis, TiO2-assisted photocatalytic degradation of azo dyes in aqueous solution: kinetic and mechanistic investigations: A review, Applied Catalysis B: Environmental, 49 (2004) 1-14.

[49] D.F. Oliveira, P.S. Batista, P.S. Muller, V. Velani, M.D. França, D.R. De Souza, A.E. Machado, Evaluating the effectiveness of photocatalysts based on titanium dioxide in the degradation of the dye Ponceau 4R, Dyes and Pigments, 92 (2012) 563-572.

[50] Y. Kohno, S. Kitamura, T. Yamada, K. Sugihara, S. Ohta, Production of superoxide radical in reductive metabolism of a synthetic food-coloring agent, indigocarmine, and related compounds, Life sciences, 77 (2005) 601-614.

[51] J. Medina, M. Bizarro, C. Gomez, O. Depablos-Rivera, R. Mirabal-Rojas, B. Monroy, A. Fonseca-Garcia, J. Perez-Alvarez, S. Rodil, Sputtered bismuth oxide thin films as a potential photocatalytic material, Catalysis Today, 266 (2016) 144-152.

[52] X. Qin, H. Cheng, W. Wang, B. Huang, X. Zhang, Y. Dai, Three dimensional BiOX (X= Cl, Br and I) hierarchical architectures: facile ionic liquid-assisted solvothermal synthesis and photocatalysis towards organic dye degradation, Materials Letters, 100 (2013) 285-288.

[53] J. Li, Y. Yu, L. Zhang, Bismuth oxyhalide nanomaterials: layered structures meet photocatalysis, Nanoscale, 6 (2014) 8473-8488.

[54] Y. Huo, J. Zhang, M. Miao, Y. Jin, Solvothermal synthesis of flower-like BiOBr microspheres with highly visible-light photocatalytic performances, Applied Catalysis B: Environmental, 111 (2012) 334-341.

[55] X. Zhang, Z. Ai, F. Jia, L. Zhang, Generalized one-pot synthesis, characterization, and photocatalytic activity of hierarchical BiOX (X= Cl, Br, I) nanoplate microspheres, The Journal of Physical Chemistry C, 112 (2008) 747-753.

[56] L. Chen, R. Huang, M. Xiong, Q. Yuan, J. He, J. Jia, M.-Y. Yao, S.-L. Luo, C.-T. Au, S.-F. Yin, Room-Temperature Synthesis of Flower-Like BiOX (X・ Cl, Br, I) Hierarchical Structures and Their Visible-Light Photocatalytic Activity, Inorganic chemistry, 52 (2013) 11118-11125.

[57] U.A. Joshi, J.S. Jang, P.H. Borse, J.S. Lee, Microwave synthesis of single-crystalline perovskite Bi Fe O 3 nanocubes for photoelectrode and photocatalytic applications, Applied Physics Letters, 92 (2008) 242106.

[58] X. Wang, Y. Lin, X. Ding, J. Jiang, Enhanced visible-light-response photocatalytic activity of bismuth ferrite nanoparticles, Journal of Alloys and Compounds, 509 (2011) 6585-6588.

[59] F. Dong, W.-K. Ho, S. Lee, Z. Wu, M. Fu, S. Zou, Y. Huang, Template-free fabrication and growth mechanism of uniform (BiO) 2CO3 hierarchical hollow microspheres with outstanding photocatalytic activities under both UV and visible light irradiation, Journal of materials chemistry, 21 (2011) 12428-12436.

[60] F. Dong, S. Lee, Z. Wu, Y. Huang, M. Fu, W.-K. Ho, S. Zou, B. Wang, Rose-like monodisperse bismuth subcarbonate hierarchical hollow microspheres: One-pot template-free fabrication and excellent visible light photocatalytic activity and photochemical stability for NO removal in indoor air, Journal of hazardous materials, 195 (2011) 346-354.

[61] T. Zhao, J. Zai, M. Xu, Q. Zou, Y. Su, K. Wang, X. Qian, Hierarchical Bi 2 O 2 CO 3 microspheres with improved visible-light-driven photocatalytic activity, CrystEngComm, 13 (2011) 4010-4017.

[62] C. Martinez Suarez, S. Hernández, N. Russo, $BiVO_4$ as photocatalyst for solar fuels production through water splitting: A short review, Applied Catalysis A: General, 504 (2015) 158-170.

[63] K. Tolod, S. Hernández, N. Russo, Recent Advances in the BiVO4 Photocatalyst for Sun-Driven Water Oxidation: Top-Performing Photoanodes and Scale-Up Challenges, Catalysts, 7 (2017) 13.

[64] L. Zhang, D. Jiang, X. Xiang, X. Li, Precursor-induced self-assembly of Bi5O7NO3 nanocrystals into superstructures and their distinct photocatalytic performance, CrystEngComm, 17 (2014) 516-519.

[65] S. Yu, G. Zhang, Y. Gao, B. Huang, Single-crystalline Bi5O7NO3 nanofibers: Hydrothermal synthesis, characterization, growth mechanism, and photocatalytic properties, Journal of Colloid and Interface Science, 354 (2011) 322-330.

[66] X. Meng, Z. Zhang, Bismuth-based photocatalytic semiconductors: introduction, challenges and possible approaches, Journal of Molecular Catalysis A: Chemical, 423 (2016) 533-549.

[67] H.-Y. Jiang, G. Liu, P. Li, D. Hao, X. Meng, T. Wang, J. Lin, J. Ye, Nanorod-like α-Bi2O3: a highly active photocatalyst synthesized using g-C3N4as a template, RSC Adv., 4 (2014) 55062-55066.

[68] X. Xiao, R. Hu, C. Liu, C. Xing, C. Qian, X. Zuo, J. Nan, L. Wang, Facile large-scale synthesis of β-Bi2O3 nanospheres as a highly efficient photocatalyst for the degradation of acetaminophen under visible light irradiation, Applied Catalysis B: Environmental, 140-141 (2013) 433-443.

[69] M. Schlesinger, M. Weber, S. Schulze, M. Hietschold, M. Mehring, Metastable β-Bi2O3 Nanoparticles with Potential for Photocatalytic Water Purification Using Visible Light Irradiation, ChemistryOpen, 2 (2013) 146-155.

[70] W. Xiaohong, Q. Wei, H. Weidong, Thin bismuth oxide films prepared through the sol–gel method as photocatalyst, Journal of Molecular Catalysis A: Chemical, 261 (2007) 167-171.

[71] A. Harriman, J.M. Thomas, W.Z. Zhou, D.A. Jefferson, A New Family of Photocatalysts Based on Bi2O3, Journal of Solid State Chemistry, 72 (1988) 126-130.

[72] N.M. Sammes, G.A. Tompsett, H. Nafe, F. Aldinger, Bismuth based oxide electrolytes - Structure and ionic conductivity, Journal of the European Ceramic Society, 19 (1999) 1801-1826.

[73] H.A. Harwig, A.G. Gerards, Polymorphism of Bismuth Sesquioxide, Thermochim Acta, 28 (1979) 121-131.

[74] N.T. Nicoleta Cornei, Francis Abraham, and Olivier Mentre, New E-Bi2O3 Metastable Polymorph, Inorganic Chemistry Communications, 45 (2006) 4886-4888.

[75] H. Cheng, B. Huang, J. Lu, Z. Wang, B. Xu, X. Qin, X. Zhang, Y. Dai, Synergistic effect of crystal and electronic structures on the visible-light-driven photocatalytic performances of Bi2O3 polymorphs, Physical Chemistry Chemical Physics, 12 (2010) 15468-15475.

[76] H.A. Harwig, A.G. Gerards, Electrical-Properties of Alpha, Beta, Gamma and Delta Phases of Bismuth Sesquioxide, J. Solid State Chem., 26 (1978) 265-274.
[77] C.-H. Ho, C.-H. Chan, Y.-S. Huang, L.-C. Tien, L.-C. Chao, The study of optical band edge property of bismuth oxide nanowires α-Bi2O3, Opt. Express, 21 (2013) 11965-11972.
[78] Y. Xin, L. Xiaojuan, L. Shangjun, W. Gang, J. Chunping, T. Jing, C. Jinwei, W. Ruilin, Enhanced photocatalytic performance: a-Bi 2 O 3 thin film by nanoporous surface, Journal of Physics D: Applied Physics, 46 (2013) 035103.
[79] H.Y. Wang, Y.C. Yang, L. Le, Y. Liu, J.H. Wei, R. Xiong, J. Shi, Photocatalytic Properties of α-Bi2O3 Nanoneedle Array Synthesized by Hydrothermal Method, Solid State Phenomena, 181-182 (2011) 332-335.
[80] D.P. Dutta, M. Roy, A.K. Tyagi, Dual function of rare earth doped nano Bi2O3: white light emission and photocatalytic properties, Dalton Transactions, 41 (2012) 10238-10248.
[81] Y.-C. Wu, Y.-C. Chaing, C.-Y. Huang, S.-F. Wang, H.-Y. Yang, Morphology-controllable Bi2O3 crystals through an aqueous precipitation method and their photocatalytic performance, Dyes and Pigments, 98 (2013) 25-30.
[82] D. Sánchez-Martínez, I. Juárez-Ramírez, L.M. Torres-Martínez, I. de León-Abarte, Photocatalytic properties of Bi2O3 powders obtained by an ultrasound-assisted precipitation method, Ceramics International, 42 (2016) 2013-2020.
[83] Y. Yan, Z. Zhou, Y. Cheng, L. Qiu, C. Gao, J. Zhou, Template-free fabrication of α- and β-Bi2O3 hollow spheres and their visible light photocatalytic activity for water purification, Journal of Alloys and Compounds, 605 (2014) 102-108.
[84] P. Ziegler, M. Ströbele, H.-J. Meyer, Crystal structure of pentabismuth heptaoxide nitrate, Bi5O7NO3, Zeitschrift für Kristallographie-New Crystal Structures, 219 (2004) 101-102.
[85] T.N. Soitah, Y. Chunhui, Y. Yong, N. Yinghua, S. Liang, Properties of Bi 2 O 3 thin films prepared via a modified Pechini route, Current Applied Physics, 10 (2010) 1372-1377.
[86] H. Kodama, Synthesis of a new compound, Bi5O7NO3, by thermal decomposition, Journal of Solid State Chemistry, 112 (1994) 27-30.
[87] K. Barrera-Mota, M. Bizarro, M. Castellino, A. Tagliaferro, A. Hernández, S.E. Rodil, Spray deposited β-Bi 2 O 3 nanostructured films with visible photocatalytic activity for solar water treatment, Photochemical & Photobiological Sciences, 14 (2015) 1110-1119.
[88] K. Fujiwara, Y. Kuwahara, Y. Sumida, H. Yamashita, Fabrication of Photocatalytic Paper Using TiO2 Nanoparticles Confined in Hollow Silica Capsules, Langmuir, 33 (2017) 288-295.
[89] P. Pradhan, J.C. Alonso, M. Bizarro, Photocatalytic performance of ZnO: Al films under different light sources, International Journal of Photoenergy, 2012 (2012).

[90] R. Ran, J.G. McEvoy, Z. Zhang, Synthesis and Optimization of Visible Light Active BiVO4Photocatalysts for the Degradation of RhB, International Journal of Photoenergy, 2015 (2015) 1-14.

[91] A.-d. TiO, Photocatalytic Degradation of Synthetic Textile Effluent by Modified Sol-Gel, Synthesized Mobilized and Immobilized TiO, (2016).

[92] S. Wu, J. Fang, W. Xu, C. Cen, Bismuth-modified rectorite with high visible light photocatalytic activity, Journal of Molecular Catalysis A: Chemical, 373 (2013) 114-120.

[93] Z. Gareeva, O. Diéguez, J. Íñiguez, A. Zvezdin, Interplay between elasticity, ferroelectricity and magnetism at the domain walls of bismuth ferrite, physica status solidi (RRL)-Rapid Research Letters, 10 (2016) 209-217.

[94] S. Li, Y.-H. Lin, B.-P. Zhang, Y. Wang, C.-W. Nan, Controlled fabrication of BiFeO3 uniform microcrystals and their magnetic and photocatalytic behaviors, The Journal of Physical Chemistry C, 114 (2010) 2903-2908.

[95] J. Li, L. Wang, J.-B. Xu, L. Bian, A.-M. Chang, P.-J. Zhao, J.-Q. Zhang, X.-Q. Xiong, F.-L. Xu, Synthesis of nano-BiFeO3 by low-heating temperature solid state precursor method: using Different Types of Alkali, Integrated Ferroelectrics, 156 (2014) 129-136.

[96] F. Gao, X. Chen, K. Yin, S. Dong, Z. Ren, F. Yuan, T. Yu, Z. Zou, J.M. Liu, Visible-Light Photocatalytic Properties of Weak Magnetic BiFeO3 Nanoparticles, Advanced Materials, 19 (2007) 2889-2892.

[97] S. Li, Y.-H. Lin, B.-P. Zhang, C.-W. Nan, Y. Wang, Photocatalytic and magnetic behaviors observed in nanostructured BiFeO 3 particles, in, AIP, 2009.

[98] Y. Huo, M. Miao, Y. Zhang, J. Zhu, H. Li, Aerosol-spraying preparation of a mesoporous hollow spherical BiFeO 3 visible photocatalyst with enhanced activity and durability, Chemical Communications, 47 (2011) 2089-2091.

[99] G. Lee, E.M. Fuentes-Fernandez, G. Lian, R.S. Katiyar, O. Auciello, Hetero-epitaxial BiFeO3/SrTiO3 nanolaminates with higher piezoresponse performance over stoichiometric BiFeO3 films, Applied Physics Letters, 106 (2015) 022905.

[100] O. Gautreau, C. Harnagea, L. Gunawan, G.A. Botton, F. Normandin, T. Veres, L. Pintilie, M. Alexe, A. Pignolet, Structural and multiferroic properties of epitaxial γ-Fe2O3–BiFeO3/Bi3. 25La0. 75 Ti3O12 composite bi-layers, Journal of Physics D: Applied Physics, 41 (2008) 112002.

[101] T.A. Gadhi, A. Hernández-Gordillo, M. Bizarro, P. Jagdale, A. Tagliaferro, S.E. Rodil, Efficient α/β-Bi2O3 composite for the sequential photodegradation of two-dyes mixture, Ceramics International, 42 (2016) 13065-13073.

[102] L. Shan, G. Wang, D. Li, X. San, L. Liu, L. Dong, Z. Wu, Band alignment and enhanced photocatalytic activation of α/β-Bi2O3 heterojunctions via in situ phase transformation, Dalton Transactions, 44 (2015) 7835-7843.

[103] S. Hernández, S. Bensaid, M. Armandi, A. Sacco, A. Chiodoni, B. Bonelli, E. Garrone, C.F. Pirri, G. Saracco, A new method for studying activity and reaction kinetics of photocatalytic water oxidation systems using a bubbling reactor, Chemical Engineering Journal, 238 (2014) 17-26.

[104] B. Lu, Y. Zhu, Synthesis and photocatalysis performances of bismuth oxynitrate photocatalysts with layered structures, Physical Chemistry Chemical Physics, 16 (2014) 16509-16514.

[105] N. Henry, O. Mentré, F. Abraham, E. MacLean, P. Roussel, Polycationic disorder in [Bi 6 O 4 (OH) 4](NO 3) 6: structure determination using synchrotron radiation and microcrystal X-ray diffraction, Journal of Solid State Chemistry, 179 (2006) 3087-3094.

[106] J. Hou, C. Yang, Z. Wang, W. Zhou, S. Jiao, H. Zhu, In situ synthesis of α–β phase heterojunction on Bi2O3 nanowires with exceptional visible-light photocatalytic performance, Applied Catalysis B: Environmental, 142–143 (2013) 504-511.

[107] S. Ivanov, R. Tellgren, H. Rundlo, V. Orlov, Structural studies of α-Bi 2 O 3 by neutron powder diffraction, Powder Diffraction, 16 (2001) 227-230.

[108] A. Salazar-Pérez, M. Camacho-López, R. Morales-Luckie, V. Sánchez-Mendieta, F. Ureña-Núñez, J. Arenas-Alatorre, Structural evolution of Bi2O3 prepared by thermal oxidation of bismuth nano-particles, Superficies y vacío, 18 (2005) 4-8.

[109] W.W. Lee, C.-S. Lu, C.-W. Chuang, Y.-J. Chen, J.-Y. Fu, C.-W. Siao, C.-C. Chen, Synthesis of bismuth oxyiodides and their composites: characterization, photocatalytic activity, and degradation mechanisms, RSC Advances, 5 (2015) 23450-23463.

[110] K. Uchida, A. Ayame, Dynamic XPS measurements on bismuth molybdate surfaces, Surface science, 357 (1996) 170-175.

[111] E. Diez, O. Monnereau, L. Tortet, G. Vacquier, P. Llewellin, F. Rouquerol, Synthesis of bismuth (III) oxide from oxalate: A study by controlled transformation rate thermal analysis (CRTA), J. Optoelectron. Adv. Mater, 2 (2000) 552-556.

[112] H. Nohira, W. Tsai, W. Besling, E. Young, J. Pétry, T. Conard, W. Vandervorst, S. De Gendt, M. Heyns, J. Maes, Characterization of ALCVD-Al 2 O 3 and ZrO 2 layer using X-ray photoelectron spectroscopy, Journal of non-crystalline solids, 303 (2002) 83-87.

[113] B. Oprea, T. Radu, S. Simon, XPS investigation of atomic environment changes on surface of B 2 O 3–Bi 2 O 3 glasses, Journal of Non-Crystalline Solids, 379 (2013) 35-39.

[114] J. Xu, Y. Teng, F. Teng, Effect of Surface Defect States on Valence Band and Charge Separation and Transfer Efficiency, Scientific Reports, 6 (2016).

[115] W. Zhong, Y. Lou, S. Jin, W. Wang, L. Guo, A new Bi-based visible-light-sensitive photocatalyst BiLa1. 4Ca0. 6O4. 2: crystal structure, optical property and photocatalytic activity, Scientific reports, 6 (2016).

[116] P. Wang, M. Cheng, Z. Zhang, On different photodecomposition behaviors of rhodamine B on laponite and montmorillonite clay under visible light irradiation, Journal of Saudi Chemical Society, 18 (2014) 308-316.

[117] C.-C. Chen, C.-S. Lu, Mechanistic studies of the photocatalytic degradation of methyl green: an investigation of products of the decomposition processes, Environmental science & technology, 41 (2007) 4389-4396.

[118] K. Yu, S. Yang, H. He, C. Sun, C. Gu, Y. Ju, Visible light-driven photocatalytic degradation of rhodamine B over NaBiO3: pathways and mechanism, The Journal of Physical Chemistry A, 113 (2009) 10024-10032.

[119] A. Hernández-Gordillo, V. Rodríguez-González, S. Oros-Ruiz, R. Gómez, Photodegradation of Indigo Carmine dye by CdS nanostructures under blue-light irradiation emitted by LEDs, Catalysis Today, 266 (2016) 27-35.

[120] T.T. Guaraldo, T.B. Zanoni, S.I. de Torresi, V.R. Gonçales, G.J. Zocolo, D.P. Oliveira, M.V.B. Zanoni, On the application of nanostructured electrodes prepared by Ti/TiO 2/WO 3 “template”: A case study of removing toxicity of indigo using visible irradiation, Chemosphere, 91 (2013) 586-593.

[121] M. Coelho, F. de Andrade, G. de Lima, R. Augusti, M. Ferreira, D. Maria, J. Ardisson, Preparation of a new composite by reaction of SnBu3Cl with TiCl4 in the presence of NH4OH□ photocatalytic degradation of indigo carmine, Applied Organometallic Chemistry, 25 (2011) 220-225.

[122] P. Palanisamy, S. Kavitha, Photocatalytic Removal of Azo Dye and Anthraquinone DyeUsing TiO2 Immobilised on Ceramic Tiles, Journal of Chemistry, 8 (2011) 581-586.

[123] N. Muhd Julkapli, S. Bagheri, S. Bee Abd Hamid, Recent advances in heterogeneous photocatalytic decolorization of synthetic dyes, The Scientific World Journal, 2014 (2014).

[124] S. Abo-Farha, Photocatalytic degradation of monoazo and diazo dyes in wastewater on nanometer-sized TiO2, Journal of American science, 6 (2010) 130-142.

[125] M. Saquib, M. Muneer, Semiconductor mediated photocatalysed degradation of an anthraquinone dye, Remazol Brilliant Blue R under sunlight and artificial light source, Dyes and Pigments, 53 (2002) 237-249.

[126] M.A. Tariq, M. Faisal, M. Saquib, M. Muneer, Heterogeneous photocatalytic degradation of an anthraquinone and a triphenylmethane dye derivative in aqueous suspensions of semiconductor, Dyes and Pigments, 76 (2008) 358-365.

[127] R. Hu, X. Xiao, S. Tu, X. Zuo, J. Nan, Synthesis of flower-like heterostructured β-Bi2O3/Bi2O2CO3 microspheres using Bi2O2CO3 self-sacrifice precursor and its visible-light-induced photocatalytic degradation of o-phenylphenol, Applied Catalysis B: Environmental, 163 (2015) 510-519.

[128] X. Liu, J. Liu, H. Chu, J. Li, W. Yu, G. Zhu, L. Niu, Z. Sun, L. Pan, C.Q. Sun, Enhanced photocatalytic activity of Bi2O3–Ag2O hybrid photocatalysts, Applied Surface Science, 347 (2015) 269-274.

[129] J.C. Medina, M. Bizarro, C.L. Gomez, O. Depablos-Rivera, R. Mirabal-Rojas, B.M. Monroy, A. Fonseca-Garcia, J. Perez-Alvarez, S.E. Rodil, Sputtered bismuth oxide thin films as a potential photocatalytic material, Catalysis Today, (2015).

[130] M. Kosmulski, Compilation of PZC and IEP of sparingly soluble metal oxides and hydroxides from literature, Adv Colloid Interface Sci, 152 (2009) 14-25.

[131] KYRIAKOS BOURIKAS, A. CHRISTOS KORDULIS, A. LYCOURGHIOTIS, Differential Potentiometric Titration: Development of a Methodology for Determining the Point of Zero Charge of Metal (Hydr)oxides by One Titration Curve, Environent Science Technology, 39 (2005) 4100-4108.

[132] Q.-Y. Li, Z.-Y. Zhao, Interfacial properties of -Bi2O3 homo-junction from first-principles calculations, Physics Letters A, 379 (2015) 2766-2771.

[133] M.L. Yola, T. Eren, N. Atar, S. Wang, Adsorptive and photocatalytic removal of reactive dyes by silver nanoparticle-colemanite ore waste, Chemical Engineering Journal, 242 (2014) 333-340.

[134] A.G.S. Prado, L.B. Bolzon, C.P. Pedroso, A.O. Moura, L.L. Costa, Nb2O5 as efficient and recyclable photocatalyst for indigo carmine degradation, Applied Catalysis B: Environmental, 82 (2008) 219-224.

[135] N. Barka, A. Assabbane, A. Nounah, Y.A. Ichou, Photocatalytic degradation of indigo carmine in aqueous solution by TiO2-coated non-woven fibres, J Hazard Mater, 152 (2008) 1054-1059.

[136] M.M. Sousa, C. Miguel, I. Rodrigues, A.J. Parola, F. Pina, J.S. Seixas de Melo, M.J. Melo, A photochemical study on the blue dye indigo: from solution to ancient Andean textiles, Photochem Photobiol Sci, 7 (2008) 1353-1359.

[137] M.G. Coelho, F.V. de Andrade, G.M. de Lima, R. Augusti, M.P. Ferreira, D.A. Maria, J.D. Ardisson, Preparation of a new composite by reaction of SnBu3Cl with TiCl4 in the presence of NH4OH□photocatalytic degradation of indigo carmine, Applied Organometallic Chemistry, 25 (2011) 220-225.

[138] M.G. Coelho, G.M. de Lima, R. Augusti, D.A. Maria, J.D. Ardisson, New materials for photocatalytic degradation of Indigo Carmine—Synthesis, characterization and catalytic experiments of nanometric tin dioxide-based composites, Applied Catalysis B: Environmental, 96 (2010) 67-71.

[139] T.T. Guaraldo, T.B. Zanoni, S.I. de Torresi, V.R. Goncales, G.J. Zocolo, D.P. Oliveira, M.V. Zanoni, On the application of nanostructured electrodes prepared by Ti/TiO2/WO3 "template": a case study of removing toxicity of indigo using visible irradiation, Chemosphere, 91 (2013) 586-593.

[140] S. Sood, A. Umar, S. Kumar Mehta, S. Kumar Kansal, α-Bi2O3 nanorods: An efficient sunlight active photocatalyst for degradation of Rhodamine B and 2,4,6-trichlorophenol, Ceramics International, 41 (2015) 3355-3364.

[141] Y. Lu, Y. Zhao, J. Zhao, Y. Song, Z. Huang, F. Gao, N. Li, Y. Li, Photoactive β-Bi2O3 architectures prepared by a simple solution crystallization method, Ceramics International, 40 (2014) 15057-15063.

[142] Z. He, C. Sun, S. Yang, Y. Ding, H. He, Z. Wang, Photocatalytic degradation of rhodamine B by Bi(2)WO(6) with electron accepting agent under microwave irradiation: mechanism and pathway, J Hazard Mater, 162 (2009) 1477-1486.

[143] J.Z. Feng Chen, and Hisao Hidaka,, Highly selective deethylation of rhodamine B: Adsorption and photooxidation pathways of the dye on the TiO2/SiO2 composite photocatalyst, INTERNATIONAL JOURNAL OF PHOTOENERGY, 05 (2003) 209-217.

[144] A. Subrahmanyam, A. Rajakumar, M. Rakibuddin, T. Paul Ramesh, M. Raveendra Kiran, D. Shankari, K. Chandrasekhar, Efficacy of titanium doped-indium tin oxide (Ti/TiO2-ITO) films in rapid oxygen generation under photocatalysis and their suitability for bio-medical application, Phys Chem Chem Phys, 16 (2014) 24790-24799.

[145] G. Liu, J. Zhao, Photocatalytic degradation of dye sulforhodamine B: a comparative study of photocatalysis with photosensitization, New Journal of Chemistry, 24 (2000) 411-417.

[146] J. Tang, D. Li, Z. Feng, Z. Tan, B. Ou, A novel AgIO4 semiconductor with ultrahigh activity in photodegradation of organic dyes: insights into the photosensitization mechanism, RSC Adv., 4 (2014) 2151-2154.

[147] H.-Y. Jiang, P. Li, G. liu, J. Ye, J. Lin, Synthesis and photocatalytic properties of metastable β-Bi2O3stabilized by surface-coordination effects, J. Mater. Chem. A, 3 (2015) 5119-5125.

[148] E. Kordouli, K. Bourikas, A. Lycourghiotis, C. Kordulis, The mechanism of azo-dyes adsorption on the titanium dioxide surface and their photocatalytic degradation over samples with various anatase/rutile ratios, Catalysis Today, 252 (2015) 128-135.

[149] A. Charanpahari, S.S. Umare, R. Sasikala, Enhanced photodegradation of dyes on Bi2O3 microflakes: Effect of GeO2 addition on photocatalytic activity, Separation and Purification Technology, 133 (2014) 438-442.

[150] S.G. Ghugal, S.S. Umare, R. Sasikala, Enhanced photocatalytic activity of TiO 2 assisted by Nb, N and S multidopants, Materials Research Bulletin, 61 (2015) 298-305.

[151] F. Deng, X. Pei, Y. Luo, X. Luo, D.D. Dionysiou, S. Wu, S. Luo, Fabrication of Hierarchically Porous Reduced Graphene Oxide/SnIn4S8 Composites by a Low-Temperature Co-Precipitation Strategy and Their Excellent Visible-Light Photocatalytic Mineralization Performance, Catalysts, 6 (2016) 113.

[152] J.-M. Herrmann, Heterogeneous photocatalysis: fundamentals and applications to the removal of various types of aqueous pollutants, Catalysis today, 53 (1999) 115-129.

[153] B. Ohtani, Hidden but Possibly Fatal Misconceptions in Photocatalysis Studies: A Short Critical Review, Catalysts, 6 (2016) 192.

[154] H.-Y. Xu, L.-C. Wu, H. Zhao, L.-G. Jin, S.-Y. Qi, Synergic effect between adsorption and photocatalysis of metal-free gC 3 N 4 derived from different precursors, PloS one, 10 (2015) e0142616.

[155] T.A. Gadhi, L.S. Gómez-Velázquez, M. Bizarro, A. Hernández-Gordillo, A. Tagliaferro, S.E. Rodil, Evaluation of the photodiscoloration efficiency of β-Bi2O3 films deposited on different substrates by pneumatic spray pyrolysis, Thin Solid Films, 638 (2017) 119-126.

[156] J.-X. Ma, H. Yang, S. Li, R. Ren, J. Li, X. Zhang, J. Ma, Well-dispersed graphene-polydopamine-Pd hybrid with enhanced catalytic performance, RSC Advances, 5 (2015) 97520-97527.

[157] Y. Zhiyong, H. Keppner, D. Laub, E. Mielczarski, J. Mielczarski, L. Kiwi-Minsker, A. Renken, J. Kiwi, Photocatalytic discoloration of Methyl Orange on innovative parylene–TiO 2 flexible thin films under simulated sunlight, Applied Catalysis B: Environmental, 79 (2008) 63-71.

[158] N. Srividya, G. Paramasivan, K. Seetharaman, P. Ramamurthy, Two-step reduction of indigo carmine by dithionite: a stopped-flow study, Journal of the Chemical Society, Faraday Transactions, 90 (1994) 2525-2530.

[159] R. Camarillo, J. Rincón, Photocatalytic discoloration of dyes: relation between effect of operating parameters and dye structure, Chemical Engineering & Technology, 34 (2011) 1675-1684.

[160] D. Chatterjee, A. Mahata, Visible light induced photodegradation of organic pollutants on dye adsorbed TiO 2 surface, Journal of Photochemistry and Photobiology A: Chemistry, 153 (2002) 199-204.

[161] J. Bandara, J. Mielczarski, J. Kiwi, 2. Photosensitized degradation of azo dyes on Fe, Ti, and Al oxides. Mechanism of charge transfer during the degradation, Langmuir, 15 (1999) 7680-7687.

[162] K. Dai, H. Chen, T. Peng, D. Ke, H. Yi, Photocatalytic degradation of methyl orange in aqueous suspension of mesoporous titania nanoparticles, Chemosphere, 69 (2007) 1361-1367.

[163] M.M. Sousa, C. Miguel, I. Rodrigues, A.J. Parola, F. Pina, J.S.S. de Melo, M.J. Melo, A photochemical study on the blue dye indigo: from solution to ancient Andean textiles, Photochemical & Photobiological Sciences, 7 (2008) 1353-1359.

[164] M. Coelho, G. De Lima, R. Augusti, D. Maria, J. Ardisson, New materials for photocatalytic degradation of Indigo Carmine—Synthesis, characterization and catalytic experiments of nanometric tin dioxide-based composites, Applied Catalysis B: Environmental, 96 (2010) 67-71.

[165] W. Kuo, P. Ho, Solar photocatalytic decolorization of methylene blue in water, Chemosphere, 45 (2001) 77-83.

[166] S. Sood, A. Umar, S.K. Mehta, S.K. Kansal, α-Bi 2 O 3 nanorods: an efficient sunlight active photocatalyst for degradation of Rhodamine B and 2, 4, 6-trichlorophenol, Ceramics International, 41 (2015) 3355-3364.

[167] T. Watanabe, T. Takizawa, K. Honda, Photocatalysis through excitation of adsorbates. 1. Highly efficient N-deethylation of rhodamine B adsorbed to cadmium sulfide, The Journal of Physical Chemistry, 81 (1977) 1845-1851.

[168] J. Luan, M. Li, K. Ma, Y. Li, Z. Zou, Photocatalytic activity of novel Y 2 InSbO 7 and Y 2 GdSbO 7 nanocatalysts for degradation of environmental pollutant rhodamine B under visible light irradiation, Chemical Engineering Journal, 167 (2011) 162-171.

[169] A.J. Kettle, B.M. Clark, C.C. Winterbourn, Superoxide Converts Indigo Carmine to Isatin Sulfonic Acid IMPLICATIONS FOR THE HYPOTHESIS

THAT NEUTROPHILS PRODUCE OZONE, Journal of Biological Chemistry, 279 (2004) 18521-18525.

[170] M.L. Chacón-Patiño, C. Blanco-Tirado, J.P. Hinestroza, M.Y. Combariza, Biocomposite of nanostructured MnO 2 and fique fibers for efficient dye degradation, Green Chemistry, 15 (2013) 2920-2928.

[171] I. Dalmázio, A.P. de Urzedo, T. Alves, R.R. Catharino, M.N. Eberlin, C.C. Nascentes, R. Augusti, Electrospray ionization mass spectrometry monitoring of indigo carmine degradation by advanced oxidative processes, Journal of mass spectrometry, 42 (2007) 1273-1278.

[172] E. Ortiz, V. Gómez-Chávez, C.M. Cortés-Romero, H. Solís, R. Ruiz-Ramos, S. Loera-Serna, Degradation of Indigo Carmine Using Advanced Oxidation Processes: Synergy Effects and Toxicological Study, Journal of Environmental Protection, 7 (2016) 1693.

[173] F. Chen, J. Zhao, H. Hidaka, Highly selective deethylation of rhodamine B: Adsorption and photooxidation pathways of the dye on the TiO2/SiO2 composite photocatalyst, International Journal of Photoenergy, 5 (2003) 209-217.

[174] S. Hisaindee, M. Meetani, M. Rauf, Application of LC-MS to the analysis of advanced oxidation process (AOP) degradation of dye products and reaction mechanisms, TrAC Trends in Analytical Chemistry, 49 (2013) 31-44.

[175] X. Hou, W. Shen, X. Huang, Z. Ai, L. Zhang, Ascorbic acid enhanced activation of oxygen by ferrous iron: A case of aerobic degradation of rhodamine B, Journal of hazardous materials, 308 (2016) 67-74.

[176] T.S. Natarajan, M. Thomas, K. Natarajan, H.C. Bajaj, R.J. Tayade, Study on UV-LED/TiO 2 process for degradation of Rhodamine B dye, Chemical Engineering Journal, 169 (2011) 126-134.

[177] A. Garg, V.K. Sangal, P.K. Bajpai, Photocatalytic Treatment of Binary Mixture of Dyes using UV/TiO2 Process: Calibration, Modeling, Optimization and Mineralization Study, International Journal of Chemical Reactor Engineering, 15 (2017).

[178] S. Sekar, S. Mahadevan, B.K. Shanmugam, A.B. Mandal, Bioenergetics and pathway of acid blue 113 degradation by Staphylococcus lentus, Biotechnology progress, 28 (2012) 1400-1408.

[179] C.L. Bianchi, E. Colombo, S. Gatto, M. Stucchi, G. Cerrato, S. Morandi, V. Capucci, Photocatalytic degradation of dyes in water with micro-sized TiO 2 as powder or coated on porcelain-grès tiles, Journal of Photochemistry and Photobiology A: Chemistry, 280 (2014) 27-31.

[180] H. Dong, G. Zeng, L. Tang, C. Fan, C. Zhang, X. He, Y. He, An overview on limitations of TiO 2-based particles for photocatalytic degradation of organic pollutants and the corresponding countermeasures, water research, 79 (2015) 128-146.

[181] T.A. Gad-Allah, S. Kato, S. Satokawa, T. Kojima, Role of core diameter and silica content in photocatalytic activity of TiO 2/SiO 2/Fe 3 O 4 composite, Solid State Sciences, 9 (2007) 737-743.

[182] T.A. Gad-Allah, S. Kato, S. Satokawa, T. Kojima, Treatment of synthetic dyes wastewater utilizing a magnetically separable photocatalyst (TiO 2/SiO 2/Fe 3 O 4): parametric and kinetic studies, Desalination, 244 (2009) 1-11.

[183] N. Kaneva, A. Bojinova, K. Papazova, D. Dimitrov, I. Svinyarov, M. Bogdanov, Effect of thickness on the photocatalytic properties of ZnO thin films, BULGARIAN CHEMICAL COMMUNICATIONS, 47 (2015) 395-401.

[184] C. Schulze, C. Schulze, A. Kroll, C. Schulze, A. Kroll, C.-M. Lehr, U.F. Schäfer, K. Becker, J. Schnekenburger, C. Schulze Isfort, Not ready to use–overcoming pitfalls when dispersing nanoparticles in physiological media, Nanotoxicology, 2 (2008) 51-61.

[185] R. Albuquerque, M.C. Neves, M.H. Mendonça, T. Trindade, O.C. Monteiro, Adsorption and catalytic properties of SiO 2/Bi 2 S 3 nanocomposites on the methylene blue photodecolorization process, Colloids and Surfaces A: Physicochemical and Engineering Aspects, 328 (2008) 107-113.

[186] C. Anderson, A.J. Bard, An improved photocatalyst of TiO2/SiO2 prepared by a sol-gel synthesis, The Journal of Physical Chemistry, 99 (1995) 9882-9885.

[187] G.R.M. Echavia, F. Matzusawa, N. Negishi, Photocatalytic degradation of organophosphate and phosphonoglycine pesticides using TiO2 immobilized on silica gel, Chemosphere, 76 (2009) 595-600.

[188] T. Hirai, Y. Bando, Immobilization of CdS nanoparticles formed in reverse micelles onto aluminosilicate supports and their photocatalytic properties, Journal of colloid and interface science, 288 (2005) 513-516.

[189] K. Hofstadler, R. Bauer, S. Novalic, G. Heisler, New reactor design for photocatalytic wastewater treatment with TiO2 immobilized on fused-silica glass fibers: photomineralization of 4-chlorophenol, Environmental science & technology, 28 (1994) 670-674.

[190] G. Li, X. Zhao, M.B. Ray, Advanced oxidation of orange II using TiO 2 supported on porous adsorbents: The role of pH, H 2 O 2 and O 3, Separation and Purification Technology, 55 (2007) 91-97.

[191] M.-J. López-Muñoz, R. van Grieken, J. Aguado, J. Marugán, Role of the support on the activity of silica-supported TiO 2 photocatalysts: structure of the TiO 2/SBA-15 photocatalysts, Catalysis Today, 101 (2005) 307-314.

[192] P. Pucher, M. Benmami, R. Azouani, G. Krammer, K. Chhor, J.-F. Bocquet, A. Kanaev, Nano-TiO 2 sols immobilized on porous silica as new efficient photocatalyst, Applied Catalysis A: General, 332 (2007) 297-303.

[193] Z. Sun, C. Bai, S. Zheng, X. Yang, R.L. Frost, A comparative study of different porous amorphous silica minerals supported TiO2 catalysts, Applied Catalysis A: General, 458 (2013) 103-110.

[194] R. Van Grieken, J. Aguado, M. Lopez-Munoz, J. Marugán, Synthesis of size-controlled silica-supported TiO 2 photocatalysts, Journal of Photochemistry and Photobiology A: Chemistry, 148 (2002) 315-322.

[195] M.S. Vohra, K. Tanaka, Photocatalytic degradation of aqueous pollutants using silica-modified TiO 2, Water Research, 37 (2003) 3992-3996.

[196] N.F. Zainudin, A.Z. Abdullah, A.R. Mohamed, Characteristics of supported nano-TiO 2/ZSM-5/silica gel (SNTZS): photocatalytic degradation of phenol, Journal of Hazardous Materials, 174 (2010) 299-306.

[197] P. Fu, Y. Luan, X. Dai, Preparation of activated carbon fibers supported TiO 2 photocatalyst and evaluation of its photocatalytic reactivity, Journal of Molecular Catalysis A: Chemical, 221 (2004) 81-88.

[198] R. Yuan, R. Guan, J. Zheng, Effect of the pore size of TiO2-loaded activated carbon fiber on its photocatalytic activity, Scripta Materialia, 52 (2005) 1329-1334.

[199] X. Wang, Y. Liu, Z. Hu, Y. Chen, W. Liu, G. Zhao, Degradation of methyl orange by composite photocatalysts nano-TiO 2 immobilized on activated carbons of different porosities, Journal of Hazardous Materials, 169 (2009) 1061-1067.

[200] X. Zhang, M. Zhou, L. Lei, Enhancing the concentration of TiO2 photocatalyst on the external surface of activated carbon by MOCVD, Materials Research Bulletin, 40 (2005) 1899-1904.

[201] X. Zhang, M. Zhou, L. Lei, TiO2 photocatalyst deposition by MOCVD on activated carbon, Carbon, 44 (2006) 325-333.

[202] J.C. Joo, C.H. Ahn, D.G. Jang, Y.H. Yoon, J.K. Kim, L. Campos, H. Ahn, Photocatalytic degradation of trichloroethylene in aqueous phase using nano-ZNO/Laponite composites, Journal of hazardous materials, 263 (2013) 569-574.

[203] H. Khalilian, M. Behpour, V. Atouf, S.N. Hosseini, Immobilization of S, N-codoped TiO2 nanoparticles on glass beads for photocatalytic degradation of methyl orange by fixed bed photoreactor under visible and sunlight irradiation, Solar Energy, 112 (2015) 239-245.

[204] D. Ljubas, L. Ćurković, V. Marinović, I. Bačić, B. Tavčar, Photocatalytic degradation of azo dyes by sol–gel TiO2 films: effects of polyethylene glycol addition, reaction temperatures and irradiation wavelengths, Reaction Kinetics, Mechanisms and Catalysis, 116 (2015) 563-576.

[205] A. Haenel, P. Moren, A. Zaleska, J. Hupka, Photocatalytic activity of TiO2 immobilized on glass beads, Physicochem. Probl. Miner. Process, 45 (2010) 49-56.

[206] M. Borges, D.M. García, T. Hernández, J.C. Ruiz-Morales, P. Esparza, Supported photocatalyst for removal of emerging contaminants from wastewater in a continuous packed-bed photoreactor configuration, Catalysts, 5 (2015) 77-87.

[207] A.S. El-Kalliny, S.F. Ahmed, L.C. Rietveld, P.W. Appel, Immobilized photocatalyst on stainless steel woven meshes assuring efficient light distribution in a solar reactor, Drink. Water Eng. Sci., 7 (2014) 41-52.

[208] D. Pérez-Mezcua, I. Bretos, R. Jiménez, J. Ricote, R.J. Jiménez-Rioboó, C.G. Da Silva, D. Chateigner, L. Fuentes-Cobas, R. Sirera, M.L. Calzada, Photochemical solution processing of films of metastable phases for flexible devices: the β-Bi2O3 polymorph, Scientific reports, 6 (2016) 39561.

[209] S.J. Moniz, C.S. Blackman, C.J. Carmalt, G. Hyett, MOCVD of crystalline Bi 2 O 3 thin films using a single-source bismuth alkoxide precursor and their use

in photodegradation of water, Journal of Materials Chemistry, 20 (2010) 7881-7886.

[210] J.C. Medina, M. Bizarro, P. Silva-Bermudez, M. Giorcelli, A. Tagliaferro, S.E. Rodil, Photocatalytic discoloration of methyl orange dye by δ-Bi2O3 thin films, Thin Solid Films, 612 (2016) 72-81.

[211] M. Bizarro, E. Martínez-Padilla, Visible light responsive photocatalytic ZnO:Al films decorated with Ag nanoparticles, Thin Solid Films, 553 (2014) 179-183.

[212] N.S. Portillo-Vélez, A. Hernández-Gordillo, M. Bizarro, Morphological effect of ZnO nanoflakes and nanobars on the photocatalytic dye degradation, Catalysis Today, 287 (2017) 106-112.

[213] Portillo-V, #xe9, N.S. lez, M. Bizarro, Sprayed Pyrolyzed ZnO Films with Nanoflake and Nanorod Morphologies and Their Photocatalytic Activity, Journal of Nanomaterials, 2016 (2016) 11.

[214] C.M. Ling, A.R. Mohamed, S. Bhatia, Performance of photocatalytic reactors using immobilized TiO 2 film for the degradation of phenol and methylene blue dye present in water stream, Chemosphere, 57 (2004) 547-554.

[215] G. Balasubramanian, D.D. Dionysiou, M.T. Suidan, I. Baudin, J.-M. Laîné, Evaluating the activities of immobilized TiO 2 powder films for the photocatalytic degradation of organic contaminants in water, Applied Catalysis B: Environmental, 47 (2004) 73-84.

[216] H. Choi, E. Stathatos, D.D. Dionysiou, Sol–gel preparation of mesoporous photocatalytic TiO 2 films and TiO 2/Al 2 O 3 composite membranes for environmental applications, Applied Catalysis B: Environmental, 63 (2006) 60-67.

[217] J.L. Yang, S.J. An, W.I. Park, G.C. Yi, W. Choi, Photocatalysis using ZnO thin films and nanoneedles grown by metal–organic chemical vapor deposition, Advanced materials, 16 (2004) 1661-1664.

[218] G.L. Puma, A. Bono, D. Krishnaiah, J.G. Collin, Preparation of titanium dioxide photocatalyst loaded onto activated carbon support using chemical vapor deposition: A review paper, Journal of hazardous Materials, 157 (2008) 209-219.

[219] Z. Ding, X. Hu, G.Q. Lu, P.-L. Yue, P.F. Greenfield, Novel silica gel supported TiO2 photocatalyst synthesized by CVD method, Langmuir, 16 (2000) 6216-6222.

[220] X. Xiao, R. Hu, C. Liu, C. Xing, C. Qian, X. Zuo, J. Nan, L. Wang, Facile large-scale synthesis of β-Bi 2 O 3 nanospheres as a highly efficient photocatalyst for the degradation of acetaminophen under visible light irradiation, Applied Catalysis B: Environmental, 140 (2013) 433-443.

[221] M. Schlesinger, M. Weber, S. Schulze, M. Hietschold, M. Mehring, Metastable β-Bi2O3 Nanoparticles with Potential for Photocatalytic Water Purification Using Visible Light Irradiation, ChemistryOpen, 2 (2013) 146-155.

[222] X. Xiao, S. Tu, C. Zheng, H. Zhong, X. Zuo, J. Nan, l-Asparagine-assisted synthesis of flower-like β-Bi 2 O 3 and its photocatalytic performance for the

degradation of 4-phenylphenol under visible-light irradiation, RSC Advances, 5 (2015) 74977-74985.

[223] X. Yang, X. Lian, S. Liu, G. Wang, C. Jiang, J. Tian, J. Chen, R. Wang, Enhanced photocatalytic performance: a β-Bi2O3 thin film by nanoporous surface, Journal of Physics D: Applied Physics, 46 (2012) 035103.

[224] Y. Lu, Y. Zhao, J. Zhao, Y. Song, Z. Huang, F. Gao, N. Li, Y. Li, Induced Aqueous Synthesis of Metastable β-Bi2O3 Microcrystals for Visible-Light Photocatalyst Study, Crystal Growth & Design, 15 (2015) 1031-1042.

[225] M. Bizarro, A. Sánchez-Arzate, I. Garduno-Wilches, J. Alonso, A. Ortiz, Synthesis and characterization of ZnO and ZnO: Al by spray pyrolysis with high photocatalytic properties, Catalysis today, 166 (2011) 129-134.

[226] M. Bizarro, High photocatalytic activity of ZnO and ZnO:Al nanostructured films deposited by spray pyrolysis, Applied Catalysis B: Environmental, 97 (2010) 198-203.

[227] L. Shan, G. Wang, D. Li, X. San, L. Liu, L. Dong, Z. Wu, Band alignment and enhanced photocatalytic activation of α/β-Bi 2 O 3 heterojunctions via in situ phase transformation, Dalton Transactions, 44 (2015) 7835-7843.

[228] J.-K. Kim, D.F. Lawler, Characteristics of zeta potential distribution in silica particles, Bulletin of the Korean Chemical Society, 26 (2005) 1083-1089.

[229] M. Kobayashi, F. Juillerat, P. Galletto, P. Bowen, M. Borkovec, Aggregation and charging of colloidal silica particles: effect of particle size, Langmuir, 21 (2005) 5761-5769.

[230] H. Li, C.P. Tripp, Infrared study of the interaction of charged silica particles with TiO2 particles containing adsorbed cationic and anionic polyelectrolytes, Langmuir, 21 (2005) 2585-2590.

[231] I.K. Konstantinou, T.A. Albanis, TiO 2-assisted photocatalytic degradation of azo dyes in aqueous solution: kinetic and mechanistic investigations: a review, Applied Catalysis B: Environmental, 49 (2004) 1-14.

[232] N.M. Mahmoodi, M. Arami, N.Y. Limaee, N.S. Tabrizi, Kinetics of heterogeneous photocatalytic degradation of reactive dyes in an immobilized TiO 2 photocatalytic reactor, Journal of colloid and interface Science, 295 (2006) 159-164.

[233] T.T. Guaraldo, T.B. Zanoni, S.I.C. de Torresi, V.R. Gonçales, G.J. Zocolo, D.P. Oliveira, M.V.B. Zanoni, On the application of nanostructured electrodes prepared by Ti/TiO2/WO3 “template”: A case study of removing toxicity of indigo using visible irradiation, Chemosphere, 91 (2013) 586-593.

[234] J. Xiao, H. Zhang, Y. Xia, Z. Li, W. Huang, Rapid and high-capacity adsorption of sulfonated anionic dyes onto basic bismuth (III) nitrate via bidentate bridging and electrostatic attracting interactions, RSC Advances, 6 (2016) 39861-39869.

[235] K. Tanaka, K. Padermpole, T. Hisanaga, Photocatalytic degradation of commercial azo dyes, Water research, 34 (2000) 327-333.

[236] Y. Liu, L. Yu, Y. Hu, C. Guo, F. Zhang, X.W.D. Lou, A magnetically separable photocatalyst based on nest-like γ-Fe 2 O 3/ZnO double-shelled hollow structures with enhanced photocatalytic activity, Nanoscale, 4 (2012) 183-187.

[237] M. He, D. Li, D. Jiang, M. Chen, Magnetically separable γ-Fe 2 O 3@ SiO 2@ Ce-doped TiO 2 core–shell nanocomposites: Fabrication and visible-light-driven photocatalytic activity, Journal of Solid State Chemistry, 192 (2012) 139-143.

[238] Z. Lou, F. Li, J. Deng, L. Wang, T. Zhang, Branch-like hierarchical heterostructure (α-Fe2O3/TiO2): a novel sensing material for trimethylamine gas sensor, ACS applied materials & interfaces, 5 (2013) 12310-12316.

[239] T.-J. Park, G.C. Papaefthymiou, A.J. Viescas, A.R. Moodenbaugh, S.S. Wong, Size-dependent magnetic properties of single-crystalline multiferroic BiFeO3 nanoparticles, Nano letters, 7 (2007) 766-772.

[240] J.T. Han, Y.H. Huang, X.J. Wu, C.L. Wu, W. Wei, B. Peng, W. Huang, J.B. Goodenough, Tunable synthesis of bismuth ferrites with various morphologies, Advanced Materials, 18 (2006) 2145-2148.

[241] S.M. Selbach, T. Tybell, M.-A. Einarsrud, T. Grande, Size-dependent properties of multiferroic BiFeO3 nanoparticles, Chemistry of Materials, 19 (2007) 6478-6484.

[242] T. Zhang, Y. Shen, Y. Qiu, Y. Liu, R. Xiong, J. Shi, J. Wei, Facial Synthesis and Photoreaction Mechanism of BiFeO3/Bi2Fe4O9 Heterojunction Nanofibers, ACS Sustainable Chemistry & Engineering, (2017).

[243] F.E. Ramirez, G.A. Pasca, J.A. Souza, Possible misleading interpretations on magnetic and transport properties in BiFeO 3 nanoparticles caused by impurity phase, Physics Letters A, 379 (2015) 1549-1553.

[244] Y. Huo, Y. Jin, Y. Zhang, Citric acid assisted solvothermal synthesis of BiFeO 3 microspheres with high visible-light photocatalytic activity, Journal of Molecular Catalysis A: Chemical, 331 (2010) 15-20.

[245] S.M. Selbach, M.A. Einarsrud, T. Tybell, T. Grande, Synthesis of BiFeO3 by wet chemical methods, Journal of the American Ceramic Society, 90 (2007) 3430-3434.

[246] J.L. Ortiz-Quiñonez, D. Díaz, I. Zumeta-Dubé, H. Arriola-Santamaría, I. Betancourt, P. Santiago-Jacinto, N. Nava-Etzana, Easy synthesis of high-purity BiFeO3 nanoparticles: new insights derived from the structural, optical, and magnetic characterization, Inorganic chemistry, 52 (2013) 10306-10317.

[247] M. Hojamberdiev, Y. Xu, F. Wang, J. Wang, W. Liu, M. Wang, Morphology-controlled hydrothermal synthesis of bismuth ferrite using various alkaline mineralizers, Ceramics–Silikáty, 53 (2009) 113-117.

[248] T. Wu, L. Liu, M. Pi, D. Zhang, S. Chen, Enhanced magnetic and photocatalytic properties of Bi 2 Fe 4 O 9 semiconductor with large exposed (001) surface, Applied Surface Science, 377 (2016) 253-261.

[249] Y. Xiong, M. Wu, Z. Peng, N. Jiang, Q. Chen, Hydrothermal synthesis and characterization of Bi2Fe4O9 nanoparticles, Chemistry letters, 33 (2004) 502-503.

[250] J. Zhao, T. Liu, Y. Xu, Y. He, W. Chen, Synthesis and characterization of Bi 2 Fe 4 O 9 powders, Materials Chemistry and Physics, 128 (2011) 388-391.

[251] T. Liu, Y. Xu, C. Zeng, Synthesis of Bi 2 Fe 4 O 9 via PVA sol–gel route, Materials Science and Engineering: B, 176 (2011) 535-539.

[252] J. Chen, X. Xing, A. Watson, W. Wang, R. Yu, J. Deng, L. Yan, C. Sun, X. Chen, Rapid synthesis of multiferroic BiFeO3 single-crystalline nanostructures, Chemistry of materials, 19 (2007) 3598-3600.

[253] G. Catalan, J.F. Scott, Physics and applications of bismuth ferrite, Advanced Materials, 21 (2009) 2463-2485.

[254] B. Sun, P. Han, W. Zhao, Y. Liu, P. Chen, White-light-controlled magnetic and ferroelectric properties in multiferroic BiFeO3 square nanosheets, The Journal of Physical Chemistry C, 118 (2014) 18814-18819.

[255] L. Fei, J. Yuan, Y. Hu, C. Wu, J. Wang, Y. Wang, Visible light responsive perovskite BiFeO3 pills and rods with dominant {111} c facets, Crystal Growth & Design, 11 (2011) 1049-1053.

[256] X. Wang, Y.g. Zhang, Z. Wu, Magnetic and optical properties of multiferroic bismuth ferrite nanoparticles by tartaric acid-assisted sol–gel strategy, Materials Letters, 64 (2010) 486-488.

[257] R.C. Haislmaier, N.J. Podraza, S. Denev, A. Melville, D.G. Schlom, V. Gopalan, Large nonlinear optical coefficients in pseudo-tetragonal BiFeO3 thin films, Applied Physics Letters, 103 (2013) 031906.

[258] P. Mallick, B. Dash, X-ray Diffraction and UV-Visible Characterizations of α-Fe 2 O 3 Nanoparticles Annealed at Different Temperature, Nanoscience and Nanotechnology, 3 (2013) 130-134.

[259] C. Jia, Y. Chen, Y. Guo, X. Liu, S. Yang, W. Zhang, Z. Wang, Valence band offset of InN/BaTiO3 heterojunction measured by X-ray photoelectron spectroscopy, Nanoscale research letters, 6 (2011) 316.

[260] J. Hou, C. Yang, Z. Wang, W. Zhou, S. Jiao, H. Zhu, In situ synthesis of α–β phase heterojunction on Bi 2 O 3 nanowires with exceptional visible-light photocatalytic performance, Applied Catalysis B: Environmental, 142 (2013) 504-511.

[261] K. Dai, L. Lu, C. Liang, G. Zhu, Q. Liu, L. Geng, J. He, A high efficient graphitic-C3N4/BiOI/graphene oxide ternary nanocomposite heterostructured photocatalyst with graphene oxide as electron transport buffer material, Dalton Transactions, 44 (2015) 7903-7910.

[262] Z. Xiang, Y. Wang, D. Zhang, P. Ju, BiOI/BiVO4 p☐n heterojunction with enhanced photocatalytic activity under visible-light irradiation, Journal of Industrial and Engineering Chemistry, 40 (2016) 83-92.

[263] S.P. Patil, B. Bethi, G.H. Sonawane, V.S. Shrivastava, S. Sonawane, Efficient adsorption and photocatalytic degradation of Rhodamine B dye over Bi2O3-bentonite nanocomposites: A kinetic study, Journal of Industrial and Engineering Chemistry, 34 (2016) 356-363.

[264] S.-R. Kim, I. Ali, J.-O. Kim, Electrochemical synthesis of co-doped RGO–Bi–TiO2 nanotube composite: Enhanced activity under visible light, Journal of Industrial and Engineering Chemistry, 54 (2017) 316-323.
[265] L. Shan, G. Wang, D. Li, X. San, L. Liu, L. Dong, Z. Wu, Band alignment and enhanced photocatalytic activation of [small alpha]/[small beta]-Bi2O3 heterojunctions via in situ phase transformation, Dalton Transactions, 44 (2015) 7835-7843.
[266] T. Sauer, G.C. Neto, H. Jose, R. Moreira, Kinetics of photocatalytic degradation of reactive dyes in a TiO 2 slurry reactor, Journal of Photochemistry and Photobiology A: Chemistry, 149 (2002) 147-154.